ENTRAINMENT BY PENETRATIVE CONVECTION AT LOW PÉCLET NUMBER

A thesis
submitted in partial fulfilment
of the requirements for the Degree
of
Doctor of Philosophy in Civil Engineering
at the
University of Canterbury
by

RICHARD ANDREW DENTON

University of Canterbury,
Christchurch, New Zealand

January 1978

ABSTRACT

A theoretical one-dimensional model of interfacial entrainment has been developed which models the temporal behaviour of an initially quiescent, stable temperature stratification heated from below. The specific two-layered stratification, analysed in the thesis, is an inverted model of penetrative convection in the surface layer of a thermal power station cooling pond. At the interface between the uniformly mixed turbulent convection layer and the essentially non-turbulent diffusion region, temperature and heat flux are taken to be continuous. However, the partial derivatives of temperature with respect to height and time are assumed to be discontinuous. The rate of rise of the interface is obtained by matching the changes in vertical temperature profile immediately above and below the interface.

The heat transfer above the interface due to penetrating interfacial domes of mixed layer fluid is parameterized by a turbulent diffusivity term and an additional molecular diffusion factor. Both these parameters decrease to zero with increasing height above the interface. However, in this low Péclet number case, molecular diffusion is found to be significant. It is also found that the "filling" (with heat) of the vertical temperature profile, due to the lower boundary heat flux, makes a major contribution to the rate of rise of the interface. As a result, the turbulent entrainment parameters make a relatively minor contribution.

The empirical relationship for the turbulent diffusivity term, used in the numerical analyses of the model, combines two previously used methods of presenting interfacial entrainment data. It is consistent with data from high Péclet number mechanical stirring grid experiments and also describes the variation of the heat flux ratio k in atmospheric studies.

Laboratory experiments using both steady and unsteady heat flux apparatus were also performed. Good agreement was found between the experimental and numerical analyses.

A review of thermal convection above and below horizontal plates is presented in the appendices. In this review, a graphical form, $c_q = Nu/Ra^{1/3}$ versus $\log Ra$, has been developed. The graphical form allows convection data to be plotted in greater detail than previous methods. It also describes the variation in the heat flux with changes in the convection layer thickness if all other variables are fixed.

ACKNOWLEDGEMENTS

The research for this thesis was carried out in the Department of Civil Engineering, University of Canterbury, under the overall guidance of its Head, Professor H.J. Hopkins.

I gratefully acknowledge the assistance given to me during the course of this project and extend my thanks to:

Professor I.R. Wood, my supervisor, for his encouragement, guidance and helpful criticisms;

Mr. H.S. Pearce of the Technical Staff of the Civil Engineering Department for the construction of the experimental apparatus and his assistance during the performance of the experiments;

Mr. P.J. Robinson of the Technical Staff who designed and built the thermocouple amplifiers and temperature controllers used during the experimental investigation;

Mrs. D.E. Ball for typing the manuscript;

Mr. H. Patterson for the photography;

The other members of the Academic and Technical Staff of the Department of Civil Engineering and my fellow students for many helpful discussions.

This research was assisted financially by the University Grants Committee of New Zealand.

Finally, I would like to thank my parents for their encouragement and support during the course of this project.

TABLE OF CONTENTS

LIST OF FIGURES

Page

Page

LIST OF TABLES

LIST OF SYMBOLS

Note: Symbols which have limited use and are defined in the text are not generally listed.

A	Area of fluid column
c_p	Specific heat per unit mass
c_q	Heat transfer coefficient $= Nu/Ra^{1/3}$
d	Interplate spacing for parallel-plate convection
d_g	Height of maximum temperature gradient
d_h	Mean temperature profile height
d_m	Interface height (mixed layer thickness)
E	Non-dimensional interfacial buoyancy heat flux based on the interfacial temperature gradient $= - Q_e/\ell_s V_s (\partial T/\partial z)_i$
E_o	Non-dimensional interfacial buoyancy heat flux based on the interfacial temperature difference $= - Q_e/V_s \Delta T_i$
E_{max}	Maximum value of E (or E_o)
f	Grid stirring frequency
g	Gravitational acceleration
h_T	Fluid column height
$I(z)$	Intermittency factor for interfacial turbulence
K_G	Thermal conductivity of glass layer
K_T	Thermal conductivity of upper boundary insulation
K_V	Thermal conductivity of side wall material and insulation
k	Heat flux ratio for Betts' (1973) model
k_e	Ratio of interfacial and lower boundary heat fluxes $= - Q_e/Q_p$
k_h	Ratio of hypothetical interfacial heat flux $\beta V_{em} \Delta T_i$ and the lower boundary heat flux Q_p
k_m	Ratio of the heat flux $\beta V_{eh} \Delta T_i$ and the lower boundary heat flux Q_p
L	Minimum plan dimension of convection layer
ℓ_i	Interfacial thickness term $= \Delta T_i/(\partial T/\partial z)_i$
ℓ_s	Turbulent convection length scale
Nu	Nusselt number $= Qd/\kappa\Delta T$
P	Fluid column perimeter
Pe	Péclet number $= \ell_s V_s/\kappa$
Pr	Prandtl number $= \nu/\kappa$
Q	Buoyancy heat flux $= q/\rho c_p$
Q_e	Interfacial buoyancy heat flux ($z = d_m$)
Q_p	Lower boundary buoyancy heat flux ($z = 0$)
q	Heat flux per unit area
q_G	Heat flux per unit area through glass layer
Ra	Rayleigh number $= \alpha g \Delta T d^3/\nu\kappa$

Re	Reynolds number $= \ell_s V_s/\nu$
Ri	Richardson number based on the interfacial temperature gradient $= \alpha g (\partial T/\partial z)_i \ell_s^2 / V_s^2$
Ri_o	Richardson number based on the interfacial temperature difference $= \alpha g \Delta T_i \ell_s / V_s^2$
S_p	Heat storage capacity of the steady heat flux apparatus between $z = 0$ and mid-height of the glass layer
T	Temperature
T_a	Maximum temperature in the diffusion region
T_{air}	Temperature of air outside experimental apparatus
T_H	Temperature of circulated heating water in unsteady heat flux experiment
T_m	Mixed layer temperature
T_p	Temperature of lower boundary plate ($z = 0$)
T_s	Turbulent convection temperature scale based on $\ell_s = Q_p/V_s$
T_*	Deardoff's (1970) temperature scale based on $d_m = Q_p/w_*$
t	Time
t_s	Time when heating commences ($Q_p > 0$)
t_T	Time when interfacial entrainment period ends
t*	Time till boundary layer breakup in Howard's (1964) convection model
u_*	Shear velocity $= (\tau/\rho)^{1/2}$
V_{eh}	Rate of increase of the mean temperature profile height d_h
V_{em}	Rate of rise of the interface $= d(d_m)/dt$
V_s	Turbulent convection velocity scale based on $\ell_s = (\alpha g Q_p \ell_s)^{1/3}$
W	Side wall heat loss factor $= K_V P/\rho c_p A$
W_{ex}	Additional empirical heat loss factor (steady heat flux experiments)
W_p	Heat loss factor for steady heat flux heating apparatus
W_T	Upper boundary heat loss factor $= K_T/\rho c_p$
w_*	Deardoff's (1970) velocity scale based on $d_m = (\alpha g Q_p d_m)^{1/3}$
z	Height above heated boundary
z_b	Thickness of buoyancy production region $= -\Delta T_p/(\partial T/\partial z)_{z=0}$
z_{grid}	Distance between mean stirring grid position and interface
z_{int}	Thickness of the intermittency region $0 < I < 1$
z_{stroke}	Stroke length of stirring grid

α	Volumetric coefficient of thermal expansion $= -(\partial\rho/\partial T)/\rho$
β	Heat storage term for fluid column and side walls per unit height
β_T	Heat storage term for upper boundary
Γ	Temperature gradient well above the interface ($z >> d_m$)
Γ_ρ	Density gradient well above the interface
γ	Turbulent diffusivity parameter
ΔT	Temperature difference between plates in parallel-plate convection

ΔT_H Temperature difference between circulated heating water and mixed layer fluid $= T_H - T_m$

ΔT_i Difference between maximum fluid column temperature and mixed layer temperature $= T_a - T_m$

ΔT_p Temperature difference between the lower boundary plate and the mixed layer $= T_p - T_m$

ΔU Horizontal velocity difference across the interface in shear experiments

Δz Spacing of finite difference nodes

δt Incremental time step

ε Turbulent dissipation

κ Molecular diffusivity

λ Additional molecular diffusion factor

ν Viscosity

ξ Non-dimensional distance from heated boundary for thermal convection $= z/2\sqrt{\kappa t}$

ρ Density

σ_T Root mean square temperature fluctuation

σ_u Root mean square horizontal velocity

σ_w Root mean square vertical velocity

τ Shear stress

$\phi(x)$ Function of x

Subscripts

Note: These subscripts are additional to those used above.

i Denotes term evaluated on the diffusion region side of the interfacial discontinuity $(z = d_m^+)$

L Heat loss value

m Mixed layer value

max Maximum value

s Denotes term evaluated at time t_s

0 Denotes term evaluated at time $t = 0$

CHAPTER 1

INTRODUCTION

1.1 GENERAL DISCUSSION

The entrainment of heat, mass and momentum across the interface between a region of turbulent fluid and the surrounding fluid has been widely studied (Chapter 2). When the turbulent region is a turbulent convection layer, caused by a significant positive buoyancy flux applied to the upper or lower boundary of a fluid column, the interfacial entrainment process is known as penetrative convection. The buoyancy flux is taken to be positive in the vertically upwards direction. Typically, the turbulent interfacial motions result in a net transfer of fluid into the turbulent region. The volume of the turbulent region increases and the turbulence spreads. If the fluid beyond the turbulent region is stably stratified, the transfer of fluid produces a net flux of heat or mass into the turbulent region (i.e. a negative buoyancy flux at the interface). The molecular diffusion of heat and mass down the stable density gradient (toward the turbulent region) also contributes to the negative interfacial buoyancy flux.

The rate of spread of the turbulent region will be governed by the turbulent intensity of the interface, the density distribution beyond the interface and the molecular diffusivity of the component causing the density difference. If there is no density difference between the turbulent region and the surrounding fluid, the rate of growth of the turbulent region will only be dependent on the turbulent intensity. If a stable density gradient exists above or below the turbulent region, small scale interfacial turbulence will be damped. The buoyancy frequency of the interfacial region will control the interfacial motions and the rate of growth of the turbulent region will be reduced.

As the interfacial turbulence decreases with increasing interfacial stability, the transfer of heat and mass by molecular diffusion will become important. The relative importance of molecular transfer of heat and mass is often expressed by the Péclet number

$$Pe = \ell_s V_s / \kappa$$

where ℓ_s and V_s are turbulent length and velocity scales and κ is the molecular diffusivity. If the Péclet number is large, molecular diffusion effects are negligible. For low Péclet numbers, molecular diffusion may make a significant contribution to the heat transfer process.

An idealized vertical density profile $\rho(z)$ for penetrative convection in a fluid column heated from below is sketched in Fig. 1.1. The height (or depth) z is positive in the vertical direction away from the heated (or cooled) boundary at $z = 0$. The turbulent convection layer, thickness d_m, is assumed to be uniformly mixed. It has uniform density and temperature (T_m), horizontally and vertically, except within the buoyancy production layer at the heated boundary where the density distribution is highly unstable. For large Rayleigh numbers, the relative thickness of the buoyancy production layer to the full mixed layer thickness d_m is negligible. The turbulent convection layer $0 < z < d_m$ will hereafter be referred to as the mixed layer.

Beyond the mixed layer is a region of stable density stratification (Fig. 1.1). To be consistent with the reported sharpening of the interface by interfacial entrainment (Rouse and Dodu 1955), the density gradient is assumed to be discontinuous at the interface. This is a departure from previous models (e.g. Betts 1973) in which the temperature $T(z)$, and hence density $\rho(z)$, were assumed to be discontinuous at $z = d_m$. The assumption that the interfacial gradients of temperature and density are discontinuous is a basic assumption in the theoretical model developed in this study. It will be discussed in more detail later (Chapter 3). The density gradient on the non-turbulent side of the interfacial discontinuity ($z = d_m^+$) is $\left.\frac{\partial \rho}{\partial z}\right|_i$. The subscript i applies to all quantities evaluated at $z = d_m^+$. At low Péclet number, molecular diffusion will prevent the interfacial density gradient from becoming too large. As will be discussed later (Chapter 3), the additional heat transfers above the interface due to turbulent entrainment can be parameterized by a turbulent diffusion term. The stable gradient region $z > d_m$ will be referred to as the diffusion region.

Stable interfacial density gradients of the type described above (Fig. 1.1) occur naturally. As more and more pollutants are being discharged into the surface layers of oceans and rivers and into the atmospheric boundary layer, the role of interfacial entrainment has become increasingly important. The penetrative convection

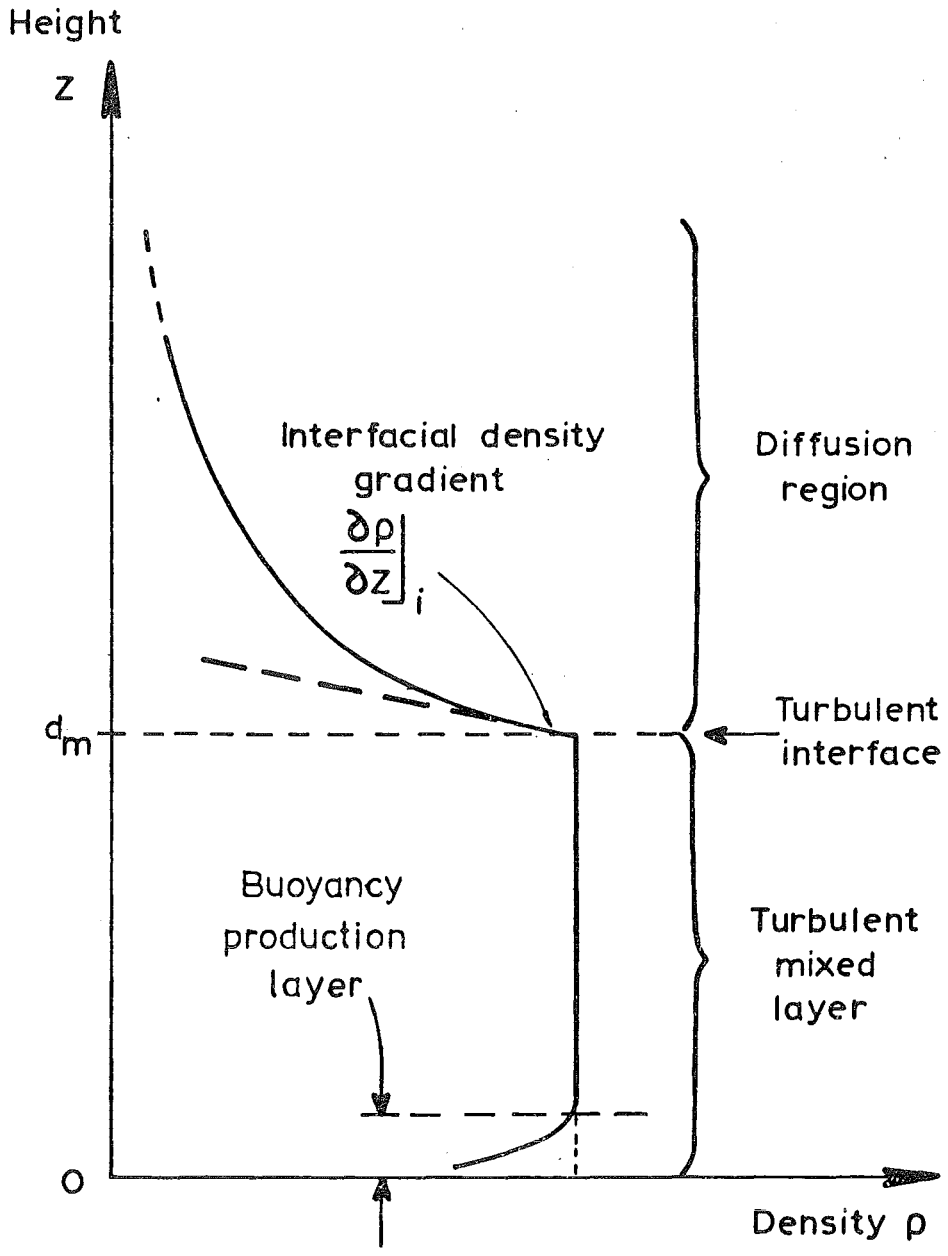

Fig. 1.1. Idealized vertical density profile for penetrative convection.

process has a major influence on the dispersion of these pollutants. Two examples of pollutant dispersion in which penetrative convection has opposite effects are discussed below.

Penetrative convection layers will form in the surface layers of the atmosphere and oceans and lakes under conditions of positive boundary heat flux and negligible mean horizontal currents. In the atmosphere, they occur during the early morning heating of the earth's surface by solar radiation and in oceans and lakes, during night-time cooling. Pollutants released into these turbulent layers will remain there, as the interface acts as a one-way valve (i.e. fluid can only enter into the turbulent region). There is the possibility of molecular diffusion of the pollutant through the interface. However, in the atmosphere, the turbulent length and velocity scales are so large that the Péclet number is also large and molecular diffusion effects are negligible. In the absence of any wind or horizontal currents, the rate of dilution of the pollutants will depend on the rate of growth of the turbulent regions. The presence of strong temperature gradients, known as inversions in the atmosphere and thermoclines in oceans and lakes, greatly reduces the rate of entrainment. Pollutant concentrations can increase to unsightly and unhealthy proportions.

The second example is the dissipation of heat from a thermal or nuclear power station cooling pond. Hot cooling water from the condensers is discharged onto the surface of the pond with the amount of mixing kept to a minimum. Keeping the pond's surface water as hot as possible ensures the maximum possible heat loss to the air. Penetrative convection, caused by the surface cooling, will reduce the temperature of the surface layer by interfacial entrainment of the deeper colder water. Because of the relatively small turbulent length and velocity scales and the relatively high molecular diffusivity of heat ($K \approx 1.43 \times 10^{-3}$ cm^2/sec), the Péclet number for the cooling pond will be low. Hence, molecular diffusion of heat is also significant.

The cooling pond case differs from the previous example, in that the dilution of the pollutant (in this case, heat) by interfacial entrainment is not beneficial as it reduces its rate of loss to the atmosphere. This low Péclet number penetrative convection problem was the initial motivation for this research and will be discussed in more detail in the next section.

There are many other examples of interfacial entrainment. In some cases, such as the interchange of material between two layers of different density flowing relative to each other or entrainment by turbulent jets, the turbulent kinetic energy is caused by interfacial shear stresses. Shear stresses may also be created by flow relative to rough boundaries. Wind shear on the surface of a lake can also contribute to the mixed layer turbulence. In laboratory models of turbulent entrainment, the turbulent region is sometimes created mechanically by oscillating stirring grids (see Chapt. 2.2.1).

Within an entrainment system the density differences may be caused by temperature variations or by dissolved or suspended solids such as salt or silt. The entrainment problem also occurs in studies of gas absorption into a stirred liquid or self-aerated flow on a spillway. In these latter cases, the density difference across the interface is due to the different fluids.

1.2 MOTIVATION FOR THIS RESEARCH

The proposed construction of thermal and nuclear power stations to meet New Zealand's future energy requirements has prompted the New Zealand Electricity Department to sponsor research into the behaviour of cooling ponds. This present study forms part of a cooling pond research program being carried out in the Department of Civil Engineering.

The efficiency of present thermal power plants requires that, for every unit of electricity produced, two units of waste heat must be removed from the condensers. For typical discharges, the cooling water circulated through the condensers increases in temperature by 10-15^{o}C. A cooling pond is one method of dissipating waste heat which is generally economically and ecologically acceptable.

Cooling ponds vary in size, depth and loading (defined as the power station electrical output per hectare of cooling pond) and hence, their cooling characteristics vary. However, they may be generally classified into one of two types: off-stream and on-stream ponds (Ryan and Harleman 1973).

When land is costly and water is scarce, off-stream cooling ponds need to be constructed. These are generally shallow (< 5 metres) and heavily loaded (3 - 4 Megawatts of electricity per hectare). They are generally unstratified and require extensive diking to prevent short-circuiting of the hot inlet water. Off-stream cooling ponds can be

numerically modelled without introducing penetrative convection effects (Ryan and Harleman 1973).

On-stream cooling ponds are often constructed by damming a river. The reservoir is generally multipurpose, being also used for water supply, hydro power, flood control and water recreation. Natural lakes also come into this category. Off-stream cooling ponds are generally deep (> 6 metres) and lightly loaded (< 1.0 Megawatt of electricity per hectare). Because of their depth, they are generally stratified. Through proper design of the cooling pond inlet, the hot cooling water can be discharged onto the surface of the pond with a minimum of mixing. At the outlet the temperature stratification can be used to selectively withdraw the coldest possible cooling water for the condensers.

For a pond of large extent, the mean velocities within the central region of the cooling pond will be negligible. Heat losses from the pond will create a turbulent convection layer at the surface. The deepening and additional cooling of this layer by interfacial entrainment reduces the heat losses from the pond.

The aim of this present research is to study the behaviour of a penetrative convection system at low Péclet number . Although this research will be related in the first instance to the cooling pond situation, it is hoped that aspects of this research can be applied to other penetrative convection problems. For example, the growth of atmospheric inversion layers at high Péclet number .

In the next section, the model of cooling pond entrainment to be studied experimentally and analytically in this thesis, will be discussed.

1.3 THE INVERTED COOLING POND MODEL

The penetrative convection process occurring in a large, deep power station cooling pond will be modelled experimentally by heating a stable two-layered temperature stratification from below. Applying a positive buoyancy flux to either the upper or lower boundary of the fluid column will produce similar convective motions at the conducting boundary ($z = 0$). By heating from below, rather than cooling from above, the need for expensive refrigeration equipment is avoided. The experimental model therefore inverts the cooling pond situation. However, as shown in Fig. 1.2, both the experimental model and the cooling pond have a region of unstable density gradient at the conducting boundary, a uniformly mixed region and a region of stable density

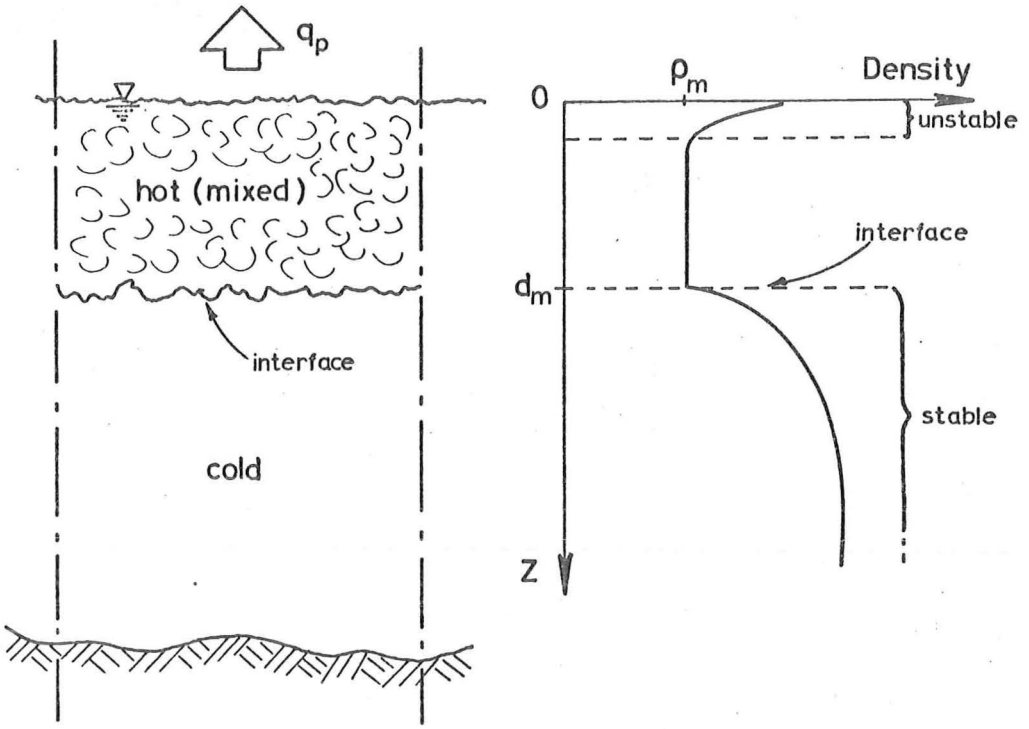

COOLING POND (Zero advection)

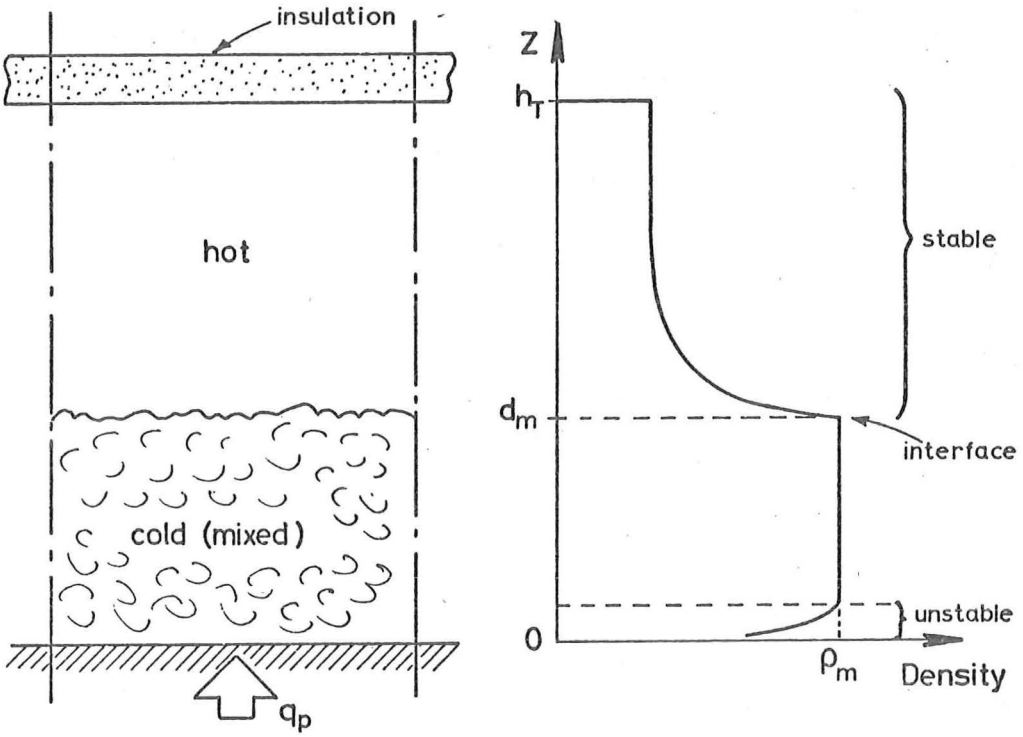

INVERTED COOLING POND MODEL

Fig. 1.2. Comparison of the conditions in the heat loss region of a cooling pond for negligible advection, and the inverted cooling pond model.

gradient. The experimental and analytical model will hereafter be referred to as the inverted cooling pond model (I.C.P.M.).

There will be no mean horizontal velocities in the I.C.P.M. The initial temperature distribution will consist of a layer of uniform temperature T_{a0} atop a colder layer of uniform temperature T_{m0} and thickness d_{g0}. The vertical temperature gradients well beyond the interface ($z \gg d_m$) will therefore be zero as is the case in a deep cooling pond (Fig. 1.2). The boundary conditions and initial conditions of the I.C.P.M. will be discussed in more detail in Chapter 3.

In discussing the transfer of heat in the I.C.P.M., the variation of the fluid properties with temperature will be neglected. The vertical heat fluxes will be described in terms of the buoyancy heat flux

$$Q(z) = q/\rho c_p$$

where q is the heat flux per unit area, ρ is the fluid density and c_p is the specific heat per unit mass. The buoyancy heat flux $Q(z)$ has the dimensions of length times degrees of temperature per unit time (cm ^{o}C/sec).

1.4 THESIS OUTLINE

In the next chapter (Chapter 2), previous work on experimental and theoretical models of atmospheric entrainment will be reviewed. In addition to penetrative convection, oscillating stirring grid experiments and horizontal shear flow entrainment problems will be discussed. A separate review of thermal convection has been included in Appendix A.

Chapter 3 will deal with the initial development of the theoretical I.C.P.M. equations. Equations for the rates of change of temperature in the diffusion region and mixed layer will be derived. The rate of rise of the interface V_{em} is then obtained by matching the temperature changes above and below the interface.

To allow for the additional heat transfer in the diffusion region, due to penetrating interfacial domes, turbulent entrainment parameters are defined (Chapter 3). In Chapter 4, empirical relationships for these turbulent entrainment parameters will be obtained. A numerical analysis of the I.C.P.M. can then be carried out. The results of several sample analyses will be presented at the end of

Chapter 4.

In Chapter 5, the entrainment ratio k, first defined by Betts (1973) and most recently reviewed by Stull (1976a), will be discussed in terms of the I.C.P.M. The validity of the constant k assumption, and other assumptions made by Betts (1973), will be investigated.

An experimental investigation of the I.C.P.M. for two different lower boundary conditions will be reported in Chapter 6.

In Chapter 7, data from the entrainment experiments will be used to assess the accuracy of the I.C.P.M. numerical analysis model.

Conclusions drawn from this study of entrainment by penetrative convection at low Péclet number and recommendations for future research are presented in Chapter 8.

Material not considered part of the main development of the I.C.P.M. is presented in the appendices. These include a discussion of thermal convection, a theoretical analysis of the linearly stratified case ($\Gamma > 0$), a description of the numerical analysis computer programs, a discussion of heat losses and several mathematical derivations.

CHAPTER 2

REVIEW OF THE LITERATURE

2.1 INTRODUCTION

The inverted cooling pond model (I.C.P.M.) is a special case of the general entrainment problem as no mean horizontal or vertical velocities are included. The only external source of turbulent kinetic energy is the positive buoyancy heat flux at the lower boundary. However, in this review of interfacial entrainment literature, other examples of the general interfacial entrainment problem will be discussed. These include vertically oscillating mechanical stirring-grid experiments (Rouse and Dodu 1955, Turner 1968) in which the turbulent kinetic energy input is controlled directly by setting the stirring frequency and stroke length. Stirring-grid experiments have the additional advantage that there is no associated buoyancy source. Hence, the only change in the mixed layer heat or mass storage is due to interfacial entrainment.

Experiments in which the mixed layer turbulence is created by interfacial or boundary shear stresses will also be reviewed. Although these experiments do not have an immediate bearing on the present study, they require similar analysis techniques and illustrate similar interfacial entrainment processes.

For the present study, the case where the mixed layer turbulence is caused by positive buoyancy fluxes at the mixed layer boundaries, is of most interest. However, even for this convective stirring case, a number of different types of interfacial entrainment experiment have been reported.

Interfacial entrainment can be expressed quantitatively in terms of the net flux of heat or mass through the interface, Q_e . The interfacial flux is a function of the stable density gradient at the interface, molecular diffusivity κ , molecular viscosity ν and the turbulent kinetic energy of the mixed layer stirring motions represented by the turbulent length scale ℓ_s and the turbulent velocity scale V_s .

In the majority of interfacial entrainment analyses reviewed in this chapter, the region of large stable density gradients between a turbulent layer and the lighter (or heavier) layer above (or below), is assumed to have negligible thickness. In some cases both layers are mixed, but in most naturally occurring examples of interfacial entrainment, there is only one mixed layer. If the interfacial gradient region

has negligible thickness, the interfacial buoyancy field must be represented by the overall interfacial density difference.

For a temperature stratification, the interfacial buoyancy field is given by $\alpha g \Delta T_i$ where α is the thermal coefficient of volumetric expansion, and ΔT_i is the temperature difference across the interface. Therefore

$$Q_e = \phi(\alpha g \Delta T_i , \kappa , \nu , \ell_s , V_s) \qquad (2.1.1)$$

Dimensional analysis of Eqn. 2.1.1 yields

$$E_o = \phi(Ri_o , Pe , Re) \qquad (2.1.2)$$

where

$$E_o = \frac{-Q_e}{V_s \Delta T_i} \qquad (2.1.3)$$

is the non-dimensional interfacial buoyancy heat flux. The Richardson number

$$Ri_o = \frac{\alpha g \Delta T_i \ell_s}{V_s^2} \qquad (2.1.4)$$

describes the stability of the interface. The Péclet number ($Pe = \ell_s V_s/\kappa$) and the Reynolds number ($Re = \ell_s V_s/\nu$) represent the molecular processes. When the mixed layer is strongly turbulent (ℓ_s and V_s large), molecular diffusion and viscous effects are negligible.

For mechanical stirring-grid experiments, the turbulent length and velocity scales are typically held constant by fixing the grid-stirring frequency (f) and maintaining the interface at a fixed distance from the grid (z_{grid}) by withdrawing mixed layer fluid.

For shear flow experiments with no external buoyancy flux, the turbulent velocity scale is assumed to be proportional to the difference in the horizontal velocities of the two layers ΔU. The length scale, taken as the faster moving layer depth, is generally constant.

The results of these entrainment experiments can therefore be analysed in terms of Eqn. 2.1.2.

However, for penetrative convection no direct velocity scale is available as there are no mean fluid velocities. In the penetrative convection experiments reported in the literature, an alternative method of analysis has been used. The interfacial buoyancy heat flux is assumed to be related to the lower boundary buoyancy heat flux by

$$Q_e = - k Q_p \qquad (2.1.5)$$

This relationship was introduced in the atmospheric models of Betts (1973), Tennekes (1973) and Carson (1973).

Equation 2.1.5 implies that some of the external flux of turbulent kinetic energy is available at the interface for entrainment and the rest is dissipated in the mixed layer. In earlier models (Ball 1960, Lilly 1968), it was assumed that the turbulent dissipation was zero (i.e. $k = 1$) or that all the external energy was dissipated in the mixed layer ($k = 0$). If k is assumed to have a constant value, Eqn. 2.1.5 can be used to solve the heat budget equation for the mixed layer and to obtain a relationship for the rate of rise of the interface. The value of k can then be evaluated by comparing the analytical solution with experimental data. Betts (1973) reported a value of $k = 0.25$.

The two relationships for the interfacial buoyancy heat flux (Eqns. 2.1.2 and 2.1.5) are different methods of analysing the same interfacial entrainment process.

This review of the literature will concentrate on experimental and analytical studies of interfacial entrainment in which there are no mean motions. Of these, mechanical stirring-grid experiments will be discussed first. Data from these experiments show the relationship between the various terms in Eqn. 2.1.2. Atmospheric models, which are examples of penetrative convection at high Péclet number, will then be reviewed. This will illustrate the use of the heat flux ratio k (Eqn. 2.1.5) to analyse penetrative convection data.

The first section of the review will be completed by discussing laboratory experiments in which convective motions have been used to stir the mixed layer. As will be shown later not all of these convective stirring experiments are examples of penetrative convection. These low Péclet number experiments illustrate further the role of molecular diffusion in interfacial entrainment.

The final section of this review will deal with laboratory shear flow experiments, in which there are no external buoyancy fluxes, and the more complex oceanographic models which include both shear and buoyancy generated turbulence.

2.2 ENTRAINMENT WITH NO MEAN VELOCITIES

2.2.1 Mechanical Stirring-Grid Experiments

The use of a vertically oscillating mechanical stirring-grid in one or both layers of a two-layered density distribution allows easy control

of the external source of turbulent kinetic energy and does not involve an external buoyancy source. By withdrawing fluid from the mixed layer in the single stirring-grid case, the interface can be maintained at a fixed distance from the mean grid position. If both layers are stirred, the interfacial region centres itself midway between the grids (Turner 1968). Entrainment experiments of this kind (Fig. 2.1) have been reported by Rouse and Dodu (1955), Turner (1968), Jenkins (1973), Wolanski and Brush (1975) and Hopfinger and Toly (1976).

A number of different density components have been used to create density stratifications: heat, salinity, sugar solution and suspensions of bentonite, kaolinite or silica spheres. These cover a range of molecular diffusivities from 10^{-9} cm^2/sec (for kaolinite) up to 1.43×10^{-3} cm^2/sec (for heat).

In these experiments, the interface (visualized by dyeing the mixed layer) remained quite distinct. Cusps of penetrating mixed layer turbulence were seen to form fluid streamers which were rapidly incorporated into the mixed layer.

The interfacial fluxes were evaluated by measuring the withdrawal rate necessary to maintain the interface at a constant height (single-layer stirring only) or by measuring the rate of change of heat or mass in the mixed layer. For a temperature stratification the latter case can be expressed by

$$Q_e = - d_m \frac{d(T_m)}{dt} \qquad (2.2.1)$$

where Q_e is the interfacial buoyancy flux and d_m and T_m are the thickness (held constant) and temperature of the mixed layer.

Thompson and Turner (1975), using Turner's (1968) apparatus, measured the turbulent length scales and r.m.s. horizontal velocity fluctuation σ_u above a mechanical stirring-grid in an unstratified fluid. Their measurements followed the relationships

$$\ell_{sT} = 0.1 \; z_{grid} \qquad (2.2.2)$$

$$\sigma_{uT} = 1.4 \; f \; (z_{grid})^{-3/2} \; (z_{stroke})^{-5/2} \qquad (2.2.3)$$

where f is the stirring frequency (cycles/sec) and z_{grid} and z_{stroke} are the mean distance from the grid and the stroke length.

Hopfinger and Toly (1976) found a similar relationship between σ_u and f although variations in the mesh size, shape and stroke length of

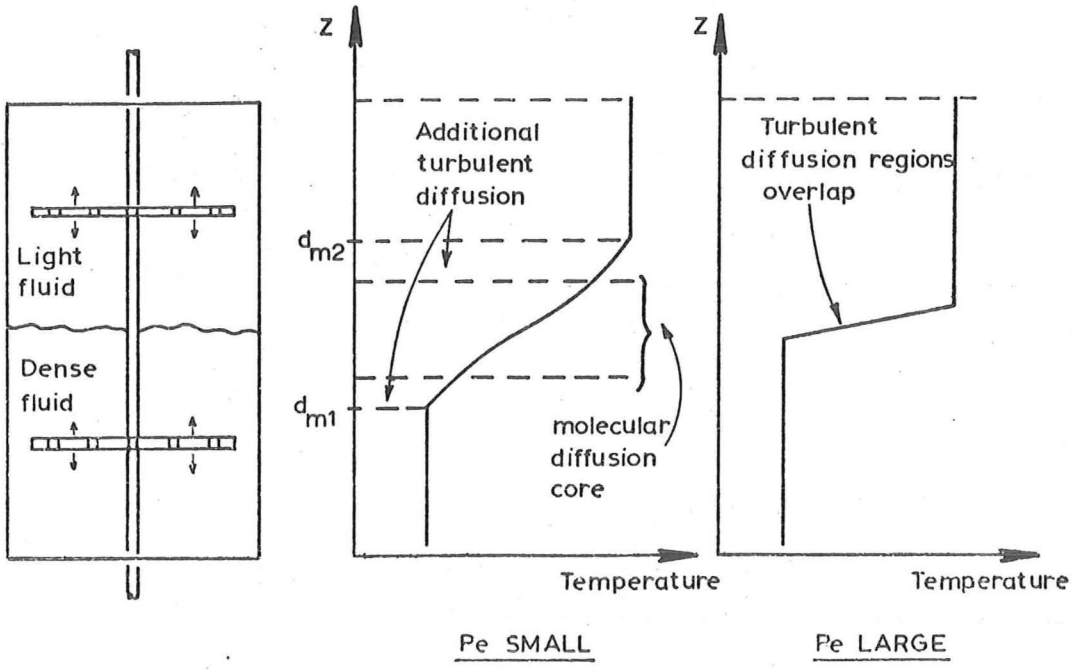

Fig. 2.1. Oscillating stirring grid experiments (double layer stirring case).

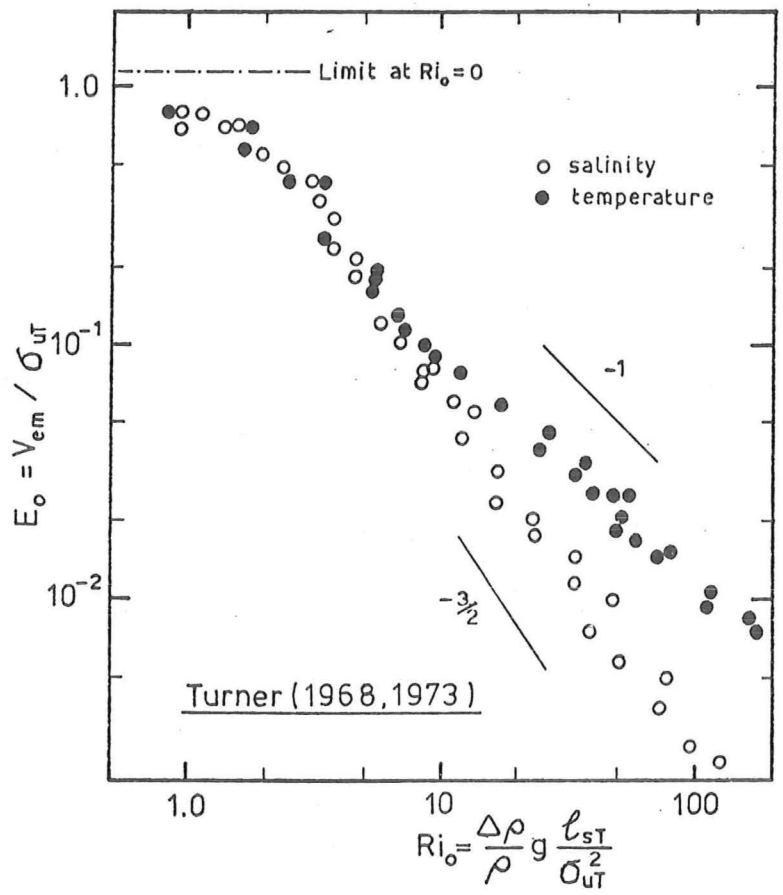

Fig. 2.2. Entrainment data from Turner's (1968) grid experiments for single-layer stirring. (From Turner 1973.)

the grid yielded different relationships between σ_u and z_{grid}. Their measurements in the presence of an inversion support earlier assumptions that V_s is proportional to f at the interface.

At large Péclet numbers, the thickness of the interfacial region in the double stirring-grid case is about 1.5 ℓ_{sT} and the interfacial region is fully turbulent (Crapper and Linden 1974). However, at low Pe , Crapper and Linden (1974) found that the interfacial region between two mixed layers included a central diffusive core (Fig. 2.1). Shadowgraph observations showed that this central core was irrotational. As the Péclet number decreased, the interfacial region thickness increased (Appendix G).

Data from mechanical stirring-grid experiments are typically reported in the form of Eqn. 2.1.2, where E_o is evaluated from Eqns. 2.1.3 and 2.2.1. For the single stirring-grid case, Turner (1968) assumed the interface to be negligibly thick so that Ball's (1960) equation

$$V_{em}\,\Delta T_i = -\,Q_e \qquad (2.2.4)$$

was assumed to hold. In this equation, $V_{em} = d(d_m)/dt$ is the rate of rise of the interface. Hence, the non-dimensional interfacial heat flux E_o (Eqn. 2.1.3) may be alternatively expressed as

$$E_o = V_{em}/V_s \qquad (2.2.5)$$

where V_{em} is evaluated from the rate of withdrawal of mixed layer fluid.

Turner's measurements showed that the values of E_o obtained by either method were approximately the same. He also found E_o to be the same whether one or both layers were being stirred. This led Turner (1968) to suggest that the entrainment process was statistically independent.

Data from Turner's (1968) single stirring-grid experiments are shown in Fig. 2.2. The non-dimensional interfacial flux E_o evaluated from Eqn. 2.2.5, using σ_{uT} as the turbulent velocity scale, is plotted against the Richardson number Ri (Turner 1973). Two different density components, temperature and salinity, were investigated. At large Ri_o, the salinity data ($\kappa \approx 1.2 \times 10^{-5}$ cm^2/sec) follow the relationship

$$E_o \propto Ri_o^{-3/2}$$

whereas the temperature data ($\kappa \approx 1.43 \times 10^{-3}$ cm^2/sec) yield higher values of E_o and follow

$$E_o \propto Ri_o^{-1}$$

As the Richardson number decreased, the difference between the salinity and temperature data decreased and the data eventually merged. At low Ri_o, the increasing value of E_o tends toward a maximum asymptote, the zero Ri_o limit.

If, as Turner's preliminary tests suggested, the entrainment rate is independent of viscosity for his apparatus, his results (Fig. 2.2) show Péclet number dependence. The difference in the buoyancy fluxes at high Ri_o (when interfacial turbulence is reduced) is due to the different rates of molecular diffusion. Because the molecular diffusivity of heat is much higher, the buoyancy flux for heat is greater.

With increasing turbulent activity at the interface (decreasing Ri_o), the effect of molecular diffusivity decreases. Turner (1973) has reported experiments by C.G.H. Rooth, who used temperature stratifications over a wide range of Péclet numbers. These experiments appear to confirm Turner's (1968) salinity data curve, of slope $-\frac{3}{2}$ at high Ri_o, as the "fundamental" curve for large Péclet number. For decreasing Pe, the data deviated from this curve at lower Richardson numbers.

The same relationships for salinity and temperature at high Ri_o have been obtained by Jenkins (1973) and Wolanski and Brush (1975) who used similar apparatus to Turner (1968). Using a different grid shape and salinity, with additional sugar solution to vary the fluid viscosity, Rouse and Dodu (1955) found

$$E_o \propto Ri_o^{-\frac{5}{4}} Re$$

However, Rouse and Dodu plotted E_o and Ri_o separately as functions of non-dimensional time and Reynolds number. The two empirical relationships obtained from these plots were then used to yield the relationship for E_o as a function of Ri_o and Re. Because of their difficulty in evaluating the non-dimensional time accurately, this indirect method of obtaining a relationship between E_o and Ri_o may have affected the power of Ri_o. However, the value of $-\frac{5}{4}$ lies within the range of slopes of the salinity data in Fig. 2.2 as Ri_o decreases.

The Reynolds number dependence obtained by Rouse and Dodu (1955) most probably applies to the developing region at the grid rather than to the interfacial entrainment process (Turner 1968).

Wolanski and Brush's (1975) experiments with sugar solution yielded a slope of -1.6 , similar to their salinity data. However, the values of E_o were about 20 - 30% lower. This may again be due to viscous effects. Sugar solution has a lower molecular diffusivity than salinity and would be expected to be on the same high Péclet number curve.

Experiments with suspensions performed by Jenkins (1973) and Wolanski and Brush (1975) yielded much lower values of E_o and in the latter experiments, slopes of -2 to -3 . The molecular diffusivity of the suspensions were even smaller than the salinity or sugar solution. An alternative explanation to a Péclet number (or Prandtl number $Pr = \nu/\kappa$) dependence must be found if the $-\frac{3}{2}$ slope is to be regarded as the large Péclet number limit.

Hopfinger and Toly (1976) suggested the lower E_o values for suspensions were due to non-Newtonian fluid effects. However, the fall velocity of the suspensions (which acts in the opposite direction to molecular diffusion) may have been responsible for the reduced interfacial buoyancy fluxes.

It is worth noting that the $-\frac{3}{2}$ slope for salinity data has also been found in entrainment experiments where a fluid jet is directed perpendicularly at a density interface (Brush 1970, Baines 1975). Brush also found a -1 relationship for temperature interfaces.

Cromwell (1960) and Turner and Kraus (1967) used grid-generated turbulence to simulate oceanic surface layer mixing. Their experiments modelled the formation of pycnoclines (stable salinity gradients) and thermoclines (stable temperature gradients) in oceans but no quantitative entrainment measurements are available.

Linden (1975) used Turner's (1968) apparatus to study the advance of a mixing layer into a linear salinity stratification. Following Niiler (1975), Linden obtained a theoretical relationship for $d_m(t)$ by assuming that the rate of increase in potential energy was proportional to the energy input of the grid. The experimental data appeared to agree with his theoretical relationship. When expressed in terms of E_o and Ri_o the data yielded a range of power law exponents of approximately -1.5 to -0.7.

Linden (1975) also compared the rate of rise of the interface V_{em} for linear salinity gradients ($\Gamma_\rho = \partial\rho/\partial z > 0$) with the corresponding value of V_{em} for $\Gamma_\rho = 0$ (the I.C.P.M. two-layer case). The interfacial density difference was held constant and the reduction in V_{em} for $\Gamma_\rho > 0$

was explained by energy losses due to internal wave action above the interface. However, the interfacial gradient $(\partial\rho/\partial z)_i$ will increase as Γ_ρ increases which may explain some of the reduction in V_{em}.

The mechanical stirring-grid experiments discussed above have illustrated the role of molecular diffusion in interfacial entrainment. At low Péclet number, molecular diffusion increases the thickness of the density gradient region at the interface. It also contributes to the interfacial buoyancy flux. At large Ri_o, this contribution becomes significant. However, the experimental data are still confusing Turner (1973) suggests the salinity data slope of $-\frac{3}{2}$ at large Ri_o is the fundamental curve for large Péclet numbers. Wolanski and Brush's (1975) data, however, suggest that at even higher Péclet numbers, lower E_o values and steeper negative slopes will occur.

Before reviewing previous low Péclet number penetrative convection experiments, atmospheric inversion models will be discussed. Because of the immense scale of atmospheric turbulence (ℓ_s and V_s large), the Péclet numbers are very large and hence, molecular diffusion may be neglected.

2.2.2 Atmospheric Inversion Models

In his model of a dry windless atmospheric boundary layer, Betts (1973) assumed the interface to have negligible thickness (Fig. 2.3). The mixed layer heat budget was therefore

$$Q_p - Q_e = d_m \frac{dT_m}{dt} \tag{2.2.6}$$

As the interfacial temperature difference is defined as $\Delta T_i = T_a - T_m$, then

$$\frac{dT_m}{dt} = \frac{dT_a}{dt} - \frac{d(\Delta T_i)}{dt} \tag{2.2.7}$$

When the interface rises, T_a increases according to

$$\frac{dT_a}{dt} = V_{em}\,\Gamma \tag{2.2.8}$$

where Γ is the temperature gradient for $z >> d_m$. As discussed in Chapt. 2.1, Betts assumed the ratio $-Q_e/Q_p$ to have a constant value k (Eqn. 2.1.5). Because the interface thickness was neglected, Ball's (1960) equation applied (Eqn. 2.2.4). Hence,

$$V_{em}\,\Delta T_i = k\,Q_p \tag{2.2.9}$$

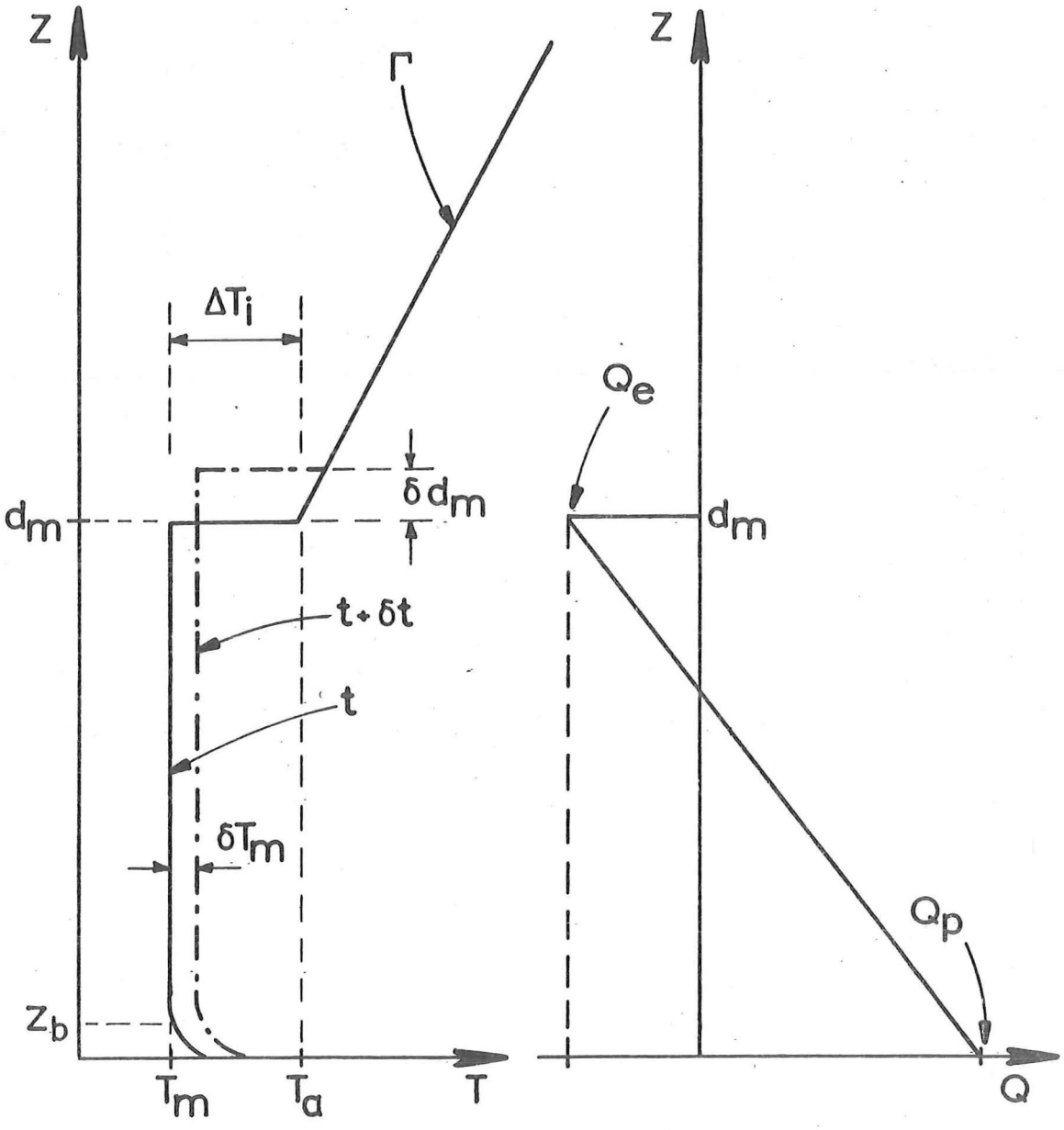

Fig. 2.3. Temperature and heat flux profiles for an atmospheric boundary layer model (following Betts 1973).

Substituting Eqns. 2.2.7, 2.2.8 and 2.2.9 into the mixed layer heat budget equation (Eqn. 2.2.6) yields

$$\frac{(1 + k)}{k} \Delta T_i \frac{d(d_m)}{dt} + d_m \frac{d(\Delta T_i)}{dt} = d_m \Gamma V_{em} \qquad (2.2.10)$$

Betts (1973) assumed the initial conditions to be $\Delta T_i = d_m = 0$ at $t = 0$. If k is constant, the solution to Eqn. 2.2.10 is

$$\Delta T_i = \frac{k}{1 + 2k} \Gamma d_m \qquad (2.2.11)$$

Eliminating ΔT_i from Eqns. 2.2.9 and 2.2.11 and resolving, yields

$$d_m^2 = \frac{2(1 + 2k)}{\Gamma} \int_o^t Q_p \, dt \qquad (2.2.12)$$

If the values of k, Γ and $Q_p(t)$ are known, Betts' model equations 2.2.11 and 2.2.12 can be used to predict the temporal variation of ΔT_i and d_m. Conversely, experimental data can be used to evaluate k. However, the accuracy of the analyses will depend on the validity of Betts' (1973) assumptions:

(i) negligible interfacial thickness

(ii) $k = - Q_e/Q_p$ is constant

(iii) the initial conditions at $t = 0$ are $d_m = \Delta T_i = 0$.

Similar model equations were developed by Carson (1973) and Tennekes (1973). Carson (1973) used his model to analyse the O'Neill data (Lettau and Davidson 1957). He assumed three phases of entrainment during the daytime heating period:

(i) nocturnal inversion erosion (k assumed zero)

(ii) rapid growth period with little mixing ($k = 0$) up to 850 metres

(iii) a maximum entrainment period when Q_p is at its maximum ($k > 0$).

An equation of the form

$$\frac{d(d_m^2)}{dt} = \frac{2(1 + 2k)}{\Gamma} Q_p \qquad (2.2.13)$$

(which is Eqn. 2.2.12 differentiated with respect to time) was used to evaluate k for the third period. The comparison of Carson's model (Eqn. 2.2.13) with the O'Neill data yielded a value of $k = 0.5$ at midday. Later, as Q_p decreased, k decreased to about 0.25. However, the assumption that k is zero until $d_m = 850$ metres implies ΔT_i is also

zero until this height. This is not consistent with Betts' (1973) assumption (iii) above. The solution for ΔT_i (Eqn. 2.2.11) assumed ΔT_i was last equal to zero when $d_m = 0$. Hence, Eqn. 2.2.13 is not valid in Carson's (1973) analysis. As discussed further in Appendix B, this causes k to be overestimated.

The relationship between Q_e and Q_p (Eqn. 2.1.5), assumed by Betts (1973), can be derived by evaluating the turbulent kinetic energy equation at the interface (Tennekes 1973, Zilitinkevich 1975). Following Lumley and Panofsky (1964), the turbulent kinetic energy equation is

$$\frac{\partial}{\partial t}\left(\frac{q^2}{2}\right) + \frac{\partial}{\partial z}\overline{\left(w'\left(\frac{p'}{\rho} + \frac{q^2}{2}\right)\right)} = \overline{w'u'}\ \frac{\partial \overline{u}}{\partial z} + \alpha g Q - \varepsilon \qquad (2.2.14)$$

where $q^2/2$ = turbulent kinetic energy (TKE)

U = horizontal velocity

w',u',p' = fluctuations of vertical and horizontal velocity and pressure about the mean

Q = buoyancy heat flux

ε = turbulent dissipation

The terms on the left hand side of the equation are the rate of increase in turbulent kinetic energy (TKE), and the vertical transport of pressure fluctuations and TKE. The terms on the right hand side of Eqn. 2.2.14 are the production of TKE, due to shear stresses and buoyancy, and the turbulent dissipation term.

In early atmospheric models, the TKE equation was integrated from $z = 0$ to d_m. The rate of increase in TKE was neglected. As the vertical velocities are negligible at the boundaries, the integrated production term was also neglected. Shear stresses were not included ($U = 0$). Hence, the integration of Eqn. 2.2.14 yields

$$\frac{\alpha g (Q_p + Q_e)\, d_m}{2} = \int_0^{d_m} \varepsilon \, dz \qquad (2.2.15)$$

For $\varepsilon > 0$, the entrainment ratio k is less than unity.

Tennekes (1973) evaluated the TKE equation (Eqn. 2.2.14) at $z = d_m$, neglecting all terms except the transport of TKE and buoyancy production term. He assumed that

$$\frac{\partial}{\partial z}\overline{\left(w'\,\frac{q^2}{2}\right)} \propto \frac{\sigma_w^3}{d_m}$$

where σ_w is the r.m.s. vertical velocity fluctuation. Hence, for his simplified TKE equation

$$- \alpha g \varrho_e \propto \frac{\sigma_w^3}{d_m}$$

Following Deardoff (1970) he assumed

$$\sigma_w \propto (\alpha g \varrho_p d_m)^{\frac{1}{3}} \qquad (2.2.16)$$

It therefore followed that $\varrho_e = - k \varrho_p$.

However, Zilitinkevich (1975) pointed out that as $Ri_o \to 0$, V_{em} becomes large and the rate of increase of TKE at the interface is significant. Zilitinkevich, using a similarity argument, assumed that

$$\frac{\partial}{\partial t} \left(\frac{q^2}{2}\right) \propto \frac{\sigma_w^2}{d_m} \cdot V_{em}$$

If shear stresses and turbulent dissipation are again neglected, the TKE equation (Eqn. 2.2.14) at $z = d_m$ can be rewritten as

$$c_1 \frac{\sigma_w^2}{d_m} V_{em} = \alpha g \varrho_e + c_2 \frac{\sigma_w^3}{d_m} \qquad (2.2.17)$$

Substituting for V_{em} (from Eqn. 2.2.4) and rearranging yields

$$\varrho_e = \frac{- c_2 \sigma_w^3 / \ell_s}{\alpha g + \frac{c_1 \sigma_w^2}{\Delta T_i \ell_s}} \qquad (2.2.18)$$

For large ΔT_i (Ri_o large), Eqns. 2.2.16 and 2.2.18 give

$$\varrho_e = - k \varrho_p$$

as before. However, for small values of ΔT_i (low Ri_o), the second term on the denominator of Eqn. 2.2.18 is large. It follows that for low Ri_o (Tennekes 1975)

$$V_{em} = \frac{c_2}{c_1} \sigma_w$$

This is in agreement with Turner's (1968) mechanical stirring grid experiments at low Ri_o (Fig. 2.2).

Using Eqn. 2.2.16, Eqn. 2.2.18 may be rewritten as

$$E_o = \frac{E_{max}}{1 + c_z Ri_o} \qquad (2.2.19)$$

where E_{max} and c_z are constants. This equation describes the variation of E_o with Richardson number and can also be written in terms of k so that

$$k = \frac{c_3 \; Ri_o}{1 + c_z \; Ri_o} \qquad (2.2.20)$$

However, the high Ri_o limit of Eqn. 2.2.19 does not fit Turner's (1968) data ($E_o \propto Ri_o^{-3/2}$). This discrepancy, which will be discussed further during the derivation of the theoretical I.C.P.M. (Chapter 4), does not appear to have been reported previously.

Atmospheric measurements of the interfacial buoyancy flux ratio k have been reported by Readings (1973), Rayment and Readings (1974) and Cattle and Weston (1975). Mean values of $0.2 < k < 0.3$ were obtained although Readings (1973) measured a maximum of $k = 0.5$ at midday. This may have been due to a lag between the peak surface heat flux and the interfacial motions (Rayment and Readings 1974).

Similar equations to Betts' (1973) model have been used to create large scale atmospheric mixed layer models (Sarachik 1974, Barnum and Rao 1975). Sarachik assumed a constant value of $k = 0.2$ but even with his allowance for subsidence (mean vertical velocities), poor quantitative results were obtained. Barnum and Rao (1975), who modelled the mixed layer over a city, obtained $k = 0.35$ at midday. However, their results were affected by their model assumption that $\Delta T_i = \Gamma \, d_m$. From Eqn. 2.2.11, this must impose a value of k on part of the model.

Zeman and Tennekes (1977) have reported an atmospheric model which expands on the work of Tennekes (1973) and Zilitinkevich (1975), by parameterizing the TKE equation (Eqn. 2.2.14) to include shear production and dissipation. Similar work has been reported by Stull (1976b).

Atmospheric models based on the actual interfacial entrainment mechanisms have also been developed (Stull 1973, Manton 1975). The interface is assumed to be composed of pairs of penetrating domes and displaced wisps of fluid. The penetration distance of the domes into the stable density gradient is found from the force equation with the time scale of interfacial turbulence (d_m/σ_w) being based on Deardoff's (1970) convection scales. Comparison of Stull's (1973) numerical results with the same O'Neill data used by Carson (1973) suggested $k \approx 0.15$. In Stull's model, non-zero initial conditions ($\Delta T_i = 0$ when $d_m > 0$) were allowed for. With increasing mixed layer thickness, the solution became less dependent on the initial conditions, tending asymptotically to the zero initial condition solution.

Three-dimensional numerical models based on the equations of motion and budgets of heat and moisture have also been used to model atmospheric boundary layers (Deardoff 1974a,b, Kuo and Sun 1976).

Deardoff (1974a) found good agreement between virtual temperature and specific humidity profiles from the Wangara data (Clarke et al. 1971) and his calculated profiles. The range of k values obtained from the interfacial buoyancy heat fluxes was

$$0.14 < k < 0.21$$

However, evaluation of the terms in Eqns. 2.2.4 and 2.2.11 from the simpler atmospheric model of Betts (1973) showed many inconsistencies, with implied values of k from zero to 0.5.

The r.m.s. vertical velocity fluctuations from the numerical model were scaled by Deardoff (1974b) using Deardoff's (1970) convection scale

$$w_* = (\alpha g \, Q_p \, d_m)^{\frac{1}{3}} \tag{2.2.21}$$

The relationship for the maximum r.m.s. velocity

$$(\sigma_w)_{max} = 0.68 \, w_* \tag{2.2.22}$$

agreed well with Willis and Deardoff's (1974) laboratory experiments.

Contour plots of temperature and specific moisture showed tilted rising plumes throughout the mixed layer (Deardoff 1974b). Under optimal conditions the specific moisture contour plots also showed cusps of dry air from above the interface being entrained through the interface on either side of a penetrating dome structure. The largest temperature fluctuations occurred in the buoyancy production region and in the stable interfacial region. In the latter region, the temperature fluctuations did not scale according to the convection temperature scale

$$T_* = Q_p / w_* \tag{2.2.23}$$

but according to ΔT_i. This implies a dependence on $\Gamma \, d_m$ (from Eqn. 2.2.11) which is consistent with internal wave motions.

For $Ri_o \to 0$, Deardoff (1974a) found V_{em} tended to a maximum value of

$$(V_{em})_{max} = 0.2 \, w_* \tag{2.2.24}$$

He therefore proposed the empirical relationship

$$V_{em} - w_{sub} = \frac{1.8 \, Q_p}{d_m \, \Gamma + \frac{9.0 \, w_*^2}{\alpha g \, d_m}} \tag{2.2.25}$$

where w_{sub} = mean vertical velocity (subsidence)
and Γ = linear potential temperature gradient above the interface.
This has similar form to the relationship derived later by Zilitinkevich (Eqn. 2.2.18).

Kuo and Sun's (1976) non-linear model was similar to Deardoff (1974a,b). However, their assumption of constant eddy viscosities and diffusivities caused the complete damping of small scale effects and unrealistically large heat fluxes above the interface.

The mixed layer growth model of Mahrt and Lenschow (1975) was based on the parameterization of the equations of motion, thermodynamics, moisture and turbulent kinetic energy integrated over the mixed layer. The model included large horizontal velocities and is therefore more closely related to the shear entrainment models to be discussed in Chapt. 2.3.

This review of large Péclet number, atmospheric models has shown how the heat flux ratio k can be used in numerical and experimental analyses of interfacial entrainment data. The values of k reported in the literature have been recently reviewed by Stull (1976a). They appear to have a mean range of

$$0.1 < k < 0.3$$

However, the value of k is not a constant. Zilitinkevich's (1975) result (Eqn. 2.2.20) shows that k will tend to zero as the Richardson number decreases. It follows that models based on a constant k assumption are not valid.

2.2.3 Convective Stirring

In this section, interfacial entrainment due to turbulent convection is discussed. The convective motions may be caused by the production of buoyancy at one of the mixed layer boundaries. Not all of these experimental models involving convective stirring can be considered as penetrative convection. In some cases the buoyancy instabilities are produced at the interface and the buoyant (or negatively buoyant) elements move away from it.

The experiments of Deardoff, Willis and Lilly (1969) are often used to illustrate the penetrative convection process. Deardoff et al. heated water, with a stable linear temperature gradient Γ, from below by circulating water at a constant temperature (T_H) beneath the lower conducting boundary. Temperature profiles were measured using a horizontally averaging probe which was vertically traversed through the

fluid column. Heat flux profiles were derived from the temporal changes in temperature between successive profiles. Temperature and heat flux profiles from Deardoff et al's. (1969) Run A are shown in Fig. 2.4 a,b . For clarity, only four typical heat flux profiles have been reproduced in Fig. 2.4b. Profile labels give the time in minutes.

In these experiments, the height of the interface was defined as the point of maximum negative heat flux (Fig. 2.4b). The values of k obtained from the heat flux profiles were only of order 0.05 although measurements of the mixed layer heat budget suggested that the extra buoyancy flux entering through the interface ($-Q_e$) was about 25% of Q_p.

Deardoff, Willis and Lilly (1974) suggested that, for non-uniform mixed layer temperature profiles, the effective interfacial heat flux can be obtained by extrapolating the linear portion of the heat flux profile up to the height of the maximum negative heat flux, $z = d_m'$. This is shown schematically in Fig. 2.5. Analysing the heat flux profile for run A at time $t = 4.85$ minutes (Fig. 2.4b) by this method yields $k \approx 0.24$.

There are obvious discrepancies between the penetrative convection profile assumed by the writer (Fig. 1.1) and the experimental profiles of Deardoff, Willis and Lilly (1969). As the former profile is a major assumption for the I.C.P.M. (see Chapt. 1.3) , and because the results of Deardoff et al. (1969) are often quoted in the literature, it is important that an explanation be given at this point.

Consider a mixed layer interface which, due to uneven heating, is not horizontal (as shown schematically in Fig. 2.6). According to the I.C.P.M. assumptions, the temperature profiles at the highest and lowest points will have gradient discontinuities at the interface. However, the horizontal mean of the one-dimensional vertical profiles will be a smooth curve with no interfacial discontinuity.

A number of factors suggest that the interface was not always horizontal in Deardoff et al's. (1969) experiments. Dyed fluid streamers from the diffusion region were observed to be more prevalent in the centre of their experimental tank. If, as this appears to indicate, the entrainment rate was greater in the centre of the tank, the interface would be higher at that point. Deardoff, Willis and Lilly (1969) also reported temperature profiles measured by two vertically traversing thermocouple probes. These one-dimensional temperature profiles, taken on the central axis of the tank and at a radius of 19.3 cm, suggest the interface was up to 2 cm higher in the centre. Because of the effect

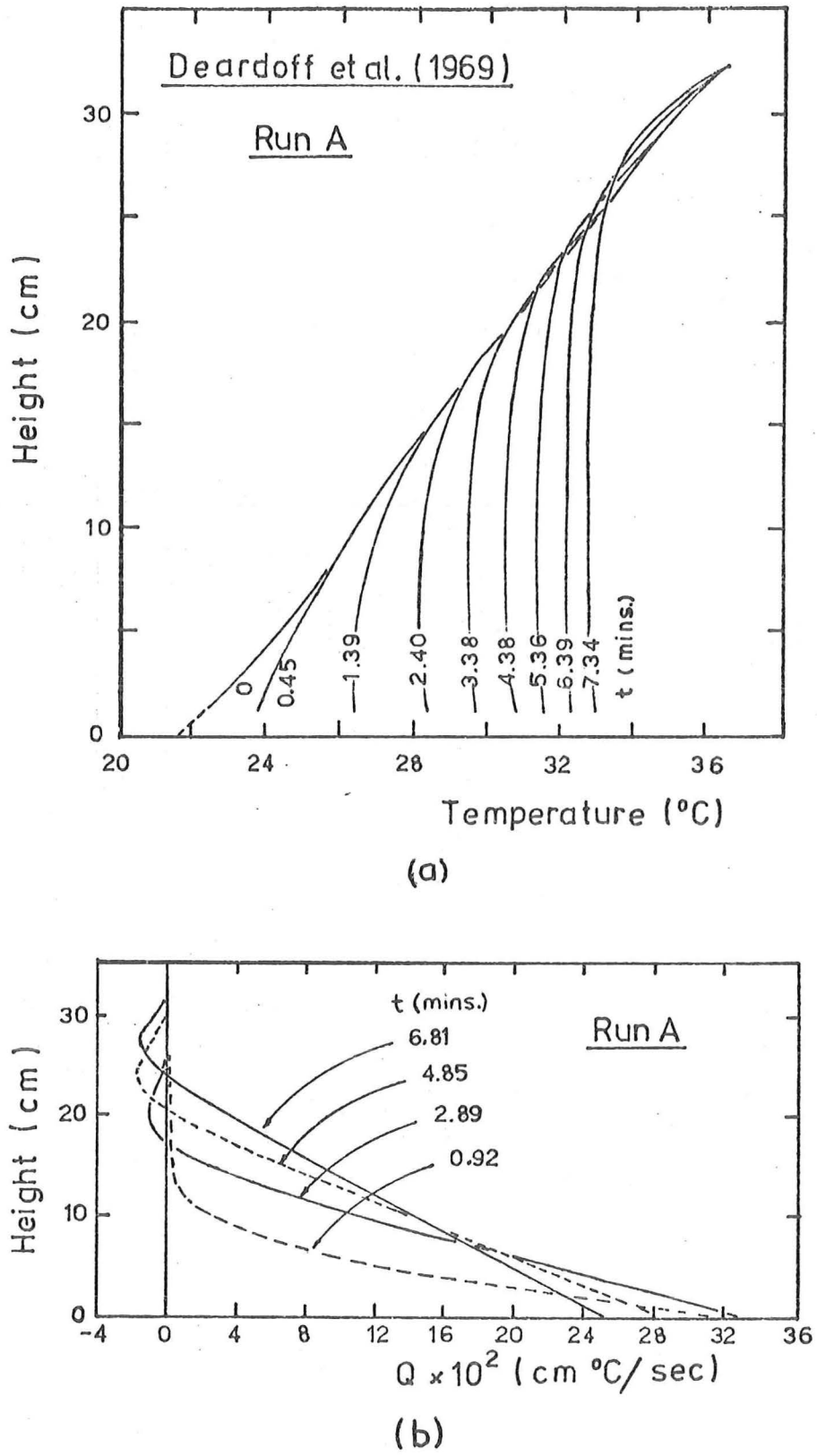

Fig. 2.4. Vertical profiles of (a) horizontally averaged temperature and (b) buoyancy heat flux from a linearly stratified penetrative convection experiment. (From Deardoff, Willis and Lilly 1969.)

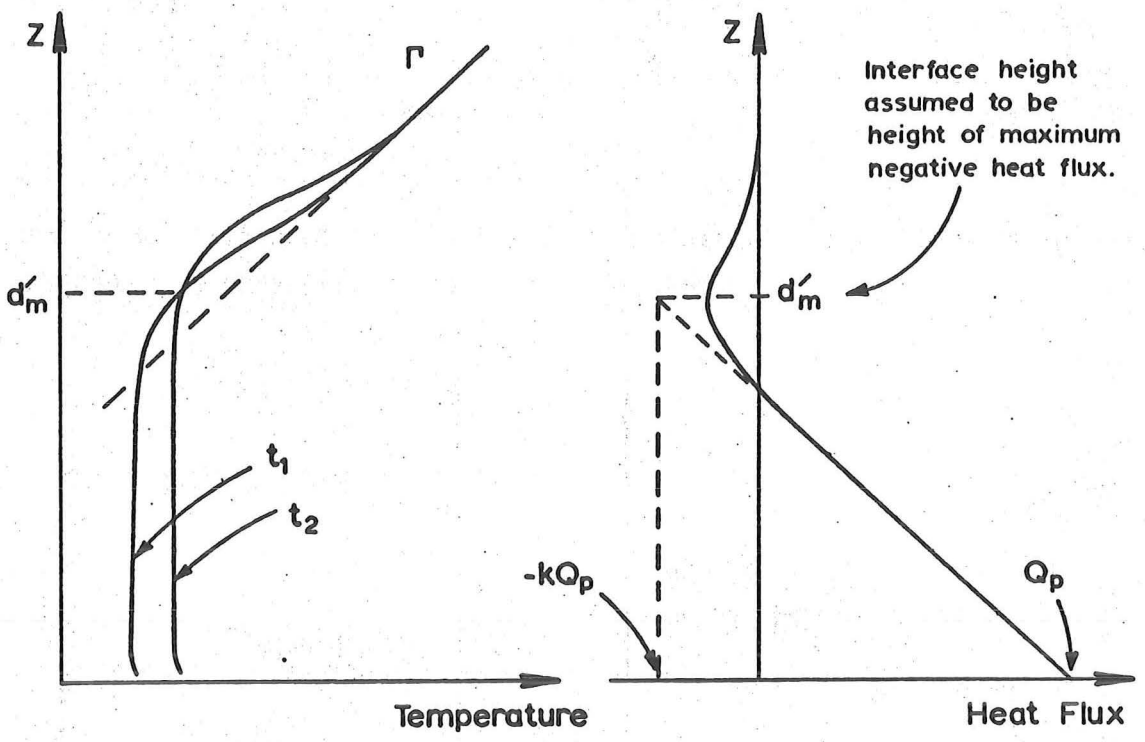

Fig. 2.5. Extrapolation technique for evaluating interfacial heat flux suggested by Deardoff, Willis and Lilly (1974).

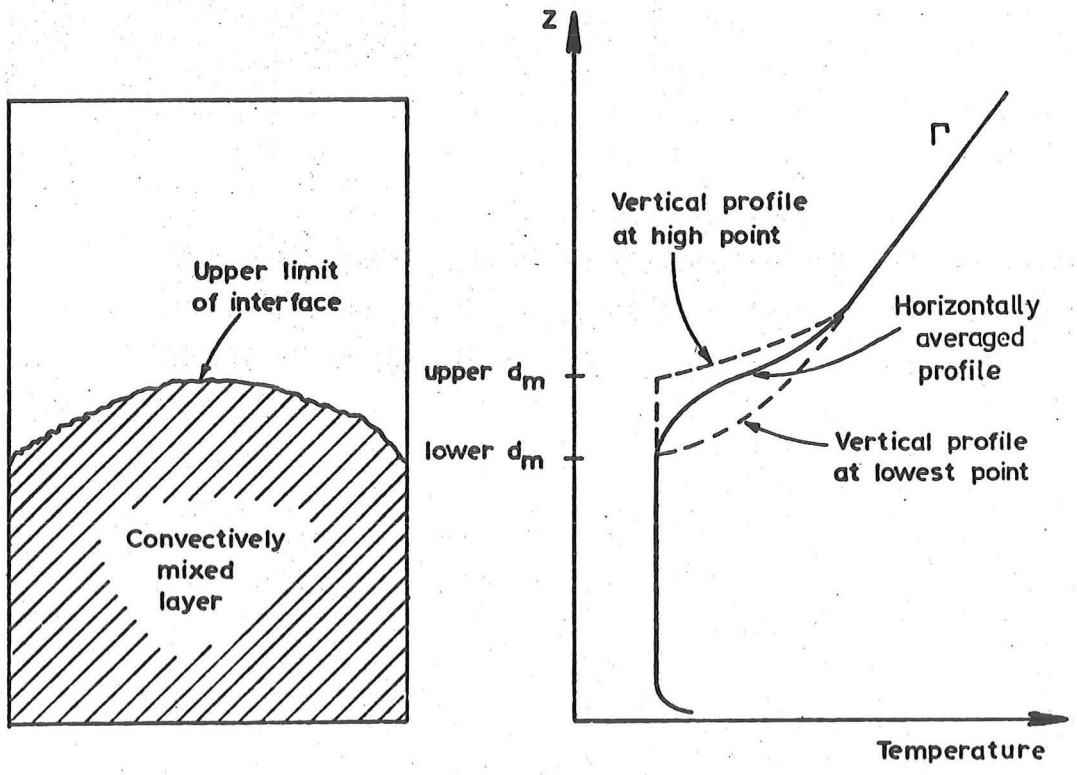

Fig. 2.6. Sketch showing smoothing of the vertical temperature profile resulting from horizontal averaging of the fluid column temperatures when the interface is not horizontal.

described above (Fig. 2.6), the horizontally average temperature profiles of Deardoff et al.(1969) do not show the sharpness of the interface (Fig. 2.4a).

If the fluctuations due to the passage of convective elements are neglected, the vertical temperature profiles from their single thermocouple probes do indicate a sharp interface and a more uniform mixed layer (Deardoff et al's.(1969) Figure 3).

Deardoff, Willis and Lilly's (1969) derivation of heat flux profiles also caused a substantial averaging effect. Neglecting heat losses, the one-dimensional heat budget equation at any height z in the fluid is

$$\frac{\partial T}{\partial t} = - \frac{\partial Q}{\partial z} \qquad (2.2.26)$$

Deardoff et al.(1969) calculated the heat flux profiles from this equation by considering the net changes in the temperature profiles δT over a finite time interval δt. Hence, from Eqn. 2.2.26, they obtained

$$Q(z) = - \kappa \Gamma + \frac{1}{\delta t} \int_{z}^{h_T'} \delta T \, dz \qquad (2.2.27)$$

where $- \kappa \Gamma$ is the heat flux, due to molecular diffusion, at some height h_T' well above the interface.

Consider the two one-dimensional temperature profiles for $t = t_1$ and t_2 shown in Fig. 2.7a. Below $z = d_{m1}$, the temperature difference between them does not vary with height ($= \delta T_m$). Over this region $0 < z < d_{m1}$, the buoyancy heat flux profile calculated from Eqn. 2.2.27 will be linear. Above d_{m1}, the temperature difference between the profiles for t_1 and t_2 decreases until $\delta T = 0$. At this point ($z = d_m'$ in Fig. 2.5), the negative buoyancy flux is a maximum. With increasing height up to $z = d_{m2}$, δT becomes increasingly more negative. Above d_{m2}, the temperature difference δT tends to zero, The time-averaged buoyancy heat flux profile which results from Eqn. 2.2.27 is shown in Fig. 2.7b (profile A).

However, the mean temperature change over a finite time interval $\delta t = t_2 - t_1$ does not accurately represent the instantaneous rate of change of temperature at the $\bar{t} = (t_1 + t_2)/2$ (Cattle and Weston 1975). The greatest inaccuracies occur within the region $d_{m1} < z < d_{m2}$. Here, the fluid spends at least some of the time interval δt in the diffusion region and the rest in the mixed layer. For the example shown

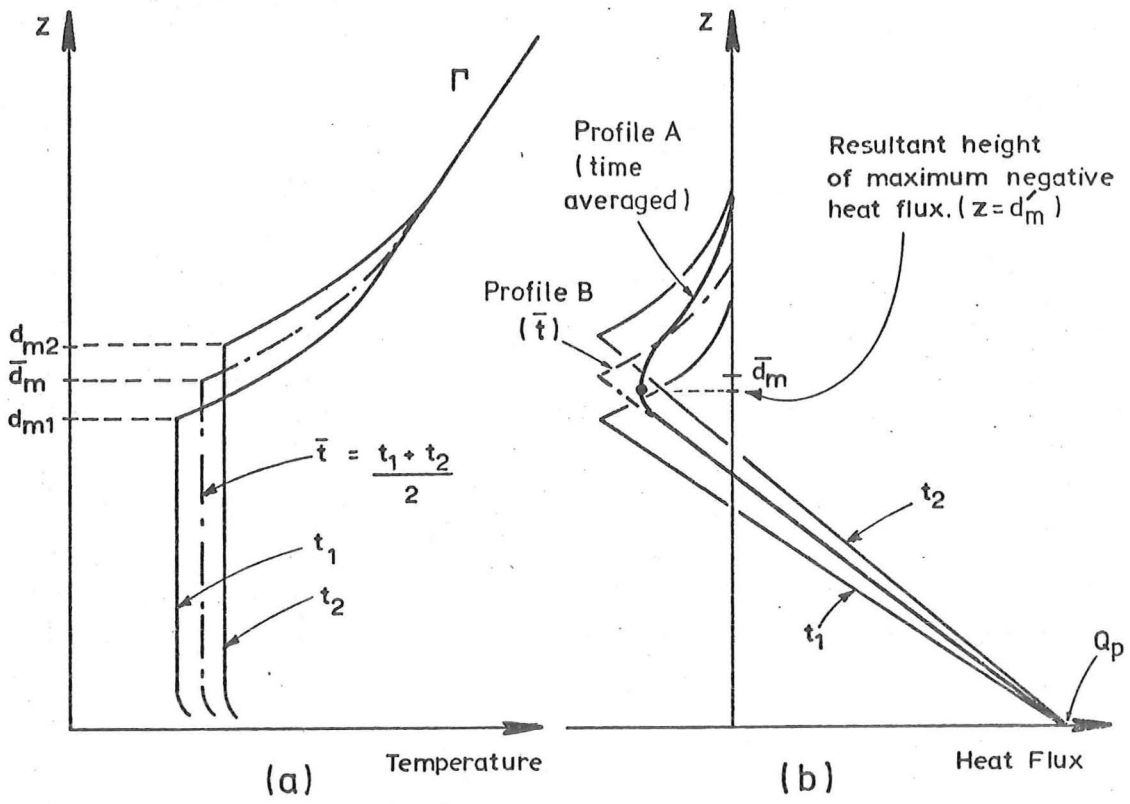

Fig. 2.7. Sketch showing differences between a vertical heat flux profile derived from time-averaged temperature profile changes and the actual heat flux profile at mean time.

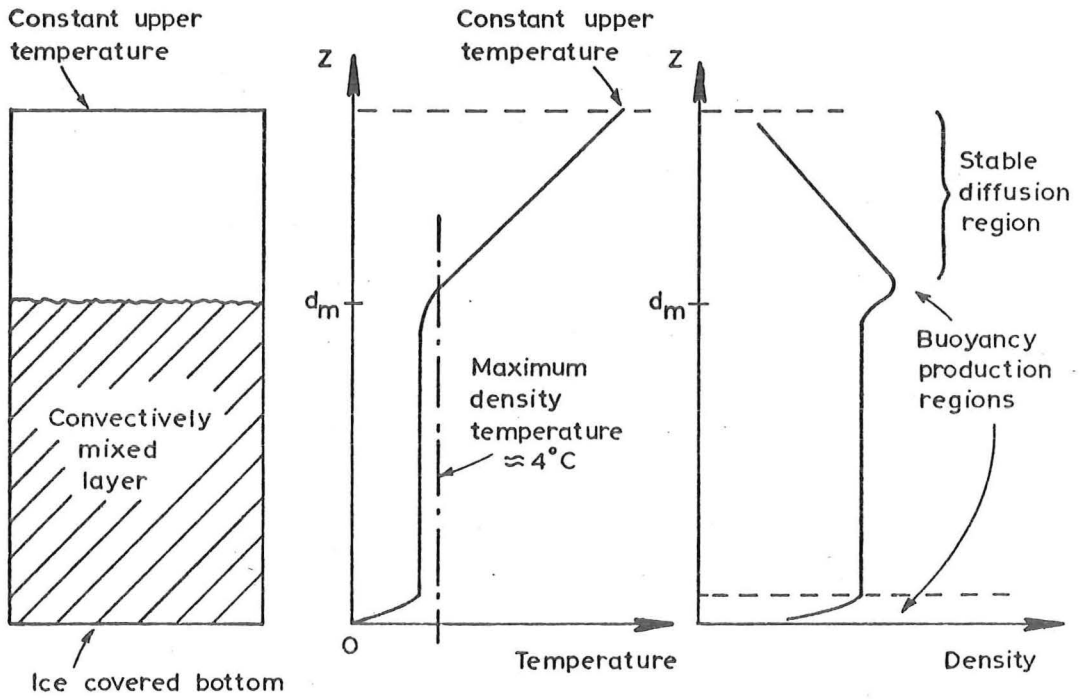

Fig. 2.8. Steady state ice-water penetrative convection experiments (Townsend 1964, Adrian 1975).

in Fig. 2.7a, the fluid in this interfacial region initially cools and then increases in temperature. Note that the I.C.P.M. assumption of a temperature gradient $(\partial T/\partial z)$ discontinuity at the interface implies an interfacial discontinuity in $\partial T/\partial t$. This will be discussed in more detail in Chapter 3. Whether the net temperature change δT is positive or negative is effectively dependent on the proportion of time spent in the mixed layer. At one height in this region (d_m' in Fig. 2.5), the net change in temperature is zero.

Consider the temperature profile for $t = \overline{t}$ (Fig. 2.7a). The instantaneous change in temperature anywhere below $z = \overline{d}_m$ is a positive value of dT_m/dt . However, the mean temperature changes for $d_{ml} < z < \overline{d}_m$ over δt are less than δT_m . In fact, the mean temperature change immediately below $z = \overline{d}_m$ is negative. The mean temperature changes between two temperature profiles therefore should not be used to obtain $\partial T/\partial t$.

The actual buoyancy heat flux profile at $t = \overline{t}$ is shown schematically in Fig. 2.7b (profile B). As the instantaneous temperature change is uniform with height up to $z = \overline{d}_m$, it follows from Eqn. 2.2.26 that the heat flux profile is linear for $0 < z < \overline{d}_m$. Above the interface in the diffusion region, the temperature changes are negative so the heat flux tends from Q_e at $z = \overline{d}_m$ to $-\kappa\Gamma$ at $z >> \overline{d}_m$. It should be noted that the molecular diffusion flux $\kappa\Gamma$ was typically less than 1% of Q_p in Deardoff, Willis and Lilly's (1969) experiments.

As can be seen from Fig. 2.7b, the derived heat flux profile of Deardoff et al.(1969), profile A, will have a maximum negative value less than the actual value of $-Q_e$ at $t = \overline{t}$. The height at which their maximum negative buoyancy heat flux occurs $(z = d_m')$ is not necessarily the height of the interface $z = \overline{d}_m$. Even if Deardoff et al's.(1969) temperature profiles (Fig. 2.4a) had shown an interfacial discontinuity like the assumed one-dimensional profile of Fig. 1.1, their derived heat flux profiles would still have underestimated $-Q_e$.

Measurements of the r.m.s. vertical velocity (σ_w) in the mixed layer of a penetrative convection experiment similar to Deardoff et al. (1969) have been reported by Willis and Deardoff (1974). The initial temperature profile consisted of a deep homogeneous layer topped by a stable temperature gradient Γ . Because d_m was large, the changes in T_m and hence, Q_p with time were small. The maximum r.m.s. vertical velocity was

$$(\sigma_w)_{max} = 0.65\ w_* \qquad (2.2.28)$$

(c.f. Eqn. 2.2.22).

F.D. Heidt (1975, private communication) of the University of Karlsruhe has performed a series of penetrative convection experiments similar to those of Deardoff, Willis and Lilly (1969). He evaluated k from Eqn. 2.2.12 and found $k = 0.18 \pm 0.06$.

Penetrative convection experiments for an initial two-layered temperature distribution ($\Gamma = 0$) have also been reported (Denton and Wood 1974, Jenkins 1974). Following Betts (1973), Denton and Wood (1974) assumed a negligibly thick interface. Rearranging Eqn. 2.2.10 for $\Gamma = 0$ yields

$$\frac{d}{dt}(\ell n\ d_m) = -\frac{k}{1+k}\ \frac{d}{dt}(\ell n\ \Delta T_i) \qquad (2.2.29)$$

Equation 2.2.29 implies that the slope of a plot of the logarithm of d_m versus the logarithm of ΔT_i at any point is $-k/(1+k)$. Data from both Denton and Wood (1974) and Jenkins (1974), when plotted in this way, were found to be approximately linear, signifying constant values of k. For individual runs, different k values were obtained.

Both sets of experiments were performed using a conducting boundary ($z = 0$) and a water bath of constant temperature (T_H). Denton and Wood heated from below whilst Jenkins cooled from above. For Denton and Wood's experiments, T_H was sometimes increased at given times throughout a run. This caused a corresponding change (decrease) in the "constant" value of k. Denton and Wood's (1974) range of k was $0.2 < k < 0.5$ whilst Jenkins (1974) obtained $k = 0.35 \pm 0.07$. It will be shown later (Chapter 5) that the apparent constancy of k was a result of the heat flux conditions (unsteady Q_p, constant T_H) and does not support Betts' (1973) assumption that k is a constant.

Many of the penetrative convection experiments discussed above have been analysed using Betts' (1973) model equations. However, at low Péclet number, molecular diffusion is important and Betts' assumption of a negligible interface thickness (Chapt.2.2.2) is not satisfied. For low Péclet number experiments, an improved entrainment model is obviously needed.

Other types of convective stirring experiments have been reported in the literature. Townsend (1964) and Adrian (1975) studied the penetrative convection occurring in a column of water above an ice-covered lower boundary (0°C) which has a constant upper boundary temperature of 20 - 30°C (Fig.2.8).

Because the density of water is a maximum at 3.94°C, the fluid at the lower boundary is buoyant and convective motions occur. The initial temperature distribution changes due to the growth of the mixed layer and molecular diffusion, until a steady state is reached. The mean steady state temperature and density profiles are shown schematically in Fig. 2.8. Adrian (1975) measured a mixed layer temperature $T_m \approx 2.85°C$ although a slight negative temperature gradient of approximately -1×10^{-2}°C/cm was recorded.

There must therefore be two buoyancy production regions, one at $z = 0$ and the other at $z \approx d_m$ (Fig. 2.8). The lower buoyancy production region creates upward rising thermal elements (see Appendix A for review of thermal convection) which penetrate the interface. At the upper negative buoyancy production region, downward falling thermal elements are created. These cannot be considered in terms of interfacial penetration because they move away from the interface. Above the interface is a stable linear density (temperature) gradient down which heat is transferred by molecular diffusion.

Townsend (1964) reported that the mixed layer consisted of rising columns of buoyant fluid with corresponding downward flows. The downward flows are probably driven by the negatively buoyant thermal elements from the interfacial buoyancy production region. The rising columns caused large temperature fluctuations at the interface and generated gravity waves on the stable density gradient.

Because of their eventual steady state condition, ice-water convection experiments are ideal for studying fluid motions. However, the interfacial entrainment process is difficult to conceptualize. There is only one turbulent layer and yet the interface is not rising.

Solar radiation penetrating the ice-covered surface of a lake also causes convective motions because the water temperature is below the maximum density value. Measurements of this phenomena (Fig. 2.9) have been reported by Farmer (1975).

Except for a transition profile at the ice-covered upper boundary, the convection layer has uniform temperature over most of its depth. Mean profiles do not reveal a buoyancy production region as the time scale of the temperature changes was of the order of days and months rather than minutes as in laboratory experiments.

This filtering of short period temperature fluctuations makes the mean temperature variations for this penetrative convection system more obvious. Figure 2.10 shows three simultaneous temperature readings

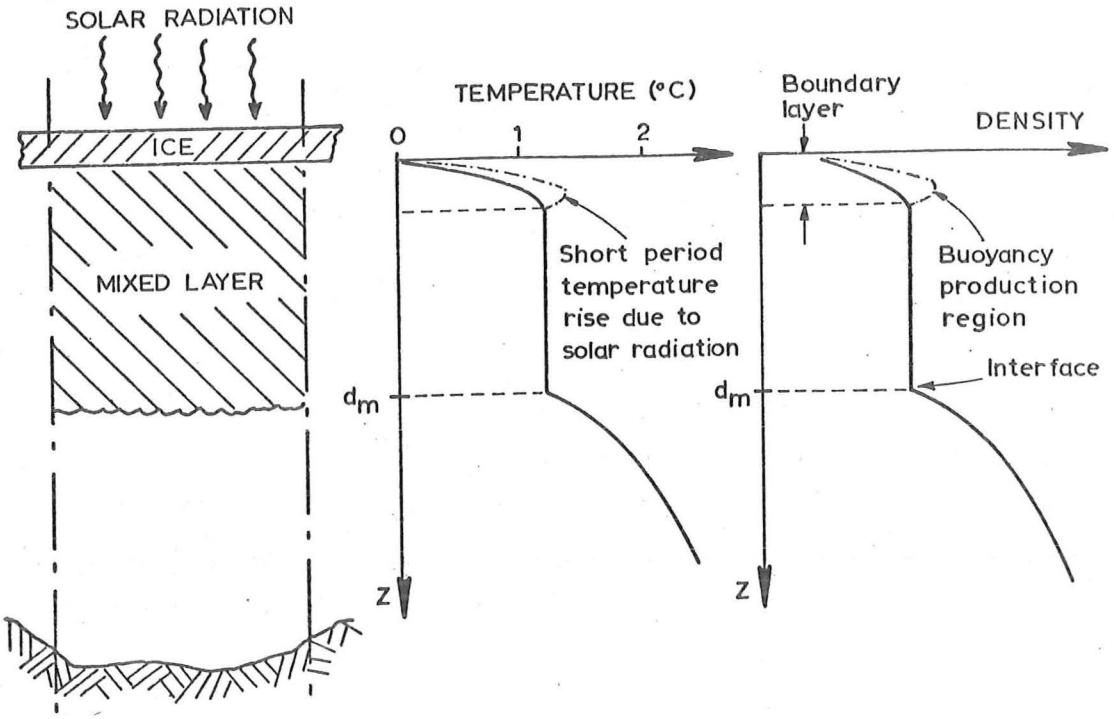

Fig. 2.9. Penetrative convection due to solar heating of an ice-covered lake (Farmer 1975).

measured continuously for several weeks at depths of 2, 14 and 31.8 metres. The upper reading shows fluctuations in the mixed layer due to the diurnal solar heating cycle. Further down in the mixed layer (14 metres), the diurnal fluctuations are not as significant but the net diurnal warming rate is the same.

The third trace at $z = 31.8$ metres shows the temperature changes due to the passage of the interface past the probe. Prior to the mixed layer penetrating to $d_m = 31.8$ metres on about the eighth day, little change in temperature (due to molecular diffusion) occurred. When the interface approached this depth, the temperature decreased (cooling) at an increasing rate. This was due to the additional turbulent motions in the diffusion region caused by mixed layer turbulence. However, once $d_m = 31.8$ metres , the temperature suddenly starts increasing and continues doing so at the mixed layer rate (dT_m/dt) .

From the output at $z = 31.8$ metres, it appears that the maximum interfacial cooling $(\partial T/\partial t)_i$ was approximately two and a half times greater than the mixed layer warming rate. This supports the sharp discontinuity in the vertical temperature profile assumed in the I.C.P.M. even though Farmer (1976) assumed a smooth transition in his analysis.

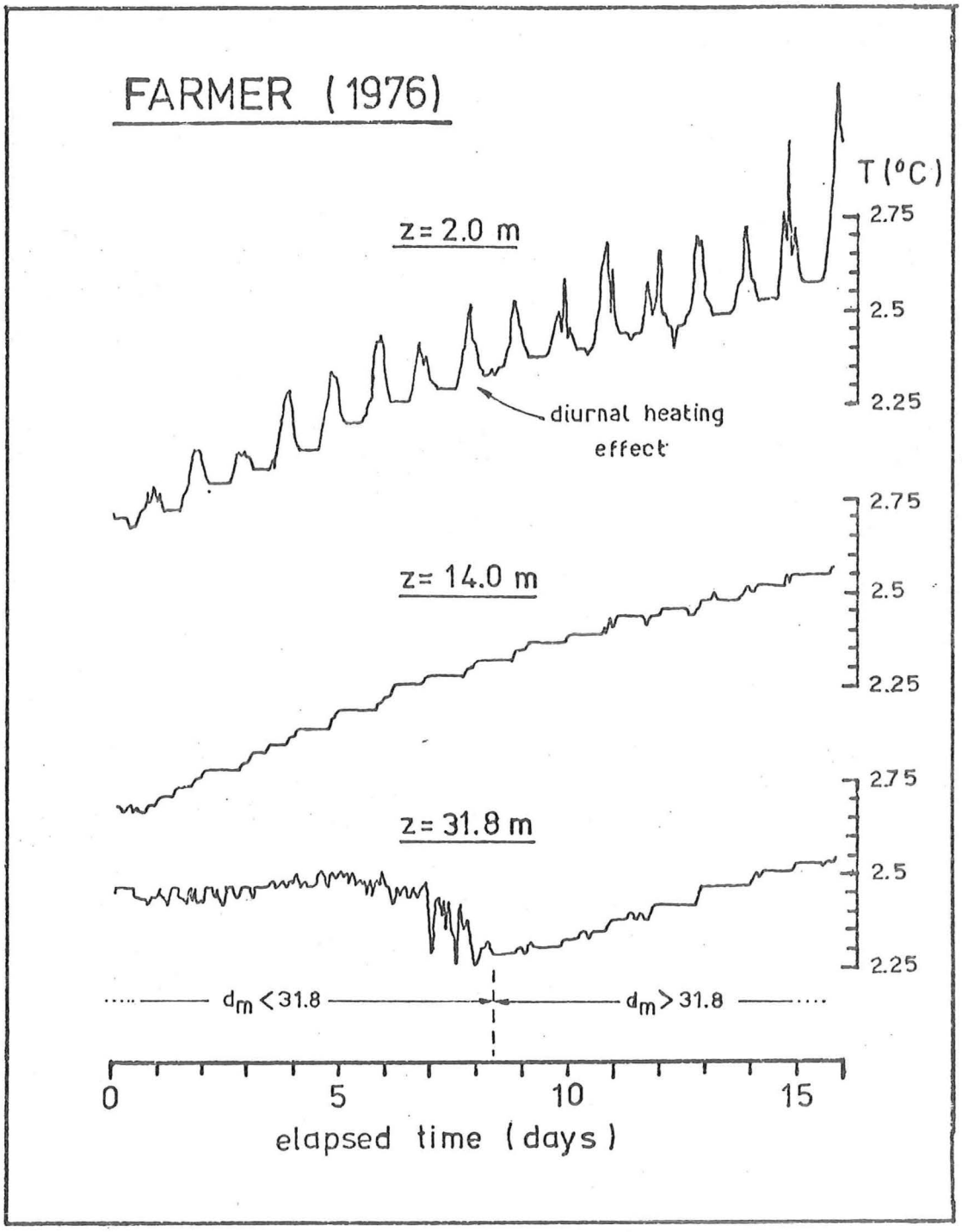

Fig. 2.10. Continuous temperature measurements at fixed depths in an ice-covered lake heated by solar radiation. Measurements show diurnal temperature variation near the surface, mixed layer temperature variation and the cooling which occurs as the deepening interface approaches the level of the measurement probe. (From Farmer 1975.)

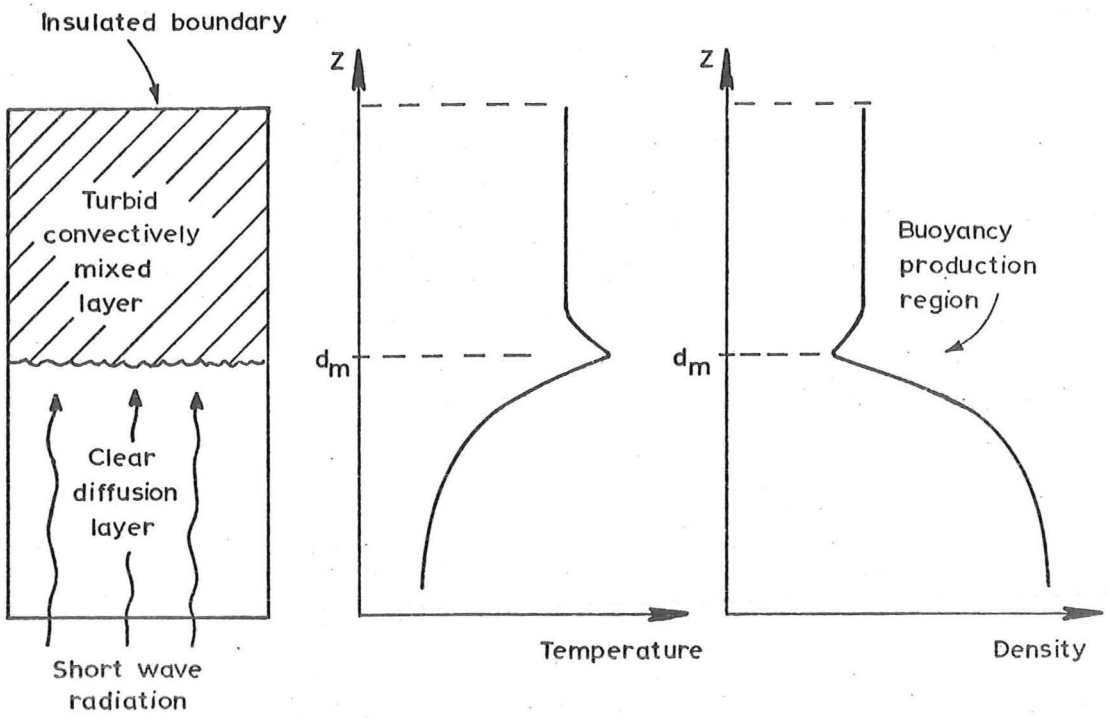

Fig. 2.11. An inverted laboratory model of convection in stratus cloud layers due to back radiation (McEwan 1974).

The range of k implied by Farmer's results was $0.05 < k < 0.34$ with a mean of 0.19.

Convective motions will occur within stratus cloud layers when they lose more heat by back-radiation than they absorb from the sun. An inverted model of this phenomena has been reported by McEwan (1974). A column of water, consisting of a light turbid layer above a dense low turbidity layer, was heated from below with short wave radiation (Fig. 2.11).

The short wave radiation absorbed at the turbid interface created buoyancy instabilities in the upper layer. This caused convective motions away from the interface. Physically the interface moved downwards but no penetration was observed. As the density differences were primarily due to temperature, a large portion of the interfacial heat flux must have been due to molecular diffusion (low Pe case). McEwan (1974) found no major correlation between the relevant parameters although the entrainment rate increased with upper layer turbidity.

When a fluid column contains two density components of different molecular diffusivity, arranged so that one component destabilizes the interface (by diffusing density upwards) and the other stabilizes the interface, an interfacial transfer phenomena known as double-diffusive

convection may occur (Turner 1973). If the component of lowest molecular diffusivity is the destabilizing component, buoyancy instabilities are created at the outer edges of the interface causing convective motions away from the interface (non-penetrative). Experiments using heat and salt (Turner 1965) and salt and sugar (Shirtcliffe 1973) have been reported. No external source of turbulent kinetic energy is required as the convective motions are driven by the potential energy of the density contributions.

These experiments have no immediate bearing on the I.C.P.M. problem which assumes a single density component. However, experiments in which an additional source of turbulent kinetic energy is applied to a double-diffusive system have been reported (Turner 1965, Crapper 1976). If the external energy source, in the form of a lower boundary heat flux (Turner 1965) or oscillating stirring-grids (Crapper 1976) is large, the additional turbulence will penetrate beyond the outer edges of the interfacial region where the double-diffusive buoyancy instabilities are created. If this occurs, the interfacial heat fluxes will be due to turbulent entrainment and molecular diffusion along the density gradients in the central interfacial region. The experiments will then behave in a similar way to the I.C.P.M.

2.3 ENTRAINMENT DUE TO SHEAR GENERATED TURBULENCE

2.3.1 Laboratory Shear Experiments

Interfacial entrainment between two horizontal fluid layers of different density, moving relative to each other with velocity ΔU, has been studied in laboratory experiments (Keulegan 1949, Lofquist 1960, Ellison and Turner 1959, Moore and Long 1971). Kato and Phillips (1969) applied a constant shear stress to the upper surface of an annular tank containing water with a stable linear salinity gradient. The shear generated turbulence caused an homogeneous mixed layer, which deepened by interfacial entrainment. Turbulent entrainment due to wind stresses at the upper surface of a water body containing a two-layered salinity distribution has also been studied experimentally (Wu 1973).

In each of the above cases, the sources of turbulent kinetic energy were shear stresses at the interface or other boundaries. There were no buoyancy fluxes across the upper or lower boundaries (i.e. $Q_p = 0$). More detailed reviews of shear-generated turbulence in stably stratified fluids have been presented by Long (1972), Thorpe (1973) and Long (1975).

Data from these experiments have been reported in a similar manner to the mechanical stirring-grid experiments, using the E_o, Ri_o form. The turbulent velocity scale V_s was generally taken as ΔU, the horizontal velocity difference across the interface, whilst the turbulent length scale was typically taken as d_m, the depth of the mixed layer or the moving layer. Figure 2.12 shows the E_o, Ri_o data from these experiments.

Kato and Phillips (1969) used the shear velocity $u_* = (\tau/\rho)^{\frac{1}{2}}$ as their turbulent velocity scale (where τ is the constant applied shear stress at the upper boundary). To convert this scale to ΔU, an approximate scale factor obtained from Kato and Phillips (1969, Figure 3) has been used. In their experiments, a shear stress of $\tau = 2.75$ gm/cm sec^2 was created by a screen velocity of $U = 30$ cm/sec and the mixed layer velocity was approximately half that value. Hence, a shear velocity of $u_* = 1.66$ cm/sec is equivalent to a relative layer velocity of $\Delta U \approx 15$ cm/sec.

Similarly, Wu's (1973) results were originally expressed in terms of the wind shear velocity and the air density. Wu's (1973) Figure 2 suggests that the surface drift current was about 0.55 times the wind shear velocity. The flow velocity at the interface (in the opposite direction to the wind due to closed basin circulation) was about one-third of the surface drift velocity.

Individual sets of data in Fig. 2.12 at high Ri_o have slopes between -1 and $-\frac{3}{2}$. As $Ri_o \to 0$ Ellison and Turner's (1959) data tend to a maximum value of E_o. This was also the case for Turner's (1968, 1973) mechanical stirring-grid data (Fig. 2.2).

However, at low flows (ΔU small and hence, larger Ri_o) it is possible for horizontal shear flows to be laminar. The interfacial transfer would then be by molecular diffusion alone, with a rapid fall-off in the value of E_o. Ellison and Turner's (1959) data, for their upper range of Ri_o, show this type of behaviour. As the I.C.P.M. entrainment process requires the presence of a turbulent region, the laminar case above is outside the scope of this study.

Molecular diffusion was also important in Moore and Long's (1971) experiments at the higher Richardson numbers. For very stable salinity interfaces (large $\Delta\rho_i$), up to 27% of the interfacial mass transfer was due to molecular diffusion.

In his discussion of the influence of shear on interfacial entrainment, Long (1975) took the relationship

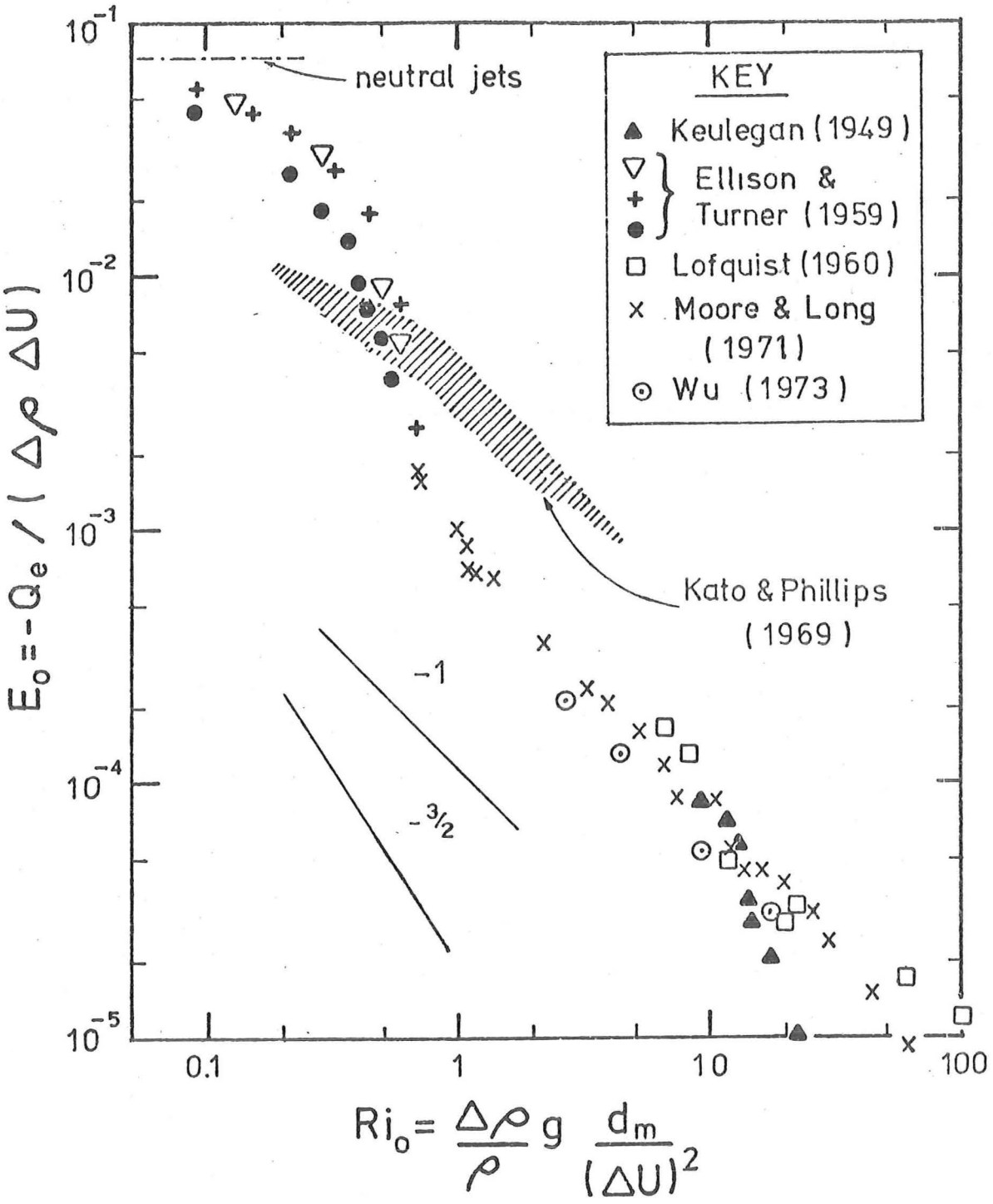

Fig. 2.12. Entrainment data from laboratory shear flow experiments. Data from Kato and Phillips (1969) and Wu (1973) have been transformed so that all the data have the same velocity scale (ΔU) and length scale (d_m).

$$E_o \propto Ri_o^{-1}$$

to be fundamental. This conflicts with Turner's (1973) adoption of the $-\frac{3}{2}$ power at large Pe (Chapt. 2.2.1). The inverse relationship between E_o and Ri_o is attractive because it has been taken to imply that the change in potential energy of the fluid column is proportional to the turbulent kinetic energy input (Rouse and Dodu 1955). It also appears to fit the data from some individual laboratory shear experiments (Fig. 2.12). However, as discussed in Chapt. 2.2.1, there is sufficient evidence to show that for large Péclet number and large Richardson number, the log E_o versus log Ri_o data curve tends to a slope of $-\frac{3}{2}$ (e.g. Fig. 2.2). The overall variation of the shear experiment data with Richardson number (Fig. 2.12) is consistent with this result.

2.3.2 Oceanographic Entrainment Models

In general, the effect of mean horizontal winds in atmospheric boundary layers is assumed to be secondary to the production of turbulent kinetic energy by surface buoyancy fluxes (Chapt. 2.2.2). In oceanographic models, the emphasis is reversed. Short-wave solar radiation during the daytime represents a stabilizing buoyancy flux. Buoyancy instabilities do occur during the night-time due to surface cooling by back-radiation. However, the turbulent kinetic energy supplied by surface wind shear and shear stresses between relative horizontal currents often has a greater effect on the mixed layer behaviour.

Earlier oceanographic models integrated the turbulent kinetic energy equation (Eqn. 2.2.13) over the whole mixed layer. The input turbulent kinetic energy due to windshear and buoyancy was apportioned to maintaining mixed layer motions and deepening the mixed layer. The remainder was assumed to be dissipated. (Turner and Kraus 1967, Denman 1973, Pollard et al. 1973, Niiler 1975, R. de Szoeke and Rhines 1976). As with Betts' (1973) atmospheric model, a step change in temperature was assumed at the interface. Denman (1973) used a Heaviside step function in his relationship for Q_e. If V_{em} was positive, $Q_e = - V_{em} \Delta T_i$ (e.g. Eqn. 2.2.4) but if V_{em} was zero or negative, the interfacial buoyancy flux Q_e was set equal to zero.

During a period of wind mixing, the turbulent mixed layer underwent the following modes of behaviour.

(i) An initial spin-up period to establish turbulent motions in the mixed layer. During this time $d_m \propto u_* t$ where u_* is the

shear velocity. This is consistent with $E = E_{max}$ in the absence of any major density gradients.

(ii) Surface wind shear is used to stir the mixed layer and to entrain interfacial fluid ($d_m \propto t^{\frac{1}{2}}$).

(iii) Mean motions are significant and shear generation also occurs at the interface. During this time $d_m \propto t^{\frac{1}{3}}$. This relationship was derived by Kato and Phillips (1969). It is consistent, in their case, with $E_o \propto Ri_o^{-1}$.

(iv) Once the layer is deep, Coriolis forces become significant and shear production is less important.

A plot of $\log d_m$ versus $\log t$, which is often used to evaluate the above relationships for $d_m(t)$, is heavily dependent on the initial conditions. In addition, the logarithmic scale compresses the later stages of behaviour. When Pollard et al.(1973) slightly altered the depth scale origin of Kato and Phillips' (1969) data and replotted them in the form $\log d_m$ versus $\log t$, they found a slope of $\frac{1}{2}$. However, over the last half of the data, a closer inspection reveals a slope of $\frac{1}{4}$. For Kato and Phillips' (1969) experimental conditions, this is consistent with $E_o \propto Ri_o^{-3/2}$.

Mean shear mixing layer models, developed more recently, have parameterized the turbulent heat and momentum fluxes by the use of Richardson number dependent stability factors. These stability factors are evaluated at every point and so it is not necessary to define in advance the existence of an isothermal mixed layer (Mellor 1973, Mellor and Yamada 1974, Mellor and Durbin 1975). Turbulent moment equations for velocity, pressure and temperature were simplified by making similarity assumptions for the pressure and dissipation terms. The similarity length scale coefficients and other constants were then evaluated using laboratory data from neutral boundary layers (Mellor 1973). It was assumed that the equations would hold for both stable and unstable layers. A check of the model against atmospheric data showed that this assumption was reasonable.

A comparison of a hierachy of models based on higher orders of simplification showed that the most complex Level 4 model was not significantly more accurate than a Level 2 model which ignored advection and diffusion terms (Mellor and Yamada 1974).

Mellor and Durbin (1975) applied a Level 2 model to the one-dimensional oceanographic surface layer. The turbulent Reynolds

stresses ($-\overline{u'w'}$, $-\overline{v'w'}$) and vertical heat flux due to turbulence ($-\overline{w'T'}$) were given by

$$(-\overline{u'w'}, -\overline{v'w'}) = \ell_s V_s \tilde{S}_M \left(\frac{\partial U}{\partial z}, \frac{\partial V}{\partial z}\right) \qquad (2.3.1)$$

and

$$-\overline{w'T'} = \ell_s V_s \tilde{S}_H \frac{\partial T}{\partial z} \qquad (2.3.2)$$

where U and V are the mean velocities and u' and v', the fluctuations about the mean, in the x and y horizontal directions. The fluctuations of vertical velocity and temperature are w' and T' respectively and ℓ_s and V_s are the turbulent length and velocity scales. The stability factors $\tilde{S}_M$ and $\tilde{S}_H$ were assumed to be functions of the flux Richardson number

$$Ri_f = \frac{-\alpha g \overline{w'T'}}{-\overline{u'w'}\frac{\partial U}{\partial z} - \overline{v'w'}\frac{\partial V}{\partial z}} \qquad (2.3.3)$$

The turbulent velocity scale is obtained from a simplified steady turbulent kinetic energy equation (Eqn. 2.2.14) so that

$$\frac{V_s^3}{B_1 \ell_s} = -\overline{u'w'}\frac{\partial U}{\partial z} - \overline{v'w'}\frac{\partial V}{\partial z} + \alpha g \overline{w'T'} \qquad (2.3.4)$$

A comparison of the model with the laboratory data of Kato and Phillips (1969) showed good agreement.

Mellor and Durbin (1975) considered the transfer of heat and mass in terms of molecular and turbulent diffusion. A similar approach will be used in the theoretical analysis of the I.C.P.M. (Chapter 3). However, the writer had adopted this turbulent diffusion approach prior to his sighting of Mellor and Durbin's (1975) paper.

Although it is not immediately obvious, the relationship $\tilde{S}_H = \phi(Ri_f)$ may be restated in terms of an effective gradient Richardson number Ri* (see Appendix F). The resulting equation for $\tilde{S}_H$ (which is equivalent to E_o from Eqn. 2.1.3) is

$$\tilde{S}_H = \frac{0.537}{1 + 1.98\ Ri^*} \qquad (2.3.5)$$

which agrees well with the penetrative convection expressions of Deardoff (1974a), (Eqn. 2.2.25) and Zilitinkevich (1975), (Eqn. 2.2.19).

Mellor and Durbin's (1975) model has the advantage that $\tilde{S}_H$ may be evaluated for all z. However, their model cannot be applied

directly to the penetrative convection case because it requires vertical gradients of horizontal velocity. In the I.C.P.M. mean horizontal motions are neglected.

2.4 SUMMARY

It has been shown in this review of the literature that the existing theories for interfacial entrainment are not suitable at low Péclet number. In the case of a single turbulent region, the fluid column has been generally assumed to consist of:

(i) A shallow boundary layer where buoyancy instabilities or shear stresses are produced $(0 \leq z < z_b)$.

(ii) The rest of the turbulent mixed layer in which the temperature distribution is neutral (or slightly stable) and the horizontal velocities do not vary with height. The full mixed layer extends from $0 \leq z < d_m$.

(iii) A negligibly thick interfacial region $(z = d_m)$.

(iv) The region above the interface $(z > d_m)$ in which the turbulent shear motions and heat transfer are neglected.

However, low Péclet number experiments have shown that molecular diffusion makes a significant contribution to the interfacial heat and mass transfers and hence to the thickness of the interfacial region (Crapper and Linden 1974). When molecular diffusion is significant, the assumption that the interfacial region has negligible thickness is not valid because the interfacial buoyancy fluxes would be infinite. At low Pe , the discontinuity in temperature (or density) gradient between regions (iii) and (iv) above, will be removed by molecular diffusion. The interfacial temperature (or density) gradient will be finite and turbulent motions may occur immediately above the interface. As will be discussed in later chapters, the interfacial gradient will play an important role in controlling the interfacial stability.

Two methods of analysing interfacial entrainment data have been reported in the literature (Eqns. 2.1.2 and 2.1.5). However, as both describe the same process, they cannot be considered independent. In Chapter 4, the relationship between these two analysis methods will be shown. This will allow the factors affecting the value of k to be discussed further.

In the next chapter, analytical equations for the rates of change of temperature and rate of rise of the interface in the inverted cooling pond model, will be developed.

CHAPTER 3

INITIAL DEVELOPMENT OF THE THEORETICAL MODEL

3.1 DESCRIPTION OF THE I.C.P.M.

The inverted cooling pond model of penetrative convection has been outlined in Chapt. 1.3. It consists of a column of water of cross-sectional area A, horizontal perimeter P and height h_T, heated from below (Fig. 3.1a). The fluid column is insulated on the top and sides. However, heat losses from the fluid column can be reduced by insulation but never eliminated. The heat budget for the I.C.P.M. will include upper boundary and side wall heat losses. The height z and the vertical heat flux per unit area q are positive in the vertically upwards direction. Side wall heat losses are positive in the outwards direction.

3.1.1 Boundary Conditions

Heat is lost from the surface of a cooling pond as sensible heat, latent heat of evaporation and by long-wave radiation. Unless the air has high humidity or is hotter than the surface fluid, these heat fluxes will always represent losses. Heat is gained by the surface of a cooling pond from solar radiation and back radiation from the atmosphere. Only some of the incident radiation is absorbed, the rest being reflected. During the daytime, the incident radiation is significant. However, in the cooling pond, the surface layer fluid is much hotter than the air. There will therefore be a net loss of heat to the atmosphere even during the daytime (i.e. q_p is positive). Heat is transferred below the surface by molecular diffusion, thermal convection and short-wave radiation.

In the I.C.P.M., heat is applied at a solid lower boundary. Any long-wave radiation will be absorbed by the water, within a negligible distance from the lower boundary. At large Rayleigh number all the lower boundary heat flux can be assumed to be transferred into the fluid column by turbulent convection.

The other boundaries are insulated (Fig. 3.1a). Heat losses from the fluid column, through these boundaries, are discussed in Appendix D. At the upper boundary ($z = h_T$)

$$q_{LT} = K_T \, (T(h_T) - T_{air}) \qquad (3.1.1)$$

where K_T is the mean thermal conductivity per unit thickness of the wall insulation and T_{air} is the temperature outside the insulation, assumed to be temporally and spatially constant.

For the side walls of the experimental apparatus

$$q_L = K_V (T(z) - T_{air}) \qquad (3.1.2)$$

Heat is also lost as stored heat in the walls of the experimental apparatus and insulation, as the temperatures increase. For the side walls, a heat storage factor β is defined. This is the ratio of the total heat storage capacity of the fluid column and experimental apparatus, per unit height, to the heat storage capacity of the fluid alone. A similar factor β_T applies to the upper boundary insulation.

Side wall and upper boundary heat losses will cause horizontal temperature gradients within the diffusion region ($z > d_m$) . The heat losses also create statically unstable density distributions at the insulated boundaries. These may result in weak convective circulations in the quiescent fluid above the interface. As the heat losses will be minor, the above effects are neglected.

If the lower boundary heat flux q_p is uniform over the fluid column area A , the fluid column can be assumed to be horizontally uniform. The I.C.P.M. will therefore be considered one-dimensional but heat losses will be allowed for in the heat budget equations.

3.1.2 Initial Conditions

In a cooling pond, hot water is continually being discharged onto the surface and the surface heat losses are always positive. The initial conditions for the I.C.P.M. will not describe a pre-entrainment situation in the pond. Instead, they will ensure that the behaviour of the model, after the commencement of lower boundary heating, is similar to the penetrative convection occurring in the cooling pond. This requires that the temperature gradient in the diffusion region well beyond the interface is zero.

Simple initial conditions, consistent with a cooling pond, are

$$\begin{aligned} T(z,0) &= T_{m0} \qquad 0 \leq z < d_{g0} \\ T(z,0) &= T_{a0} \qquad d_{g0} < z \leq h_T \end{aligned} \qquad (3.1.3)$$

These describe a layer of fluid of thickness d_{g0} and uniform temperature T_{m0} below a warmer layer of thickness $h_T - d_{g0}$ and temperature T_{a0}

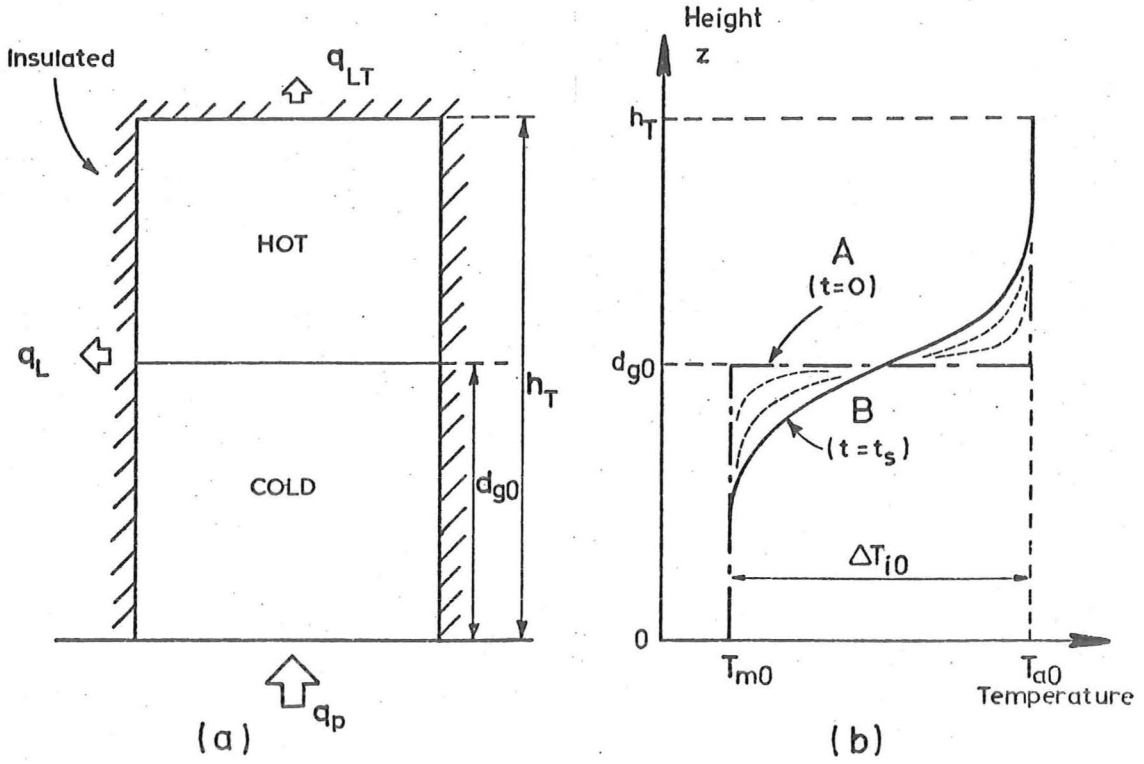

Fig. 3.1. Inverted cooling pond model - (a) elevation of fluid column showing boundary conditions, (b) initial temperature profiles ($t = 0$, t_s).

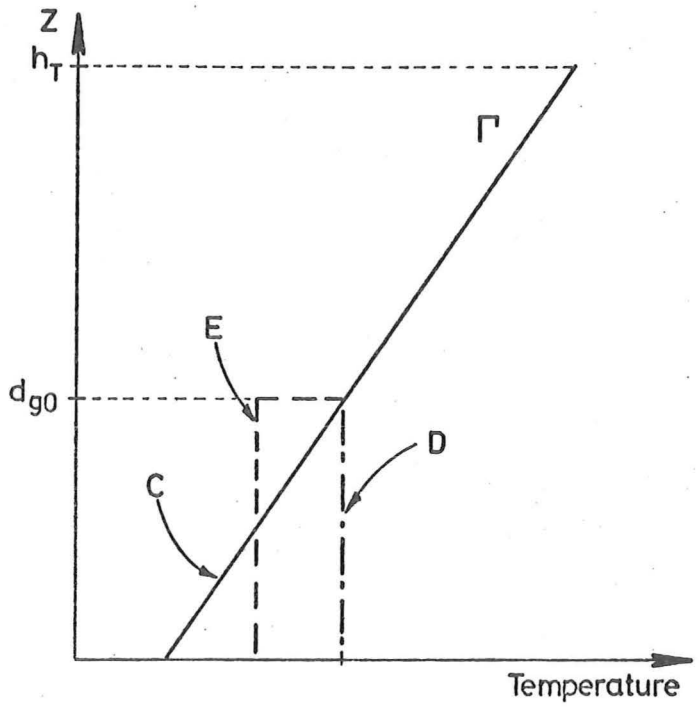

Fig. 3.2. Initial temperature profiles for atmospheric boundary layer models (linearly stratified case $\Gamma > 0$).

(Fig. 3.1b, profile A). The total fluid column thickness is h_T. As $T_{a0} > T_{m0}$, the two-layered temperature distribution is stable. For $z >> d_{g0}$, representing large cooling pond depths, the temperature is uniform ($= T_{a0}$). At time $t = 0$, the heat flux q_p is zero so there is no mixed layer ($d_m = 0$). The initial temperature difference between the mixed layer (T_m) and the maximum fluid temperature (T_a) is ΔT_{i0}.

Establishing the initial two-layered temperature distribution in an experimental tank takes a finite period of time. During this time, the boundary between the two layers will thicken by molecular diffusion. There will also be some turbulent entrainment due to the filling motions. Hence, at time $t = t_s$, when the penetrative convection experiment is commenced by applying a positive heat flux at $z = 0$, the temperature profile will be diffuse about $z = d_{g0}$ (Fig. 3.1b, profile B). In the theoretical analysis of the I.C.P.M., the temperature distribution at $t = t_s$ will be assumed to be caused by a period of molecular diffusion, $0 < t < t_s$, during which $q_p = 0$.

It should be noted that the initial conditions for the I.C.P.M. differ from those required for atmospheric models. Well above an atmospheric inversion, the potential temperature profile is more closely approximated by a stable linear gradient Γ. Three initial profiles for atmospheric models which satisfy

$$\frac{\partial T}{\partial z} \to \Gamma \qquad \text{for} \qquad z >> d_m$$

are shown in Fig. 3.2. Profile C given by

$$T(z,0) = T_{m0} + \Gamma z \qquad \text{for all} \quad z > 0$$

was used by Deardoff, Willis and Lilly (1969). The initial conditions of Willis and Deardoff (1974) also included a lower layer of uniform temperature and thickness d_{g0} (Fig. 3.2, profile D). Another possible initial condition is profile E (Fig. 3.2) which has a temperature discontinuity at height $z = d_{g0}$.

Atmospheric entrainment models, where $\Gamma > 0$, are discussed further in Appendix B.

3.2 TEMPORAL BEHAVIOUR OF THE I.C.P.M.

The temporal behaviour of the inverted cooling pond model is shown schematically in Fig. 3.3. From $t = 0$ until the commencement of heating at $t = t_s$, the lower boundary heat flux q_p is assumed to

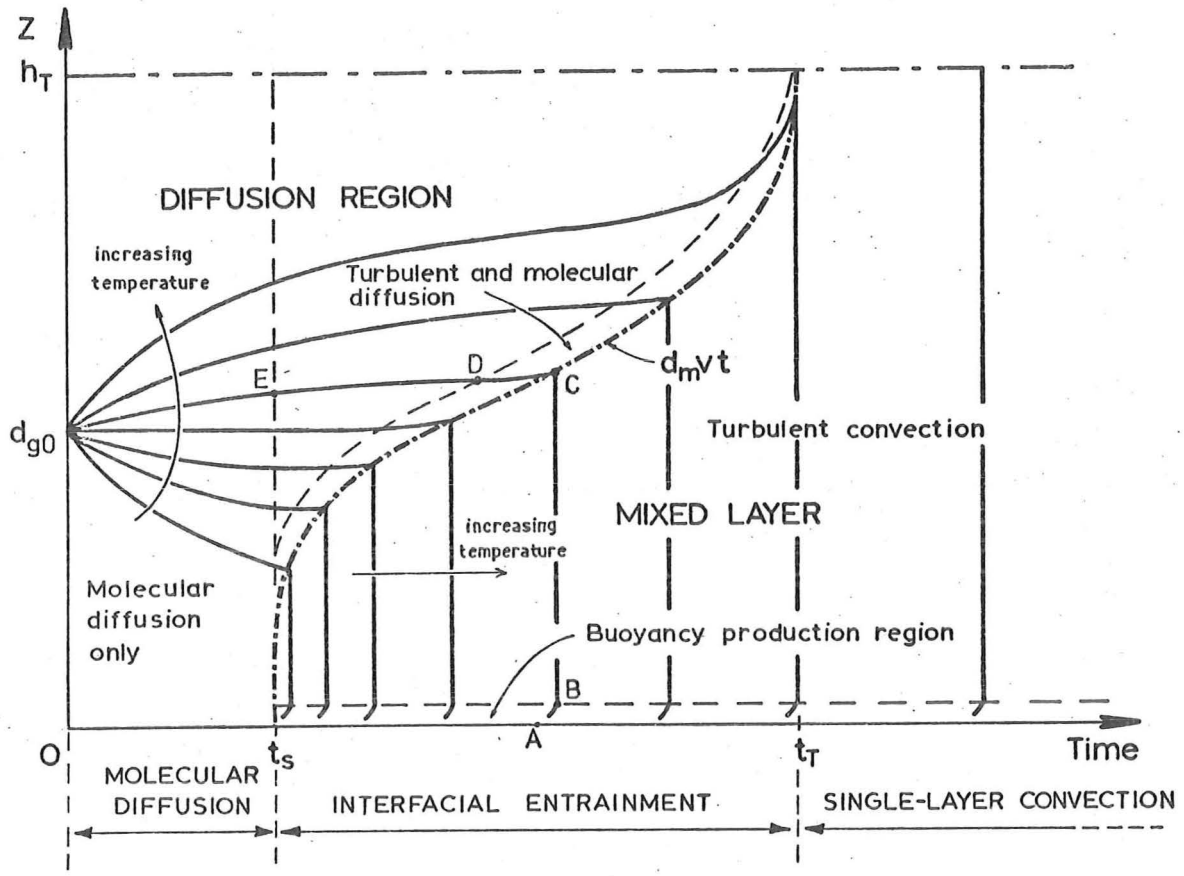

Fig. 3.3. Schematic plot of height versus time showing the interface height d_m as a function of time and contours of constant temperature.

be zero. Everywhere within the fluid column, the temperature distribution is stable. The only heat transfer vertically is by molecular diffusion which causes the temperature contours to expand about d_{g0}, the initial height of the boundary between the two layers (see also Fig. 3.1b).

It is important to note that the height of the maximum temperature gradient d_g is not the same as the height of the turbulent interface d_m. In oceanography, the depth of maximum temperature gradient ($\partial^2 T/\partial z^2 = 0$) is defined as the thermocline depth. In diurnal thermocline studies, this depth d_g could, therefore, be confused with the mixed layer interface. However, in the I.C.P.M., the initial value of d_g is d_{g0} whereas d_m is initially zero. The

time period $0 \leq t < t_s$ is defined as the molecular diffusion period (Fig. 3.3).

After the commencement of heating at $t = t_s$, a turbulent mixed layer of thickness d_m will be created. The rate at which the mixed layer thickens by interfacial entrainment is partly dependent on the strength of the interfacial temperature gradient. The role of the interfacial temperature gradient will be discussed in more detail later in this chapter. As the interfacial gradients are small for $z << d_{g0}$, the interface height d_m initially increases rapidly. In the vicinity of $z = d_{g0}$, the temperature gradients are large. When the interface is at these heights, it rises slowly. Later when $d_m >> d_{g0}$, the interfacial gradients are again small and the interface rises rapidly. Eventually the interface reaches height $z = h_T$ and the mixed layer occupies the full height of the fluid column. There is no longer an interface between turbulent and non-turbulent fluid. The time $t = t_T$, when $d_m = h_T$, marks the end of the interfacial entrainment period.

Four types of temperature contour can be seen in Fig. 3.3 during the interfacial entrainment period. The type of temperature contour depends on the heat transfer mechanism. It should be noted that in Fig. 3.3, the temperatures represented by these contours increase with both height and time.

Within the main body of the mixed layer, the temperature contours are straight and vertical as the temperature is uniform with height (B - C in Fig. 3.3). At the lower boundary of the mixed layer, in the buoyancy production region, the temperature contours are curved, with a positive slope, due to the unstable temperature gradients (A - B in Fig. 3.3). Well above the interface, the fluid is unaffected by the presence of the mixed layer, so molecular diffusion is the only vertical heat transfer mechanism. The temperature contours continue to spread with time, as in the earlier molecular diffusion period $0 < t < t_s$ (E - D in Fig. 3.3). However, in the diffusion region close to the interface, there is an additional heat transfer. This is due to the penetration of domes of turbulent mixed layer fluid above the interface. The temperature contours in this region will tend to curve upwards at a greater rate than for molecular diffusion alone (D - C in Fig. 3.3). The additional interfacial heat transfer due to turbulent entrainment will be discussed in more detail in the next section. Figure 3.3 also implies that there is a discontinuity in the rate of change of temperature, with constant height, at the interface. The reasons for this

$\partial T/\partial t$ discontinuity will be discussed in subsequent sections of this chapter.

After $t = t_T$, the model behaves like a single-plate convection experiment as there is only a single homogeneous layer of thickness h_T (Appendix A). The third time period for the I.C.P.M. ($t > t_T$) is called the single-layer convection period.

3.3 THE INTERFACIAL HEAT TRANSFER PROCESS

The one-dimensional temperature profile for the inverted cooling pond model (I.C.P.M.) during the interfacial entrainment period $t_s < t < t_T$ consists of a mixed layer profile $0 \leq z < d_m$ and a diffusion region profile $d_m < z \leq h_T$. In the mixed layer, the temperature is uniform with height ($= T_m$) except in the buoyancy production region, of thickness z_b, at the lower boundary (Fig. 3.4a). At large Rayleigh number, z_b is negligible compared to d_m. The diffusion region is a region of stable temperature gradients. If the mixed layer is continually deepening by interfacial entrainment, the temperature gradient can be assumed to be discontinuous at the interface (Fig. 3.4a). As will be shown in this section, turbulent entrainment causes additional cooling of the diffusion region fluid which maintains the stable interfacial gradient $(\partial T/\partial z)_i$ rather than destroys it.

Consider a buoyant thermal element released from the lower heated boundary ($z = 0$). As it travels upwards through the fluid, it will lose heat (and hence buoyancy) through mixing with the surrounding fluid, and by molecular diffusion. The continuous release of thermals from the heated boundary creates circulation cells of upwards and downwards moving fluid within the mixed layer. Although a thermal element may lose most or all of its buoyancy before reaching $z = d_m$, it will be carried on upwards by its momentum and the overall circulation. When it reaches $z = d_m$, it overshoots (Stull 1973). The temperature of the rising thermal element and its corresponding buoyancy variation with height are shown schematically in Fig. 3.4 a,b. Once the thermal is beyond a height of about $z = d_m$ (depending upon whether its temperature is equal to or slightly greater than T_m), it will be heavier than the surrounding fluid (Fig. 3.4b). It will rise into the diffusion region ($z > d_m$) until it has lost all of its initial kinetic energy.

The overshooting thermals penetrate into the diffusion region in the form of domes of mixed layer fluid. These interfacial domes can be

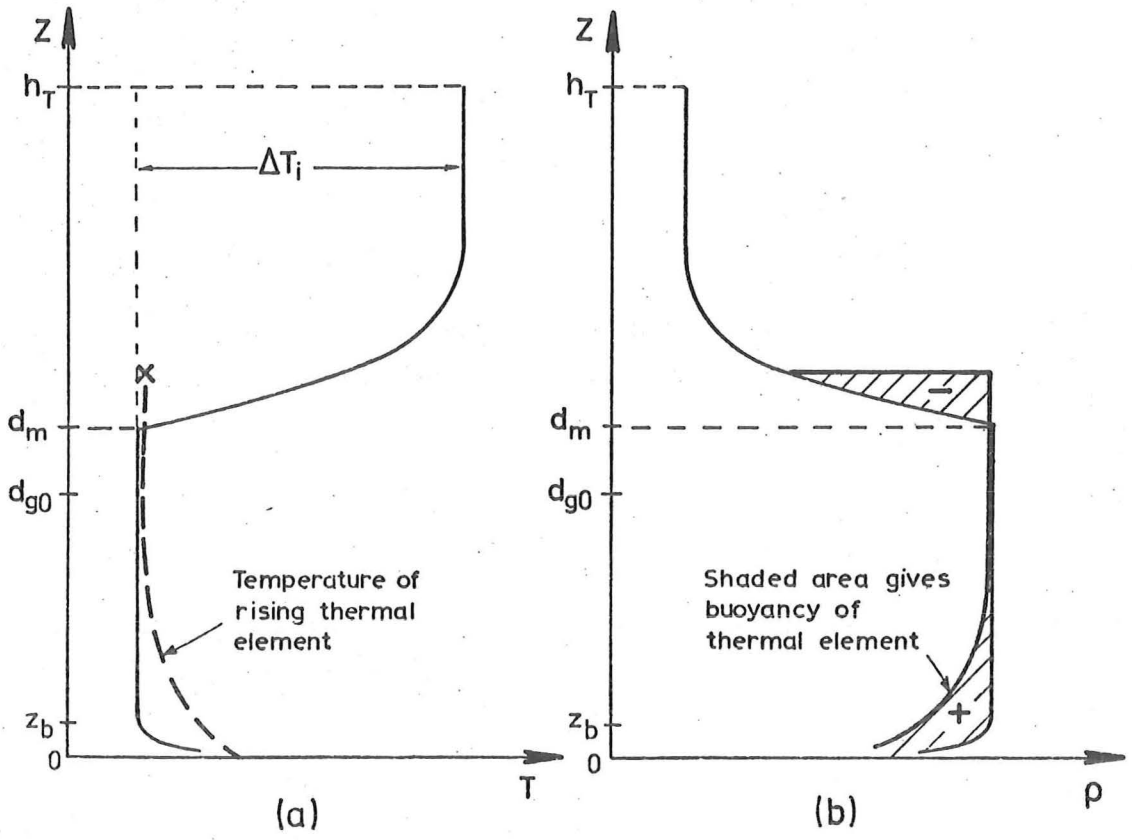

Fig. 3.4. Sketch showing the relationship between (a) the temperature and (b) density of rising thermal elements and surrounding fluid.

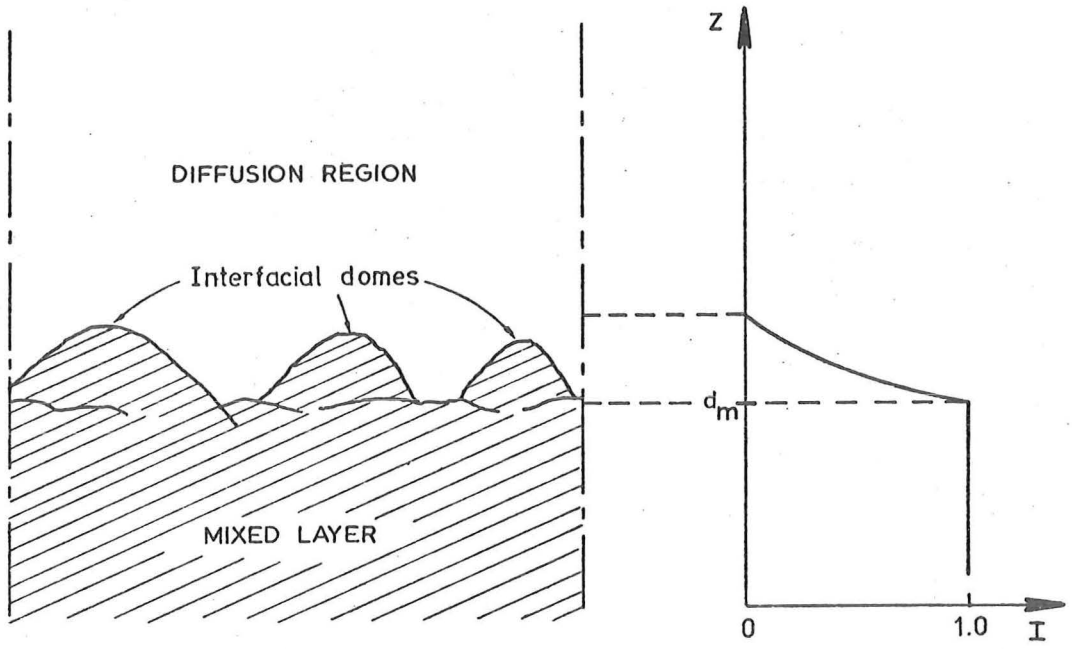

Fig. 3.5. Sketch of the interface between the turbulent mixed layer and the diffusion region showing the extent of the intermittency region $0 < I < 1$.

visualized by dyeing the mixed layer fluid (Fig. 3.5). The presence of a penetrating interfacial dome in the diffusion region is generally temporary. After the penetrating dome comes to rest in the lighter surroundings, it is forced to recede back into the mixed layer. An exception to this occurs when the interfacial temperature difference ΔT_i is negligible. The negative buoyancy forces are insufficient to return the penetrated fluid to the mixed layer.

A similar interfacial boundary between turbulent and non-turbulent fluid occurs in unrestricted shear flows (Townsend 1976). Fluid within the mixed layer and in the penetrating interfacial domes is fully turbulent, whilst the fluid into which the domes penetrate, may be considered non-turbulent. Any small scale transfer of turbulence across the interfacial boundary will be subjected to strong viscous damping.

The boundary between the turbulent mixed layer and penetrating dome fluid, and the non-turbulent fluid above is subject to temporal and spatial variations. The height of the interface d_m on the I.C.P.M. vertical temperature profile (Fig. 3.4a) is defined as the highest point at which the intermittency of turbulence $I = 1$. The intermittency factor $I(z)$ is taken as the fraction of turbulent fluid present at height z, measured as the mean over a short period of time. There will be a large scale variation of d_m with time due to the overall rise of the interface. Because of uneven lower boundary heating or topography, the interface height d_m may also vary horizontally. Hence, the intermittency $I(z)$ must be measured over a small horizontal area (following the one-dimensional assumption).

Throughout the mixed layer, $I(z) = 1$ (Fig. 3.5). Above the interface $z = d_m$, the intermittency will decrease with height. Beyond the maximum penetration of the interfacial domes, $I = 0$. The thickness of the intermittency region $0 < I < 1$ will depend on the interfacial temperature gradient $(\partial T/\partial z)_i$ and on the turbulent intensity in the mixed layer.

The penetration of turbulent interfacial domes beyond the interface and their subsequent motion back into the mixed layer $(z < d_m)$ causes a net downwards heat transfer. This is additional to that caused by molecular diffusion alone. There are two contributions to this additional heat flux.

The first is a direct turbulent interchange of fluid by the downwards displacement of diffusion region fluid, into the turbulent

mixed layer. This displacement of fluid results in an increase in the mixed layer thickness and a downwards transfer of heat. Two differing theories as to the exact nature of the displacement mechanism have been suggested (Stull 1973, Linden 1973) but no experimental confirmation of either mechanism has been reported. However, it is the effect of the displacement mechanism that is of primary interest here. The resulting heat flux may be considered to be independent of the molecular diffusivity of the fluid as the displaced diffusion region fluid is rapidly mixed with its new surroundings by the convective motions in the mixed layer.

The additional heat flux due to turbulent displacement of fluid can be parameterized by a turbulent diffusivity γ acting on the diffusion region temperature gradients. As the interfacial dome motions are related to the temperature gradients above the interface, this assumption appears to be reasonable. However, the use of a turbulent diffusivity parameter may not be valid when the temperature gradients are negligible.

The second contribution to the additional heat flux immediately above the interface, is due to the irrotational distortion of the diffusion region fluid by the penetrating domes. This can cause local increases in the temperature gradients and increase the effective area of the interfacial boundary. Any increase in the vertical heat flux will be proportional to the molecular diffusivity κ. Hence, an additional molecular diffusion factor λ is introduced to account for any extra heat flux due to the stretching and distortion of the intermittency region fluid.

At any height $z > d_m$, the vertical buoyancy heat flux is therefore given by

$$Q(z) = - ((1 + \lambda) \kappa + \gamma) \frac{\partial T}{\partial z} \qquad (3.3.1)$$

The variation of $\gamma(z)$ and $\lambda(z)$ with increasing height above $z = d_m$ will be closely linked to the variation of $I(z)$ (Fig. 3.5). Where $I = 0$, the values of γ and λ will also be zero. At the interface, where $I(z)$ is a maximum for $z \geq d_m$, it is reasonable to assume that $\gamma(z)$ will be a maximum ($= \gamma_i$). It should be noted that γ and λ only apply to the diffusion region. The assumption will be made that the variation of γ with height above the interface, at any time t, is given by

$$\gamma(z) = \gamma_i \, \phi_1 (z - d_m)$$

where $\phi_1(z - d_m)$ decays from unity at $z = d_m$ to zero for $z >> d_m$. A similar function is assumed for the additional molecular diffusion factor $\lambda(z)$.

The theoretical I.C.P.M. will be developed in the following manner:

(i) A one-dimensional heat diffusion equation (with losses) will be derived for the diffusion region $d_m < z \leq h_T$. This will include the parameters γ and λ to account for the additional heat transfer by interfacial dome action. For the molecular diffusion period ($t < t_s$) , $\gamma = \lambda = d_m = 0$. This simplifies the equation which will then be solved to obtain the vertical temperature distribution $T(z,t)$ for $t \leq t_s$.

(ii) A heat budget equation for the mixed layer $0 < z < d_m$ will be obtained.

(iii) The equations for the rates of change of temperature $(\partial T/\partial t)$ above and below the interface resulting from (i) and (ii) will be matched at the interface to obtain an expression for the rate of rise of the interface V_{em}.

3.4 DIFFUSION REGION EQUATIONS

By considering the heat budget for a one-dimensional element of thickness δz , with allowance for heat losses, the following heat budget equation may be derived

$$\beta \frac{\partial T}{\partial t} = - \frac{\partial Q}{\partial z} - W(T - T_{air}) \qquad (3.4.1)$$

This equation applies at any height within the fluid column. The term on the left hand side of Eqn. 3.4.1 corresponds to the heat stored by the fluid, the containing walls and insulation. The factor β accounts for the additional heat storage of the element due to the walls and insulation (Chapt. 3.1.1).

The first term on the right hand side of Eqn. 3.4.1 is the rate of change of the vertical buoyancy heat flux with height, and represents the difference between the heat fluxes entering and leaving the element in the vertical direction. The second term on the right hand side of Eqn. 3.4.1 allows for heat losses from the fluid column to the air (temperature T_{air}). The heat loss factor W is defined by

$$W = \frac{K_V P}{\rho c_p A} \qquad (3.4.2)$$

where K_V is the mean thermal conductivity of heat through the total thickness of the walls and insulation, per unit side wall area. P and A are the horizontal perimeter and plan area of the fluid column (c.f. Eqn. 3.1.2).

Within the diffusion region ($d_m < z \leq h_T$, $0 \leq t < t_T$), the vertical buoyancy heat flux $Q(z)$ is given by Eqn. 3.3.1. For $t < t_s$, there is no mixed layer ($d_m = 0$) so that both γ and λ are zero. After $t = t_s$, well above the mixed layer interface ($z >> d_m$), these two terms are also zero. Within the intermittency region, however, they are typically greater than zero. Substituting Eqn. 3.3.1 into Eqn. 3.4.1 yields

$$\beta \frac{\partial T}{\partial t} = \frac{\partial}{\partial z} ((1 + \lambda)\kappa + \gamma) \frac{\partial T}{\partial z} - W(T - T_{air}) \qquad (3.4.3)$$

The upper boundary condition for Eqn. 3.4.3, at $z = h_T$, is

$$Q(h_T) = W_T(T - T_{air})$$

where W_T is the heat loss factor for the column top material, given by

$$W_T = K_T / \rho c_p$$

A storage factor β_T which allows for the heat storage capacity of the material on top of the fluid column was discussed earlier (Chapt. 3.1.1). It is defined as the heat storage capacity of the full thickness of column top material normalized by the heat storage capacity per unit height of the fluid column alone. In general, where the height of the fluid column is large, the contribution due to β_T will be negligible.

During the molecular diffusion time period ($t < t_s$) , the lower boundary condition is $Q_p = 0$. The lower boundary heat flux may also be negative as it still satisfies the stable temperature distribution assumption.

For the interfacial entrainment period ($t_s < t < t_T$) , the lower boundary is at $z = d_m$ where d_m is an unknown function of time. The interfacial buoyancy flux Q_e , from Eqn. 3.3.1 evaluated at $z = d_m$, is

$$Q_e = - ((1 + \lambda_i) \kappa + \gamma_i) \left.\frac{\partial T}{\partial z}\right|_i \qquad (3.4.4)$$

The boundary conditions for the interfacial entrainment period will be found later, by matching the diffusion region equations with the mixed layer equations.

The initial conditions for the diffusion region of the I.C.P.M. are given by Eqn. 3.1.3.

For $t < t_s$, when $d_m = 0$ and $\gamma = \lambda = 0$, Eqn. 3.4.3 may be solved directly to obtain the vertical temperature distribution $T(z,t)$. At the lower boundary, $Q_p = 0$ and to simplify the solution, the upper boundary losses are ignored $(Q(h_T) = 0)$. Hence, the boundary conditions are

$$\left.\begin{aligned} \frac{\partial T(0,t)}{\partial z} &= 0 \\ \frac{\partial T(h_T,t)}{\partial z} &= 0 \end{aligned}\right\} \qquad (3.4.5)$$

The solution to equation 3.4.3 is (Appendix E.1).

$$T(z,t) = T_{air} + \left[T_{a0} - \frac{\Delta T_{i0}\, d_{g0}}{h_T} - T_{air} - \frac{2}{\pi}\Delta T_{i0} \sum_{n=1}^{\infty} \sin\left(\frac{n\pi d_{g0}}{h_T}\right) \cdot \cos\left(\frac{n\pi z}{h_T}\right) \cdot \exp(-\zeta_n^2 t) \right] \cdot \exp\left(-\frac{Wt}{\beta}\right) \qquad (3.4.6)$$

where $T_{i0} = T_{a0} - T_{m0}$

$$\zeta_n = \frac{n\pi}{h_T}\sqrt{\frac{\kappa}{\beta}}$$

If the thicknesses of the two initial layers (d_{g0} and $h_T - d_{g0}$) are large enough, an infinite boundary condition can be assumed. In this case, the solution to equation 3.4.3 (Appendix E.1) is

$$T(z,t) = T_{air} + \left[\left(\frac{T_{a0} + T_{m0}}{2}\right) - T_{air} + \frac{\Delta T_{i0}}{2} \operatorname{erf}\left(\frac{z - d_{g0}}{2\sqrt{\frac{\kappa t}{\beta}}}\right) \right] \cdot \exp\left(-\frac{Wt}{\beta}\right) \qquad (3.4.7)$$

where the error function is defined as

$$\operatorname{erf}\,\xi = \frac{2}{\sqrt{\pi}} \int_0^{\xi} e^{-x^2}\, dx$$

This solution is a good approximation of the molecular diffusion equation provided the arguments of the error function at the upper and lower boundaries

$$\frac{h_T - d_{g0}}{2\sqrt{\frac{\kappa t_s}{\beta}}} \quad , \quad \frac{d_{g0}}{2\sqrt{\frac{\kappa t_s}{\beta}}}$$

are greater than three so that the error function is approximately equal to unity. This condition was generally satisfied for the range of initial layer thicknesses and values of t_s used during this research.

The thermal diffusion equation cannot be solved analytically during the interfacial entrainment period as the functions $d_m(t)$, $\lambda(z,t)$ and $\gamma(z,t)$ are unknown. For $t_s < t < t_T$, Eqn. 3.4.3 will have to be solved numerically.

3.5 MIXED LAYER EQUATIONS

The temperature gradient within the mixed layer is assumed to be zero. In the absence of any significant temperature gradient, a relationship between heat flux and temperature gradient (c.f. Eqn. 3.3.1) becomes meaningless. Because the mixed layer has a uniform temperature T_m, Eqn. 3.4.1, for $0 < z < d_m$, becomes

$$\frac{\partial Q}{\partial z} = - \beta \frac{dT_m}{dt} + W (T_m - T_{air}) \qquad (3.5.1)$$

The buoyancy heat flux profile is therefore linear in the mixed layer. Integrating Eqn. 3.5.1 from $z = 0$ to $z = d_m$, and rearranging, yields the mixed layer heat budget equation

$$Q_p - Q_e - W d_m (T_m - T_{air}) = \beta d_m \frac{dT_m}{dt} \qquad (3.5.2)$$

This equation applies for $0 < z < d_m$ and $t_s < t < t_T$.

During the single-layer convection period when $d_m = h_T$, the upper boundary heat flux is not Q_e but $Q(h_T) = W_T (T_m - T_{air})$. For $t > t_T$, therefore,

$$Q_p - (W + W_T) d_m (T_m - T_{air}) = (\beta d_m + \beta_T) \frac{dT_m}{dt} \qquad (3.5.3)$$

where β_T accounts for the storage of heat in the upper boundary insulation.

3.6 THE RATE OF RISE OF THE INTERFACE

The height of the interface $z = d_m$ has been defined as the upper limit of the fully turbulent mixed layer of intermittency $I = 1$ (Chapt. 3.3). It is the point on the vertical temperature profile where the mixed layer (uniform temperature T_m) and the diffusion region meet. At $z = d_m$, the temperature gradient $\partial T/\partial z$ is discontinuous.

The partial derivative of temperature with respect to time $\partial T/\partial t$ is also discontinuous at the interface.

A vertical temperature profile for the case where $d_m > d_{g0}$ is sketched in Fig. 3.6. In this case, $\partial^2 T/\partial z^2$ is negative throughout the diffusion region. Consider the rate of change of temperature in the diffusion region. Expanding Eqn. 3.4.3 yields

$$\frac{\partial T}{\partial t} = \frac{1}{\beta}\left[(1 + \lambda)\kappa + \gamma\right]\frac{\partial^2 T}{\partial z^2} + \frac{1}{\beta}\left[\kappa\frac{\partial \lambda}{\partial z} + \frac{\partial \gamma}{\partial z}\right]\frac{\partial T}{\partial z} - \frac{W}{\beta}(T_m - T_{air}) \tag{3.6.1}$$

As both the turbulent entrainment parameters decay with height, $\partial\gamma/\partial z$ and $\partial\lambda/\partial z$ are negative. Hence, all the terms on the right hand side of Eqn. 3.6.1 make a negative contribution to $\partial T/\partial t$ for this example $(d_m > d_{g0})$. There is a net cooling of the diffusion region fluid. On the upper side of the interfacial discontinuity $(z = d_m^+)$, the fluid temperature decreases in time δt (from point A to point C, Fig. 3.6).

Consider the temperature changes in the mixed layer. From Eqn. 3.5.2

$$\frac{dT_m}{dt} = \frac{Q_p - Q_e}{\beta d_m} - \frac{W}{\beta}(T_m - T_{air}) \tag{3.6.2}$$

As Q_p is positive and Q_e is negative and the heat losses are minor, the mixed layer temperature will increase. In time δt, as shown in Fig. 3.6, the temperature at $z = d_m^-$ will increase from point A to point B. However, this situation does not satisfy the interfacial stability criterion. Fluid at $z = d_m^+$ is denser than the fluid below it. Thermal elements from the lower boundary will rise past $z = d_m$ to the point on the new diffusion region profile $(t = t + \delta t)$ where the mixed layer and diffusion region temperatures match (point D, Fig. 3.6). Above this height, the thermal elements become heavier than their surroundings. This is therefore, the new height of the interface. The change in interfacial height δd_m in time δt is due to changes in both the mixed layer and diffusion region temperatures.

It should be noted that the temperature at point D is slightly less than the temperature at point B because of the increased thickness of the mixed layer. While the case $d_m > d_{g0}$ was chosen to simplify the above discussion, the same principle applies when both $(\partial T/\partial t)_i$ and $(\partial^2 T/\partial z^2)_i$ are positive. This will occur initially when $d_m << d_{g0}$.

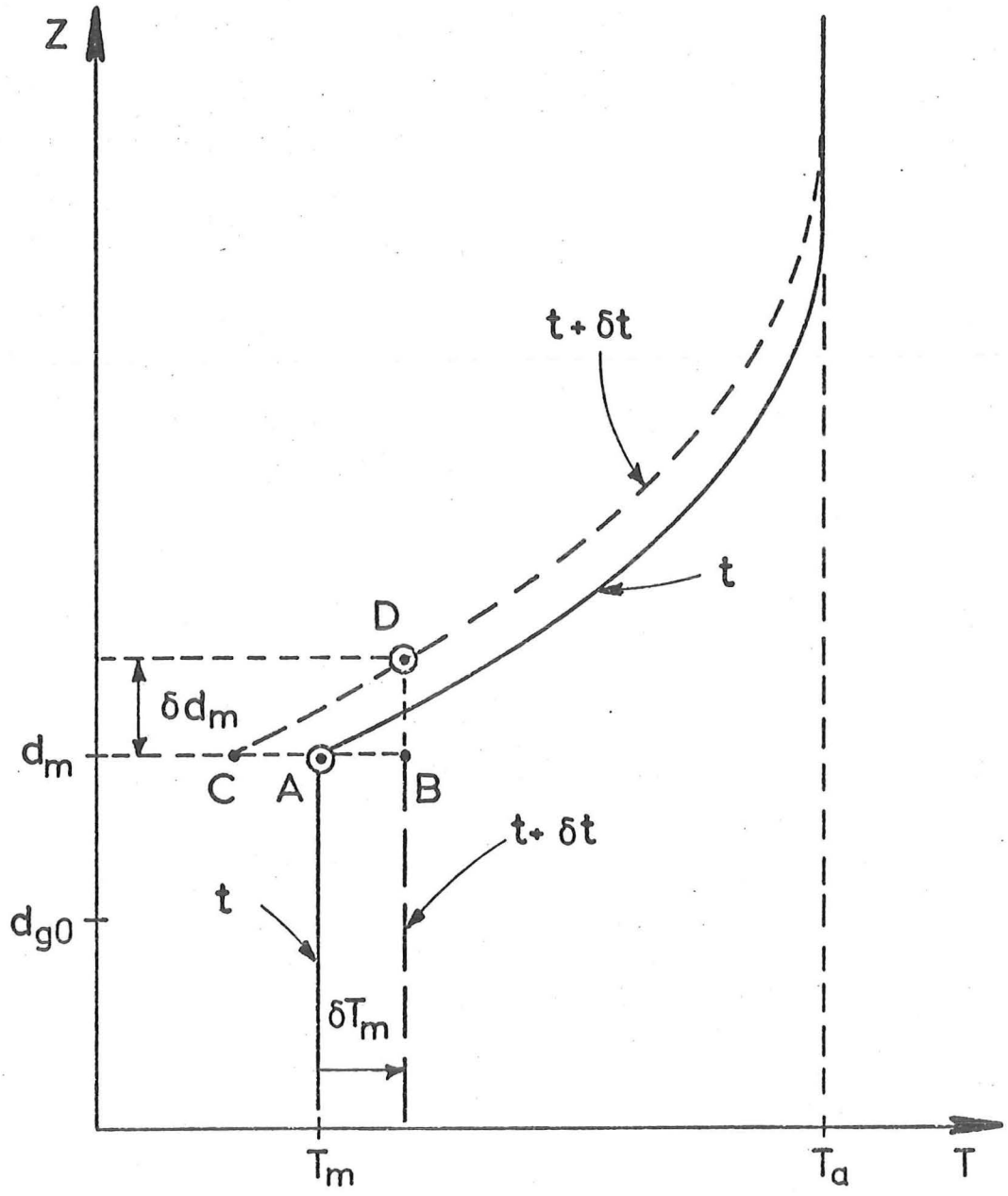

Fig. 3.6. Diagram showing the changes in the vertical temperature profile after a time increment δt .

For the I.C.P.M., the value of $(\partial T/\partial t)_i$ is restricted to being less than the rate of change of the mixed layer temperature. The reasons for this are discussed later in this section.

The above discussion showed in simple terms, the method of obtaining the rate of rise of the interface by matching the temperature changes immediately above and below the interface (Fig. 3.6). This can be expressed mathematically by considering the total derivative of temperature $T(z,t)$ with respect to time.

$$\frac{dT}{dt} = \frac{\partial T}{\partial t} + \frac{dz}{dt}\frac{\partial T}{\partial z} \tag{3.6.3}$$

In the mixed layer at $z = d_m^-$, the temperature gradient is negligible so that

$$\left.\frac{dT}{dt}\right|_m = \frac{dT_m}{dt}$$

In the diffusion region at $z = d_m^+$, the temperature gradient $(\partial T/\partial z)_i$ is not negligible. The total derivative of z with respect to time at this height is

$$\frac{dz}{dt} = \frac{d(d_m)}{dt} = V_{em}$$

From Eqn. 3.6.3, the total derivative of temperature is therefore

$$\left.\frac{dT}{dt}\right|_i = \left.\frac{\partial T}{\partial t}\right|_i + V_{em}\left.\frac{\partial T}{\partial z}\right|_i$$

As the temperature $T(z,t)$ is continuous at the interface, the total changes in temperature at $z = d_m^+$ and $z = d_m^-$ must be equal, so that

$$\frac{dT_m}{dt} = \left.\frac{\partial T}{\partial t}\right|_i + V_{em}\left.\frac{\partial T}{\partial z}\right|_i \tag{3.6.4}$$

Rearranging Eqn. 3.6.4 in terms of V_{em} yields

$$V_{em} = \left(\frac{dT_m}{dt} - \left.\frac{\partial T}{\partial t}\right|_i\right) \Big/ \left.\frac{\partial T}{\partial z}\right|_i \tag{3.6.5}$$

Equations for the rates of change of temperature in the diffusion region and mixed layer have been derived in Chapts. 3.4 and 3.5. From Eqn. 3.6.2 and the expression for Q_e (Eqn. 3.4.4)

$$\frac{dT_m}{dt} = \frac{Q_p}{\beta d_m} + \frac{((1+\lambda_i)\kappa + \gamma_i)}{\beta d_m}\left.\frac{\partial T}{\partial z}\right|_i - \frac{W}{\beta}(T_m - T_{air})$$

From Eqn. 3.6.1, evaluated at $z = d_m^+$

$$\left.\frac{\partial T}{\partial t}\right|_i = \frac{((1+\lambda_i)\kappa + \gamma_i)}{\beta} \left.\frac{\partial^2 T}{\partial z^2}\right|_i + \frac{1}{\beta}\left(\kappa \left.\frac{\partial \lambda}{\partial z}\right|_i + \left.\frac{\partial \gamma}{\partial z}\right|_i\right) \left.\frac{\partial T}{\partial z}\right|_i - \frac{W}{\beta}(T_m - T_{air})$$

The rate of rise of the interface V_{em}, from Eqn. 3.6.5, is therefore

$$V_{em} = \underbrace{\frac{Q_p}{\beta d_m \left.\frac{\partial T}{\partial z}\right|_i}}_{\text{I}} + \underbrace{\frac{((1+\lambda_i)\kappa + \gamma_i)}{\beta d_m}}_{\text{II}} - \underbrace{\frac{((1+\lambda_i)\kappa + \gamma_i)}{\beta} \left.\frac{\partial^2 T}{\partial z^2}\right| \Big/ \left.\frac{\partial T}{\partial z}\right|_i}_{\text{III}} - \underbrace{\frac{1}{\beta}\left(\kappa \left.\frac{\partial \lambda}{\partial z}\right|_i + \left.\frac{\partial \gamma}{\partial z}\right|_i\right)}_{\text{IV}} \quad (3.6.6)$$

It is worth noting that the heat loss terms have cancelled out of this equation.

Consider the contribution of each of the four terms in Eqn. 3.6.6 to the rate of rise of the interface V_{em}. Term I describes the rate of rise of the interface due to the "filling" (with heat) of the existing temperature profile by the lower boundary heat flux Q_p. The increase in the mixed layer temperature T_m, due to Q_p, is converted into an increase in d_m because of the positive interfacial gradient. Just after the commencement of heating at $t = t_s$, the mixed layer thickness d_m is very small and the interfacial gradient $(\partial T/\partial z)_i$ is negligible. The contribution of term I to V_{em} is therefore very large. Even if the interfacial gradient is significant initially, as in the linearly stratified experiments of Deardoff, Willis and Lilly (1969), the contribution to V_{em} is still large because d_m is small. The rate of rise of the interface will be much larger than would be predicted by turbulent entrainment alone. In the I.C.P.M., term I of Eqn. 3.6.6 will be referred to as the <u>filling velocity</u>. When the interface is in the region of $z = d_{g0}$, the temperature gradients are large and the filling velocity will have a minimum value. Although d_m continues to increase, the filling velocity will increase again, because of the more rapidly decreasing interfacial gradients . Term II in Eqn. 3.6.6 is the additional contribution to the "filling" of the temperature profile made by the interfacial heat flux. Both terms make a positive contribution to V_{em}.

Because $\partial^2 T/\partial z^2$ may be positive at the interface during the initial stages of the interfacial entrainment period, term III may make a negative contribution to V_{em}. However, as both the turbulent entrainment parameters decrease with height above the interface, term IV

of Eqn. 3.6.6 will always make a positive contribution. Terms III and IV are the contributions made to V_{em} by changes in the diffusion region temperature profile.

Provided the lower boundary heat flux is significant, the filling velocity (term I) will be large enough to ensure V_{em} is positive. However, it should be noted that if Q_p is very small and $(\partial^2 T/\partial z^2)_i$ is positive, the negative contribution by term III may act to reduce the height of the interface. Because Q_p is small, the turbulent entrainment terms are negligible and molecular diffusion dominates. Only the case when V_{em} is positive will be considered at this stage.

In experiments where the mixed layer turbulence is created by a vertically oscillating grid (Rouse and Dodu 1955, Cromwell 1960, Turner 1968) there is no external source of heat or mass, only mechanical energy. In these experiments the filling velocity term is zero but the other terms of Eqn. 3.6.6 will be valid.

The explicit equation for V_{em} (Eqn. 3.6.6) and other theoretical equations for the rate of change of temperature and vertical heat flux in the fluid column can be solved numerically for $d_m(t)$ and $T(z,t)$. The boundary conditions, initial conditions and fluid properties can all be specified. However, the turbulent entrainment parameters $\gamma(z)$ and $\lambda(z)$ for $z \geq d_m$ are unknown at this stage. Empirical relationships for these parameters will be obtained in Chapter 4.

In the next two sections, the heat budget for the full fluid column and an analytical relationship for the time at which the interfacial entrainment period ends t_T, will be derived. Neither of these results require the values of $\gamma(z)$ and $\lambda(z)$ to be known. The final section of this chapter will present simple analyses of the I.C.P.M. for which the turbulent parameters are neglected $(\gamma = \lambda = 0)$.

3.7 FULL FLUID COLUMN HEAT BUDGET

As will be shown in the next section, the full fluid column heat budget can be used to obtain a relationship for the time when the interfacial entrainment period ends, t_T. To simplify the derivation of this heat budget, the heat storage factor for the upper boundary insulation will be neglected $(\beta_T = 0)$. Integrating Eqn. 3.4.1 over the full fluid column yields

$$Q(h_T) - Q_p = -\beta \int_0^{h_T} \frac{\partial T}{\partial t}\, dz - W \int_0^{h_T} (T - T_{air})\, dz \qquad (3.7.1)$$

To evaluate the integrals, a mean temperature profile height, d_h, is defined where

$$d_h = \frac{1}{\Delta T_i} \int_0^{h_T} (T_a - T)\, dz \tag{3.7.2}$$

It can easily be shown from the solution of the heat diffusion equation for deep layers (Eqn. 3.4.7), that at $t = t_s$, $d_h = d_{g0}$. For any time $t_s < t < t_T$, the area under the vertical temperature profile will be $d_h\, \Delta T_i$. From the definition of d_h, it follows that

$$\int_0^{h_T} (T - T_{air})\, dz = (T_a - T_{air})\, h_T - \Delta T_i\, d_h \tag{3.7.3}$$

and that

$$\int_0^{h_T} \frac{\partial}{\partial t} (T - T_{air})\, dz = h_T \frac{dT_a}{dt} - \frac{d}{dt} (\Delta T_i\, d_h) \tag{3.7.4}$$

The full fluid column heat budget is therefore given by

$$Q_p - Q(h_T) - W \left[(T_a - T_{air})\, h_T - \Delta T_i\, d_h\right] = \beta\, h_T \frac{dT_a}{dt} - \beta \frac{d}{dt} (\Delta T_i\, d_h) \tag{3.7.5}$$

This equation can be further simplified, when the diffusion region is assumed to be deep, because the temperature gradients are negligible for $z >> d_m$. If the upper boundary losses are also considered negligible ($Q(h_T) = 0$), then the change in T_a is completely due to side wall losses. For $z >> d_m$ therefore,

$$\beta \frac{dT_a}{dt} + W (T_a - T_{air}) = 0 \tag{3.7.6}$$

Substituting Eqn. 3.7.6 into Eqn. 3.7.5 yields

$$Q_p + W\, d_h\, \Delta T_i = - \beta \frac{d}{dt} (\Delta T_i\, d_h) \tag{3.7.7}$$

3.8 THE LENGTH OF THE INTERFACIAL TIME PERIOD

The time t_T, when the interface reaches height h_T and the interfacial entrainment period ends, can be found by considering the increase in the heat stored in the fluid column, from t_s to t_T.

The values of d_h, T_a, T_m and hence ΔT_i, at time t_s, may all be obtained from the deep layer solution to the molecular diffusion equation (Eqn. 3.4.7). From these values, the heat storage at $t = t_s$

can be calculated. To evaluate the heat storage at $t = t_T$, only the mixed layer temperature at this time is required as there is no diffusion region ($d_m = h_T$).

Consider the variation of the maximum temperature T_a and the minimum temperature in the fluid column, T_m, prior to time t_T. If the diffusion region is deep then T_a is slowly decreasing due to heat losses. Because of the two heat fluxes into the mixed layer (Q_p and $-Q_e$), T_m is increasing. Eventually the interfacial temperature difference $\Delta T_i = T_a - T_m$ must become equal to zero. At this time, the interface between the turbulent mixed layer and the non-turbulent fluid will be rising at a finite maximum value of V_{em} (Chapt. 2.2). If the diffusion region is sufficiently deep, ΔT_i will become zero before the interface reaches the upper boundary. However, as the interface is rising at a rate which is of order 10^3 times greater than the typical minimum values of V_{em}, the difference in the times when $\Delta T_i = 0$ and when $d_m = h_T$ is negigible relative to $t_T - t_s$. The time when the interfacial temperature difference becomes zero is approximately equal to t_T.

It should be noted that if the initial upper layer thickness ($h_T - d_{g0}$) is small, the diffusion region will be completely entrained before the mixed layer temperature T_m becomes equal to the value of T_a predicted by heat losses (i.e. the solution to Eqn. 3.7.6). Conversely, if the fluid column is infinitely deep, the mixed layer will eventually become hotter than the diffusion region fluid. For this case ($\Delta T_i < 0$), the interfacial heat flux at the rapidly rising interface would be positive.

In the I.C.P.M. it will be assumed that the initial value $h_T - d_{g0}$ is always large. Hence, t_T is also the time when the mixed layer temperature T_m becomes equal to T_a. The variation of T_a will be assumed to be governed by Eqn. 3.7.6. Integrating the heat budget equation for the full fluid column (Eqn. 3.7.7) from t_s to t_T yields an implicit equation for t_T. From Appendix E.2

$$\int_{t_s}^{t_T} Q_p \exp\left(\frac{Wt}{\beta}\right) dt = \beta \, \Delta T_{i0} \, d_{g0} \qquad (3.8.1)$$

If Q_p is held constant an explicit equation results

$$t_T = \frac{\beta}{W} \ell n \left[\exp\left(\frac{Wt_s}{\beta}\right) + \frac{W \Delta T_{i0} d_{g0}}{Q_p} \right] \qquad (3.8.2)$$

If the heat losses are negligible ($W = 0$) then Eqn. 3.8.2 reduces to

$$t_T = t_s + \frac{d_{g0}\,\Delta T_{i0}}{Q_p} \tag{3.8.3}$$

This final result was given by Tennekes (1973) for his atmospheric model when $\Gamma = 0$.

It should be noted from the equations for t_T , that the result is independent of the temporal variation of the interface, provided $h_T - d_{g0}$ is large. In other words, as long as $\Delta T_i \to 0$ prior to d_m reaching h_T , the amount of interfacial entrainment occurring will not affect the overall fluid column heat budget or the value of t_T . Even if the turbulent entrainment parameters, γ and λ , are neglected in a numerical analysis of the I.C.P.M., the time when the interfacial entrainment period ends t_T will be unaffected.

3.9 PRELIMINARY ANALYSES OF THE THEORETICAL MODEL WITH A NON-TURBULENT DIFFUSION REGION

For large lower boundary heat fluxes and shallow mixed layers, the filling velocity term (term I in Eqn. 3.6.6) will make a major contribution to the rate of rise of the interface V_{em} . At low Péclet number , the contribution made by molecular diffusion to the heat transfer in the diffusion region, and to the rate of rise of the interface, will also be significant. It is therefore possible to gain some understanding of the temporal behaviour of the inverted cooling pond model (I.C.P.M.) by considering the interfacial entrainment process when the turbulent entrainment parameters $\gamma(z)$ and $\lambda(z)$ are equal to zero. By neglecting these terms and assuming the diffusion region to be non-turbulent, the I.C.P.M. equations can be greatly simplified.

Consider first the simple case, where the molecular diffusivity κ and the turbulent entrainment parameters γ and λ are all set to zero during the interfacial entrainment period $t_s < t < t_T$. The temperature profile existing at $t = t_s$, will remain unaltered within the diffusion region $(z > d_m)$, for all of the interfacial entrainment period. From Eqn. 3.6.6, the rate of rise of the interface V_{em} is therefore

$$V_{em} = \frac{Q_p}{\beta\, d_m \left.\frac{\partial T}{\partial z}\right|_i} \tag{3.9.1}$$

The only contribution is the filling velocity. This simple analysis model will be referred to as filling model entrainment. It can still be considered as an entrainment process as the turbulent mixed layer is continually thickening. However, this only occurs because the mixed layer fluid is continually becoming more buoyant than the diffusion region fluid immediately above. The interfacial entrainment process does not include any of the effects of the turbulent mixed layer ($z < d_m$) on the diffusion region ($z > d_m$), or molecular diffusion.

If the effect of molecular diffusion is included, with γ and λ still equal to zero, the I.C.P.M. analysis remains quite simple. After $t = t_s$, the diffusion region temperature profile changes by molecular diffusion. As the turbulent entrainment parameters are zero, the mixed layer has no effect on the diffusion region. This allows the diffusion region equations to be solved independently of the mixed layer. Hence, the molecular diffusion period equations will continue to hold after $t = t_s$ for $z > d_m$. This analysis will be referred to as molecular entrainment. There are still turbulent motions in the mixed layer, maintaining a uniform temperature distribution, but only the filling velocity and molecular diffusion are contributing to the interfacial entrainment process.

It should be noted that the concepts of filling model and molecular entrainment only apply because the interface ($z = d_m$) is a moving frame of reference. Turbulent mixed layer motions will penetrate beyond the existing interface height. However their effect on the diffusion region fluid (above the rising interface) may be negligible.

Despite the independence of the diffusion region equations from the mixed layer, the converse does not apply. The mixed layer heat budget will include the heat flux through the interface from the diffusion region. In the molecular entrainment case, equation 3.6.6 simplifies to give

$$V_{em} = \frac{Q_p}{\beta\, d_m \left.\frac{\partial T}{\partial z}\right|_i} + \frac{\kappa}{\beta\, d_m} - \frac{\kappa}{\beta} \frac{\left.\frac{\partial^2 T}{\partial z^2}\right|_i}{\left.\frac{\partial T}{\partial z}\right|_i} \qquad (3.9.2)$$

From Eqn. 3.4.4, the interfacial heat flux Q_e is given by

$$Q_e = -\kappa \left.\frac{\partial T}{\partial z}\right|_i \qquad (3.9.3)$$

Using equations 3.9.1, 3.9.2 and 3.9.3 and a solution to the molecular diffusion equation, it is possible to obtain numerical solutions for $d_m(t)$ and $T(z,t)$ for the filling model and molecular entrainment cases. The computer program for these numerical analyses is discussed in Appendix C. The infinite layer depth solution to the molecular diffusion equation was used to evaluate the diffusion region temperatures (Eqn. 3.4.7). For the range of conditions used to test the model (Table 3.1), the maximum difference in temperature between the infinite and finite layer solutions (Eqns. 3.4.6 and 3.4.7) was less than 0.01 °C. The infinite layer depth solution, based on the error function, allowed simple evaluation of the first and second derivatives of temperature with respect to height, both of which are required to evaluate V_{em}.

If the infinite layer depth solution is used, an analytical solution of the filling model entrainment equation (Eqn. 3.9.1) can be found (Appendix E.3). The solution, which gives the time t for a given interface height d_m, was used to complement the numerical solution.

Because the equations for the rate of rise of the interface predict V_{em} is infinite just after $t = t_s$ and just prior to t_T, a maximum value of $V_{em} = 1.5$ cm/sec was used in the numerical analyses. As discussed earlier, the maximum rate of rise of a turbulent interface occurs when there are no stable density gradients. For this case, V_{em} is of the same order as the r.m.s. vertical velocity fluctuation (Chapt. 2.2). The maximum values of V_{em} for the range of conditions to be studied are unknown. However, as the maximum value used in the numerical analyses, was 10^3 times greater than the minimum values of V_{em}, it had a negligible effect on the temporal behaviour.

A list of the initial conditions, boundary conditions, fluid properties and heat loss terms used in the numerical analyses is given in Table 3.1. The lower boundary heat flux Q_p was held constant and the variations of the fluid properties with temperature were neglected. Upper boundary heat losses were not included. All the values used were similar to those tested in the laboratory investigation (Chapter 6).

The temporal variation of the interface height d_m and the temperature contours for the filling model entrainment analysis are shown in Fig. 3.7. The numerical data covers the three I.C.P.M. time periods: molecular diffusion, interfacial entrainment and single-layer convection (Chapt. 3.2). As discussed earlier, the interface initially rises

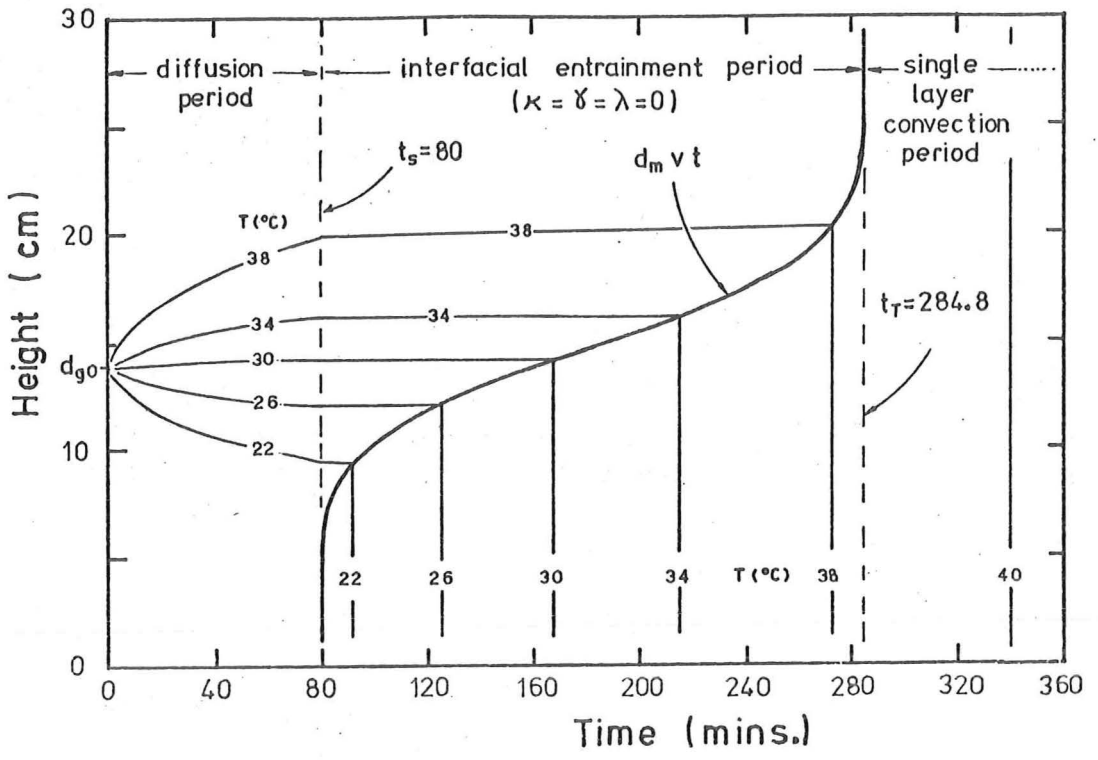

Fig. 3.7. Graph of height versus time for a filling model entrainment analysis ($\kappa = \gamma = \lambda = 0$) showing the interface height as a function of time and contours of constant temperature.

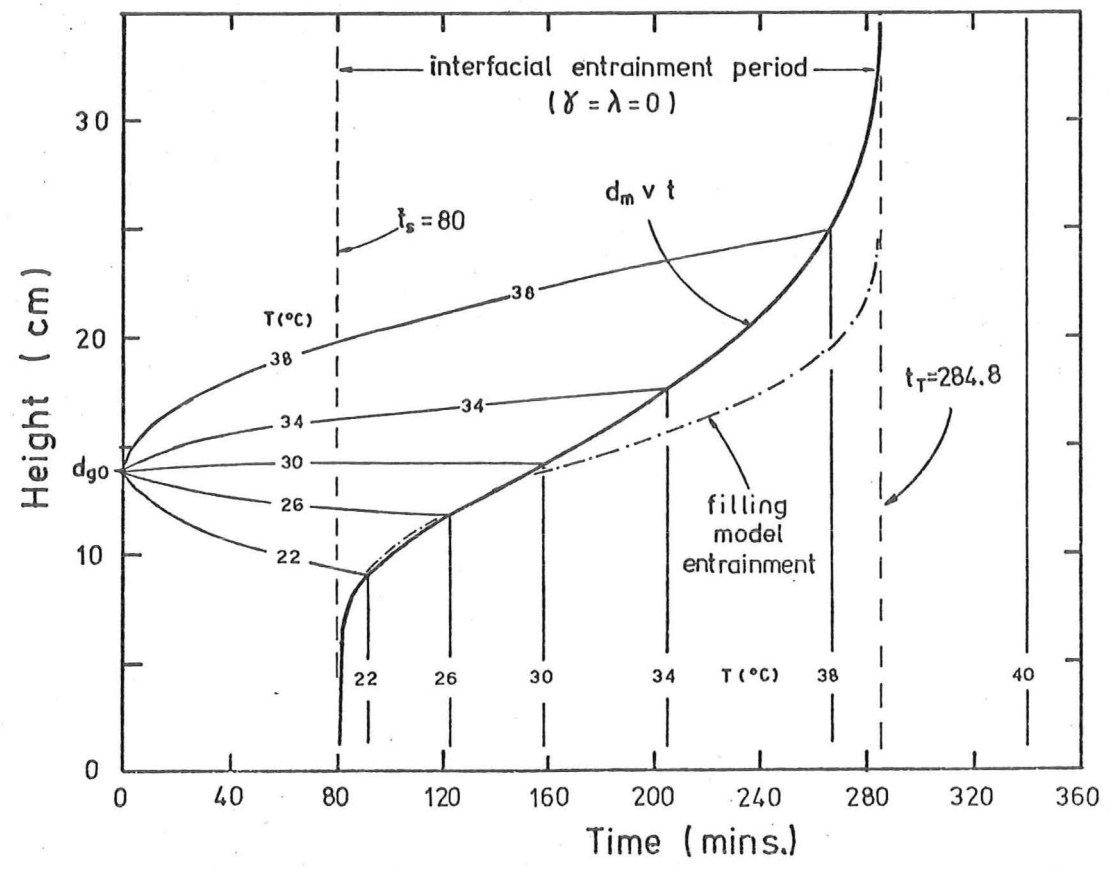

Fig. 3.8. Graph of height versus time for a molecular entrainment analysis ($\gamma = \lambda = 0$) showing the interface height as a function of time and contours of constant temperature.

TABLE 3.1 - LIST OF INPUT VALUES FOR THE NUMERICAL ANALYSES OF FILLING MODEL AND MOLECULAR ENTRAINMENT

Initial conditions	$T_{a0} = 39°C$
	$T_{m0} = 20°C$
	$d_{g0} = 13.93$ cm
	$h_T = 55$ cm
Boundary conditions	$Q_p = 0.023$ cm °C/sec
	$t_s = 80$ mins.
Fluid properties	$\kappa = 1.43 \times 10^{-3} cm^2/sec$
	$\rho c_p = 1.0$ cal/cm^3°C
Heat loss terms	$W = 7.44 \times 10^{-7} (sec)^{-1}$
	$\beta = 1.08$
	$T_{air} = 21°C$

rapidly as $(\partial T/\partial z)_i$ and d_m are small. With the increase in temperature gradient in the vicinity of $z = d_{g0}$, the rate of rise of the interface decreases to a minimum value. For $d_m > d_{g0}$, the temperature gradients decrease with height and V_{em} increases.

Prior to the commencement of heating at $t = t_s$, the temperature contours spread about $z = d_{g0}$, due to molecular diffusion downwards and heat losses. After $t = t_s$, the molecular diffusivity $\kappa = 0$ and the temperature contours remain at almost constant heights except for minor heat losses. The heat losses were retained in the filling model entrainment analysis to illustrate that their overall effect is not significant.

Once d_m reaches height h_T, the vertical mixed layer temperature contours occupy the full tank height. Because of the greater depth of water being heated, dT_m/dt is smaller and the temperature contours are spaced further apart.

Figure 3.8 shows the results of the molecular entrainment analysis plotted in the same form as Fig. 3.7. The curve of $d_m(t)$ from the filling model entrainment analysis is also shown. After $t = t_s$, the diffusion region temperatures continue to change due to molecular diffusion downwards and heat losses. They are unaffected by the

presence of the mixed layer. As the diffusion region temperatures are initially increasing, the interface heights for molecular entrainment are initially lower than for the filling model entrainment analysis. However, once the interface is above $z = d_{g0}$, the net diffusion region cooling (indicated by rising temperature contours in Fig. 3.8) enhances the rate of rise of the interface. Because of the additional interface heat flux Q_e in the molecular entrainment case, the mixed layer temperatures increase more rapidly (initially). This also causes the values of V_{em} to be larger. Eventually, the curve of interface height versus time for molecular entrainment rises well above the filling model curve.

Vertical temperature profiles from the molecular entrainment analysis show how the mixed layer and diffusion region temperature changes allow the interface to rise (Fig. 3.9). Also shown in Fig. 3.9 are the mixed layer temperatures for filling model entrainment. As the diffusion region temperatures hardly varied after t_s = 80 mins. (Fig. 3.7), they are not shown. The height of the mixed layer for the filling model entrainment analysis will approximately lie on the temperature profile for t_s.

At t = 120 minutes, the mixed layer temperature for molecular entrainment is greater than for filling model entrainment. However, due to the net warming of the diffusion region fluid just above the mixed layer, the interface is lower. For the later profiles in Fig. 3.9, both d_m and T_m are greater in the molecular entrainment case.

As the time nears t_T, the differences in the corresponding values of T_m decrease. Because the interface is higher for the molecular entrainment analysis, the heat storage capacity is also higher. Therefore, even though there has been an additional heat flux into the mixed layer $(-Q_e)$, the values of T_m for the two analyses are similar.

At $t = t_T$, the two values of T_m will be equal because the total increase in heat storage during $t_s < t < t_T$ for molecular entrainment and filling model entrainment will be the same (Chapt. 3.8). For the same reasons, the interface for a turbulent entrainment analysis $(\gamma = \lambda \geq 0)$ should also reach $z = h_T$ at approximately the same time t_T, and have the same value of T_m. Provided ΔT_i becomes equal to zero before $d_m = h_T$, the conditions at $t = t_T$ will be independent of the interfacial behaviour.

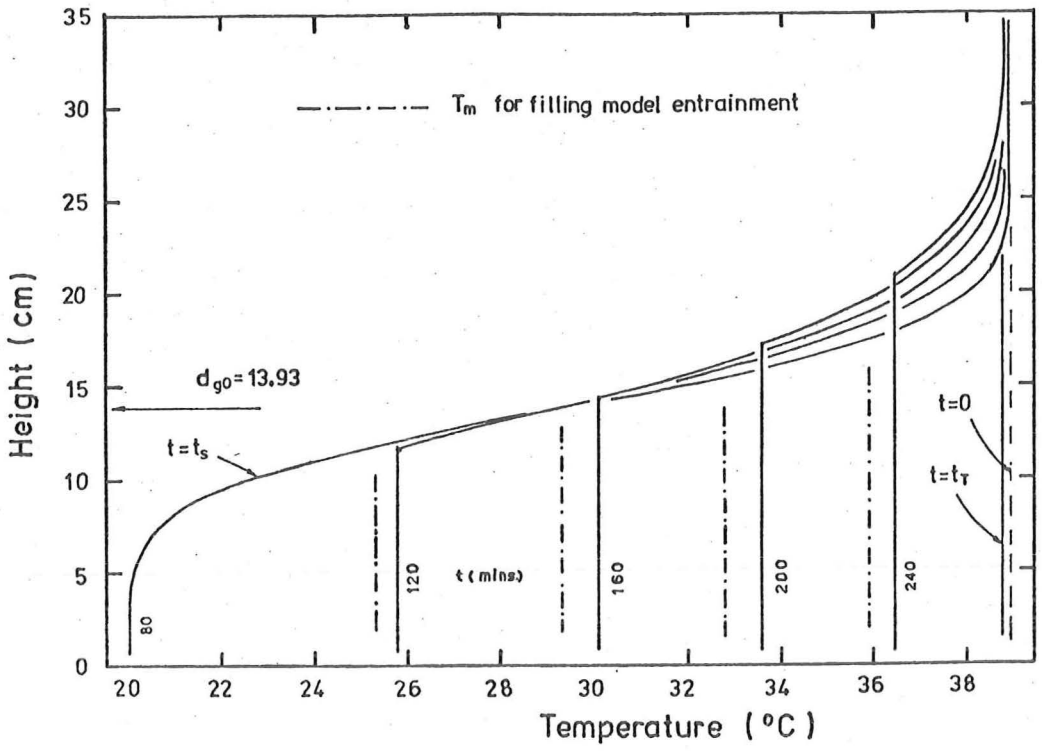

Fig. 3.9. Vertical temperature profiles from a molecular entrainment analysis. Also shown are mixed layer temperatures from the corresponding filling model entrainment analysis.

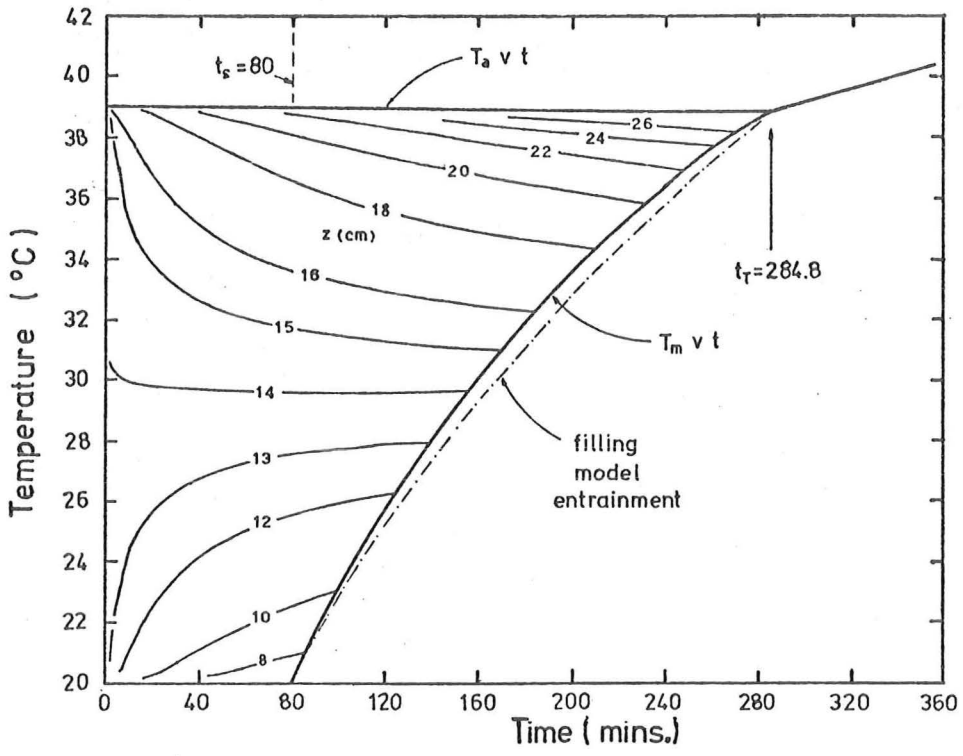

Fig. 3.10. Graph of temperature versus time for a molecular entrainment analysis with contours of constant height. Also shown is the mixed layer temperature curve for the corresponding filling model entrainment analysis.

From equation 3.8.2, the interfacial entrainment period for this example (using the values given in Table 3.1) ended at t_T = 284.8 mins. If there had been no heat losses (W = 0), the value of t_T would have been t_T = 286.4 mins.

A third method of presenting the temporal behaviour of the I.C.P.M. is a plot of temperature T(z,t) against time with contours of constant height (Fig. 3.10). This plot corresponds with the method of collecting temperature data in the experimental investigation (Chapter 6). The temperatures are measured at integer (centimetre) heights above the lower boundary. Figure 3.10 shows the results of the molecular entrainment analysis presented in this form. The mixed layer temperature T_m is represented by a single curve representing all $0 < z < d_m$. As the mixed layer thickens, the rate of increase of T_m decreases. From Eqn. 3.4.3, the temperature changes at constant height $z > d_m$, for molecular entrainment, are given by

$$\beta \frac{\partial T}{\partial t} = \kappa \frac{\partial^2 T}{\partial z^2} - W (T - T_{air}) \qquad (3.9.4)$$

It can easily be shown from the infinite layer depth solution to the molecular diffusion equation (Eqn. 3.4.7), that the height of the maximum temperature gradient d_g remains unchanged. Therefore, $d_g = d_{g0}$ = 13.93 cm until the interface reaches this height. Thereafter, the maximum temperature gradient occurs at $z = d_m$.

Below d_g, the temperatures at constant height in the diffusion region increase with time. This follows from Eqn. 3.9.4 as $\partial^2 T/\partial z^2$ is positive. As the molecular diffusion process acts to reduce the magnitude of $\partial^2 T/\partial z^2$, the rates of change of temperature decrease with time. For $z > d_g$, the temperatures decrease (cooling) with the rate of cooling again decreasing with time. The temperature at any height z will initially increase or decrease by molecular diffusion until $d_m = z$. Thereafter, the fluid is part of the mixed layer and the temperature (T_m) increases. In the case of turbulent entrainment ($\gamma = \lambda > 0$), there is additional cooling in the intermittency region (Chapt. 3.3). This will cause the temperatures at constant height to decrease at an increasing rate, as the interface approaches.

On a plot of temperature versus time, the height of the interface d_m at time t is represented by the contour height which meets the T_m curve at that time. Hence, from Fig. 3.10, the interface height at t = 210 mins. is 18 cm.

After $t = t_T$, the fluid column is fully mixed and the contours of constant height all lie on the single curve, T_m versus t . The variation of mixed layer temperature for the numerical analysis of filling model entrainment is also shown in Fig. 3.10. For filling model entrainment, the contours of constant height would show only slight decreases in temperature after $t = t_s$, due to minor heat losses.

For filling model entrainment, the interfacial buoyancy heat flux Q_e is zero, during $t_s < t < t_T$. The ratio $k = - Q_e / Q_p$ used by Betts (1973) and others in their atmospheric models is therefore zero. In the molecular entrainment case, Q_e is due to the molecular diffusion of heat along the interfacial temperature gradient. The value of k varies from zero at $t = t_s$ to a maximum value of $k = 0.1$, when $d_m = 13$ cm . It then decreases again, becoming equal to zero at t_T . The maximum value of k is not much different from the range of previously reported k values, $0.1 < k < 0.3$ (Stull 1976a).

In order to perform a more realistic analysis of the I.C.P.M., relationships for $\gamma(z)$ and $\lambda(z)$ are required. In the next chapter, empirical relationships for these terms are obtained.

CHAPTER 4

TURBULENT INTERFACIAL ENTRAINMENT

4.1 INTRODUCTION

Before a full numerical analysis of the I.C.P.M. can be performed, relationships for the turbulent diffusivity $\gamma(z)$ and additional molecular diffusion factor $\lambda(z)$ $(z \geq d_m)$ must be obtained. As was discussed earlier (Chapt. 3.3), both these terms may be assumed to have maximum values at the interface (γ_i and λ_i) and decay with height above the interface according to

$$\left.\begin{aligned} \gamma(z) &= \gamma_i \ \phi_1(z - d_m) \\ \lambda(z) &= \lambda_i \ \phi_2(z - d_m) \end{aligned}\right) \qquad (4.1.1)$$

The first step in evaluating either $\gamma(z)$ or $\lambda(z)$ is to obtain a relationship for the interfacial values γ_i and λ_i. The method that will be used to evaluate γ_i and λ_i from experimental data is as follows: Consider the interfacial buoyancy heat flux Q_e. From Eqn. 3.4.4

$$Q_e = - ((1 + \lambda_i) \kappa + \gamma_i) \left.\frac{\partial T}{\partial z}\right|_i \qquad (4.1.2)$$

This equation shows how the unknown quantities γ_i and λ_i are related, by $(\partial T/\partial z)_i$, to the interfacial buoyancy heat flux. Experimental measurements of Q_e and $(\partial T/\partial z)_i$ may therefore be used to evaluate γ_i and λ_i. In the special case of a high Péclet number experiment, molecular diffusion is negligible so that

$$\gamma_i = - Q_e / \left.\frac{\partial T}{\partial z}\right|_i \qquad (4.1.3)$$

In previous experimental work, Q_e has been related to the interfacial stability and mixed layer turbulence parameters in either of two ways (Chapt. 2.1). The first method considers Q_e as a function of the interfacial temperature difference ΔT_i, the molecular diffusivity κ and viscosity ν, and the mixed layer turbulence scales ℓ_s and V_s. Dimensional analysis then yields the non-dimensional interfacial buoyancy heat flux E_o $(= - Q_e/\Delta T_i V_s)$ as a function of the Richardson number Ri_o, Péclet number Pe and Reynolds number Re (Eqn. 2.1.2). The second method merely considers the interfacial buoyancy heat flux to be related to the boundary heat flux according to Eqn. 2.1.5, so that

$$Q_e = - k \, Q_p$$

Initially, we shall consider experimental measurements of Q_e in the non-dimensional form, E_o . However, it is necessary to reconsider the dimensional analysis. Because the interfacial thickness was neglected in earlier experimental analyses (Rouse and Dodu 1955, Turner 1968), the interfacial temperature difference ΔT_i was taken as being representative of the interfacial buoyancy field. It has been shown, however, that even for high Péclet numbers, a turbulent interfacial region has a finite thickness for a range of Richardson numbers (Crapper and Linden 1974).

The interfacial temperature gradient $(\partial T/\partial z)_i$ will therefore be used to represent the interfacial buoyancy field. This is consistent with the I.C.P.M. assumption that the temperature gradient, and not the temperature profile, is discontinuous at $z = d_m$. The use of the interfacial gradient is important in the I.C.P.M., where initially ΔT_i $(= T_a - T_m)$ is large but the interfacial gradients are small.

Dimensional analysis in terms of $(\partial T/\partial z)_i$ yields

$$Ri = \frac{\alpha g \left.\frac{\partial T}{\partial z}\right|_i \ell_s^2}{V_s^2} \qquad (4.1.4)$$

$$E = \frac{- Q_e}{\ell_s \left.\frac{\partial T}{\partial z}\right|_i V_s} \qquad (4.1.5)$$

The interfacial gradient Richardson number (Eqn. 4.1.4) is also the ratio of the buoyancy frequency

$$\left(\alpha g \left.\frac{\partial T}{\partial z}\right|_i\right)^{\frac{1}{2}}$$

to the mixed layer turbulence frequency V_s/ℓ_s , all squared. If the frequency with which the mixed layer turbulence attacks the interface is low relative to the interfacial response (high Ri), the interfacial motions will be controlled by the interfacial buoyancy field. If the mixed layer frequency is high relative to the frequency response of the buoyancy field (low Ri), the interfacial motions will be controlled by the mixed layer turbulence.

The dimensional ratios based on the overall temperature difference (E_o and Ri_o) and the interfacial gradient terms (E and Ri) are

related by the interfacial thickness term ℓ_i , where

$$\ell_i = \Delta T_i \Big/ \left.\frac{\partial T}{\partial z}\right|_i \qquad (4.1.6)$$

From Eqns. 2.1.3 and 2.1.4 and Eqns. 4.1.4 and 4.1.5,

$$\left.\begin{aligned} E_o &= E\,(\ell_i/\ell_s)^{-1} \\ Ri_o &= Ri\,(\ell_i/\ell_s) \end{aligned}\right\} \qquad (4.1.7)$$

To obtain a relationship for γ_i , we consider the special case of a high Péclet number entrainment experiment in which an oscillating stirring-grid is used on one side of the interface. As molecular diffusion is negligible, Eqns. 4.1.3 and 4.1.5 yield

$$E = \frac{\gamma_i}{\ell_s V_s} \qquad (4.1.8)$$

From a relationship for $E = \phi(Ri)$ at large Péclet number, it follows that $\gamma_i = \ell_s V_s \phi(Ri)$.

An alternative but more approximate method of obtaining Eqn. 4.1.8 comes from considering the rate of rise of the interface V_{em} (Eqn. 3.6.6). As there is no external buoyancy source, $Q_p = 0$, and at large Pe terms containing κ are neglected. Therefore

$$V_{em} = \frac{\gamma_i}{d_m} - \left.\frac{\partial \gamma}{\partial z}\right|_i - \gamma_i \left.\frac{\dfrac{\partial^2 T}{\partial z^2}}{\dfrac{\partial T}{\partial z}}\right|_i \qquad (4.1.9)$$

The storage factor β has been assumed to be unity. At large Pe , it is reasonable to assume that

$$\left.\frac{\partial^2 T}{\partial z^2}\right|_i \ll \left.\frac{\partial T}{\partial z}\right|_i$$

The third term on the right hand side of Eqn. 4.1.9 will, therefore, not make a significant contribution. In a grid stirring experiment (e.g. Turner 1968), the turbulent length scale ℓ_s is approximately one-tenth of the distance between the mean grid position and the interface z_{grid} . Crapper and Linden's (1974) measurements suggest the interface thickness is of the same order as ℓ_s . The rate of change of γ with height at the interface will be related to the interface thickness. Hence, the second term on the right hand side of Eqn. 4.1.9 is given by

$$-\left.\frac{\partial\gamma}{\partial z}\right|_i \approx \frac{\gamma_i}{\ell_i} \qquad (4.1.10)$$

As the oscillating grid is typically placed at mid-height in the mixed layer, d_m is approximately twice z_{grid} or twenty times ℓ_s. The second term on the right hand side of Eqn. 4.1.9 will be approximately twenty times larger than the first term.. Therefore, from Eqns. 4.1.9 and 4.1.10,

$$V_{em} \approx -\left.\frac{\partial\gamma}{\partial z}\right|_i \approx \frac{\gamma_i}{\ell_i}$$

At large Pe , Eqn. 2.2.5 holds so that

$$E_o \approx \ell_i \frac{\gamma_i}{V_s}$$

From Eqn. 4.1.7

$$E \approx \ell_s \frac{\gamma_i}{V_s}$$

The agreement of this derivation with Eqn. 4.1.8 suggests that Eqn. 4.1.10 is a good approximation.

Once a relationship for $\gamma_i = \ell_s V_s \phi(Ri)$ has been obtained, the decay of γ with height above the interface may be considered. An assumption as to the form of the decay function will have to be made. Equation 4.1.10 will be used as a guide to the magnitude of the interfacial gradient of the decay function.

To find the order of magnitude of the additional molecular diffusion term λ_i, low Péclet number data from a grid-stirring experiment will be used. Equation 4.1.2 states that the contributions made by the molecular and turbulent diffusivities to Q_e, sum arithmetically. From the empirical relationship for γ_i and the known value of κ, the contribution of λ_i to Q_e may be ascertained.

Before proceeding with the evaluation of $\gamma(z)$, the turbulent scales of length ℓ_s and velocity V_s for the I.C.P.M. need to be defined.

4.2 TURBULENT LENGTH AND VELOCITY SCALES

In the I.C.P.M. the mixed layer turbulence is caused by large Rayleigh number convection. The relevant scales of length and velocity for a convection layer, beyond the buoyancy production region, will be dependent on the layer depth d_m and the external supply of turbulent kinetic energy, represented by Q_p. Due to the turbulent nature of

the convective motions beyond the buoyancy production region, molecular diffusion and viscosity effects will be negligible. Only the coefficient of volumetric thermal expansion α needs to be considered. Therefore

$$\ell_s , V_s = \phi(\alpha, g, Q_p, d_m)$$

Dimensional analysis yields

$$\ell_s \propto d_m \tag{4.2.1}$$

$$V_s \propto (\alpha g Q_p d_m)^{\frac{1}{3}} \tag{4.2.2}$$

The corresponding turbulent time scale (Lilly 1968) is

$$\frac{\ell_s}{V_s} \propto \left[\frac{d_m^2}{\alpha g Q_p}\right]^{1/3} \tag{4.2.3}$$

A similar dimensional analysis for the convection temperature scale T_s yields

$$T_s \propto \frac{Q_p}{(\alpha g Q_p d_m)^{\frac{1}{3}}} \tag{4.2.4}$$

For his turbulent convection scales, Deardoff (1970) chose the layer depth as the length scale and defined the velocity and temperature scales as w_* (Eqn. 2.2.21) and T_* (Eqn. 2.2.23) respectively. Away from the heated boundary and the interface, Deardoff found that r.m.s. vertical velocity fluctuations and r.m.s. temperature fluctuations from atmospheric data (Telford and Warner 1964, Lenschow and Johnstone 1968) scaled with these convection scales. Data from the parallel plate convection experiments of Deardoff and Willis (1967) were also able to be scaled using w_* and T_*. More recent convection experiments have been analysed using these scales (Deardoff 1974b, Willis and Deardoff 1974 and Fitzjarrald 1976). Further discussion of convection scales is given in Appendix A. It therefore appears to be valid to use the relationships given by Eqns. 4.2.1 and 4.2.2 in the I.C.P.M.

For the I.C.P.M., ℓ_s and V_s will be defined as

$$\left.\begin{aligned} \ell_s &= 0.1\, d_m \\ V_s &= (\alpha g Q_p \ell_s)^{\frac{1}{3}} \end{aligned}\right\} \tag{4.2.5}$$

The choice of a turbulent length scale that is one-tenth of the mixed layer depth (and, therefore, one-tenth Deardoff's (1970) scale) brings ℓ_s into line with experimental measurements. The linear spread

of plumes and isolated thermals with height suggests $\ell_s \approx 0.1\, z$. Similarly Thompson and Turner's (1975) measurements above a vertically oscillating stirring grid yielded $\ell_s \propto 0.1\, z_{grid}$ (Eqn. 2.2.2). Atmospheric measurements of entrainment interfaces (large Pe) have revealed that the interfacial thickness is approximately one-tenth the mixed layer depth (Stull 1973, Betts 1974, Mahrt and Lenschow 1976). As will be discussed in the next section, Crapper and Linden's (1974) measurements of the thickness of the interfacial region between two stirred layers (thickness $\approx 1.5\, \ell_s$) suggest the thickness of the interfacial region for a single stirred layer is of order ℓ_s. The atmospheric measurements discussed above are therefore consistent with $\ell_s = 0.1\, d_m$.

The definition of the turbulent velocity scale (Eqn. 4.2.5) was not chosen to equate V_s with actual experimental measurements. When Turner (1973) plotted his (1968) experimental data in the form $\log E_o$ versus $\log Ri_o$, he used the measured turbulent length scales and r.m.s. horizontal velocity fluctuations (Eqns. 2.2.2 and 2.2.3) reported by Thompson and Turner (1975). Turner's (1973) data plot, $\log E_o$ versus $\log Ri_o$ (Fig. 2.2), is therefore applicable to other stirring experiments where σ_u and ℓ_s are measured directly. However, large Rayleigh number convection differs from grid generated turbulence as discussed below.

In a homogeneous layer above an oscillating grid, an array of jets are formed which merge, well away from the grid, to form a turbulence flow field. The variation of σ_u with height above the grid may be measured. For Turner's (1968) apparatus, Thompson and Turner (1975) found

$$\sigma_u \propto z_{grid}^{-3/2}$$

Mean motions do not make a major contribution to the turbulent energy transfer. In a similar set of measurements, Hopfinger and Toly (1976) found mean motions represented less than 10% of the total kinetic energy. Provided there is a reasonable thickness of fluid above and below the mean grid position, the r.m.s. velocity fluctuations should be unaffected by mean motions and therefore, are independent of the layer depth.

In the turbulent convection layer of the I.C.P.M., buoyant thermal elements are present (Appendix A). These are produced at the heated lower boundary and rise upwards toward the upper boundary. The mean motions of the thermal elements have a major influence on the transfer

of turbulent kinetic energy. Because the mean motions are controlled by the layer depth, the distribution of turbulent kinetic energy and hence, r.m.s. vertical velocity, will scale according to z/d_m (Deardoff 1970, Willis and Deardoff 1974 , Deardoff 1974b)

$$\frac{\sigma_w}{V_s} = \phi\left(\frac{z}{d_m}\right)$$

Therefore, the r.m.s. vertical velocities for turbulent convection cannot be calibrated in the same way as grid-stirring experiments. The value of σ_w in a deep homogeneous convection layer at height z will not be independent of the full layer thickness d_m .

The chosen I.C.P.M. definition of V_s (Eqn. 4.2.5) conforms with the second method of analysing interfacial buoyancy heat flux data (Chapts. 2.1 and 4.1). i.e.

$$Q_e = -k Q_p$$

This is the method typically used in penetrative convection studies (Betts 1973, Tennekes 1973 and others).

It should be noted at this stage that in the atmospheric model of Betts (1973), Ball's (1960) equation (Eqn. 2.2.4) was assumed to hold. Hence, k could be calculated from either Eqn. 2.1.5 or Eqn. 2.2.9. At low Péclet numbers, Eqn. 2.2.4 does not hold and the values of k obtained from Eqns. 2.1.5 and 2.2.9 will differ. This is discussed further in Chapt. 5.1. To differentiate between several possible definitions of k , the interfacial heat flux ratio for the I.C.P.M. is defined as

$$k_e = -Q_e / Q_p \qquad (4.2.6)$$

Consider the definitions of E and Ri (Eqns. 4.1.4 and 4.1.5). From the chosen I.C.P.M. definition of V_s (Eqn. 4.2.5), it follows that for all Péclet numbers

$$E\,Ri = k_e \qquad (4.2.7)$$

The loci of constant k_e values on a log E versus log Ri plot are, therefore, lines of slope -1. From Eqn. 4.1.6, it also follows that

$$E_o\,Ri_o = E\,Ri = k_e \qquad (4.2.8)$$

The I.C.P.M. definition of V_s allows direct evaluation of k_e from the E and Ri values.

4.3 TURBULENT DIFFUSIVITY $\gamma(z)$

4.3.1 Interfacial Turbulent Diffusivity γ_i

A method for obtaining a relationship for γ_i from high Péclet number grid-stirring data has been outlined in Chapt. 4.1. If the Péclet number is large, molecular diffusion effects are negligible. It will be shown later in this section that Turner's (1968, 1973) grid-stirring experiments fit this large Pe criterion.

From Eqns. 4.1.2 and 4.1.5, the full relationship for E is

$$E = (1 + \lambda_i)\, Pe^{-1} + \frac{\gamma_i}{\ell_s V_s} \qquad (4.3.1)$$

However, Turner's data was presented in the form $E_o = \phi(Ri_o)$ where the two terms E and E_o are related by the interfacial thickness ℓ_i (Eqn. 4.1.7).

Crapper and Linden's (1974) measurements using salinity and a similar range of conditions to Turner (1968), showed that, for large Pe , the interfacial region between two grid-stirred layers had a thickness of approximately 1.5 ℓ_s . Hopfinger and Toly (1976) measured both the static and dynamic thicknesses of a very stable salinity interface above a single stirring-grid. For two cases, which had Richardson numbers differing by a factor of 10, the thickness of the interface shortly after stopping the stirring-grid (static value) was $\approx \ell_s$. The interfacial thicknesses with the stirrer in action (dynamic values) were slighly larger and Richardson number dependent.

For the purposes of this empirical evaluation of γ_i for the I.C.P.M., the assumption will be made that for large Péclet number

$$\ell_i = \ell_s \qquad (4.3.2)$$

This equation will be used to relate Turner's $E_o = \phi(Ri_o)$ salinity data with the I.C.P.M. terms E and Ri. It will be shown later that if ℓ_i/ℓ_s is slightly different from unity but still constant, the form of the resulting $E = \phi(Ri)$ and γ_i relationships will be unaffected. Only the empirical constants will be different. From Eqns. 4.1.7 and 4.3.2, it follows that $E = E_o$ and $Ri = Ri_o$ at large Péclet number.

Consider Eqn. 4.3.1 for E , and hence E_o , evaluated from Turner's (1968) salinity experiments. For $z_{grid} = 9$ cm and a minimum stirring frequency of 166 revs per minute, the length and velocity scales (Eqns. 2.2.2 and 2.2.3) were

$$\ell_{sT} = 0.9 \text{ cm} , \quad \sigma_{uT} = 0.144 \text{ cm/sec}$$

It should be noted that z_{grid} is the distance from the mean grid position to the interface $z = d_m$. In Turner's (1968) single stirring-grid experiments, the interface was maintained at the central height of his experimental tank. The value of z_{grid} was therefore fixed. In his double stirring-grid experiments, the interfacial region between the two mixed layers remained stationary, midway between the two grids. However, due to the thickness of the interfacial region, the distances to the two interfaces z_{grid} were less than the single stirring grid value. This is significant at low Péclet numbers where the interfacial region thickness is large (Crapper and Linden 1974). It is not apparent whether Turner (1968, 1973) accounted for this reduction in z_{grid}. In this thesis, only data from the single stirring-grid experiments (Fig. 2.2), which more closely conform with the I.C.P.M., are used quantitatively.

Assuming the molecular diffusivity for salinity to be 1.2×10^{-5} cm^2/sec,

$$Pe_T = \frac{\sigma_{uT} \ell_{sT}}{\kappa} = 1.1 \times 10^4$$

At the lowest value of $E_o = 2 \times 10^{-3}$ (Fig. 2.2) and λ_i of order unity, the first term on the right hand side of Eqn. 4.3.1 is less than 10% of E_o. As E_o increases with decreasing Richardson number, this contribution from molecular diffusion will become even smaller. Turner's (1968, 1973) salinity data may therefore be considered to be representative of high Péclet number data.

An empirical relationship is now required which fits the form of Turner's high Péclet number data (Fig. 2.2). At large Richardson number, the data varies according to

$$E \propto Ri^{-3/2}$$

This large Ri limit is well established experimentally (Chapt. 2.2.1). With decreasing Richardson number, the data tends to the zero Ri limit

$$E = E_{max}$$

The form for an empirical formulae to interpolate between these two limits is suggested by Zilitinkevich's (1975) equation (Eqn. 2.2.19). Adopting this form yields the large Péclet number relationship

$$E = \frac{E_{max}}{1 + c_t \, Ri^{3/2}} \qquad (4.3.3)$$

This relationship gives a good fit of Turner's (1968,1973) salinity data (Fig. 4.1).

However , because of the different turbulence scales, the empirical constants E_{max} and c_t from a fit of Turner's data will not conform with the I.C.P.M. Turner's data needs to be transformed according to the length and velocity scales and the ratio ℓ_i/ℓ_s . As the turbulent length scale definition for the I.C.P.M. has the same form as that used by Turner (1973), they will be assumed to be of approximately equal magnitude. The ratio ℓ_i/ℓ_s , following Crapper and Linden (1974), has previously been assumed to be equal to unity. Hence, the only transformation necessary is due to the velocity scale V_s .

As discussed in Chapt. 4.2, the choice of V_s for the I.C.P.M. allows the product E Ri to yield the value of k_e at all points. Turner's data, and hence E_{max} and c_t , require transformation until the range of k_e values matches previously reported experimental values for high Péclet number.

Because of the large turbulent length and velocity scales in the atmosphere, atmospheric data can be considered to have high Pe . The most recent review of k values from atmospheric, oceanographic and laboratory data has been presented by Stull (1976a). The typical range of k is

$$0.1 < k < 0.3$$

although values outside this range have been reported. As will be discussed later in this section, not all the reported k values are reliable.

From Eqns. 4.2.7 and 4.3.3, the range of k_e for the I.C.P.M., at large Pe , is given by

$$k_e = \frac{E_{max} \, Ri}{1 + c_t \, Ri^{3/2}} \qquad (4.3.4)$$

It can easily be shown that k_e has a maximum value, for large Pe , of

$$(k_e)_{max} = \left(\frac{E_{max}}{3} \right) \left(\frac{2}{c_t} \right)^{\frac{2}{3}} \qquad (4.3.5)$$

which occurs when

$$Ri = \left(\frac{2}{c_t}\right)^{\frac{2}{3}} \qquad (4.3.6)$$

As the Richardson number tends to zero or infinity, k_e tends to zero. Hence, for the I.C.P.M. at high Pe

$$0 \leq k_e \leq (k_e)_{max}$$

In comparing atmospheric values of k_e with the I.C.P.M., it is important to allow for the variation of k_e with Richardson number. Stull (1976 b) reanalysed both the O'Neill data (Lettau and Davidson 1957) and Day 33 of the Wangara data (Clarke et al. 1971). He suggested the value of k_e due to buoyancy fluxes alone was 0.1. Typical values from his analyses are: q_p = 200 watts/m^2, d_m = 850 metres, T_m = 305°K, $(\partial T/\partial z)_i$ = 24°K/km . These values yield a gradient Richardson number (in air) of Ri $\approx$ 10 . Transforming Turner's salinity data, by the velocity scale, to fit the point (Ri = 10, k_e = 0.1) yields a value of $(k_e)_{max} \approx 0.2$ (Fig. 4.1).

Because k_e varies with both Richardson and Péclet number and because of a number of other factors (outlined in Chapter 5.6), such as the improper use of Bett's (1973) model equations, many previously published values of k_e are unreliable. However, when these factors are taken into account the atmospheric range of k_e values appear to be consistent with the value of $(k_e)_{max}$ obtained above.

For the I.C.P.M., it will be assumed the maximum value of k_e at high Péclet number is

$$(k_e)_{max} = 0.2$$

Transforming Turner's (1968,1973) salinity data, according to the velocity scale to satisfy this value in Eqn. 4.3.5, yields the I.C.P.M. empirical constants

$$\left.\begin{aligned} E_{max} &= 0.66 \\ c_t &= 2.31 \end{aligned}\right) \qquad (4.3.7)$$

The transformed data and the empirical relationship for E (Eqn. 4.3.3) are shown in Fig. 4.1. As well as Turner's (1968) salinity data, his low Ri temperature stratification data are also plotted. For low Richardson numbers, molecular diffusion becomes negligible, even for the low Péclet number temperature data. These data points have therefore joined the fundamental high Pe curve. The empirical constants (Eqn. 4.3.7) infer the ratio $V_s/\sigma_{uT} = 1.79$.

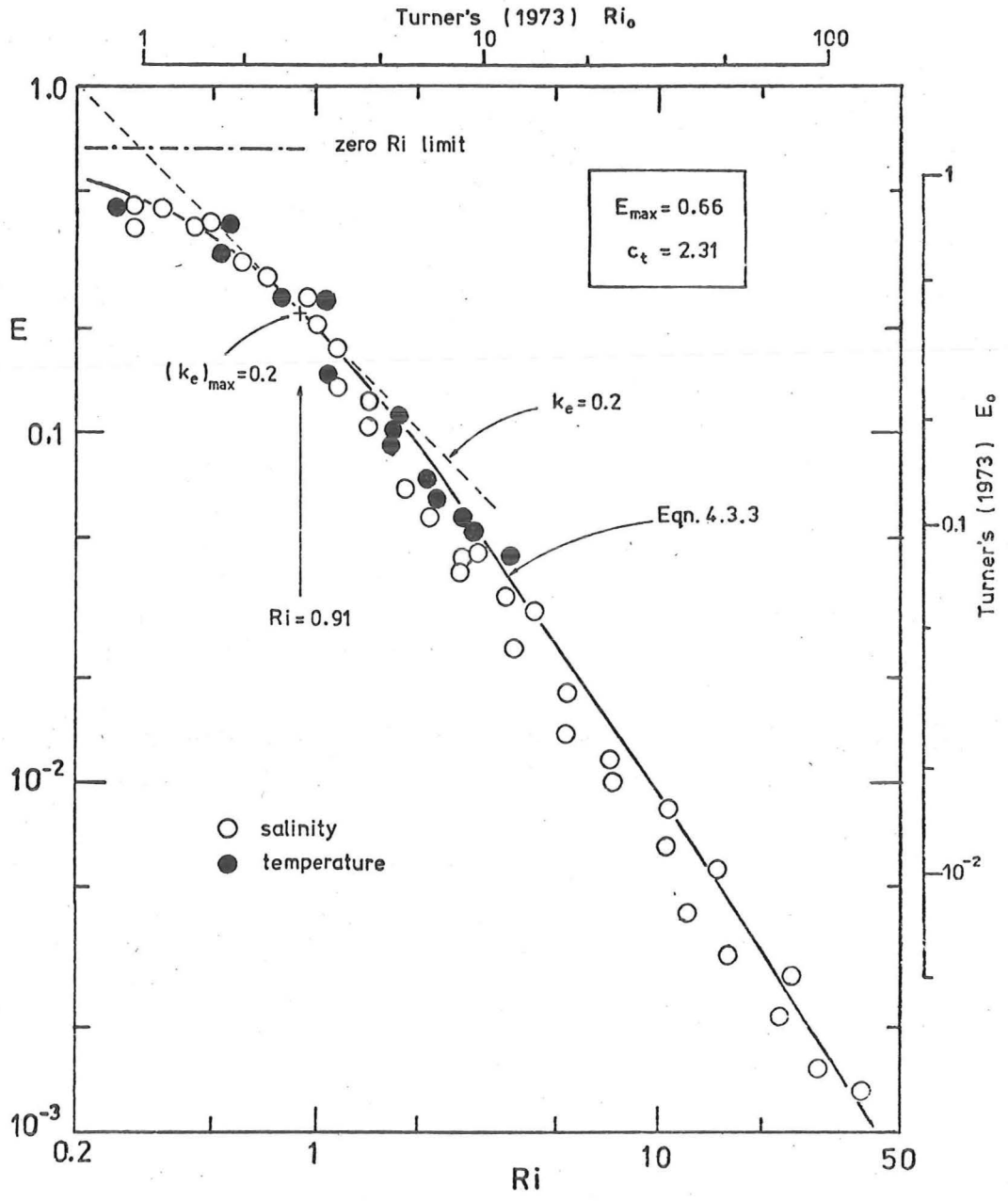

Fig. 4.1. Empirical curve of log E versus log Ri for large Péclet number. Experimental points are transformed data from Turner (1968,1973).

The interfacial turbulent diffusivity γ_i is therefore described by the empirical relationship (from Eqns. 4.1.8 and 4.3.3)

$$\gamma_i = \frac{E_{max}\, \ell_s\, V_s}{1 + c_t\, Ri^{3/2}} \qquad (4.3.8)$$

This relationship will be used to evaluate γ_i in the numerical analysis of the I.C.P.M.

It should be noted that the use of Eqn. 4.3.8 in a low Péclet number penetrative convection model, requires the assumption that γ_i is independent of the other factors influencing the rate of rise of the interface (Chapt. 3.6). However, if the filling velocity term in Eqn. 3.6.6

$$Q_p / \beta\, d_m \left.\frac{\partial T}{\partial z}\right|_i$$

is large, this assumption may not hold. As discussed in Chapter 3.6, large filling velocities occur when the mixed layer fluid is rapidly being made more buoyant than the diffusion region above it. (i.e. dT_m/dt large and $(\partial T/\partial z)_i$ small). The penetrating interfacial domes are quickly overtaken by other penetrating domes from below. As a result they do not penetrate far beyond the rising interface. The turbulent diffusivity term $\gamma(z)$ for $z \geq d_m$ is therefore reduced.

In Turner's (1968) stirring grid experiments there was no external source of buoyancy ($Q_p = 0$). There was only a relatively slow increase in T_m due to the interfacial buoyancy flux so the filling velocity was not significant.

Provided the filling velocity is small, the use of Eqn. 4.3.8 to evaluate γ_i in the I.C.P.M. should be acceptable. The effect of overestimating γ_i, when the filling model term is large, will be discussed in more detail in Chapter 7.

4.3.2 Comparison With Other Empirical Formulae

The empirical formulae for $E = \phi(Ri)$ at high Pe (Eqn. 4.3.3) differs from previous formulae reported by Zilitinkevich (1975), (Eqn. 2.2.19); Deardoff (1974 a), (Eqn. 2.2.25); and Mellor and Durbin (1975), (Eqn. 2.3.5); because it tends to a $-\frac{3}{2}$ power relationship at high Ri rather than a -1 power. Munk and Anderson (1948) suggested an empirical formula which satisfies the same limits as Eqn. 4.3.3.

$$E = \frac{E_{max}}{(1 + 3.33\, Ri)^{3/2}} \qquad (4.3.9)$$

However, the interpolation form, with the whole denominator to the power of $\frac{3}{2}$, appears to have been arbitrarily chosen. The interpolation form for the I.C.P.M. formula was chosen because it is consistent with Zilitinkevich's (1975) analysis of the turbulent kinetic energy equation at the interface. It also provides a significantly better interpolation fit of Turners (1968) salinity data. Schiller and Sayre (1973) suggested a similar formula to Munk and Anderson (1948) except that it was based on a $\frac{5}{4}$ denominator power. Their data did not extend to high enough Richardson numbers to reveal a $-\frac{3}{2}$ slope.

The empirical constant E_{max} may be compared with data from neutral jets and neutral boundary layers ($Ri \to 0$). At very low Richardson numbers, turbulent motions are dominant and Eqn. 2.2.4 can be assumed to hold. Hence, from the definition of E (Eqn. 4.1.5), the limit as $Ri \to 0$ is

$$E = E_{max} = \frac{(V_{em})_{max}}{V_s} \qquad (4.3.10)$$

In his numerical model, Deardoff (1974 a) found that, for low Ri , V_{em} tended to a maximum value (Eqn. 2.2.24) which yields $E_{max} = 0.43$. Mellor and Durbin's (1975) formula infers a value of $E_{max} \approx 0.54$ (Appendix F). From neutral atmospheric boundary layer data, Tennekes (1975) deduced that

$$(V_{em})_{max} = 0.35 \ \bar{\sigma}_w$$

where $\bar{\sigma}_w$ was taken as the mean value of the r.m.s. vertical velocity fluctuations for the mixed layer. If, as Willis and Deardoff (1974) measurements suggest, $\bar{\sigma}_w \approx 0.55 \ w_* = 1.18 \ V_s$ then, this infers $E_{max} \approx 0.41$.

Obviously more detailed measurements are needed before the empirical values of E_{max} and c_t can be evaluated accurately. The empirical value of $E_{max} = 0.66$ for the I.C.P.M. appears to be reasonably consistent with previously reported measurements.

4.3.3 The Variation of the Turbulent Diffusivity $\gamma(z)$ above the Interface.

The decay of $\gamma(z)$ above $z = d_m$ was approximated by

$$\gamma(z) = \gamma_i \ \phi_1(z - d_m)$$

where $\phi_1(z - d_m) = 1$ at $z = d_m$ and tended to zero for $z >> d_m$ (Chapt. 3.3). The form of the decay function $\phi_1(z - d_m)$ is not

available from the literature.

Adrian (1975) has reported measurements of the r.m.s. vertical velocity fluctuation σ_w in the diffusion region, just above the interface, in his ice-water experiments. As shown in Fig. 4.2, σ_w, normalized by Adrian's (1975) turbulent velocity scale (for ice-water convection) V_{Ad}, decayed with increasing height. Adrian fitted two asymptotic decay curves to the data (Fig. 4.2) but a simple exponential curve

$$\frac{\sigma_w}{V_{Ad}} \propto \exp\left(-\frac{z - d_m}{\ell_{Ad}}\right)$$

where ℓ_{Ad} is Adrian's turbulent length scale, can also be used to fit the data.

Measurements of vertical particle displacements above a deepening mixed layer (Linden 1975) also illustrate the decay of turbulence with height. Figure 4.3 shows Linden's (1975) data, his asymptotic power decay curve ($-\frac{5}{6}$ slope), and another fitted exponential decay curve. The vertical particle displacements η are non-dimensionalized by the interfacial value η_i and ℓ_{Li} is Linden's turbulent length scale.

Both sets of data suggest that the function $\phi_1(z - d_m)$ could be approximated to an exponential decay curve. From the discussion in Chapt. 4.1, it also appears that

$$\left.\frac{\partial \gamma}{\partial z}\right|_i \approx -\frac{\gamma_i}{\ell_s}$$

for large Péclet numbers. Any relationship for $\phi_1(z - d_m)$ should also be consistent with this relationship. Hence,

$$\left.\frac{\partial \phi_1}{\partial z}\right|_i \approx -\frac{1}{\ell_s} \qquad (4.3.11)$$

A numerical analysis computer program for the I.C.P.M. is described in Appendix C. The turbulent diffusivity $\gamma(z)$ and $\phi_1(z - d_m)$ were assumed to become equal to zero at a finite distance z_{int} above the interface. This is also the height where the intermittency I becomes zero. The decay function $\phi_1(z - d_m)$ was taken as the power curve

$$\phi_1(z - d_m) = \left[1 - \left(\frac{z - d_m}{z_{int}}\right)\right]^2 \qquad (4.3.12)$$

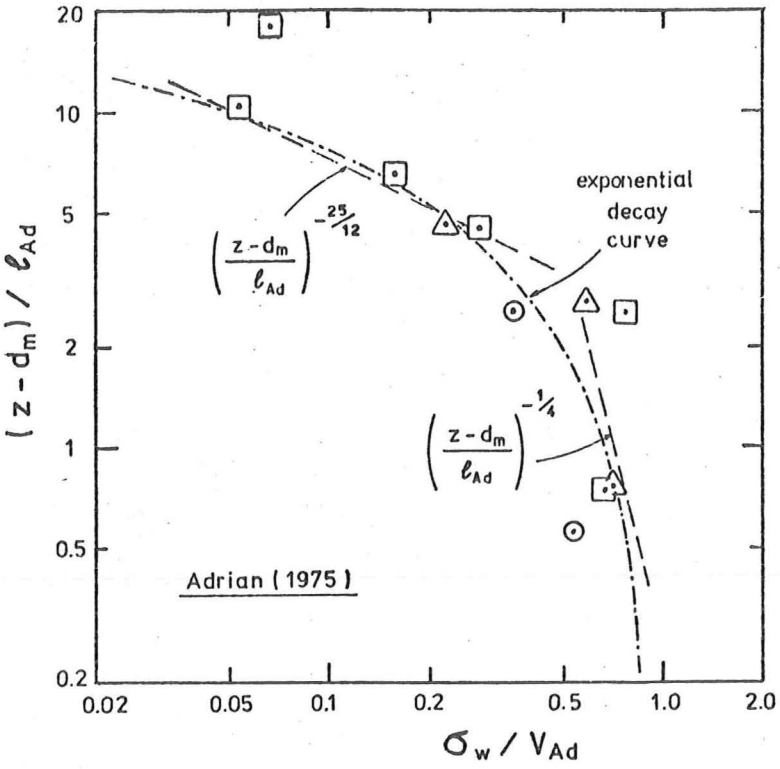

Fig. 4.2. Decay of r.m.s. vertical velocity with height above the interface in ice-water convection experiments. (From Adrian 1975.)

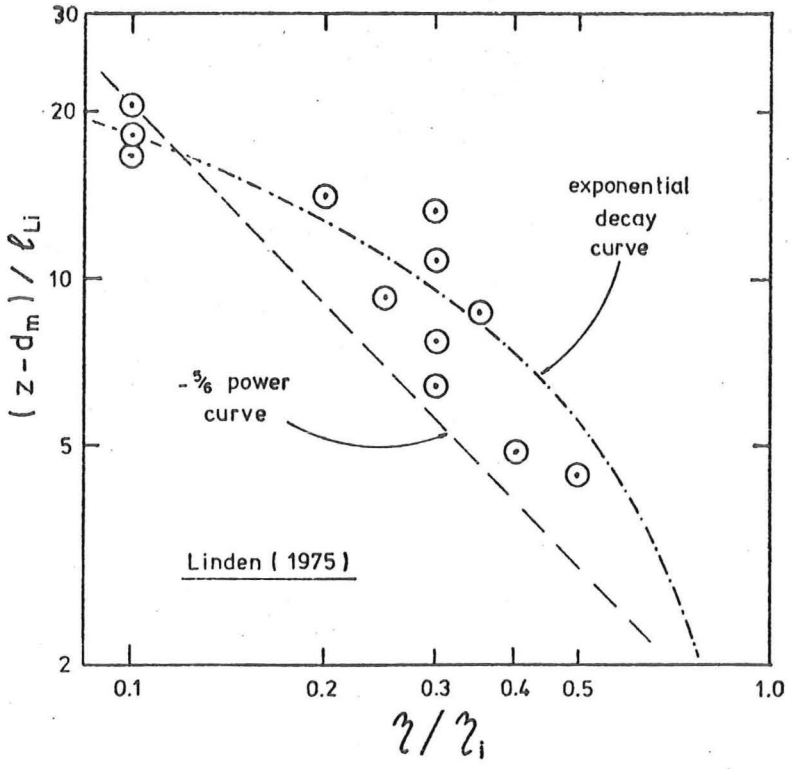

Fig. 4.3. Decay of vertical particle displacements with height above a deepening mixed layer. (From Linden 1975.)

for $0 < z - d_m < z_{int}$. Hence,

$$\left.\frac{\partial \phi_1}{\partial z}\right|_i = - \frac{2}{z_{int}} \qquad (4.3.13)$$

To complete the description of $\gamma(z)$ the intermittency region thickness z_{int} was defined empirically as

$$z_{int} = \frac{2.5\, \ell_s}{1 + 0.01\ Ri} \qquad (4.3.14)$$

The form of the relationship allowed for a finite limit on z_{int} at low Richardson number whilst also allowing for the dependence of the interfacial dome penetration distance on the Richardson number.

The increase in the dome penetration distance with decreasing Richardson number has been previously reported by Hopfinger and Toly (1976) and is included in the models of Linden (1973) and Stull (1973). The empirical constants were chosen from observations of the experimental I.C.P.M. interface when the mixed layer was dyed (Chapt. 6.3.3).

As the range of Richardson numbers for the I.C.P.M. was typically

$$10 < Ri < 30 ,$$

for the majority of the time, the range of z_{int}/ℓ_s was

$$1.9 < z_{int}/\ell_s < 2.3$$

This is consistent with Eqns. 4.3.11 and 4.3.13.

4.4 THE ADDITIONAL MOLECULAR DIFFUSION FACTOR $\lambda(z)$

To account for the extra molecular transfer of heat in the intermittency region, due to the stretching and distortion of the interface, an additional molecular diffusion factor $\lambda(z)$ was defined (Chapt. 3.3). As was assumed for the turbulent diffusivity $\gamma(z)$, the additional molecular diffusion factor $\lambda(z)$ has a maximum value λ_i at the interface and decays to zero with increasing height. It is expected that the value of λ_i will be of order one or less.

Consider Eqn. 4.3.1 for all Péclet numbers

$$E = \frac{\gamma_i}{\ell_s V_s} + (1 + \lambda_i) \frac{\kappa}{\ell_s V_s} \qquad (4.4.1)$$

Substituting for γ_i from Eqn. 4.3.8 yields

$$E = \frac{E_{max}}{1 + c_t \, Ri^{3/2}} + (1 + \lambda_i) \, Pe^{-1} \qquad (4.4.2)$$

A plot of log E versus log Ri for constant values of $Pe/(1 + \lambda_i)$ is shown in Fig. 4.4. The empirical constants given by Eqn. 4.3.7 have been assumed. The variation of E with Richardson number, for a constant low Péclet number, will depend on the value of λ_i. If λ_i were zero, the curves in Fig. 4.4 would be curves of constant Pe.

The probable variation of constant Pe data if λ_i is greater than zero, is shown schematically in Fig. 4.5. The contributions of the terms of Eqn. 4.4.1 to the value of E, at a given Ri and low Pe, are also shown (point A). At very high Richardson number, the turbulent diffusivity γ_i (Eqn. 4.3.8) is negligible. It is logical to assume that as γ_i becomes negligible, λ_i will also tend to zero. The interfacial heat flux will only be due to molecular diffusion. From Eqn. 4.4.2, the data at large Richardson number will tend to

$$E = Pe^{-1} \qquad (4.4.3)$$

as shown in Fig. 4.5.

As the Richardson number decreases, interfacial turbulence will become more important and λ_i will increase. In the case sketched in Fig. 4.5, the value of λ_i is assumed to increase to unity as Ri decreases. At very low Richardson numbers, γ_i becomes very large and the total contribution of molecular diffusion (whatever the value of λ_i) is negligible.

It should be noted that specifying either the Richardson number or Péclet number alone, will not describe the relative effects of interfacial turbulence and molecular diffusion. For instance, at low Péclet number but also low Richardson number, the contribution of γ_i is much greater than κ. The relative importance of the turbulent and molecular processes is best described by the ratio γ_i / κ. Although λ_i and γ_i vary differently, λ_i increases as γ_i increases. Hence, the ratio γ_i / κ does not need to include the effect of λ_i.

When the contribution of λ_i is taken into account (as illustrated in Fig. 4.5), Figure 4.4 shows that for decreasing Péclet numbers, the entrainment data will deviate from the fundamental ($Pe = \infty$) curve at decreasing values of Ri. This phenomenon was observed by G.G.H. Rooth in a series of grid-stirring experiments (reported by

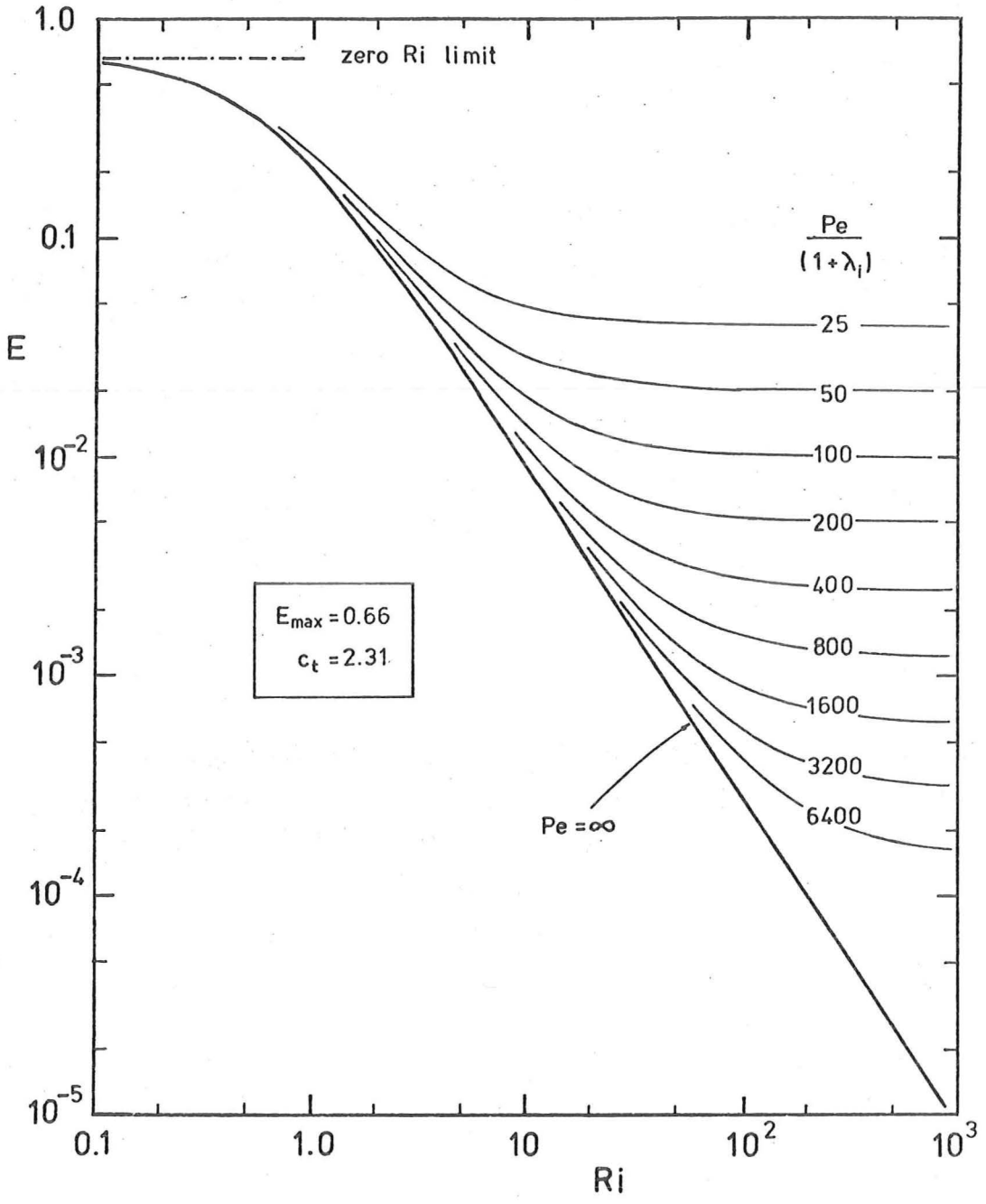

Fig. 4.4. Non-dimensional interfacial heat flux E as a function of Richardson number with contours of constant $Pe/(1 + \lambda_i)$. From the empirical I.C.P.M. relationships (Eqns. 4.3.8 and 4.4.1).

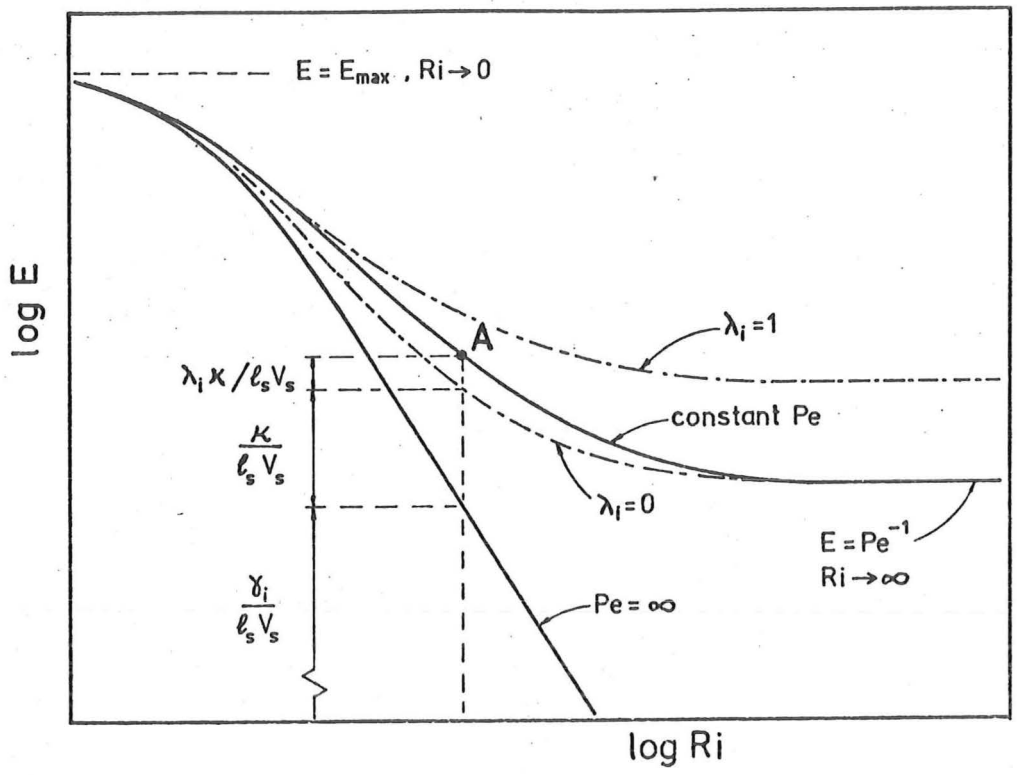

Fig. 4.5. Sketch of log E versus log Ri for a constant low Péclet number showing the variation of λ_i as the ratio γ_i/κ varies.

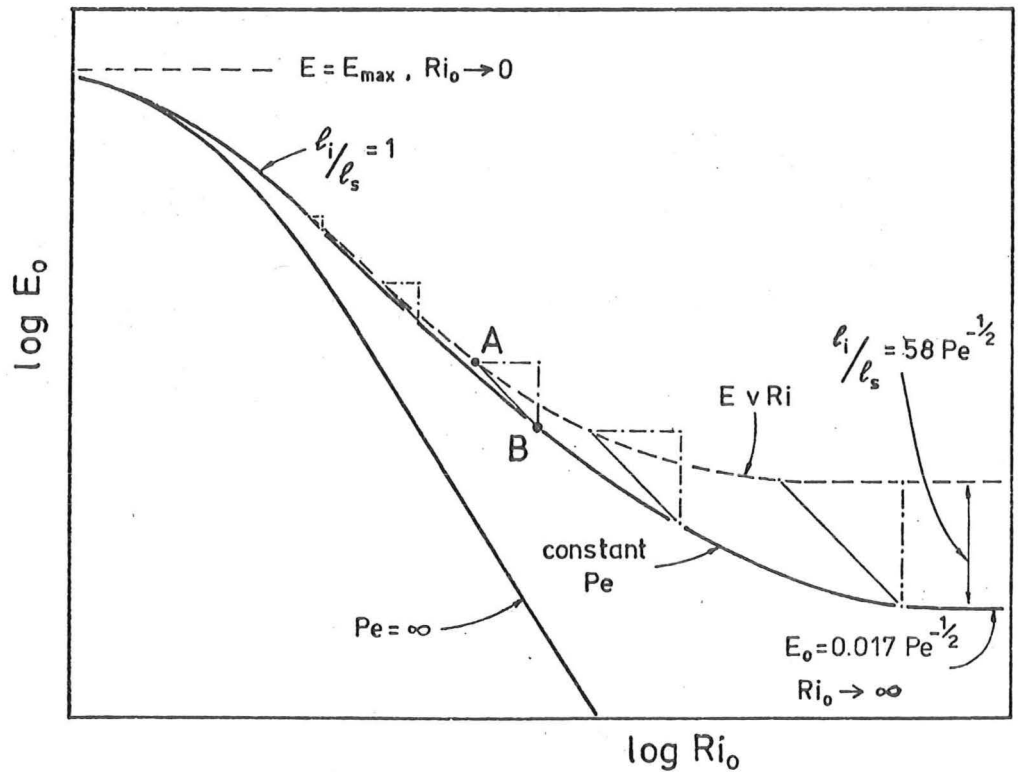

Fig. 4.6. Sketch showing the transformation of low Péclet number data from the (E, Ri) form to the (E_o, Ri_o) form.

Turner 1973). For large Richardson number, the low Péclet number data will tend to a constant value given by Eqn. 4.4.3.

The approximate magnitude of λ_i may be determined by comparing the empirical I.C.P.M. curves (Fig. 4.4) with Turner's (1968,1973) low Péclet number data (Fig. 2.2). The method used will be the same as that used to evaluate γ_i (Chapt. 4.3.1).

In the high Péclet number evaluation of γ_i, the interfacial thickness of ℓ_i in Turner's salinity experiments was assumed to be approximately equal to the turbulent length scale ℓ_s. Hence, from Eqn. 4.1.6, Turner's (1968,1973) scales E_o and Ri_o were equivalent to the interfacial gradient scales of the I.C.P.M., E and Ri. However, Crapper and Linden (1974), using Turner's (1968) apparatus, showed that at low Péclet number, ℓ_i was greater than ℓ_s. As Pe decreased, the ratio ℓ_i/ℓ_s increased. It should be noted that Crapper and Linden (1974) varied only V_s and ΔT_i during their temperature experiments. By decreasing V_s to lower the Péclet number, they increased the Richardson number, for a given range of ΔT_i.

To relate Turner's low Péclet number data to the I.C.P.M. empirical equations, the variation of ℓ_i/ℓ_s with Péclet number (and Richardson number) will have to be discussed.

The transformation of log E versus log Ri data into the form log E_o versus log Ri_o, according to ℓ_i/ℓ_s, is shown schematically in Fig. 4.6. Consider the same low Péclet number data curve that was sketched in Fig. 4.5. It follows from Eqn. 4.1.7, that for ℓ_i/ℓ_s greater than zero, log E versus log Ri data are transformed into log E_o versus log Ri_o data by a shift along a line of slope -1 in the increasing Ri direction. For example, in Fig. 4.6, point A shifts to point B. When γ_i/κ is very high (i.e. whenever the data are close to the fundamental Pe = ∞ curve), the ratio ℓ_i/ℓ_s is approximately unity. Hence, no shift is required. As γ_i/κ decreases, ℓ_i/ℓ_s increases and the data is shifted by increasing amounts. As a result of the transformation, low Péclet number log E_o versus log Ri_o data lies below the empirical I.C.P.M. curve for log E versus log Ri.

An approximate evaluation of the range of ℓ_i/ℓ_s for Turner's low Péclet number experiments can be obtained from the results of Crapper and Linden (1974). This is discussed in more detail in Appendix G. Crapper and Linden's (1974) data infers that the limit

at low γ_i/κ , in terms of the I.C.P.M. turbulence scales is

$$E_o \approx 0.0172\ Pe^{-\frac{1}{2}} \qquad (4.4.4)$$

This is consistent with the results of Fortescue and Pearson (1967) who studied the high Ri case of the entrainment of carbon dioxide gas into a turbulent layer of water.

From Eqns. 4.4.3 and 4.4.4, it follows that, at low Pe and high Ri , ℓ_i/ℓ_s tends to

$$\ell_i/\ell_s \approx 58.1\ Pe^{-\frac{1}{2}} \qquad (4.4.5)$$

The low Péclet number curve shown schematically in Fig. 4.6 will therefore tend toward the high Richardson number limit value of E_o given by Eqn. 4.4.4. The maximum value of ℓ_i/ℓ_s which will occur for large Ri_o , is given by Eqn. 4.4.5.

This relationship will only apply to the range of low Péclet numbers studied by Crapper and Linden (1974) and to their type of double-layer grid-stirring experiment. Because of the similarities between the experimental conditions of Turner (1968) and Crapper and Linden (1974), it will be assumed to be valid to apply Eqn. 4.4.4 to Turner's low Pe data. Note that Eqns. 4.4.3 and 4.4.4 cannot hold for $Pe > 3300$ as ℓ_i/ℓ_s is less than unity. No intermediate relationship for the variation of ℓ_i/ℓ_s is available.

It is apparent from Figs. 4.4, 4.5 and 4.6 that the slope of -1 for Turner's (1968,1973) low Péclet number data (Fig. 2.2) is the result of a number of factors. These are the variation of ℓ_i/ℓ_s and λ_i and the range of Ri_o and Pe . Had Turner's temperature data extended to much higher Richardson numbers, the data would probably have tended toward a constant value of E_o (i.e. a slope of zero), as shown in Fig. 4.6. As discussed earlier (Chapt. 4.3), the low Péclet number data also tends to a constant E_o value at low Ri_o (viz. E_{max}).

Hopfinger and Toly (1975) proposed the empirical formula

$$E_o = Ri_o^{-\frac{3}{2}} \left(c_1 + c_2\ (Ri_o/Pe)^{\frac{1}{2}}\right) \qquad (4.4.6)$$

where c_1 and c_2 are constants, to fit Turner's (1968) stirring-grid data and their own data for medium and larger Ri_o . This is an improvement on an earlier empirical formula suggested by Turner (1968) which tended to

$$E_o \propto Ri_o^{-3/2} Pe^{-1/2}$$

as the Péclet number increased. However, many possible slopes of $\log E_o$ versus $\log Ri_o$ data, due to variations in Richardson and Péclet number , are inferred by Fig. 4.4. Empirical formulae such as Eqn. 4.4.6 are not sufficiently general to cover these possibilities.

A quantitative comparison between Turner's (1968,1973) data in the $\log E_o$ versus $\log Ri_o$ form and a plot of $\log E$ versus $\log Ri$ from Eqn. 4.4.2 will be made by plotting both sets of data on the same graph (Fig. 4.7). The maximum value of ℓ_i/ℓ_s may be inferred from the high Richardson number limits of E and E_o . The minimum value of ℓ_i/ℓ_s at low Richardson number is unity (i.e. $E = E_o$, $Ri = Ri_o$).

Turner (1968) used a range of grid stirring frequencies from 166-333 rpm and kept $z_{grid} = 9$ cm . The transformed range of Péclet numbers for the temperature data ($\kappa = 1.43 \times 10^{-3}$ cm^2/sec) is therefore

$$161 < Pe < 323$$

Curves of E for the limits of this range of Pe and for $\lambda_i = 0$ are shown in Fig. 4.7. As the range of Pe is approximately a factor of two, the corresponding curves of E for $\lambda_i = 1$ are approximately given by the curves for $Pe/(1 + \lambda_i) = 81$ and 161. The large Ri_o limits of E_o for this Péclet number range (from Eqn. 4.4.4) are also shown in Fig. 4.7. Because only the range of ℓ_i/ℓ_s is known an accurate evaluation of λ_i from Fig. 4.7 is not possible. However, when all the factors illustrated schematically in Figs. 4.5 and 4.6 are taken into account, the maximum value of λ_i appears to be of order unity or less.

As the experimental I.C.P.M. range of γ_i/κ was, for the majority of the time, less than unity (Chapter 6), the value of λ_i is expected to be much less than unity. Because an accurate value of λ_i is difficult to obtain empirically the numerical analysis of the fully turbulent I.C.P.M. will be simplified by setting λ_i , and hence $\lambda(z)$, equal to zero.

4.5 NUMERICAL ANALYSIS OF THE THEORETICAL I.C.P.M.

It is now possible to proceed with a numerical analysis of the theoretical I.C.P.M. using the model equations developed in Chapter 3 and the turbulent entrainment parameters, evaluated empirically in this chapter. The turbulent diffusivity $\gamma(z)$ is described by Eqns. 4.3.8,

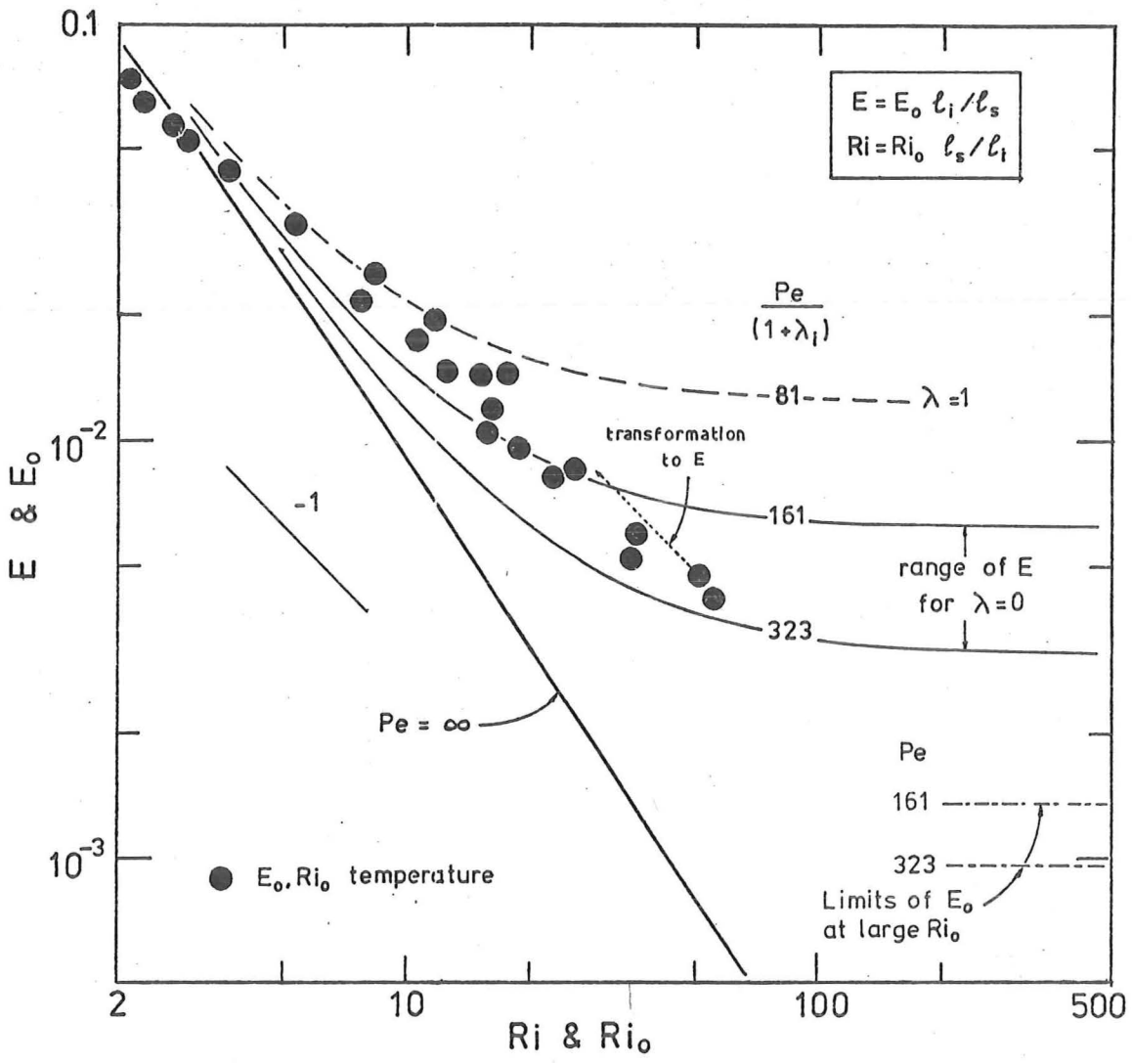

Fig. 4.7. Comparison between the empirical I.C.P.M. curves for log E versus log Ri and Turner's (1968) transformed low Péclet number data in the form log E_o versus log Ri_o .

4.3.12 and 4.3.14 and the additional molecular diffusivity factor $\lambda(z)$ is assumed to be zero. A description of the computer program used for the numerical analysis is given in Appendix C. The values of the constant parameters used in the computer program are listed in Table 4.1.

TABLE 4.1 - CONSTANT PARAMETERS USED IN THE I.C.P.M. NUMERICAL ANALYSIS PROGRAM

Fluid properties (water)

$\rho c_p = 1.0 \text{ cal/cm}^3\text{°C}$

$\alpha = 2.5 \times 10^{-4} (\text{°C})^{-1}$

$\kappa = 1.43 \times 10^{-3} \text{ cm}^2/\text{sec}$

Heat loss factors

$W = 7.44 \times 10^{-7} (\text{sec})^{-1}$

$W_T = 6.77 \times 10^{-6} \text{ cm/sec}$

$\beta = 1.08$

$\beta_T = 0.053 \text{ (cm)}^{-1}$

$T_{air} = 21 \text{ °C}$

Steady heat flux heating equation (Eqn. 6.5.8)

$$q_p = q_G - S_p \frac{dT_m}{dt} - (W_p + W_{ex})(T_p - T_{air})$$

$q_G = 0.0268 \text{ cal/sec. cm}^2$

$S_p = 1.89 \text{ cal/cm}^2\text{°C}$

$W_p = 3.8 \times 10^{-6} \text{ cal/sec. cm}^2 \text{ °C}$

$W_{ex} = 2.6 \times 10^{-5} \text{ cal/sec. cm}^2 \text{ °C}$

Unsteady heat flux heating equation (Eqn. 6.4.2)

$Q_p = (7.98 \Delta T_H - 8.30) \times 10^{-3} \text{ cm °C/sec}$

The results of a numerical analysis of a steady heat flux experiment are shown in Figs. 4.8 and 4.9. In Fig. 4.8, the temperature versus time data are presented for the mixed layer and for constant

integer (centimetre) heights in the diffusion region. Also plotted in Fig. 4.8 is the corresponding variation of the mixed layer height d_m with time. For comparison, the d_m versus t curve for a molecular entrainment analysis, using the same initial and boundary conditions, is also shown. This numerical analysis was based on an actual experimental run ES2 (Chapter 6). The initial conditions and boundary conditions used were slightly different than those used in Chapt. 3.9 (Table 3.1).

As the temperature distribution in the diffusion region was obtained by finite difference methods (c.f. the use of Eqn. 3.4.7 in the molecular entrainment analysis, Chapt. 3.9), upper boundary heat losses could be included. To simulate the actual experimental conditions for ES2, a slight increase in Q_p with time, due to the lower aluminium plate heat storage capacity, was allowed for (see Chapter 6 for a discussion of the experimental heating apparatus). Over the time period $80 < t < 274$ mins., the lower boundary heat flux increased from 0.022 to 0.025 cm°C/sec. However, the mean value of Q_p was approximately equal to the constant value of 0.023 cm°C/sec used in the molecular entrainment analysis of Chapt. 3.9 (Table 3.1).

The numerical analysis of ES2 (Fig. 4.8) commenced at $t = 80$ mins. with non-zero mixed layer values ($d_m = 8.70$ cm , $T_m = 21.5$ °C) . Because of thermal lag in the experimental heating apparatus, the initial lower boundary heat fluxes were not able to be controlled. Hence, the numerical analyses of the experiments were started shortly after the actual time heating commenced $t = t_s$. For this particular numerical analysis (ES2), the temperature distribution at $t = 80$ mins. was taken as the best fit of a molecular diffusion profile (Eqn. 3.4.7) to the experimental data. In later numerical analyses, the actual experimental temperature distribution was used (Chapter 7).

As discussed above, there are a number of small quantitative differences between the initial and boundary conditions for the earlier molecular entrainment analysis (Chapt. 3.9, Table 3.1) and this numerical analysis of ES2. However, a comparison of the two temperature-time graphs (Figs. 3.10 and 4.8) shows, qualitatively, the effect of the turbulent diffusivity term $\gamma(z)$.

Consider the temperature in the diffusion region at height $z = 14$ cm. In the molecular entrainment model (Fig. 3.10), this is approximately the height d_{g0} of the initial two-layer boundary. For molecular diffusion only, the temperature at height $z = 14$ cm remains almost

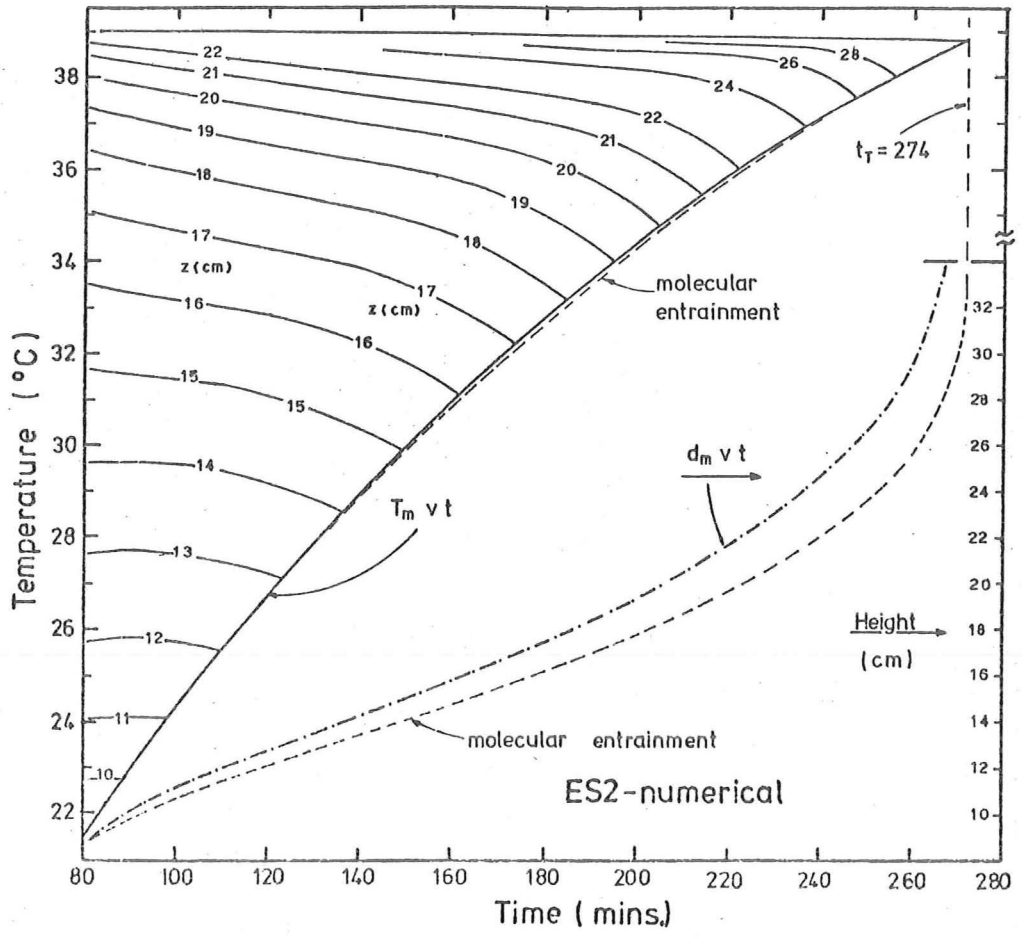

Fig. 4.8. Temperature versus time and interface height versus time graphs from a turbulent entrainment analysis ($\lambda = 0$) of steady heat flux experiment ES2. Curves of mixed layer thickness and temperature from the corresponding molecular entrainment analysis ($\gamma = \lambda = 0$) are also shown.

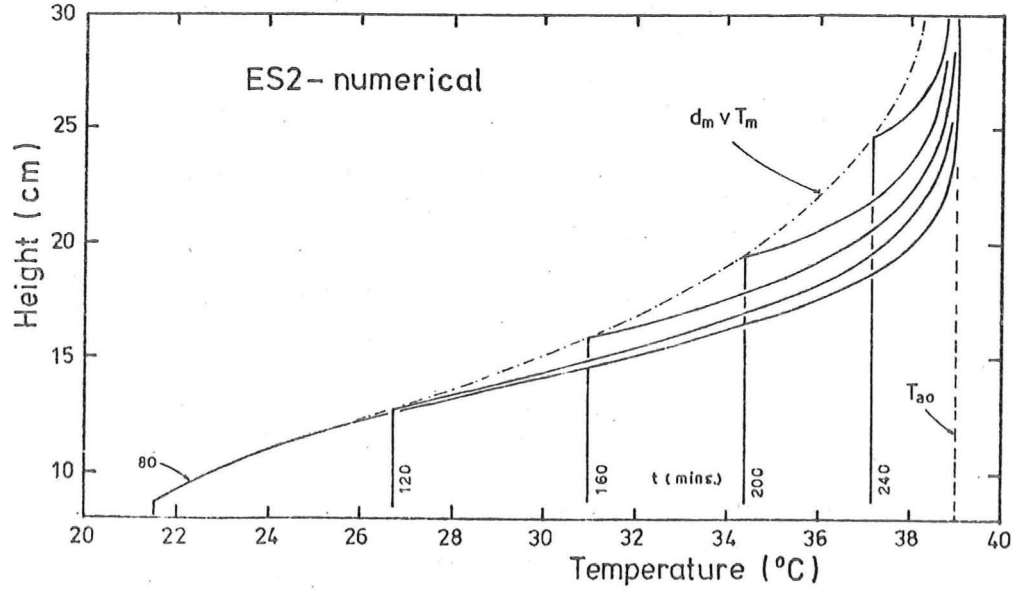

Fig. 4.9. Temperature profiles from a turbulent entrainment analysis ($\lambda = 0$) of steady heat flux experiment ES2. Locus of the mixed layer thickness and temperature is also shown.

constant until the arrival of the mixed layer at $t \approx 160$ mins. In the fully turbulent I.C.P.M. analysis (Fig. 4.8), the temperature at $z = 14$ cm decreases more and more rapidly as the interface approaches. The additional turbulent diffusion $\gamma(z)$ has a net cooling effect on the diffusion region fluid.

Fig. 4.8 shows a comparison of the rates of rise of the interface for the fully turbulent analysis and another molecular entrainment analysis ($\gamma = \lambda = 0$). Both analyses had the same initial and boundary conditions (Table 4.1). As a result of the increased cooling above the interface, the interface rises more rapidly.

Despite the increased diffusion region cooling, the mixed layer temperature T_m for this numerical analysis of ES2 is never more than 0.2°C higher than the corresponding molecular entrainment value (Fig. 4.8). The extra interfacial heat flux for the fully turbulent analysis (due to $\gamma(z)$) is spread over a deeper mixed layer so the temperature is only slightly increased. As discussed earlier (Chapt. 3.8), the final interfacial entrainment time t_T is the same for both analyses. Note that because of the different initial and boundary conditions, the value of t_T for Fig. 3.10 is not the same as for Fig. 4.8.

Vertical temperature profiles (Fig. 4.9) further illustrate the role played by turbulent diffusion in altering the diffusion region temperature profile and raising the interface. The locus of the mixed layer values d_m and T_m, shown in Fig. 4.9, is in effect a minimum temperature envelope. For a filling model entrainment analysis, the diffusion region temperatures only slightly decrease due to minor heat losses. Hence, the minimum temperature envelope (d_m versus T_m) is approximately the same as the molecular diffusion temperature profile at $t = t_s$ (Chapt. 3.9). In a molecular entrainment analysis, the minimum temperature envelope deviates from the $t = t_s$ profile because of molecular diffusion (Fig. 3.9). In a fully turbulent I.C.P.M. analysis, the deviation is even greater (Fig. 4.9).

Until the results of the experimental investigation are presented (Chapter 6), the numerical analysis of the steady heat flux experiment ES2 will not be discussed any further. This will enable the numerical model to be evaluated against the actual experimental data.

However, it is interesting at this point to use the numerical model to illustrate the temporal behaviour of an unsteady heat flux entrainment experiment. Experiments of this type have previously

been reported by Denton and Wood (1974) and Jenkins (1974). For the numerical analysis, the same initial conditions and heat loss factors used in the numerical analysis of the steady heat flux experiment ES2, will be applied (Table 4.1). In unsteady heat flux experiments, the lower boundary heat flux is controlled by maintaining a constant temperature T_H beneath the lower boundary (Chapter 6).

In this representative example of an unsteady heat flux experiment, T_H is initially set at 36°C. The heat flux Q_p is then evaluated by a linear empirical calibration equation (Eqn. 6.4.2).

$$Q_p = (7.98\ \Delta T_H - 8.30) \times 10^{-3}$$

where $\Delta T_H = T_H - T_m$.

This equation was obtained from a best fit of the writer's experimental convection data (Chapt. 6.4, Fig. 6.13). Later, when Q_p decreases to an arbitrary minimum value ($\simeq 0.011$ cm °C/sec) , T_H is increased to 41°C.

Graphs of temperature versus time and interface height versus time for this unsteady heat flux example are shown in Fig. 4.10a. The resulting lower boundary heat flux $Q_p(t)$ is also shown (Fig. 4.10b). Because the mixed layer temperature is continually increasing, Q_p decreases with time for a constant value of T_H .

Immediately after $t = 80$ mins., the heat flux Q_p is large and the mixed layer values d_m and T_m increase rapidly. However, as the lower boundary heat flux decreases, the rates of change of d_m and T_m both decrease. The rate of change of diffusion region temperature also decreases because γ_i is decreasing. At $t = 146$ mins., when T_H increases from 36°C to 41°C, the lower boundary heat flux undergoes an instantaneous increase. This increase in Q_p causes a simultaneous increase in V_{em} and dT_m/dt .

It should be noted that in an experiment it is not possible to change T_H instantaneously and the changes in Q_p , V_{em} and dT_m/dt will be more continuous. However, it is obvious from Fig. 4.10, that the additional unsteadiness caused by the decreasing heat flux Q_p, and the changes in T_H , make the temporal behaviour of this type of penetrative convection experiment quite confusing. The much smoother variations in the diffusion region temperatures and in T_m and d_m for steady heat flux experiments (e.g. ES2, Fig. 4.8), show more clearly the process of penetrative convection at low Péclet number.

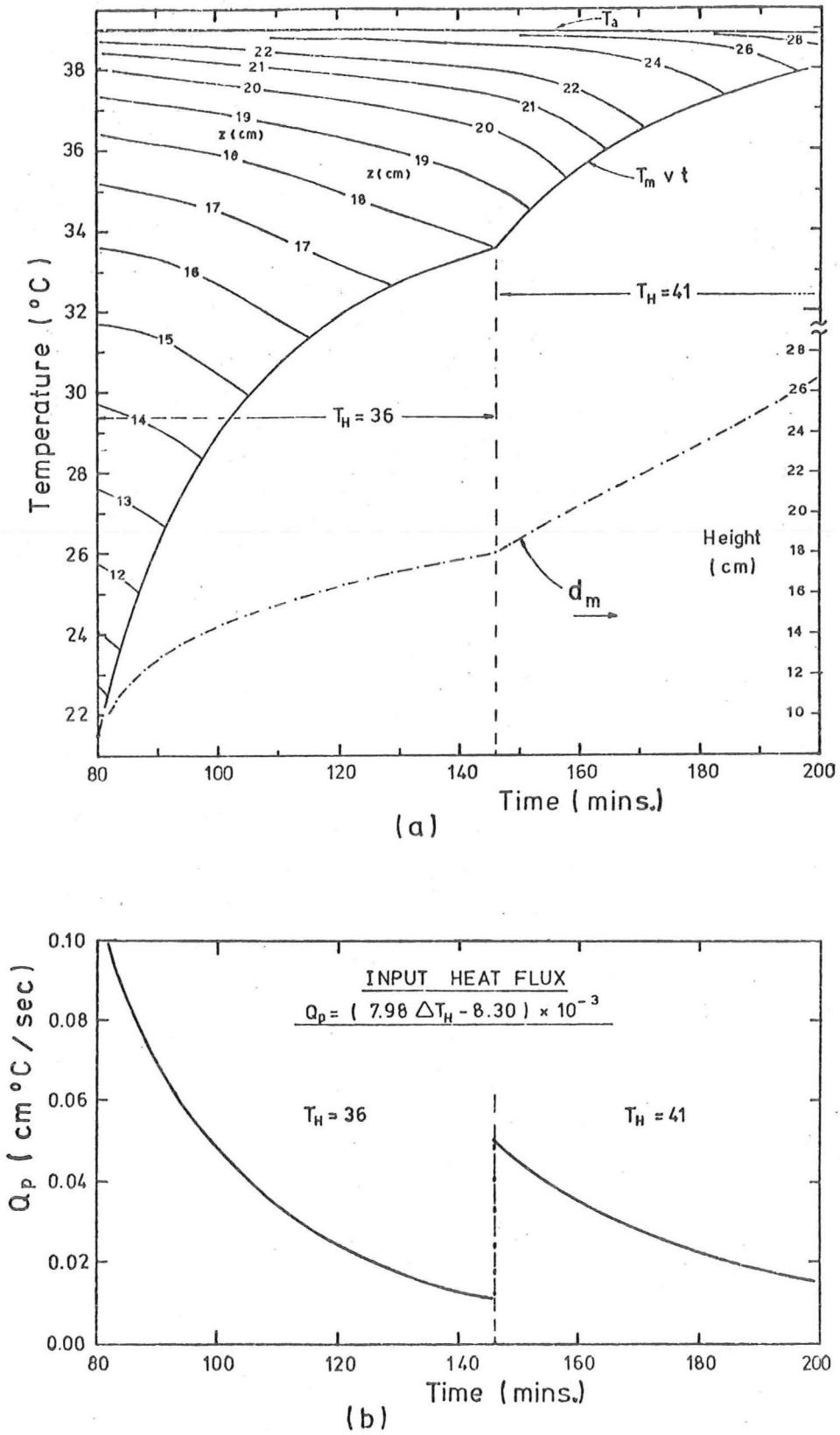

Fig. 4.10. (a) Temperature versus time and interface height versus time graphs, and (b) lower boundary buoyancy heat flux versus time graph from a turbulent entrainment analysis ($\lambda = 0$) of an unsteady heat flux example.

Before discussing the experimental investigations, it is important to consider some of the consequences of the theoretical model. In the next chapter, the entrainment ratio k, introduced by Betts (1973), and now widely used in atmospheric modelling, will be discussed.

CHAPTER 5

THE ENTRAINMENT RATIOS k_e, k_m AND k_h.

5.1 INTRODUCTION

In Chapter 2.2, the atmospheric entrainment models of Betts (1973), Tennekes (1973) and Carson (1973) were discussed. It was shown that if the interfacial density gradient region is assumed to have negligible thickness, and if the interfacial buoyancy heat flux Q_e is parameterized as being a constant proportion of the lower boundary flux Q_p, then

$$k = -Q_e/Q_p = V_{em}\,\Delta T_i/Q_p \qquad (5.1.1)$$

The entrainment ratio k could then be used to simplify the heat budget equation and yield a solution for the temporal variations of d_m and ΔT_i. However, in the development of the theoretical I.C.P.M. (Chapters 3 and 4), it has been shown that the thickness of the interfacial density gradient region is not negligible. This is especially so at low Péclet number (e.g. Fig. 4.9). Generally, Ball's (1960) equation (Eqn. 2.2.4) does not hold and Eqn. 5.1.1 is invalid.

It has also been shown that two heat budget equations are relevant to the analysis. One for the mixed layer and one for the full fluid column. In Betts' (1973) model, these reduce to a single equation. If a similar method of simplifying and solving the two heat budget equations is to be used, three entrainment ratios or k values must be defined.

The first, defined in Chapt. 4.2 (Eqn. 4.2.6), is the ratio of the interfacial and lower boundary buoyancy heat fluxes

$$k_e = -Q_e/Q_p$$

The second is the ratio of the hypothetical heat flux represented by the product of V_{em} and ΔT_i, to the lower boundary flux Q_p,

$$k_m = \frac{\beta\, V_{em}\, \Delta T_i}{Q_p} \qquad (5.1.2)$$

where β is included to account for heat storage in the fluid column walls and insulation. The third ratio is required to analyse the

full fluid column heat budget equation (Eqn. 3.7.7). It has a similar form to k_m but is based on the mean temperature profile height d_h.

i.e. $$k_h = \frac{\beta V_{eh} \Delta T_i}{Q_p} \qquad (5.1.3)$$

where $$V_{eh} = d(d_h)/dt$$

In Betts' (1973) model, the two heights d_m and d_h are equal, so that

$$k_e = k_m = k_h$$

In this chapter, the relationship between $k_e = E\,Ri$ and the two interfacial entrainment terms Ri and Pe will be discussed. A simple relationship between k_h and k_m will then be derived. To illustrate that none of the k values are generally constant, the temporal variations of k_e, k_m and k_h obtained from numerical analyses of the I.C.P.M. will be presented.

If k is a variable with time, Betts' (1973) solution of the heat budget equation for his simple model is invalid. His analysis included two integrations with respect to time for which it was assumed that k did not vary with time. However, by following Betts' (1973) analysis up to the first integration, a method of evaluating the I.C.P.M. k values from experimental measurements of d_m, d_h and ΔT_i will be derived.

It should be noted that Betts' (1973) atmospheric model was applied to the linearly stratified case ($\Gamma > 0$). As the I.C.P.M. deals with $\Gamma = 0$, only this case will be discussed here. A similar analysis of the heat budget equations for linear stratifications is given in Appendix B.

5.2 THE VARIATION OF k_e WITH RICHARDSON AND PÉCLET NUMBER

From the definition of V_s and ℓ_s in the I.C.P.M. it followed that (Eqn. 4.2.7)

$$k_e = E\,Ri$$

Hence, from the empirical equation for E at all Péclet number (Eqn. 4.4.2)

$$k_e = \frac{E_{max}\,Ri}{1 + c_t\,Ri^{3/2}} + (1 + \lambda_i)\frac{Ri}{Pe} \qquad (5.2.1)$$

The variation of k_e with Richardson number for the empirical constants,

$E_{max} = 0.66$ and $c_t = 2.31$, is shown in Fig. 5.1. Contours of constant $Pe/(1 + \lambda_i)$ are plotted. It should be noted that Fig. 5.1 is just a transformed version of Fig. 4.4. In both cases, the abscissa is log Ri and the ordinates are E Ri and log E respectively.

The value of k_e for $Pe = \infty$ is seen to increase with increasing Richardson number to a maximum value of $k_e = 0.2$. This was the maximum value of k_e used in the evaluation of E_{max} and c_t . From Eqn. 4.3.6, the maximum k_e occurs at $Ri = (2/c_t)^{\frac{2}{3}} = 0.91$. Thereafter, for increasing Ri , k_e decreases to a zero asymptote at large Ri . The decrease of k_e to zero as the Richardson number tends to zero has been reported by Zilitinkevich (1975). Tennekes (1975) suggested intuitively that k_e should also decrease to zero at large Ri_o in atmospheric models. However, to the writer's knowledge, no relationship which describes the decrease of k_e for high Ri and large Péclet number, has previously been reported.

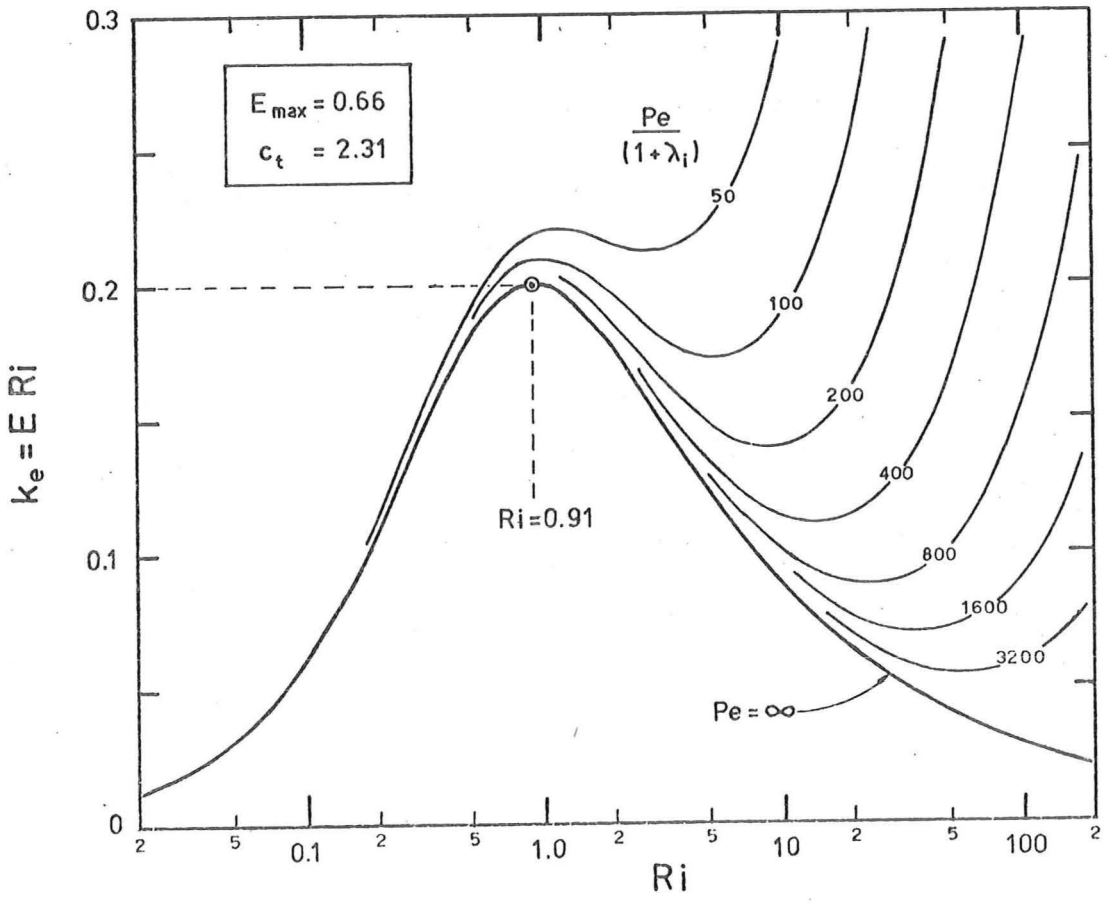

Fig. 5.1. Variation of the heat flux ratio k_e as a function of Richardson number showing contours of constant $Pe/(1 + \lambda_i)$. (From Eqn. 5.2.1.)

At low Péclet number, additional heat transfer by molecular diffusion increases the value of k_e. This contribution by molecular diffusion becomes increasingly more important at high Ri. For low Péclet number and increasing Richardson number, k_e becomes greater than 0.2, eventually tending to infinity (Fig. 5.1).

5.3 THE RELATIONSHIP BETWEEN k_h AND k_e

From the two heat budget equations, a simple relationship between k_h and k_e can be obtained. Expanding the right hand side of the full fluid column heat budget equation (Eqn. 3.7.7) and rearranging, yields

$$Q_p + \beta V_{eh} \Delta T_i = -\beta d_h \frac{d(\Delta T_i)}{dt} - W d_h \Delta T_i \qquad (5.3.1)$$

where $V_{eh} = d(d_h)/dt$

From the definition of ΔT_i

$$\frac{d(\Delta T_i)}{dt} = \frac{d T_a}{dt} - \frac{d T_m}{dt} \qquad (5.3.2)$$

If the diffusion region is assumed to be deep and upper boundary heat losses can be ignored, then Eqn. 3.7.6 applies. Both these equations, substituted in Eqn. 5.3.1, yield

$$Q_p + \beta V_{eh} \Delta T_i = d_h \left(\beta \frac{dT_m}{dt} + W(T_m - T_{air})\right) \qquad (5.3.3)$$

From the definition of k_h, it follows that

$$(1 + k_h) Q_p = d_h \left(\beta \frac{dT_m}{dt} + W(T_m - T_{air})\right) \qquad (5.3.4)$$

Similarly, the mixed layer heat budget (Eqn. 3.5.2) can be expressed in terms of k_e, so that

$$(1 + k_e) Q_p = d_m \left(\beta \frac{dT_m}{dt} + W(T_m - T_{air})\right) \qquad (5.3.5)$$

Eliminating Q_p from Eqns. 5.3.4 and 5.3.5 yields a relationship between k_h and k_e.

$$k_h = \frac{d_h}{d_m} (1 + k_e) - 1 \qquad (5.3.6)$$

Because the mean profile height d_h is always greater or equal to the interface height d_m, it follows that $k_h \geq k_e$. There does not appear

to be a similar relationship for k_m .

A plot of the vertical buoyancy heat flux profile also illustrates the relationship between k_h and k_e . Figure 5.2 shows the heat flux profile from the numerical analysis of ES2 at t = 140 minutes. The heat flux and height axes have been non-dimensionalized by Q_p and d_m respectively.

As the temperature throughout the mixed layer is assumed to be uniform (T_m) , it follows from Eqn. 3.4.1 that the mixed layer heat flux profile is linear.

$$\left.\frac{\partial Q}{\partial z}\right|_m = \frac{Q_e - Q_p}{d_m} = -\beta \frac{dT_m}{dt} - W(T_m - T_{air}) \qquad (5.3.6)$$

At the interface, the buoyancy heat flux is Q_e . In the non-dimensional form of Fig. 5.2, the value at the interface height is $-k_e$. From Eqns. 5.3.3 and 5.3.6, it follows that extrapolating the linear mixed layer profile to the mean temperature profile height d_h , allows k_h to be evaluated. The value of V_{eh} need not be known.

For this example (Fig. 5.2), the two k values are $k_e = 0.18$ and $k_h = 0.47$. The buoyancy heat flux profile in the diffusion region due to molecular diffusion alone is also shown in Fig. 5.2. At the interface, molecular diffusion contributes about 68% of k_e . The corresponding value of k_m in this example is $k_m = 0.61$.

To illustrate that none of the three k values (k_e , k_m and k_h) are generally constant, the temporal variation of these terms for the I.C.P.M. will be discussed in the next section.

5.4 THE TEMPORAL VARIATIONS OF k_e , k_m AND k_h IN THE I.C.P.M.

The temporal variation of the k values for a steady heat flux experiment will be illustrated using the results of the numerical analysis of ES2. The variations of temperature and interface height with time, for this numerical analysis, have been discussed earlier (Chapt. 4.5). Figure 5.3 shows the variation of k_e , k_m and k_h as well as the variation of k_e from a molecular entrainment analysis of the same experiment.

The value of k_e from the turbulent entrainment analysis is seen to increase from $k_e = 0.10$ at t = 80 mins. to a maximum value of $k_e = 0.18$ when t = 140 mins. Thereafter, k_e decreases slowly, only dropping below $k_e = 0.10$ near the end of the interfacial entrainment period. It should be noted that the numerical analysis started

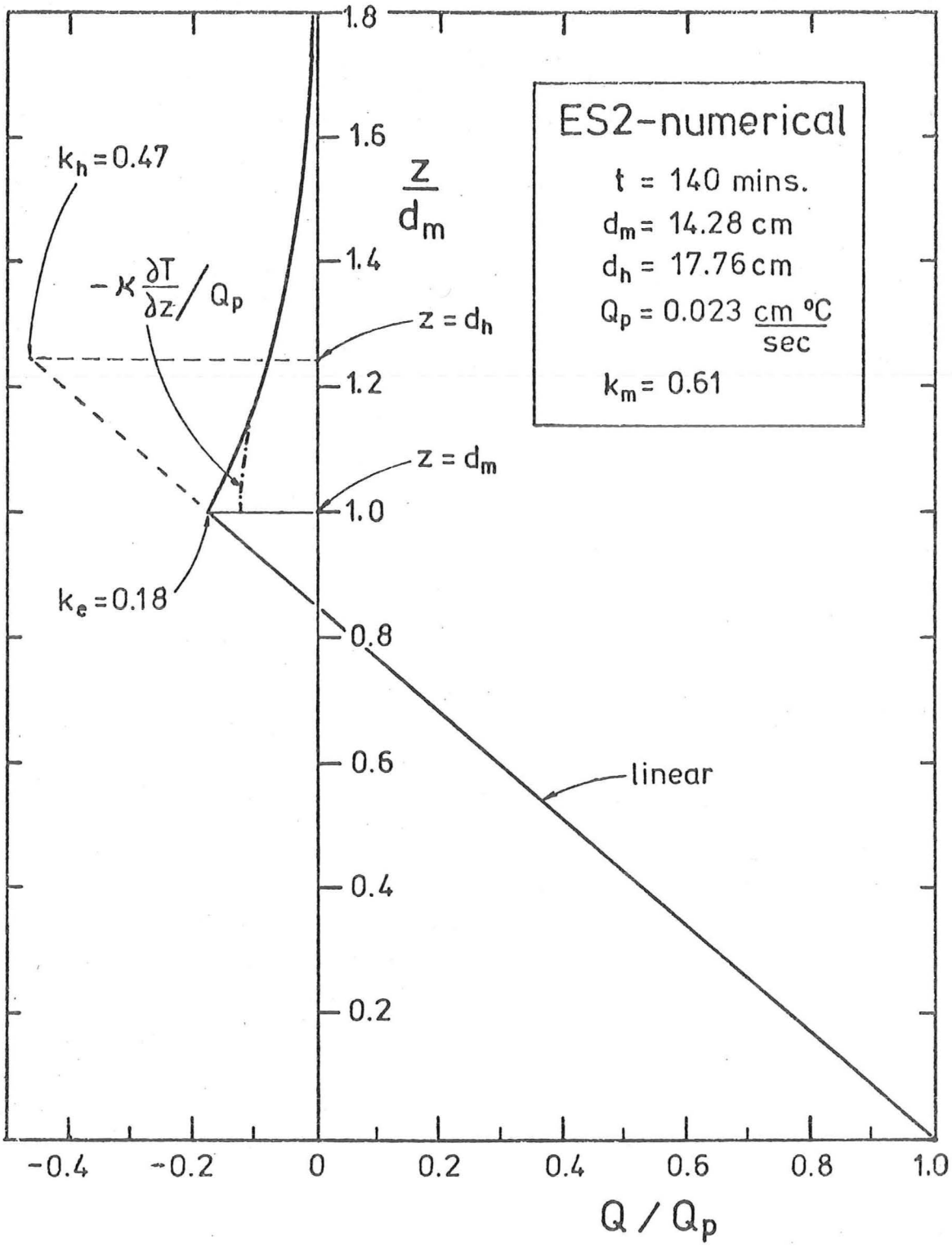

Fig. 5.2. Non-dimensional buoyancy heat flux profile from a turbulent entrainment analysis of experiment ES2 at t = 170 minutes showing the extrapolation method for evaluating k_e and k_h.

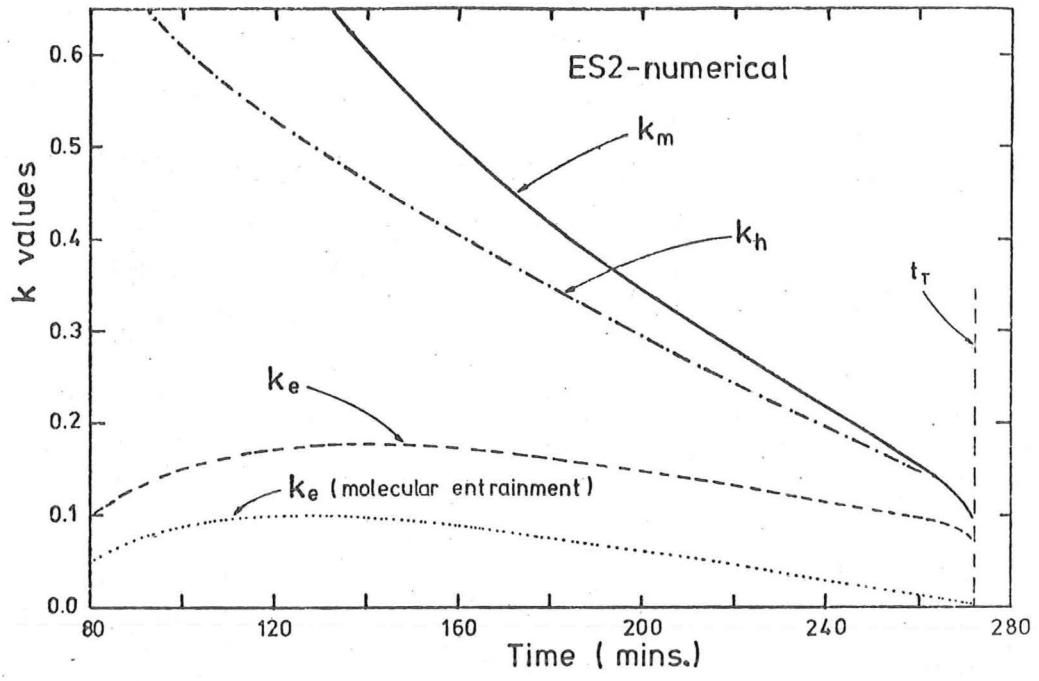

Fig. 5.3. Temporal variation of the entrainment ratios (k_e, k_m and k_h) from a turbulent entrainment analysis of steady heat flux experiment ES2. Variation of k_e from a corresponding molecular entrainment analysis is also shown.

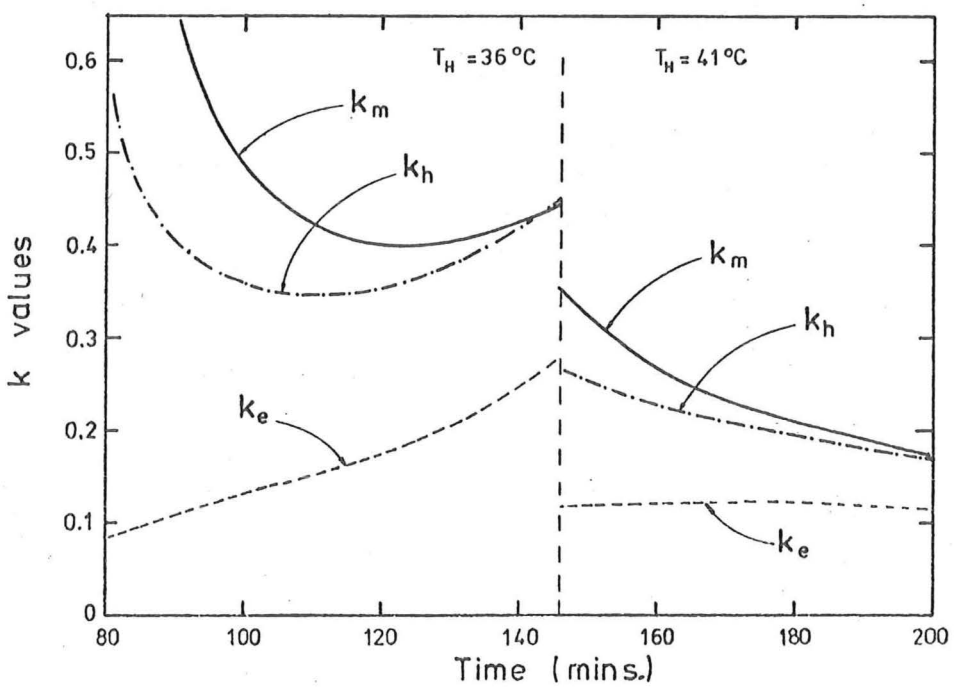

Fig. 5.4. Temporal variation of the entrainment ratios (k_e, k_m and k_h) from the turbulent entrainment analysis of an unsteady heat flux example. The circulated heating water temperature T_H increased once during the interfacial entrainment period.

shortly after $t = t_s$. The value at the start of the analysis ($t = 80$ mins) is therefore non-zero. In the molecular entrainment analysis, the value of k_e varies in a similar manner but is smaller. For this case the maximum value of k_e is 0.1. For turbulent entrainment, the turbulent diffusivity $\gamma(z)$ tends to sharpen the interface, causing increased interfacial temperature gradients. In the molecular entrainment analysis ($\gamma = 0$), this does not occur and k_e tends more rapidly to zero during the latter half of the interfacial entrainment period.

The variations of k_m and k_h are very much different. As the interface initially rises very rapidly and ΔT_i is a maximum, the values of k_m and k_h are initially very large. Both continuously decrease with time, with k_m being at all times greater than k_h. In this low Péclet number case, both k_m and k_h are much greater than k_e.

Under unsteady heat flux conditions the I.C.P.M. values of k_e, k_m and k_h vary quite differently from the steady heat flux case. The k values from the unsteady heat flux example discussed in Chapt. 4.5 are shown in Fig. 5.4. The most marked difference is in the variation of k_m and k_h. Because Q_p is initially decreasing for $80 < t < 146$ mins. (Fig. 4.10b), the values of k_m and k_h do not continuously decrease. For $120 < t < 146$ mins., both values are increasing. As Q_p becomes very small and approaches the chosen minimum changeover value ($Q_p = 0.011$ cm °C/sec), k_h becomes greater than k_m. For the I.C.P.M. this is an atypical situation. It occurs because the changes in the diffusion region temperature profile are greater than the changes in the mixed layer profile. Therefore, $d_h - d_m$ increases faster than d_m. This will only occur in the I.C.P.M. when Q_p is very small. At $t = 146$ mins., the value of T_H is increased instantaneously from 36 to 41°C. Both k_m and k_h undergo corresponding decreases. As Q_p is then much greater (Fig. 4.10b), k_m and k_h again decrease with time.

The variation of k_e is similarly discontinuous, reaching a maximum of $k_e = 0.28$ when Q_p is a minimum at $t = 146$ mins. During the latter stages when $T_H = 41$°C, k_e remains relatively constant at approximately 0.12.

The most interesting feature of the unsteady heat flux results is the tendency of the k values to remain relatively constant for long periods of time. For instance, for $90 < t < 140$ mins., the range of

k_h is only $0.35 < k_h < 0.42$. The decreasing value of Q_p in the numerator of Eqn. 5.1.3 counteracts the simultaneous decreases in V_{em} and ΔT_i. This apparent constancy of the k values should be seen as a result of the particular heat flux conditions and does not support the assumption that any of the k values are universally constant.

It could be argued that as none of the k values are universally constant, they no longer have a useful purpose in analysing interfacial entrainment systems. Betts (1973) initially defined the parameter k to simplify the solution of his heat budget equation for $d_m(t)$. As his assumption that k is a constant is incorrect, his analytical solution for $d_m(t)$ is also invalid. However, k_e, and to a lesser degree k_m and k_h, are still useful in describing non-dimensionally the interfacial entrainment process occurring in the I.C.P.M. As the parameter k is widely used in the literature, it is worthwhile continuing to use it in this thesis. This will enable the reasons for the wide range of previously reported k values to be discussed.

Although the k values vary with time, an analysis procedure similar to that used by Betts (1973), may be used to obtain useful relationships between the k values and the major variables d_m, d_h and ΔT_i. These relationships which suggest a method of evaluating the k values from experimental temperature profile measurements, are derived in the next section.

5.5 EVALUATION OF THE I.C.P.M. k VALUES FROM EXPERIMENTAL TEMPERATURE PROFILE DATA

Following the method of Betts (1973), a relationship for the k values may be obtained from each of the two heat budget equations. The mixed layer equation will be considered first. From Eqns. 3.7.6 and 5.3.2, the mixed layer heat budget equation (Eqn. 3.5.2) may be rewritten in terms of ΔT_i.

$$Q_p - Q_e = - \beta d_m \frac{d(\Delta T_i)}{dt} - W \Delta T_i d_m \qquad (5.5.1)$$

Using the two k ratios, k_e and k_m, the heat flux terms may be eliminated from Eqn. 5.4.1. Therefore

$$\frac{(1 + k_e)}{k_m} \beta V_{em} \Delta T_i = - \beta d_m \frac{d(\Delta T_i)}{dt} - W \Delta T_i d_m$$

Dividing by $\beta \Delta T_i d_m (1 + k_e)/k_m$ and rearranging yields

$$\frac{d}{dt}(\ell n\ d_m) = -\frac{k_m}{1+k_e}\frac{d}{dt}(\ell n\ \Delta T_i) - \frac{k_m}{1+k_e}\frac{W}{\beta} \qquad (5.5.2)$$

At this stage in his analysis, Betts (1973) assumed the k values to be constant and integrated his differential equation with respect to time. In the I.C.P.M. the k values do not remain constant and this same step cannot be carried out. However, consider a plot of the logarithm of d_m versus the logarithm of ΔT_i. The slope of the data at any time t is equal to

$$\frac{\frac{d}{dt}(\ell n\ d_m)}{\frac{d}{dt}(\ell n\ \Delta T_i)}$$

From Eqn. 5.5.2, this slope may be rewritten as

$$\frac{-k_m}{1+k_e}\left[1 + \frac{W}{\beta}\frac{\Delta T_i}{\frac{d}{dt}(\Delta T_i)}\right]$$

For the I.C.P.M., the heat loss term above is negligible. For the values given in Table 7.1, for example, the contribution to the slope by the heat losses is less than 1% of the total. It can therefore be assumed that the slope of the data on a log-log plot of d_m versus ΔT_i is

$$\frac{-k_m}{1+k_e}$$

A similar relationship applies to the full fluid column. Eliminating Q_p from the full fluid column heat budget equation (Eqn. 3.7.7) using k_h and rearranging yields

$$\frac{d}{dt}(\ell n\ d_h) = -\frac{k_h}{1+k_h}\frac{d}{dt}(\ell n\ \Delta T_i) - \frac{k_h}{1+k_h}\frac{W}{\beta} \qquad (5.5.3)$$

As discussed above the heat loss term is negligible. Hence, the slope of the data on a log-log plot of d_h versus ΔT_i will be

$$\frac{-k_h}{1+k_h}$$

The two slope relationships may be used to evaluate the three k values from temperature profile measurements at any given time. From the profiles, the value of d_m, d_h and ΔT_i can be obtained and plotted on a log-log graph. If heat losses are negligible, then k_h may be evaluated directly from the slope of the log d_h versus log ΔT_i

data curve. From Eqn. 5.3.6, the value of k_e could be obtained. The slope of the log d_m versus log ΔT_i graph at the same time value could then be measured and from the known value of k_e, k_m could be evaluated. This method, does not require the lower boundary heat flux Q_p to be known.

Denton and Wood (1974) derived a similar slope relationship for two-layered ($\Gamma = 0$) entrainment. However, they made the same assumptions as Betts (1973); that the interface had negligible thickness and that k was a constant. Neither of these assumptions appear to be valid for low Péclet number penetrative convection.

The form of the graphs of log d_m and log d_h versus log ΔT_i for the I.C.P.M. can be illustrated by the two numerical analyses already discussed (Chapts. 4.6 and 5.3). Figure 5.5 shows data from the numerical analysis of steady heat flux experiment ES2. As the analysis commenced at $t = 80$ mins. and not t_s, the data curves commence at values slightly greater than $d_h = d_{g0}$ and $d_m = 0$. As $(1 + k_e)$ was reasonably constant and both k_m and k_h decrease with time (Fig. 5.3), the curves show smooth decreases in slope, from large to small negative values, with time (decreasing ΔT_i). At all times, the slopes of the log-log plots of d_m and d_h versus ΔT_i are consistent with $-k_m/(1 + k_e)$ and $-k_h/(1 + k_h)$ respectively.

In the unsteady heat flux example (Fig. 5.6), the approximately constant values of k_m and k_h, during portions of the periods of constant T_H, are reflected in the approximately constant slope of the curves. Where T_H and the k values are discontinuous, the slopes of the log d_m and log d_h versus log ΔT_i curves are also discontinuous.

This apparent constancy of slope during periods of constant T_H, has been reported by Denton and Wood (1974). In their work the difference between d_m and d_h was not fully appreciated and the single height values plotted were in fact d_g, the height of maximum temperature gradient. In the I.C.P.M., the values of d_h and d_g are initially equal ($= d_{g0}$) but much later the interface height d_m is the height of maximum temperature gradient so that $d_g = d_m$.

Similar unsteady heat flux entrainment experiments by Jenkins (1974) also yielded constant slopes of the log-log plots of d_g versus ΔT_i. As discussed above, the constancy of slope does not suggest any of the k values are universal constants. This was apparent from the

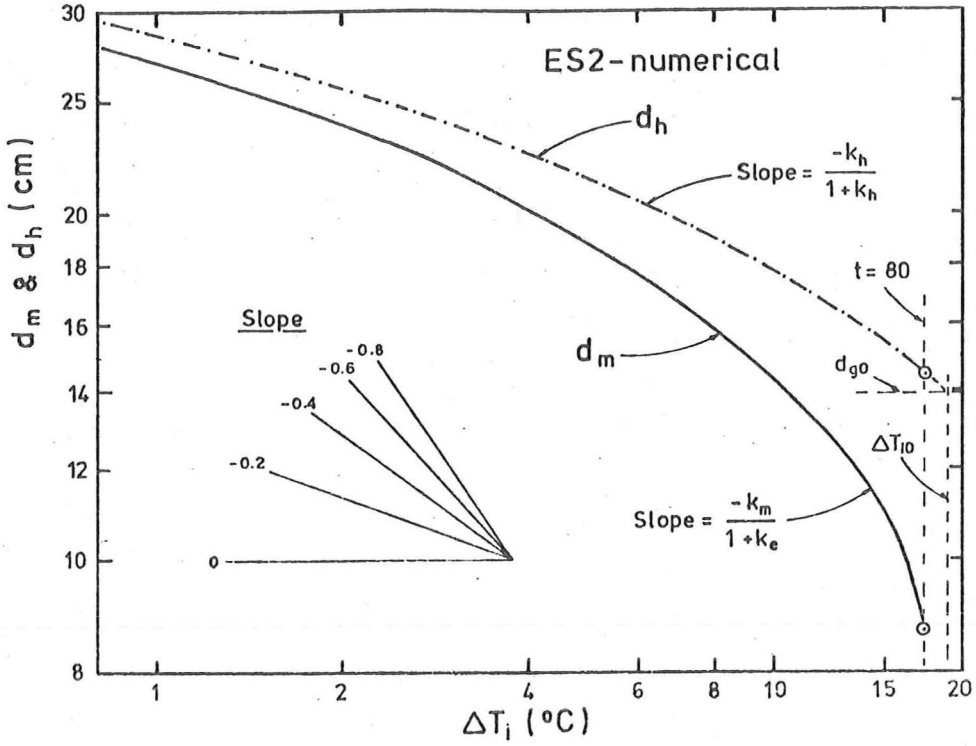

Fig. 5.5. Graph of the logarithm of d_m and d_h versus the logarithm of ΔT_i from the turbulent entrainment analysis of steady heat flux experiment ES2.

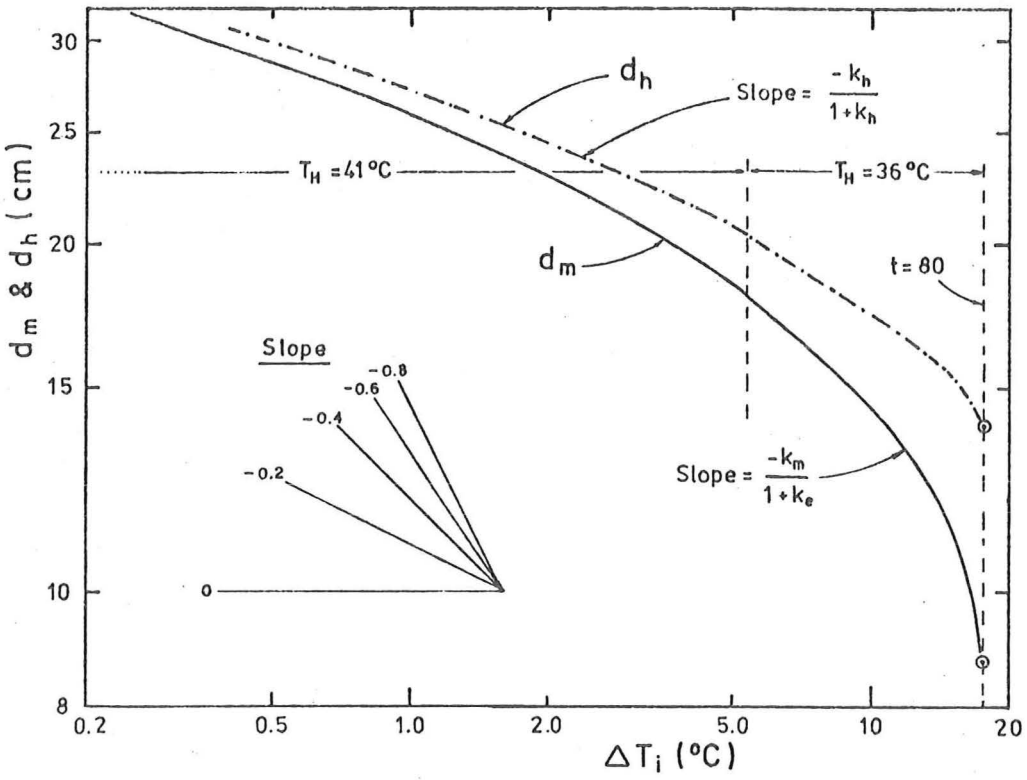

Fig. 5.6. Graph of the logarithm of d_m and d_h versus the logarithm of ΔT_i from the turbulent entrainment analysis of an unsteady heat flux example.

different constant slopes for individual experiments of Denton and Wood (1974), and the two different slopes in Fig. 5.6.

5.6 SUMMARY

It is apparent from the discussion of k values in this chapter, that the simple model of Betts (1973) cannot accurately analyse penetrative convection at low Péclet number. To use a similar approach requires the definition of three different k values (k_e, k_m and k_h), whose magnitude varies greatly with time. It is not correct to consider any one of these k values universally constant. For example, the ratio k_e has been shown to vary significantly with Richardson number and Péclet number (Chapt. 5.2). Even at high Péclet number the interfacial thickness cannot be neglected so that Betts' (1973) model equations will still yield erroneous values of k.

The wide range of k values reported in the literature, which have been recently reviewed by Stull (1976a), may be seen to be the result of a number of factors. Some of these factors are outlined below.

(i) The application of Betts' (1973) model equations to interfacial regions that do not have negligible thickness.

(ii) The use of analytical model equations which assume zero initial conditions ($d_m = \Delta T_i = 0$ when $t = 0$) when the virtual $\Delta T_i = 0$ origin occurs at $d_m > 0$ (Appendix H).

(iii) The use of Betts' (1973) model equations to evaluate k when an additional relationship $\Delta T_i = \phi(d_m)$ is also imposed on the system (e.g. Barnum and Rao 1975).

(iv) Richardson and Péclet number variation.

(v) Evaluation of k_e from time averaged and horizontally averaged vertical heat flux profiles which have underestimated Q_e (e.g. Deardoff, Willis and Lilly 1969, 1974).

(vi) Additional sources of turbulent kinetic energy such as shear stresses due to wind and current, which also contribute to Q_e.

The apparent values of k from any entrainment analysis model may therefore be overestimated or underestimated by one or more of the above effects. An example of this is the overestimation of k which occurred during Carson's (1973) analysis (Appendix H).

It should be noted that the range of k_e values used during the evaluation of the empirical constants E_{max} and c_t (Chapt. 4.3.1), were obtained from atmospheric measurements. However, allowance was made for the above mentioned factors when the range of representative atmospheric k values was chosen.

Provided the factors affecting the k values are appreciated during an experimental data analysis, the k values (k_e , k_m and k_h) can be successfully used to analyse and present experimental results.

CHAPTER 6

EXPERIMENTAL INVESTIGATION

6.1 INTRODUCTION

The initial object of the experimental investigation was to study the temporal behaviour of a laboratory model of the I.C.P.M. in terms of long and short period temperature variation. From this study it was hoped to gain an understanding of the deepening of a mixed layer by penetrative convection. As a consequence of these preliminary investigations, a theoretical model was derived. The object of the second phase of the experimental investigation was to evaluate the results of numerical analyses of the theoretical I.C.P.M.

Two types of laboratory experiment were performed. In the first series of experiments, the lower boundary heat flux was controlled by circulating water at constant temperature $T_H (> T_m)$ beneath the lower conducting boundary. A sketch of the experimental configuration and the vertical temperature distribution for an unsteady heat flux entrainment experiment is shown in Fig. 6.1a.

From thermal convection theory (Appendix A), the lower boundary buoyancy heat flux Q_p is given by

$$Q_p = c_q \left(\frac{\alpha g \kappa^2}{\nu} \right)^{1/3} (2 \Delta T_p)^{4/3} \qquad (6.1.1)$$

where $\Delta T_p = T_p - T_m$, is the temperature difference between the lower boundary plate and the mixed layer fluid. As shown in Fig. A.8, c_q is not a constant but is a function of Rayleigh number, Prandtl number and the experimental aspect ratio. However, at large Rayleigh number, this variation of c_q is small. The temperature difference ΔT_p is less than the corresponding temperature difference $\Delta T_H = T_H - T_m$ because forced convection is occurring between the circulated heating water and the underside of the lower boundary plate. As the circulating water temperature T_H is a constant, it is simpler in some cases to discuss Q_p as a function of ΔT_H.

As there is a net flux of heat into the mixed layer, its temperature continually increases. This reduces ΔT_H and hence Q_p is continually decreasing. This unsteady heat flux method was used by Deardoff et al. (1969). Problems arising from this type of

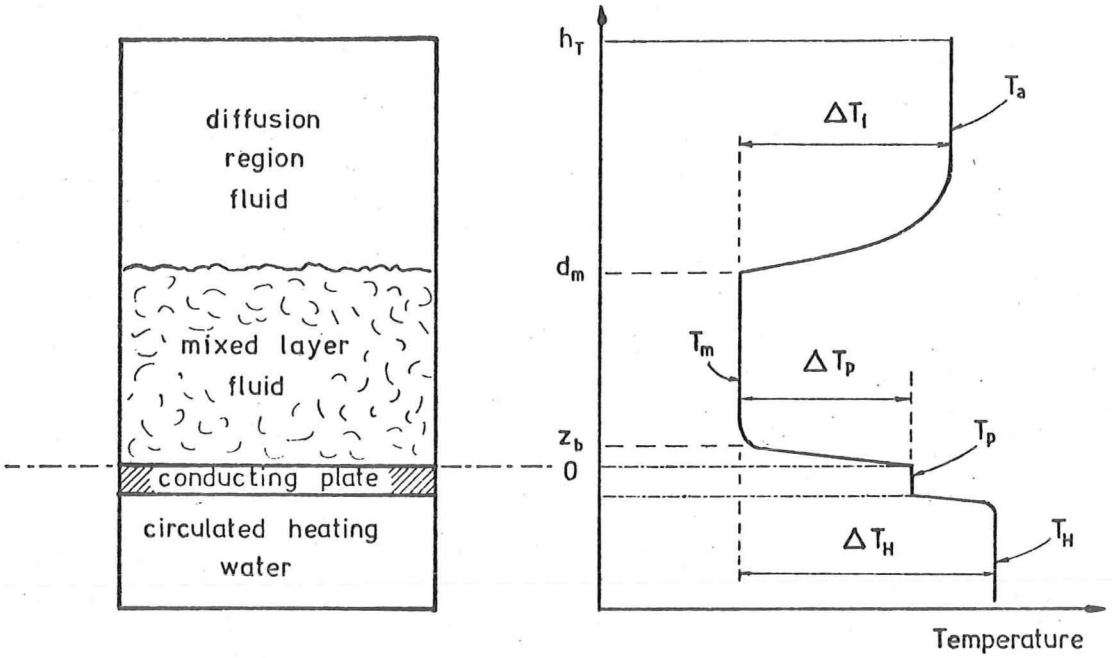

(a) Unsteady heat flux (T_H held constant) .

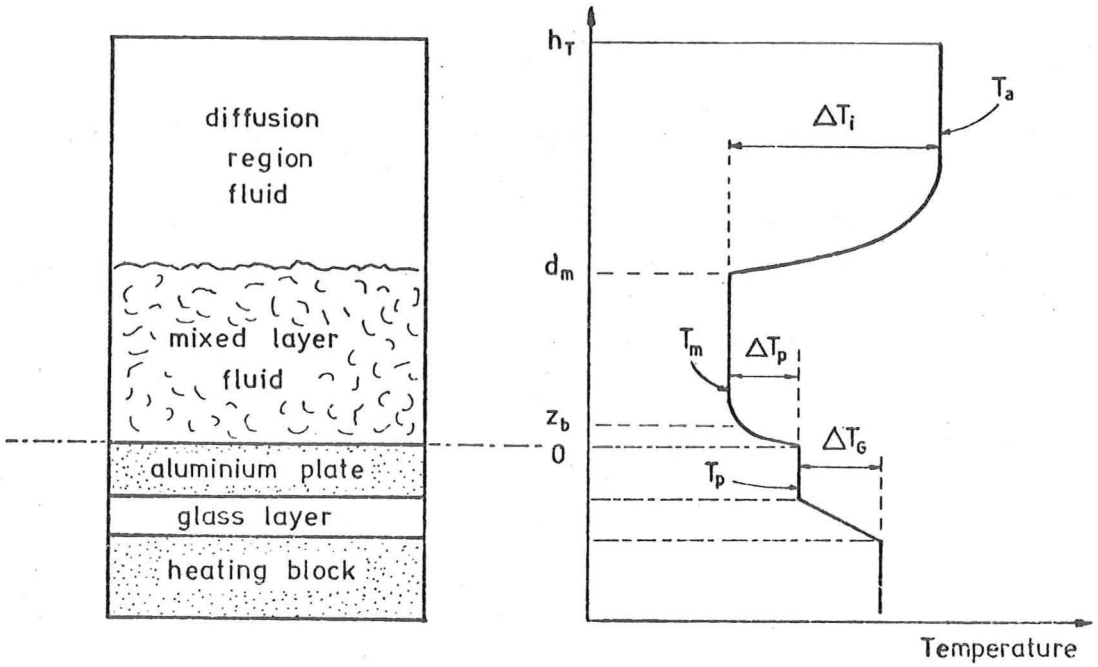

(b) Steady heat flux (ΔT_G held constant) .

Fig. 6.1. Sketches of the experimental configuration and typical vertical temperature profiles for the unsteady and steady heat flux experiments.

experiment due to the numerous unsteady parameters have already been discussed (Chapters 4 and 5). These unsteady heat flux experiments constituted the preliminary experimental investigation and initial quantitative runs. They revealed the need to eliminate at least one of the unsteady factors of the model by keeping the lower boundary heat flux constant.

In the second series of laboratory experiments, the heat flux was kept steady through the use of a multilayered lower boundary. Following a similar method used by Krishnamurti (1970a,b), a low conductivity layer of glass was sandwiched between the metal boundary plate and a metal heating block. A sketch of the experimental configuration and the vertical temperature distribution for a steady heat flux entrainment experiment is shown in Fig. 6.1b. The temperature difference across the glass layer ΔT_G was monitored and kept constant by a control circuit, which regulated the electrical input to the resistance heating wire in the heating block. Apart from minor heat storage effects in the boundary plate, Q_p was kept constant. The external energy source for these steady heat flux experiments was therefore constant.

Insufficient time was available to mount an extensive experimental investigation, using the steady heat flux apparatus, to verify and evaluate the numerical model. The steady heat flux experiments were restricted to a few representative runs.

6.2 EXPERIMENTAL APPARATUS

The experimental apparatus will be discussed under four headings: experimental working area, unsteady heat flux apparatus, steady heat flux apparatus and instrumentation.

6.2.1 Experimental Working Area

The fluid column ($0 < z < h_T$) was contained within an experimental tank, 60 cm high and 30 cm square, constructed from 1.22 cm perspex (methyl methacrylate) sheeting (Fig. 6.2). The maximum fluid column height h_T was restricted to 55 cm. This allowed a 5.1 cm polystyrene sheet to be floated on the fluid surface as part of the tank insulation. The sides of the tank were insulated with 7.6 cm polystyrene sheets. In the earlier unsteady heat flux experiments, only a single insulation thickness was used (Fig. 6.2). However, to further minimize the heat losses in the steady heat flux experiments, a second layer of 7.6 cm polystyrene

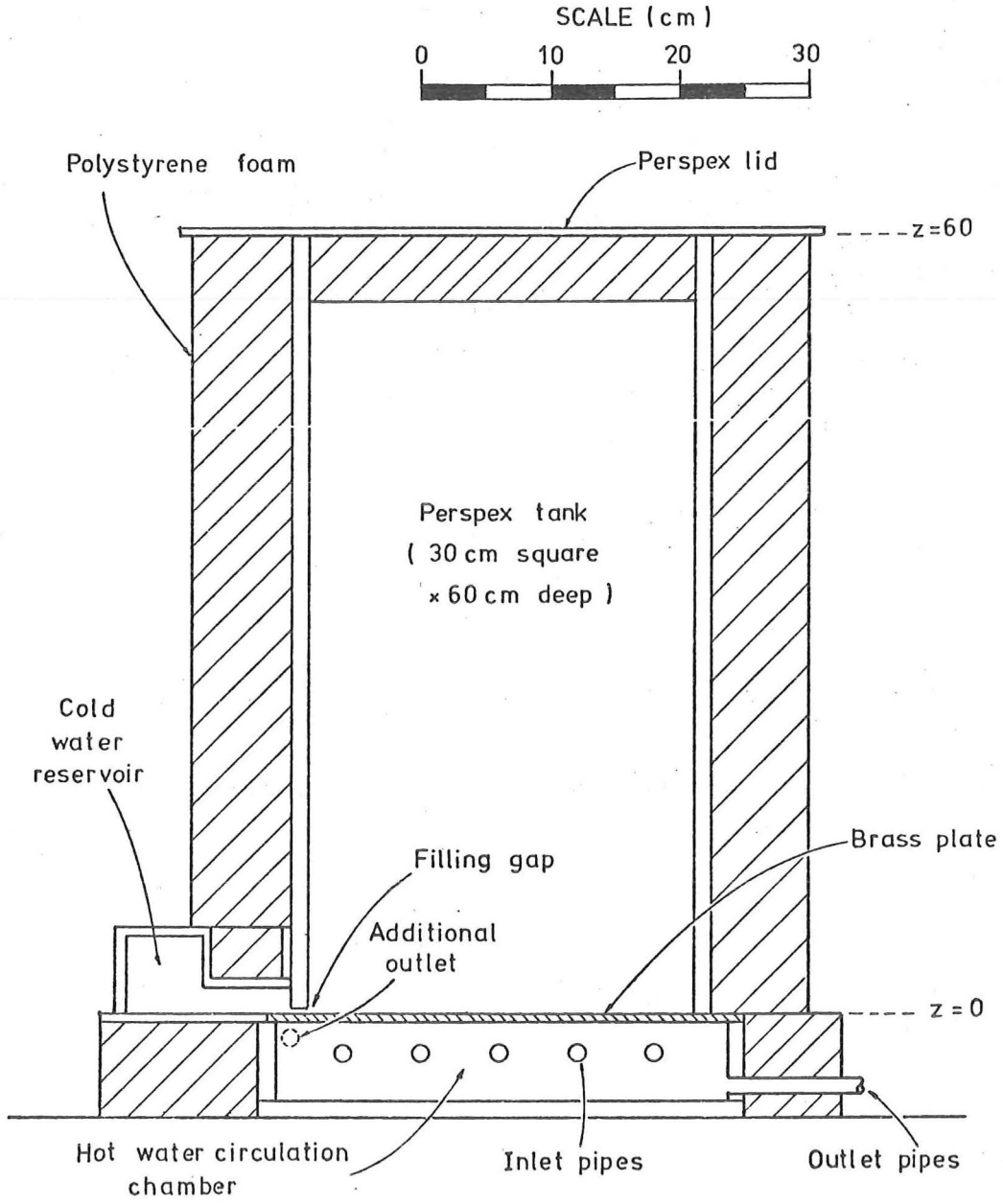

Fig. 6.2. Experimental tank for the unsteady heat flux experiments.

sheeting was added to the top and sides (Fig. 6.4). A discussion of the experimental heat losses is given in Appendix D.

To enable the introduction of dense fluid (cold water) into the experimental tank beneath an existing layer of lighter fluid (warm water), a 0.16 cm gap was left between the base of one wall and the lower boundary plate (the procedure for establishing a density stratification is discussed in Chapt. 6.3.1). A small perspex inlet reservoir (1.6 litre capacity) was fitted against this wall. Inflowing fluid was uniformly introduced along the full width of the wall. The gap could be sealed from the reservoir side by a rubber wedge.

Water for the experimental fluid column was obtained directly from the water mains. The presence of impurities and dissolved air bubbles in the water will affect the fluid properties and hence, the model behaviour. Any build-up of air bubbles on the heated lower boundary can cause a reduction of heat flux for the measured values of ΔT_p and ΔT_H. A distillation and de-aerating system, consisting of a 5 litre/hour capacity still and two stainless steel tanks of 46 and 91 litre capacity, was constructed. One of the tanks contained a heating element so that the distilled fluid could be de-aerated by heating under vacuum pressure. However, the distillation/de-aeration process was both time and energy consuming. It was therefore decided that the added purity of the water did not contribute significantly to the learning process to warrant its continued use.

A method of maintaining a constant mixed layer thickness by the withdrawal of fluid (Rouse and Dodu 1955, Turner 1968) was initially tested. A circumferential withdrawal jacket was constructed on the outside of the tank, at height $z = 10$ cm. Preliminary tests indicated that the additional horizontal withdrawal currents had too great an effect on the mixed layer convection motions. This method was therefore abandoned and the withdrawal holes were sealed.

6.2.2 Unsteady Heat Flux Apparatus

The conducting lower boundary plate for the unsteady heat flux experiments was a machined brass sheet (Alloy 209) of 37 cm by 38 cm plan dimension and 0.635 cm thick. It formed the top of a 6.1 cm deep perspex circulation chamber which was completely filled with water. All air bubbles on the underside of the brass plate were removed, through bleeder holes, after filling.

Heated water was pumped into the lower chamber through five copper tubes, which extended the full length of the chamber (Fig.6.3).

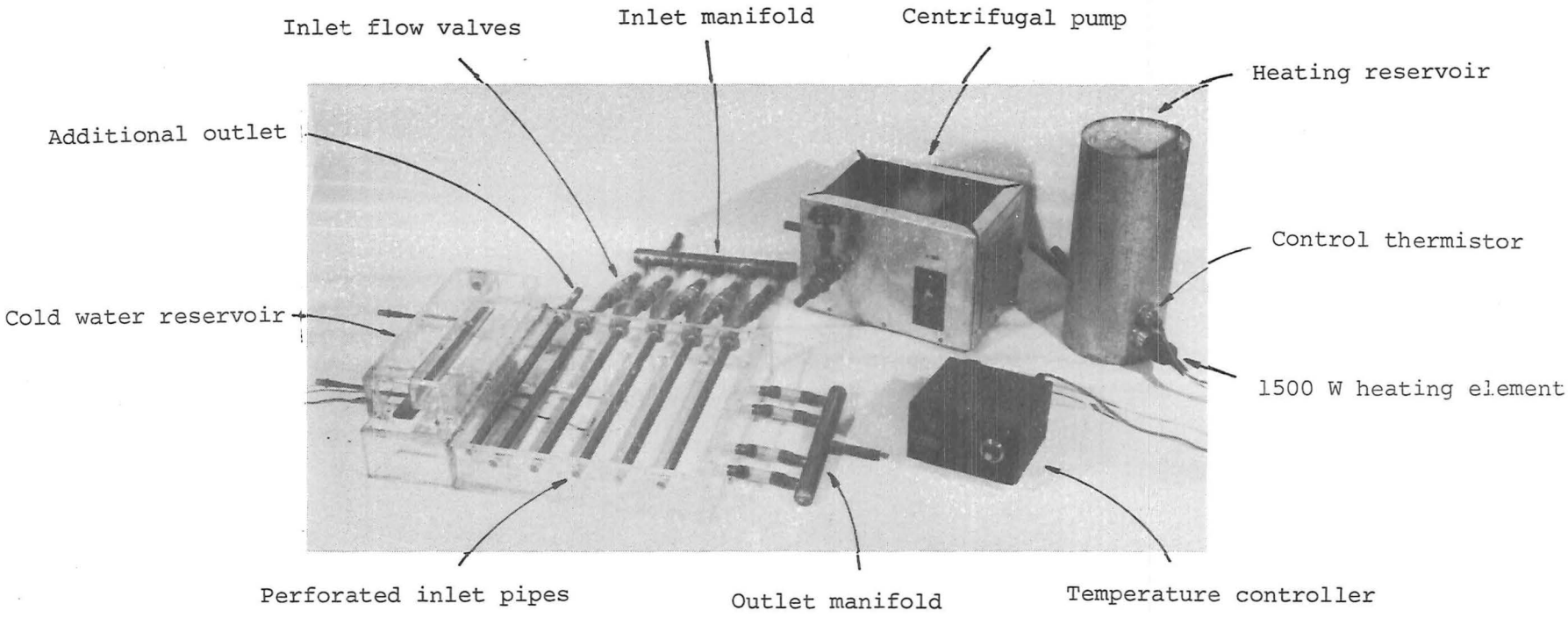

Fig. 6.3. Unsteady heat flux heating apparatus.

The inlet tubes were perforated along their underside to allow the inlet water to be fully mixed before contacting the brass plate. Equal flow through each inlet tube was ensured through the use of Marac flow valves which were specified at 2.3 litres/minute over a range of inlet heads.

Water was withdrawn through four outlets set at the base of one of the chamber walls. This asymmetric withdrawal configuration produced uneven plate heating, so an additional perforated withdrawal pipe was mounted along the adjacent wall. The relative withdrawal rates were adjusted to ensure an even brass plate temperature distribution.

Water withdrawn from the chamber was circulated through a small reservoir, where it was reheated by a 1500 watt commercial heating element, operated by a thermistor based control circuit. The water then passed through a centrifugal pump and back into the heating chamber.

The unsteady heat flux apparatus with the brass plate removed is shown in Fig. 6.3. A side elevation diagram of the assembled and insulated unsteady heat flux experimental apparatus is given in Fig. 6.2.

6.2.3 Steady Heat Flux Apparatus

The heating apparatus for the steady heat flux experiments consisted of an aluminium-glass-aluminium sandwich (Fig. 6.4). The upper plate was made from rolled aluminium alloy (B.S. 1470, Alloy 5154) machined to a final thickness of 2.34 cm. Its upper surface formed the lower boundary ($z = 0$) of the fluid column. The sides were machined to the outer dimensions of the perspex tank except along the inlet reservoir side so that its plan dimensions were 31.7 cm by 32.8 cm. However, a 0.48 cm thick lower flange was left to allow for the sandwich assembly (Fig. 6.5).

Beneath the upper plate was a glass sheet (average thickness 0.217 cm). As glass is a poor thermal conductor (typical thermal conductivity of 2.3×10^{-3} cal/sec cm °C), this provided a measurable heat flux temperature difference. The glass sheet was 30 cm square, the same plan dimensions as the fluid column. Thermal paste applied to both sides of the glass prior to assembly ensured good thermal contact with the aluminium layers.

The lower heating block was made of cast aluminium (aluminium alloy LM6, 12 - 13% silicon). After casting, the aluminium block was

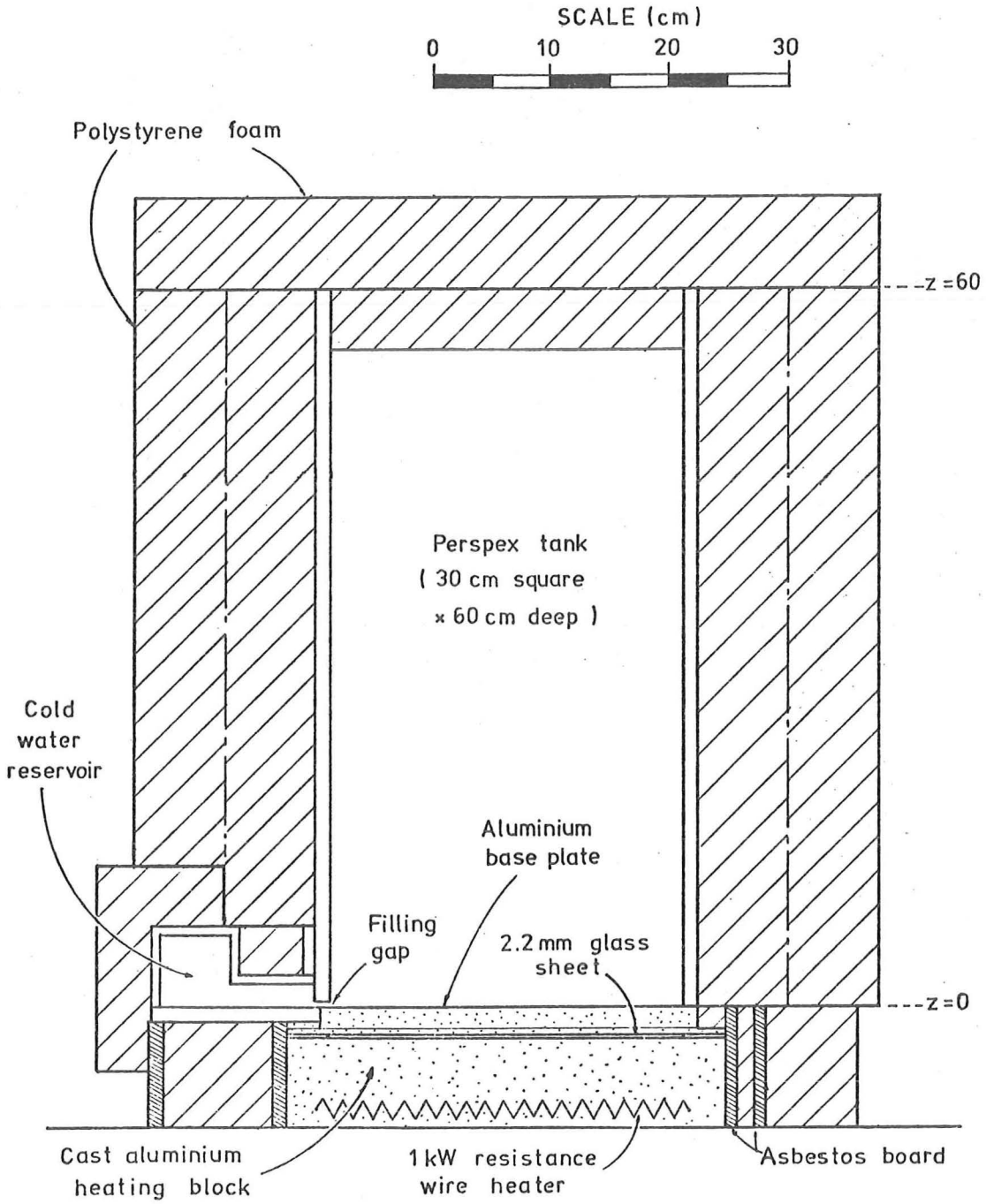

Fig. 6.4. Experimental tank for the steady heat flux experiments.

x-rayed to check that no major porosity regions existed. The block was machined flat to a final thickness of 7.3 cm. Eighteen grooves, $1\frac{3}{4}$ cm apart, were machined on the underside of the block to allow the installation of a length of resistance heating wire (1000 watt, 230 volt nominal capacity). The final plan dimensions were 37.3 cm by 38.3 cm.

A mock-up of the steady heat flux apparatus, prior to the installation of the resistance heating wire, is shown in Fig. 6.5. The interplate spacing shown is larger than the final assembled value of 0.22 cm.

The heat flux input was controlled by an eight thermocouple thermopile. These chromel-alumel thermocouples were mounted, alternatively above and below the glass sheet, in shallow grooves machined in the aluminium. The thermopile output was linked to a temperature control circuit which maintained a fixed temperature difference across the glass (further details are given in Chapt.6.2.4). Four additional chromel-alumel thermocouples were arranged on each side of the glass sheet to provide direct temperature measurement. A further thermocouple was fitted into a hole drilled into the centre of the upper plate.

Figure 6.6 shows the lower aluminium heating block with the glass sheet and lower thermocouples in place. The thermocouples marked C constitute the control thermopile. The wooden pegs in the four corners of the aluminium block held the assembled sandwich in position. Heat transfer across the air gap, to the side of the glass layer, was calculated to be small (less than 2 percent of the total). This would not have affected the heat flux control system. Care had to be taken to remove any thermal paste squeezed from between the glass layer and the aluminium. Otherwise, the heat transfer through the glass would be short-circuited.

6.2.4 Instrumentation

Instrumentation was required for the control of the heat flux apparatus and for the measurement of the fluid column and heating apparatus temperatures.

(i) Control systems

For the unsteady heat flux experiments, the temperature of the circulated heating water T_H was maintained at a constant value by a thermistor based control system which regulated the power supply to a 1500 watt heating element. The thermistor was placed several centimetres

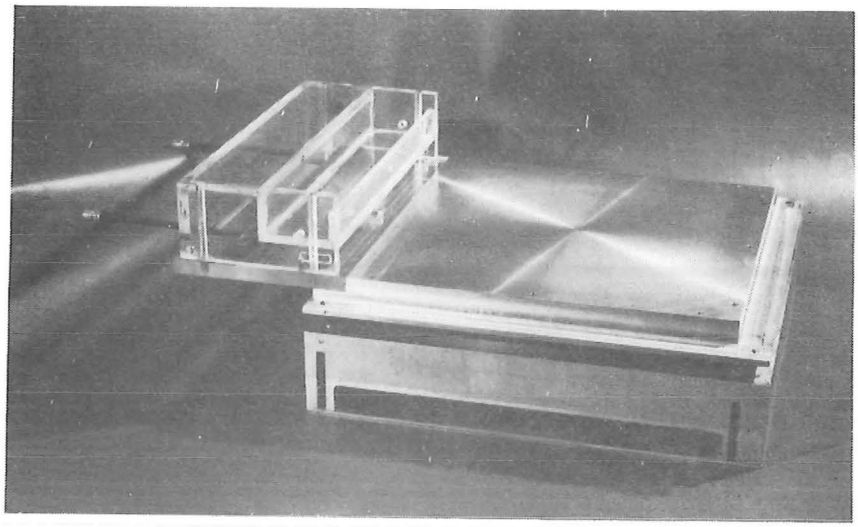

Fig. 6.5. Mock-up of steady heat flux heating apparatus before heating wire was embedded into the base of the aluminium heating block. Gap between the aluminium layers is greater than the final separation (0.22 cm).

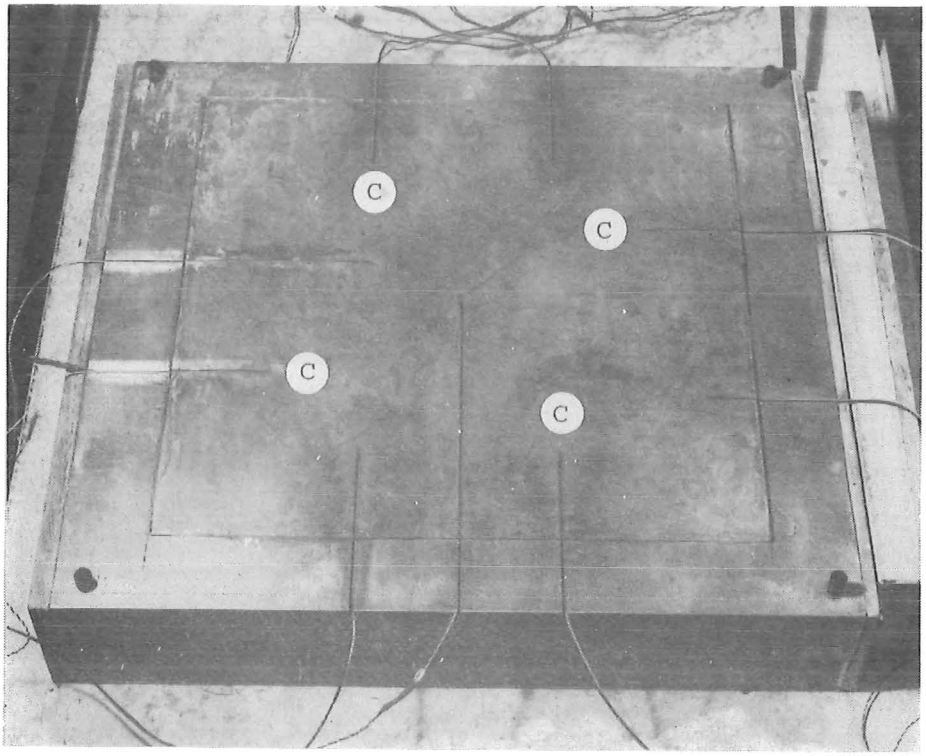

Fig. 6.6. View of aluminium heating block with thermocouples for control circuit thermopile (labelled with C) and other measurement thermocouples in place. Glass sheet is also in position.

above the heating element in the heating reservoir (Fig. 6.3). This kept the thermal lag between the sensor and the heater at a minimum.

In the steady heat flux experiments the heat flux across the glass layer was held constant. A thermopile, consisting of eight chromel-alumel thermocouples mounted alternatively above and below the glass layer, monitored the temperature difference across the glass layer ΔT_G . A sketch showing the vertical temperature distribution for the steady heat flux experiments is given in Fig. 6.1b. The thermopile was linked to a control circuit which kept ΔT_G constant by on - half on - off switching of the electrical supply to the heater. As the control circuit was unable to vary the voltage supply, an additional set of variable load resistors were connected in series with the heating block. By adjusting the load resistance, the system could be tuned so that the control circuit switched off infrequently.

(ii) Direct temperature measurement

Temperature measurements within the fluid column were made using a single chromel-alumel thermocouple probe mounted above the tank, which could be raised or lowered manually over the fluid column height ($0 < z < 55$ cm). Filing the thermocouple junction flat reduced its thermal capacity and ensured a rapid thermal response. The response time of the thermocouple probe, taken as the time to reach 63% of the new temperature value after a step change, was 0.08 seconds. Preliminary measurements across the tank and the behaviour of the dyed mixed layer, indicated that the horizontal temperature distributions were fairly uniform.

The use of a single probe, rather than a mean horizontal averaging probe, and the use of a manual rather than automatic vertical traversing system, may invite some criticism. A horizontally averaging probe, which consisted of resistance wire strung back and forth across a circular support ring, was constructed and tested. However, any change in tension of the wire due to creep or knocking the probe, altered the calibration to an unacceptable degree. If the interface is not quite horizontal a horizontally averaging probe will not show the discontinuity of vertical temperature gradient at the interface. This has been discussed in Chapt. 2.2.3, with reference to the experiments of Deardoff et al. (1969). For these reasons, the single probe, which gave a one-dimensional vertical temperature profile, was used. It was positioned off-centre and away from the walls to reduce the chance of measuring container geometry and side wall heat loss effects.

When the probe was raised or lowered manually it was found that fluid was drawn along with the moving probe. When the probe came to rest in a region of significant density gradients, a brief damped buoyancy oscillation was produced. It was apparent that a continually moving probe would yield erroneous temperature readings due to this displacement of fluid. The method of sampling temperature adopted for these experiments, was to move the probe in discrete steps to whole number centimetre heights above the lower boundary. Temperature readings were then taken with the probe stationary. An advantage of this measurement system was that the temperature versus time data could be plotted directly as contours of constant height.

Preliminary measurements showed that no major vertical temperature gradients existed in the mixed layer, except close to the lower boundary. Temperature changes in the upper reaches of the diffusion region were also found to be small with respect to both height and time. A single representative mixed layer temperature T_m could be measured anywhere within the mixed layer and only infrequent measurements of the temperature at the top of the diffusion region were necessary. The interfacial density gradient region, where the rates of change of temperature with height and time were greatest, was clearly the region of most interest. More frequent sampling of temperature was carried out in this area.

Two additional fixed copper-constantan thermocouples were mounted in one of the tank walls at $z = 8$ and 41 cm. These probes which protruded 8 cm into the fluid column provided a check on the vertical probe measurements. For most of the interfacial entrainment period, these represented the temperatures T_m and T_a respectively.

In the unsteady heat flux experiments, copper-constantan thermocouples were used to measure the lower boundary plate temperature T_p (from the underside) and the circulation chamber water temperature T_H. A partial immersion thermometer (graduated to 0.1°C) was also mounted in the circulation chamber to give direct temperature measurement.

The direct reading thermocouples in the experimental tank and heating apparatus were linked via a switch box to a thermocouple amplifier. Amplified output was read off digital voltmeters. Figure 6.7 shows the experimental apparatus (for an unsteady heat flux experiment) with temperature measuring instrumentation in position. The mixed layer has been dyed and the front insulation removed to allow the stratified fluid column to be seen. The rotameter to the immediate

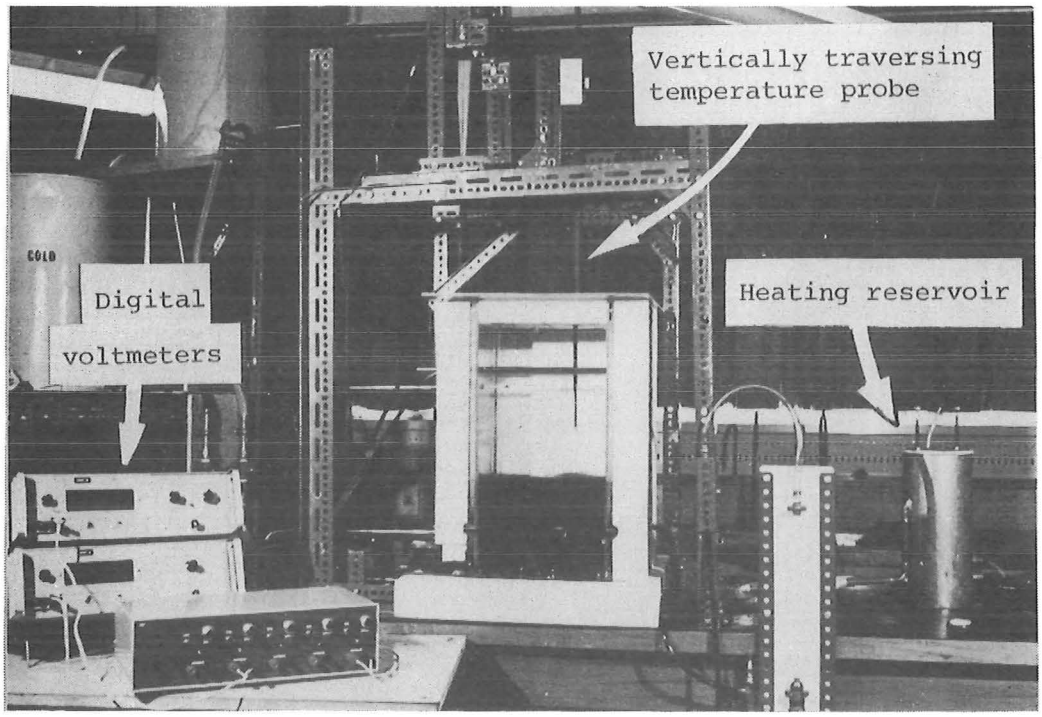

Fig. 6.7. View of experimental apparatus during an early unsteady heat flux experiment. Front insulation has been removed to show fluid column with dyed mixed layer.

right of the experimental tank was part of the fluid withdrawal system for the mixed layer. This system was not used in any of the quantitative experimental runs.

The choice of thermocouples over thermistors was made early in the experimental program. The slow response time of the thermistors and their non-linear output were seen as major disadvantages. Recent technological advances in electronics have produced linearizing intergrated circuits which eliminate the latter problem. However, these became available too late in the experimental program to warrant any changes. Readymade copper-constantan thermocouples were available in the laboratory at the commencement of the project. These were later replaced by chromel-alumel thermocouples which had better linearity.

Problems were encountered in keeping the ice-bath reference junction at 0°C and in switching low e.m.f. signals. The temperature measurements were therefore only accurate to about 0.1°C. However, the temperature fluctuations within the fluid column were often as large as 1 or 2°C (Chapt. 6.3.2). These will have a greater effect on the accuracy of the mean fluid temperatures.

6.3 EXPERIMENTAL PROCEDURES

In this section, an explanation of the method of establishing a two-layered temperature stratification is given. A series of continuous temperature measurements taken at fixed heights within the fluid column are then presented. As well as illustrating the methods of heat transfer in a penetrative convection experiment, these measurements also illustrate the problems involved in measuring the fluid column temperature profile, when large temperature fluctuations are occurring. Finally, the behaviour of a penetrative convection experiment, as revealed by flow visualization techniques, is discussed.

6.3.1 Establishment of Temperature Stratification

The initial conditions for the I.C.P.M. (Eqn. 3.1.3) are

$$T(z) = T_{a0} \qquad d_{g0} < z < h_T$$

$$T(z) = T_{m0} \qquad 0 < z < d_{g0}$$

where $T_{a0} > T_{m0}$

To establish this two-layered temperature stratification in the experimental tank, the tank was first filled with water at temperature

T_{a0} , to a height of $h_T - d_{g0}$ (the upper layer thickness). In all the experiments, $h_T \approx 55$ cm but a range of lower layer thicknesses (d_{g0}) was used. Colder water at temperature T_{m0} was then slowly discharged into the tank, through the gap at the base of the reservoir wall. Initially a density current nose formed, which moved across the lower boundary. The inlet flow was kept small at this stage to prevent the density current from climbing the far wall. Otherwise the nose, after rising up the wall 3 or 4 cm, would spread horizontally across the tank trapping a layer of warmer fluid. In the preliminary experiments, when the incoming cold water was dyed with potassium permangenate, the behaviour of the initial density current provided much visual interest. When the inlet flow was kept low, the nose of the density current did not rise in this manner. Instead, the cold layer thickened as a whole. Once the cold layer was more than 5 cm deep, the inlet flow could be increased. The inter-layer density difference and the inlet losses prevented any large scale mixing between the two layers. When the fluid column reached height h_T , the cold layer thickness was the required thickness d_{g0} .

Due to molecular diffusion and filling current shear stresses, the temperature profile at the end of the filling process was not ideally two-layered. A relatively thick density gradient region (of order 10 cm) typically occurred between the layers. It may have been possible to sharpen these density gradients by mechanical grid stirring in both layers and therefore more closely approximate the initial two-layered conditions. However, in these Péclet number experiments, molecular diffusion will still continue to thicken the density gradient region during the interfacial entrainment period.

In the theoretical model, the initial density gradient region has been allowed for (Chapter 3). To relate the experimental results to the theoretical model, a virtual initial time $t = 0$ can be calculated. This is obtained by comparing the experimental temperature profile at $t \approx t_s$ with the solution of the molecular diffusion equation (Eqn. 3.4.7).

6.3.2 Continuous Temperature Measurements At Fixed Heights

In a preliminary series of entrainment experiments, continuous temperature measurements were made at fixed heights in the fluid column, and recorded on an X-Y plotter. These measurements illustrated the types of temperature fluctuations occurring in a penetrative convection system. The passage of convecting thermal elements past the

measurement point was found to be the major cause of temperature fluctuations.

In determining the vertical temperature profile for the I.C.P.M., it is important to differentiate between the fluid temperature during a quiescent period (temporary absence of thermal elements) and the mean fluid temperature over a short period of time (including thermal element activity). The former temperature represents the density distribution which affects the motion of the thermal elements and is therefore more relevant to the penetrative convection system.

The temperature fluctuations occurring over the fluid column height may be considered in terms of four major regions of interest. These regions, in order of increasing height, are:

(i) buoyancy production region $0 \leq z < z_b$

(ii) uniform temperature region of the mixed layer $z_b < z < d_m$

(iii) interfacial intermittency region $d_m < z < d_m + z_{int}$

(iv) molecular diffusion region $z > d_m + z_{int}$

Representative measurements from each of these regions are shown in Fig. 6.8. The combined frequency responses of the thermocouple probe and the X-Y plotter probably led to some filtering of the high frequency fluctuations. However, this has made the intermittent nature of the fluctuations more obvious.

Similar temperature records have been presented by Deardoff, Willis and Lilly (1969) and Willis and Deardoff (1974). The relatively short interfacial entrainment period ($t_T - t_s$) for Deardoff et al's. experiments (c.f. Figures 2.4 and 4.8) meant that the mean variation of temperature was also significant. A probe initially in the stable molecular diffusion region ((i) above) was rapidly engulfed by the rising interface and thereafter remained in the mixed layer ((iii)). The mean temperature variations in Fig. 6.8 are not significant.

The data shown in Fig. 6.8 was measured during an unsteady heat flux experiment. Data for each height was measured at different times and hence slightly different values of Q_p. It is not possible to compare the simultaneous occurrence of individual events at each level.

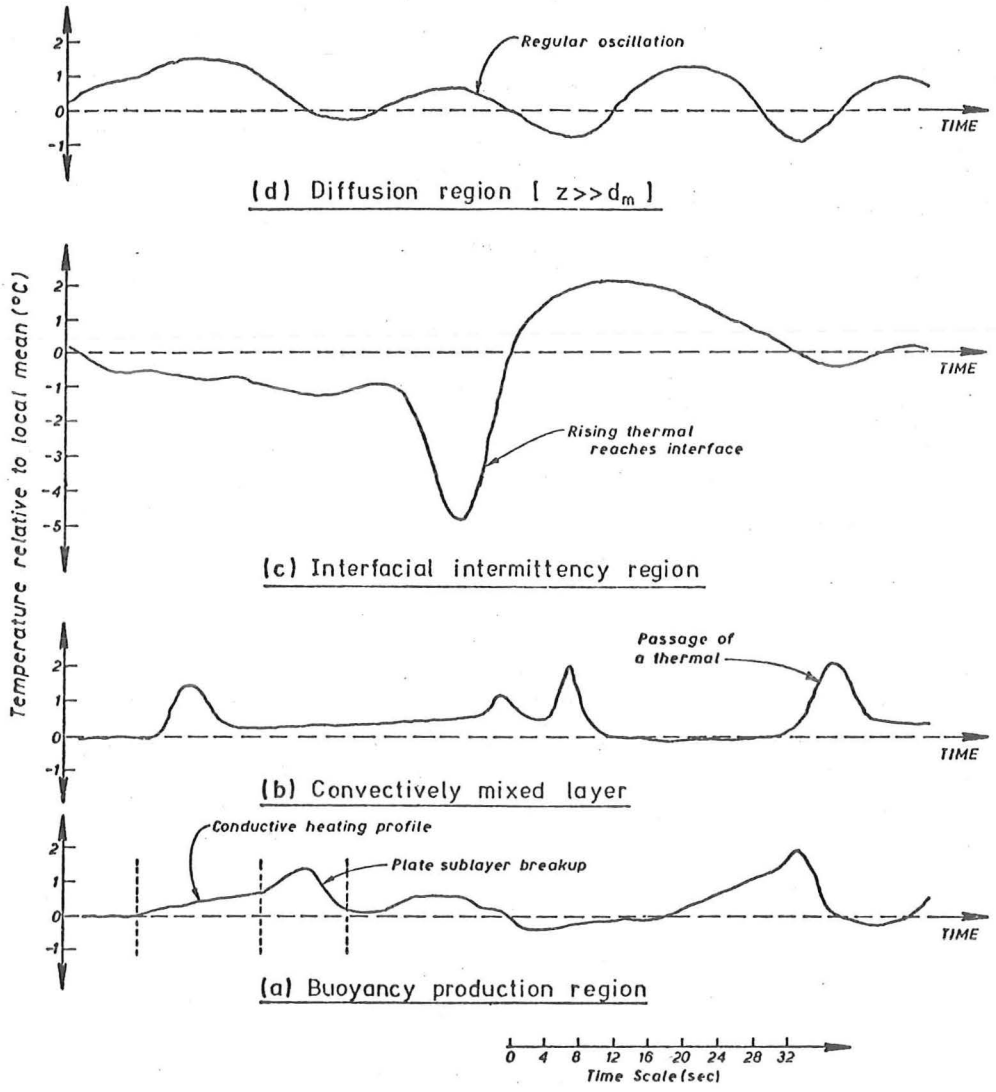

Fig. 6.8. Continuous temperature measurements at four fixed heights within the fluid column. As measurements were not taken simultaneously, the occurrence of the individual events at different heights are not directly related.

(i) Buoyancy production region

The temperature fluctuations in the buoyancy production region may be interpreted in terms of Howard's (1964) convection theory (Appendix A.5). For large Rayleigh number and medium and large Prandtl numbers, Howard considered the convection process as the periodic build-up of a molecular diffusion boundary layer, and its subsequent break-up due to buoyancy instability. Following Howard (1964), the temperature measured by the probe at height z prior to the layer break-up is given by Eqn. A.5.1.

$$T = T_m + \Delta T_p \left(1 - \text{erf} \frac{z}{2\sqrt{\kappa t}}\right) \qquad (6.3.1)$$

where t is the time elapsed since the last boundary layer break-up. When the boundary layer breaks up, two possibilities exist. The probe may be in the descending portion of the overturning break-up motions, in which case it would measure fluid temperatures rapidly decreasing to T_m. If the probe was in an ascending portion of the boundary layer overturning motions, it will measure a momentarily increasing temperature as warmer fluid from below passes the probe. An approximate measure of the maximum temperature recorded in this latter case is the mean temperature of the fluid below the probe at break-up, time t^*. Integrating Eqn. 6.3.1 from 0 to z yields

$$\overline{T}(<z) = T_m + \Delta T_p \left[\left(1 - \text{erf} \frac{z}{2\sqrt{\kappa t^*}}\right) + \frac{2\sqrt{\kappa t^*}}{\sqrt{\pi}} \left(1 - \exp\left(-\frac{z^2}{4\kappa t^*}\right)\right)\right] \qquad (6.3.2)$$

These two equations (Eqns. 6.3.1 and 6.3.2) may be used to show schematically, the variation of temperature with time at a fixed height in the buoyancy production region. The temperature data in Fig. 6.8a was measured with the probe as close as possible to the lower boundary. Because of the finite dimensions of the thermocouple junction, the mean measurement height was approximately $z = 0.2$ cm. If the boundary layer is assumed to remain static for 16 seconds (c.f. Fig. 6.8a), then the temperature measured by the probe for $0 < t < 16$ is $T(z)$ given by Eqn. 6.3.1. Figure 6.9 shows the temporal variation of $T(z)$ for $z = 0.2$ cm and $\kappa = 1.43 \times 10^{-3}$ plotted in the non-dimensional form $(T - T_m)/\Delta T_p$. The variation of $\overline{T}(<z)$ with time, from Eqn. 6.3.2, is also shown. When the boundary layer breaks up at $t = 16$ seconds, the temperature either drops rapidly to T_m (descending case) or rises toward $\overline{T}(<z)$ before dropping to T_m (ascending case).

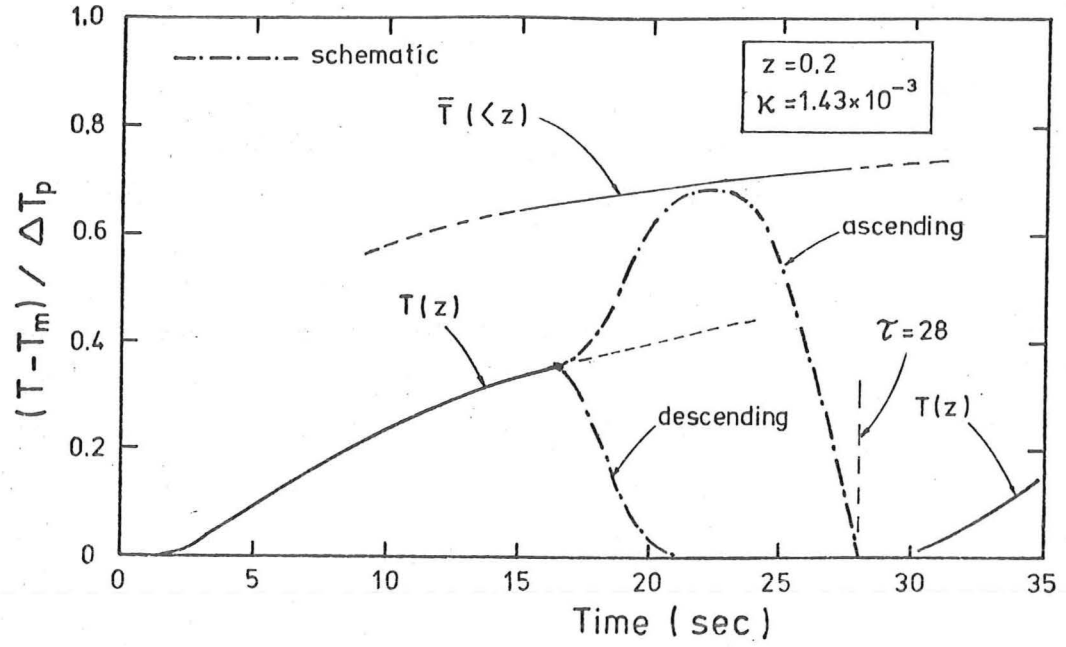

Fig. 6.9. Representation of the temperature variation in the buoyancy production region predicted by Howard's (1964) convection theory. Ascending and descending curves are schematic only.

This is shown schematically in Fig. 6.9. If the convection period of boundary layer build-up and break-up is about 28 seconds (c.f. Fig. 6.8a) then after $t = 28$, the process will be repeated.

A comparison of Figs. 6.8a and 6.9 suggests that three convection periods occurred during the measurement of the experimental temperature data in the buoyancy production region. The probe was in an ascending region for the first and third periods but in a descending region for the second.

(ii) Mixed layer

The continuous temperature reading from the mixed layer (Fig. 6.8b) shows the passage of discrete thermal elements past the probe. Following Howard (1964), it is assumed that these elements originate from the buoyancy production region and are rising vertically through the mixed layer. This was checked using a special probe which consisted of two thermocouples strung horizontally across the tank so that their hot junctions were set one above the other and 2 cm apart. Any thermal elements passing both junctions produced two "blips" separated in a temporal sense. The spacing was always positive confirming an upward motion and quantitatively suggested vertical velocities of about 1.5 cm/sec.

Because of the difference in refractive index between the thermal elements and the surrounding fluid (caused by temperature differences), the rising elements were sometimes visible to the naked eye. It appeared from these observations that the thermal elements were in the form of discrete thermals rather than continuous plumes. However, additional heat transfer within the mixed layer may have occurred due to overall plume-like circulations. The presence of thermals agrees with Sparrow, Husar and Goldstein's (1970) observations.

The period of passage of the thermals, recorded with the probe in the mixed layer, was quite regular. No quantitative comparison between thermal period and heat flux was attempted because Q_p was unsteady.

(iii) Intermittency region

The continuous temperature measurements in the intermittency region just above the interface (Fig. 6.8c), illustrate the behaviour of the interfacial domes. These domes are the result of thermal elements rising through the mixed layer and over-shooting into the stable temperature gradient. When visualized by dyeing the mixed layer (Chapt. 6.3.3), the domes were seen to penetrate through the interface before coming to rest. The penetration distance was dependent on the strength of the interfacial temperature gradient. Unless Ri was very small, the interfacial domes would then retreat back into the mixed layer. The dome surfaces were smooth suggesting that there was no significant turbulent transfer across the dome boundaries.

Figure 6.8c shows the temperature fluctuation due to a penetrating dome for a medium Richardson number interface. Initially there is a net cooling effect as fluid above the interface is being lifted by an approaching interfacial dome. This is shown schematically in Fig. 6.10. Level (c) is the position of the probe. When the dome reaches the height of the probe (profile B in Fig. 6.10b), the temperature drops towards T_m. With the eventual retreat of the dome, the temperature increases again. The rising and falling of the interfacial dome sets up a damped oscillation in the fluid in the stable gradient region. This shows up in Fig. 6.8c as a damped temperature oscillation. The time period of the oscillations will be dependent on the strength of the interfacial temperature gradient. At level (c) in Fig. 6.10a, the temperatures will fluctuate from a maximum at point C, due to the minimum depression of the oscillating

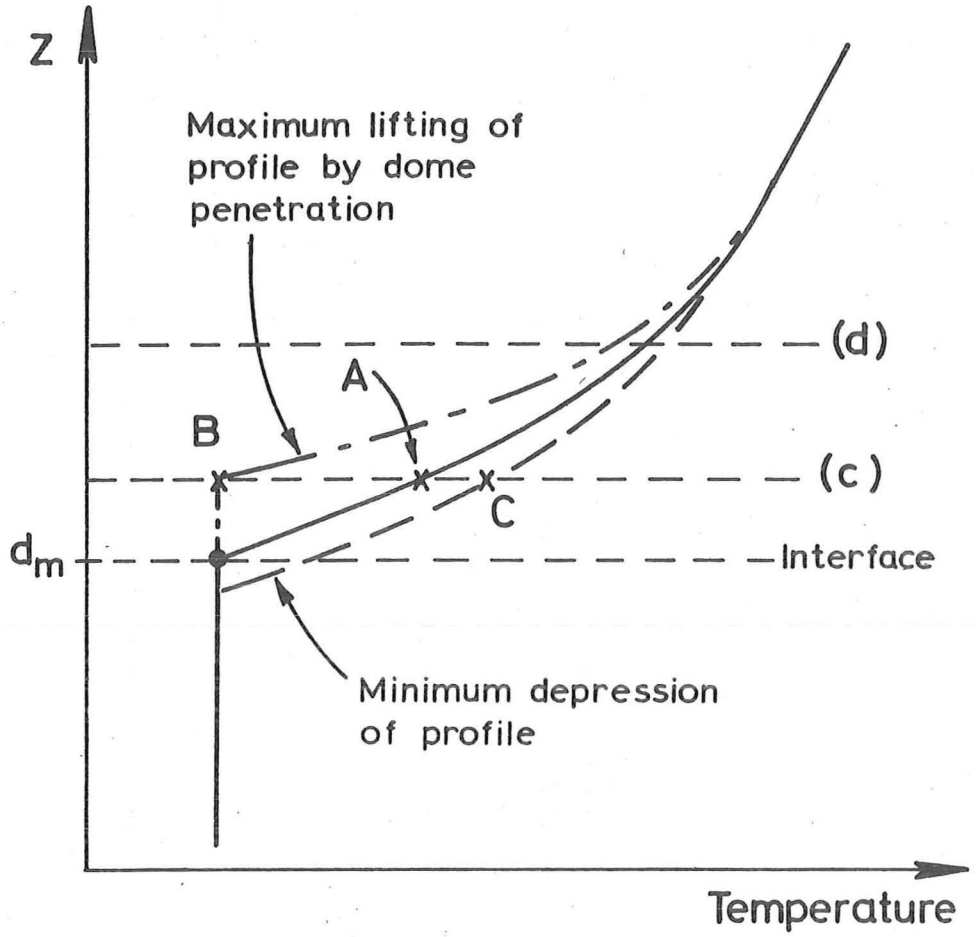

(a) Variation of the vertical temperature profile due to the penetration of interfacial domes.

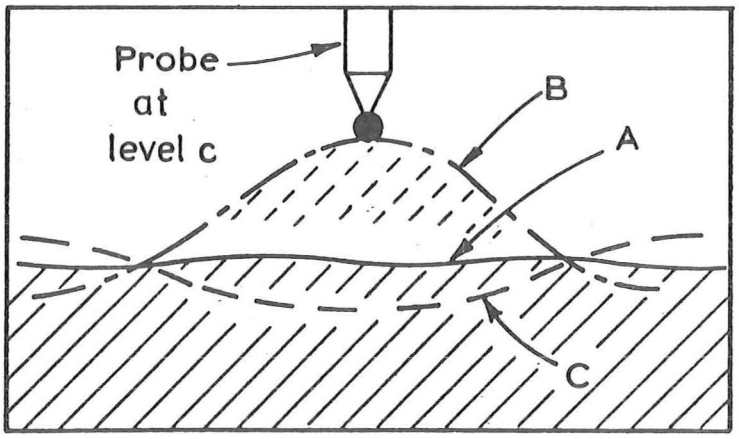

(b) Instantaneous shape of small section of interface during penetration of dome.

Fig. 6.10. Sketches showing the temperature fluctuations within the diffusion region caused by penetrating interfacial domes.

fluid, to a minimum value of approximately T_m, due to the dome reaching level (c).

(iv) Molecular diffusion region.

At level (d) in the molecular diffusion region well above the interface, the oscillation of the fluid is less pronounced and more regular. The regular, almost sinusoidal temperature fluctuations from this region are shown in Fig. 6.8d. The oscillation frequency will be related to the buoyancy frequency $N = (\alpha g \frac{\partial T}{\partial z})^{\frac{1}{2}}$. However, it will also be dependent to some extent on the forcing frequency, the frequency of thermal generation.

The internal wave action occurring above the interface has previously been reported by Townsend (1964) and Deardoff, Willis and Lilly (1969). As is apparent from Fig. 6.10a, the r.m.s. temperature fluctuation σ_T will have a maximum value slightly above the interface near the average penetration height of the interfacial domes. The magnitude of σ_T will be primarily dependent on the interfacial temperature gradient $\left.\frac{\partial T}{\partial z}\right|_i$ rather than on the convection temperature scale $T_s = Q_p / V_s$ (Eqn. 4.2.4). This was the case in Deardoff's (1974a,b) numerical model (Chapt. 2.2.2). Mixed layer values of σ_T scaled well with the convection scale, but above the interface, σ_T increased as the temperature gradient increased. When there was no significant interfacial temperature gradient (time 10.4 hours in Deardoff (1974b)), σ_T was negligible. Similarly, Deardoff et al. (1969) found that as the interface height increased, the maximum value of σ_T in the diffusion region also increased. This occurred even though Q_p was decreasing markedly. However, with increasing d_m in Deardoff et al's. experiments, the interfacial temperature difference and temperature gradient were increasing.

The continuous temperature measurements from fixed levels in the fluid column illustrate that instantaneous temperature readings or short period means will not yield the vertical temperature profile, assumed in the theoretical I.C.P.M. This is especially so at the interface, where a mean of the temperature fluctuations will not reveal the assumed discontinuity in temperature gradient. Ideally, the theoretical I.C.P.M. profile is obtained by measuring the temperature during a temporary quiescent period. Hence, rapidly fluctuating data were not used to evaluate $T(z,t)$ for the I.C.P.M.

The procedure used in the entrainment experiments to measure the fluid temperature was as follows. After the probe was moved to the required height there was a brief delay whilst the disturbed fluid motions decayed and the probe and surrounding fluid came to an equilibrium temperature. If the reading remained momentarily steady it was recorded. If the reading was rapidly fluctuating, the maximum and minimum values were recorded but the probe was left at that level until a quiescent reading could be taken. The average time to take a reading at any height was about 30 seconds.

6.3.3 Flow Visualization

To further investigate the behaviour of the convection and entrainment processes occurring in the experimental I.C.P.M., different regions of the fluid column were dyed to visualize the fluid motions.

Dyeing the mixed layer ($0 \leq z < d_m$) allowed the observation of the interfacial domes of mixed layer fluid as they penetrated the interface. Figure 6.11 shows the appearance of a relatively low Ri interface when the mixed layer was dyed. The interfacial domes in this case were quite large and penetrated large distances. At higher Richardson numbers, the domes were more regularly spaced, appearing as rising and falling hemispheres.

Dyeing the diffusion region ($z > d_m$) visualizes the transfer of diffusion region fluid into the mixed layer. Observation of the action of the mixed layer turbulence on the interfacial fluid showed no obvious cusp formation as described elsewhere (Townsend 1964, Deardoff et al. 1969, Stull 1973). Very diffuse wisps occurred but these had no regular pattern. The theory of Linden (1973) suggests that the impact and rebound of a thermal element on the underside of the stable temperature gradient causes a downwards spout of diffusion region fluid. This spout would occur along the central impact axis. No such behaviour was observed. It is suggested that low frequency of oscillation of the interfacial fluid due to the buoyancy fluid, would preclude the formation of a rebound spout. The dome-wisp behaviour assumed by Stull (1973) seems a more likely description of the interfacial entrainment behaviour.

A third dyeing technique was developed by the writer to visualize the initial convection boundary layer break-up. A small amount of denser (colder) dyed fluid was discharged through the filling gap at the base of the side wall. This formed a thin dyed layer at the lower boundary of the fluid column. The thickness of the dyed layer was of

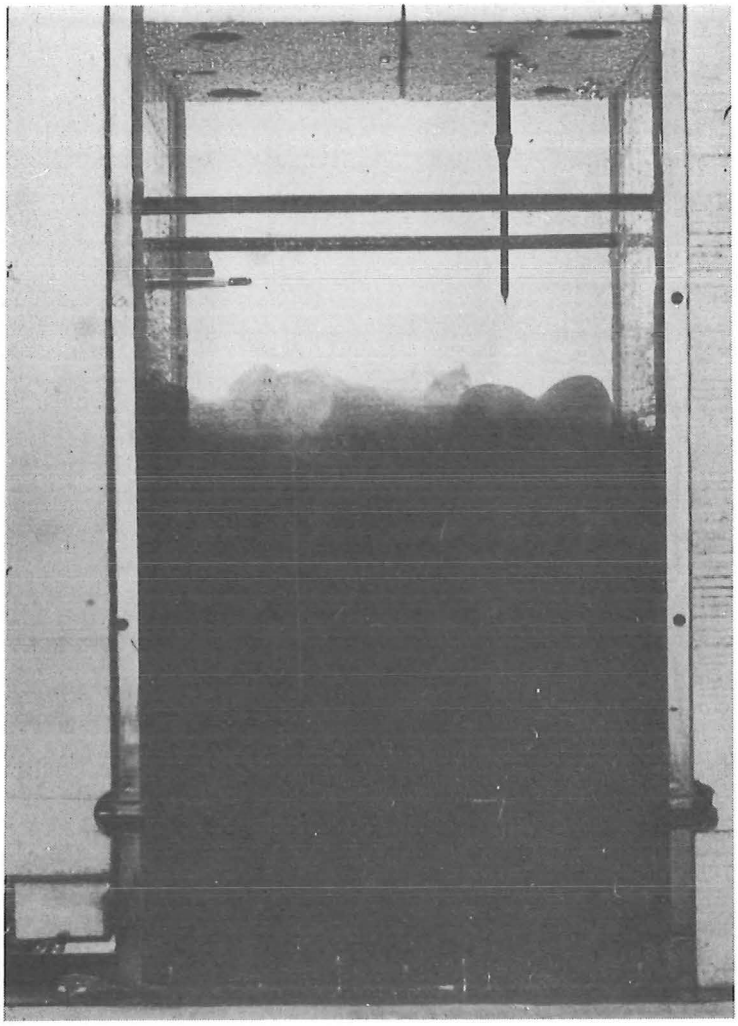

Fig. 6.11. Side view of fluid column with mixed layer dyed. The Richardson number in this case was low so that there is large scale interfacial penetration.

the same order as the buoyancy production layer which was soon to be created. Before the commencement of heating, the temperature of the dyed layer was allowed to adjust by molecular diffusion to the temperature of the fluid above. Viewed from above, the dyed layer appeared diffuse and evenly spread over the lower boundary area. This condition persisted for a short while after heating commenced. However, once the buoyant boundary layer reached its critical break-up condition, the dyed fluid was seen to form into long irregular rolls. These then rapidly broke up into single clumps of dye (Fig. 6.12). The clumps of dye then rose upwards. Because of the lag in increasing the lower boundary temperature T_H, the heat flux involved was quite small and the fluid motions were slow. The first burst of thermal elements rose only 2 to 3 centimetres above the heated boundary.

Figure 6.12 shows the dyed buoyancy production layer viewed from above. Initially the heating was uneven so two-dimensional rolls, single dye clumps and rising thermals are all visible. As the distance between the walls is 30 cm, the inter-thermal spacings are about 1 - 1.5 cm.

The second wave of thermals could not be seen clearly as the new boundary layer was made up of un-dyed fluid. However, after several thermal generation periods an evenly dyed mixed layer was formed.

Sparrow, Goldstein and Husar (1970) used an electrochemical dyeing technique to visualize thermal generation above a heated boundary. The technique involves the use of sodium hydroxide and a pH. - indicator, Thymol-blue. The fluid is made slighly basic so that the indicator is yellow. If electricity is passed through a copper electrode anywhere in the fluid, H^+ ions are liberated. As the fluid at the electrode is now slightly acidic, it turns blue. The motions of the blue fluid can then be observed. An attempt to use this technique during the steady heat flux experimental program had to be abandoned when it became apparent that the basic fluid was attacking the aluminium heating plate.

6.4 RESULTS OF THE UNSTEADY HEAT FLUX EXPERIMENTS

These unsteady heat flux entrainment experiments formed the first part of the experimental program. In the steady heat flux entrainment experiments, which were performed later, there were fewer unsteady factors. They therefore illustrate the behaviour of the

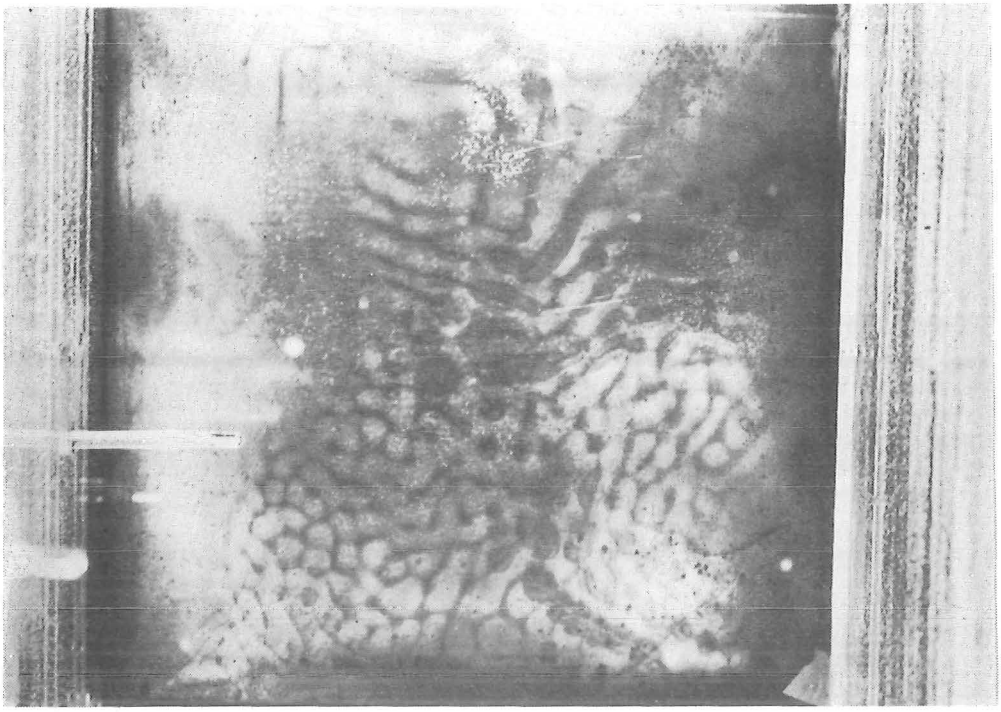

(a) Initial boundary layer motions in the form of two-dimensional rolls which eventually break up into thermal elements.

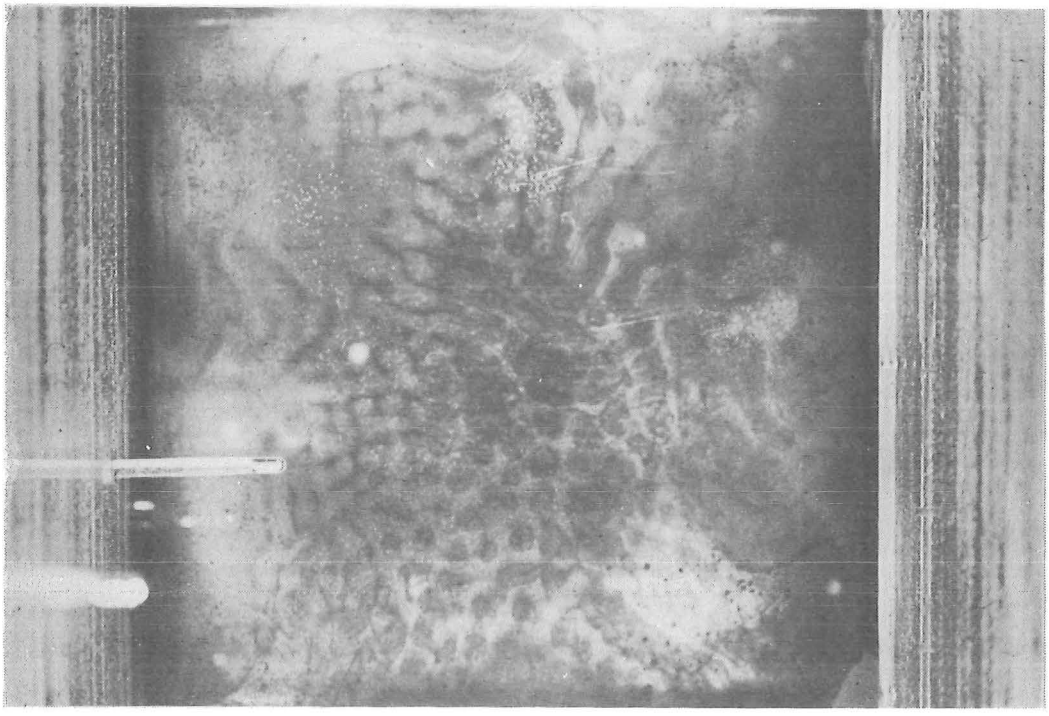

(b) Seconds later showing rising thermals.

Fig. 6.12. View from above of dyed buoyancy production region as convective motions begin.

I.C.P.M. more clearly. It is suggested that the reader initially skip this section and proceed to the discussion of the steady heat flux results (Chapt. 6.5).

6.4.1 Lower Boundary Heat Flux Calibration

A series of non-stratified, single layer convection experiments were performed to calibrate the lower boundary heat flux for given values of ΔT_H and d_m (Table 6.1). From the heat budget for a single convecting layer of thickness d_m (Eqn. 3.5.3)

$$Q_p = (\beta\, d_m + \beta_T)\frac{dT_m}{dt} + (W\, d_m + W_T)(T_m - T_{air})$$

The values of d_m and the heat loss factors (β , β_T , W and W_T) are fixed for individual runs. The heating chamber temperature T_H was also held constant. From the experimental measurements of $T_m(t)$, the buoyancy heat flux Q_p could be calculated.

To keep the convection experiments as steady as possible, the full experimental tank depth was utilized. The range of convection layer depths used was

$$53.1 < d_m < 54.6 \text{ cm}$$

The major variable affecting Q_p was therefore the temperature difference between the mixed layer fluid and the lower boundary, ΔT_p . A sketch of the lower boundary temperature distribution in the unsteady heat flux experiments is given in Fig. 6.1. In the single-layer convection experiments, $d_m = h_T$ so there was no diffusion region.

Because T_H was maintained at an approximately constant value, it is simpler to present Q_p in terms of ΔT_H . Figure 6.13 shows the experimental data from five convection runs in the form Q_p versus ΔT_H . Because the convection layer depths were approximately the same, the data should lie on a single curve.

As discussed in Appendix A, plotting steady state thermal convection data in the form Nu Ra versus Ra reveals the occurrence of heat flux transitions. When the convection layer depth is constant, this form corresponds to a plot of Q_p versus ΔT where, for steady state parallel plate convection, $\Delta T = 2\Delta T_p$. If the Rayleigh number is slowly varying (increasing or decreasing), hysteresis effects may occur in the region of the heat flux transition (Krishnamurti 1970a,b). Because the convection experiments described in this section were highly unsteady, the data will be more scattered and hysteresis effects will be significant.

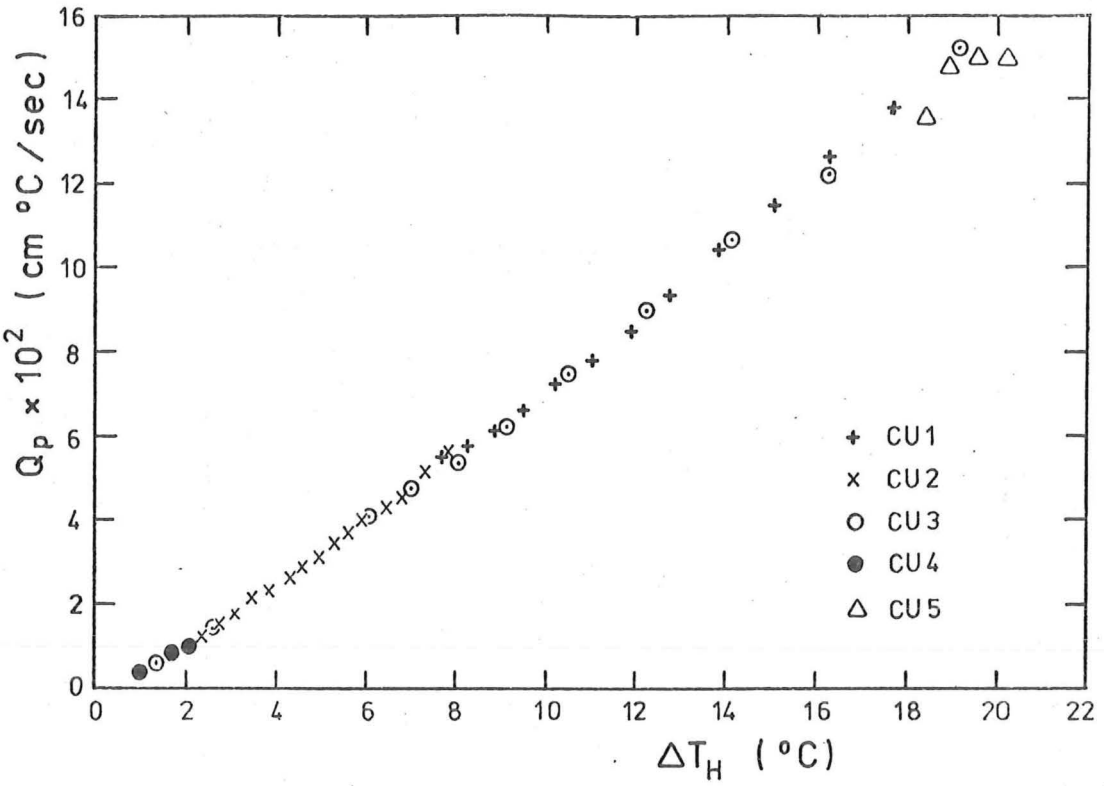

Fig. 6.13. Calibrated lower boundary buoyancy heat flux Q_p for the unsteady heat flux experiments as a function of the temperature difference between the mixed layer and the circulated heating water ΔT_H.

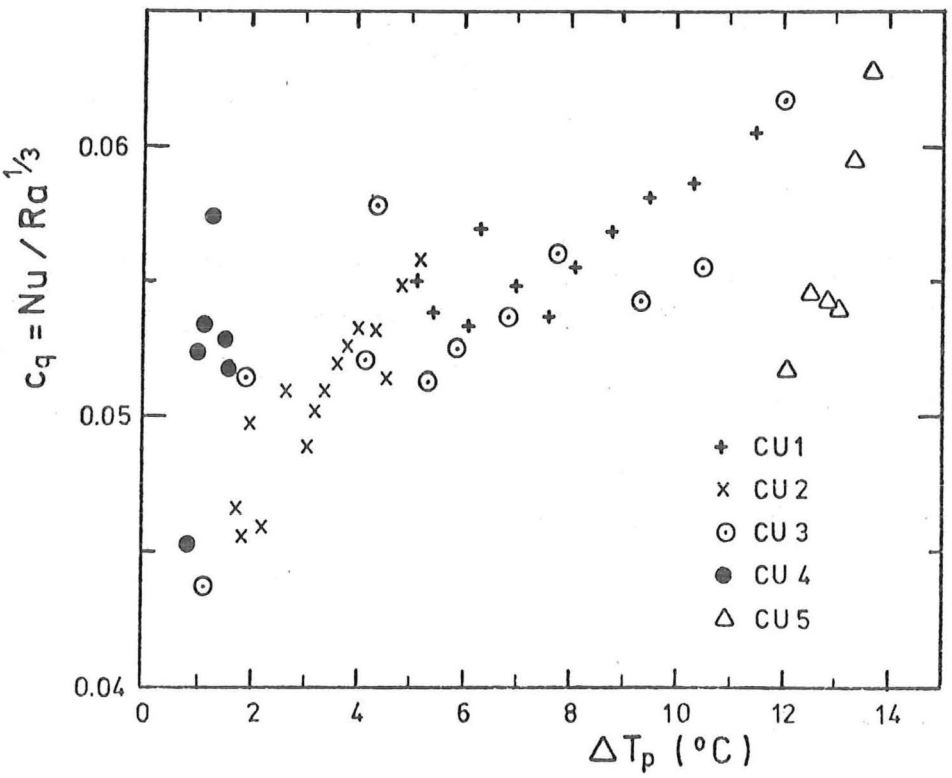

Fig. 6.14. Heat transfer coefficient c_q from the unsteady heat flux convection experiments as a function of the lower plate - fluid temperature difference ΔT_p .

TABLE 6.1 - UNSTEADY HEAT FLUX CONVECTION EXPERIMENTS

Experiment	d_m (cm)	$\overline{T}_H$ (°C)
CU1	54.0	40.1
CU2	53.9	40.0
CU3	54.6	40.0
CU4	54.5	32.4
CU5	53.1	41.3

Hence, the plot of Q_p versus ΔT_H (Fig. 6.13) does not show any obvious heat flux transitions.

To be able to apply the convection calibration results (Fig. 6.13) to the entrainment experiments, the variation of Q_p with mixed layer thickness d_m must be discussed. Whilst the convection layer thickness was kept at approximately 54 cm in the calibration experiments, the mixed layer thickness in the entrainment experiments varied continuously from zero to h_T. During the initial stages of each entrainment experiment, the interface rose rapidly. Hence, the time during which d_m was less than about 6 cm was negligible. The accuracy of the heat flux calibrations for these small values of d_m is therefore not critical.

The variation of Q_p versus d_m for constant ΔT_p and constant fluid properties is represented by a plot of $c_q = Nu/Ra^{\frac{1}{3}}$ versus log Ra (Appendix A). At large Rayleigh numbers, the heat transfer coefficient c_q tends toward a constant c_q asymptote (Fig. A.8). This implies the heat flux becomes independent of the convection layer depth. If the Rayleigh number for the convection calibration experiments is defined by

$$Ra = \frac{\alpha g}{\nu K} (2 \Delta T_p) (2 d_m)^3 \qquad (6.4.1)$$

and the fluid properties are evaluated at $T = T_m$, the experimental range of Ra represented by the data in Fig. 6.13 is

$$5 \times 10^{10} < Ra < 5 \times 10^{11}$$

From Fig. A.8, the variation of c_q with Rayleigh number over this range is small.

For the range of depths in the entrainment experiments (d_m > 6 cm), the Rayleigh numbers were generally greater than 5 x 10^8. The lowest Rayleigh numbers occurred during the initial stages of the entrainment experiments when d_m was low (and ΔT_p high). From Fig. A.8, the heat fluxes during these initial stages may have been up to 10% higher than would be predicted by the convection calibration data (Fig. 6.13). However, it was decided to use Q_p versus ΔT_H data (Fig. 6.13) to calibrate all the unsteady heat flux entrainment experiments. The entrainment experiments were highly unsteady during their initial stages as the three quantities d_m, T_m and Q_p were varying rapidly. Even if the heat fluxes could have been calibrated more accurately for these initial stages, other errors will occur because of the rapidly changing quantities.

For the purposes of the numerical model, an empirical formulae which fitted the data in Fig. 6.13 was required. The experimental range of ΔT_H was typically 3 - 14°C for the major part of each entrainment experiment. For this range, a linear relationship was found to give a good fit. The empirical relationship used in the numerical analyses was

$$Q_p = (7.98\ \Delta T_H - 8.30) \times 10^{-3} \qquad (6.4.2)$$

As the lower boundary plate temperature T_p was measured, the values of c_q for the experimental data shown in Fig. 6.13 could be calculated. The corresponding Nusselt number Nu was defined as

$$Nu = \frac{Q_p\ d_m}{\kappa\ \Delta T_p} \qquad (6.4.3)$$

and all fluid properties were evaluated at $T = T_m$. The definitions of Nu and Ra (Eqns. 6.4.3 and 6.4.1) are consistent with the definitions used to evaluate c_q and Ra from parallel-plate experiments (Appendix A, Fig. A.8).

The experimental values of c_q from the unsteady heat flux convection calibration runs are shown in Fig. 6.14 plotted against ΔT_p. The parameter ΔT_p rather than Ra was chosen to illustrate the time sequence of the data points (ΔT_p decreasing with time). In some cases, the variations of the fluid properties with temperature were sufficient for Ra to initially increase slightly with time.

The c_q data in Fig. 6.14 show a great deal of scatter. As each convection run commenced with a minimum value of T_m and fixed d_m and T_H, ΔT_p decreases with time. Initially, the lower boundary

heat flux was high and the convection experiment was highly unsteady. Hence, the high ΔT_p values are less accurate. Because of a possible thermal convection lag between the cause (ΔT_p) and the effect (dT_m/dt), these values of c_q are likely to be overestimated. Inaccuracies are also likely for low values of ΔT_p. In this case, mixed layer temperatures are high and the heat losses (Q_L) are important. Because Q_p is small any errors in calculating the heat losses will greatly affect the value of c_q. Errors in calculating dT_m/dt will also have a greater effect. If the heat losses are underestimated, c_q is also underestimated.

Only the values of c_q for the medium range of ΔT_p in Fig. 6.12 can be viewed with confidence. Over this range

$$0.050 < c_q < 0.058$$

Over the experimental range of Rayleigh numbers, this range of c_q compares well with other convection data reported in the literature (Fig. A.8). Values of c_q from CU3 and CU4 have been plotted in Fig. A.8 to show the comparison.

Figures 6.13 and 6.14 were plotted in terms of ΔT_H and ΔT_p respectively. A sketch showing the relationship between the two temperature differences is given in Fig. 6.1a. Typically, the ratio of these terms was

$$0.62 < \Delta T_p/\Delta T_H < 0.72$$

although as $\Delta T_H \rightarrow 0$, the ratio became much larger.

6.4.2 Entrainment Experiments

The experimental data from a typical unsteady heat flux run (EU4) are shown in Fig. 6.15. Temperature (°C) versus time (minutes) data for integer (centimetre) heights above the heated boundary are plotted in Fig. 6.15a. This corresponds with the method of data collection. Only temperature data measured with the vertically traversing thermocouple probe are plotted. Additional values of T_m and T_a obtained from the side-mounted probes (at $z = 8$ and 41 cm) were, however, used to define the mixed layer and maximum temperature curves (Fig. 6.1a). The height contour curves represent the best fit by eye through the available data. Also shown in Fig. 6.15a is the corresponding variation in the interface height d_m, obtained from the temperature - time plot. Values of ΔT_H and the corresponding input heat flux Q_p (evaluated from Fig. 6.13) are plotted in Fig.6.15b.

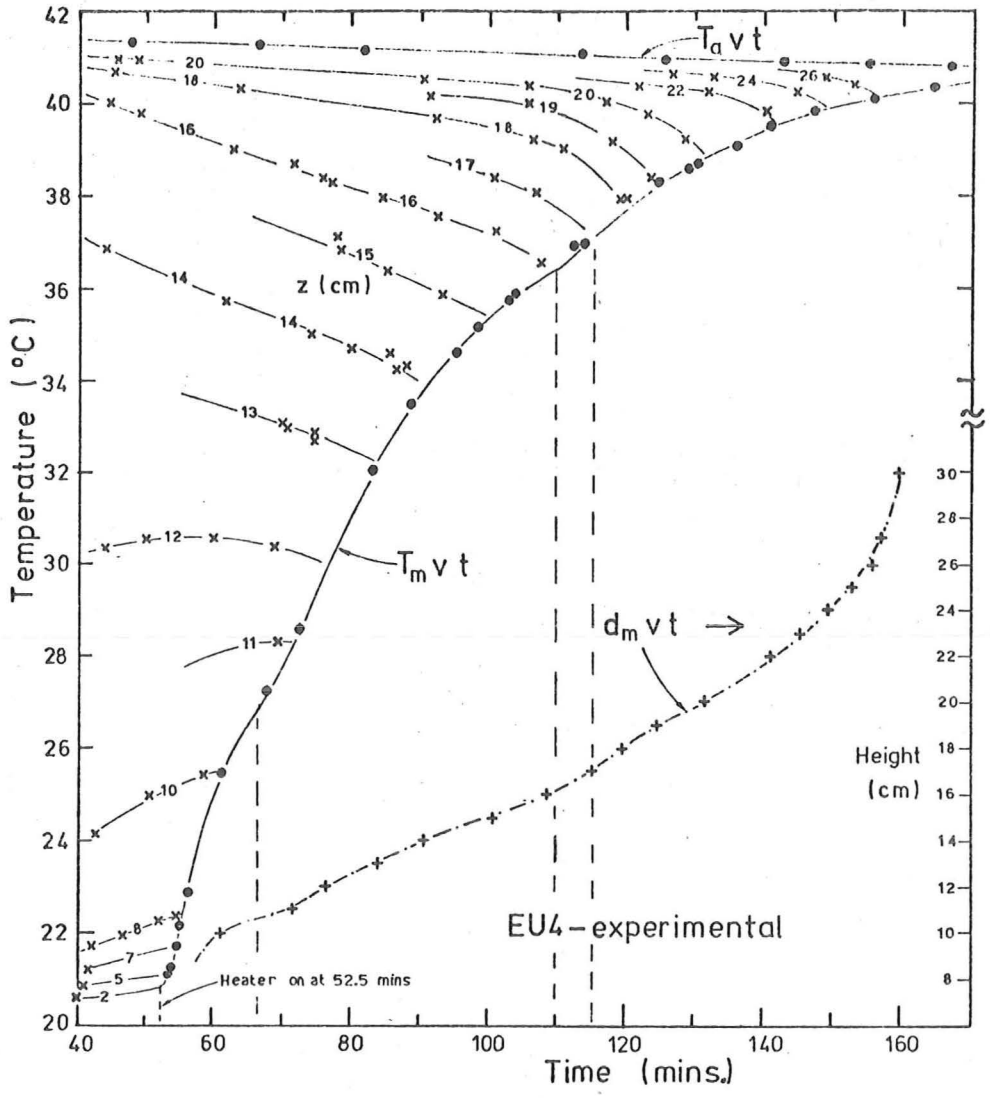

(a) Temperature versus time graph. Contour labels give height in centimetres. Interface height d_m as a function of time is also plotted.

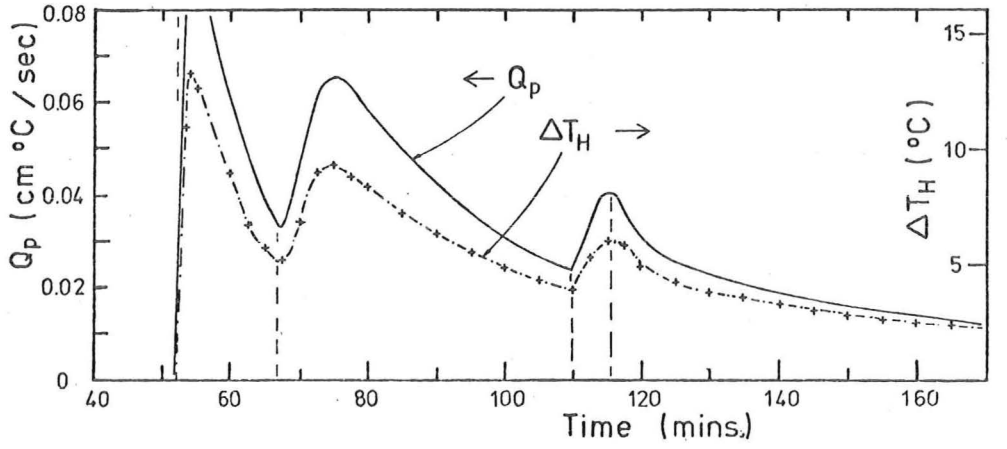

(b) Lower boundary buoyancy heat flux Q_p as a function of time.

Fig. 6.15. Entrainment data from unsteady heat flux experiment EU4.

In preliminary tests it was found that, if the heat flux became too small, the convective motions within the mixed layer became too weak to maintain turbulent motions up to d_m. With the thermal elements failing to reach the interface, molecular diffusion became important and smoothing of the interfacial temperature profile occurred. For significant interfacial temperature gradients, this breaking down of penetrative convection at the interface occurred when $\Delta T_H < 2.5°C$. To confine the experimental investigation to the fully turbulent mixed layer case, T_H was increased to a higher value whenever ΔT_H approached 2.5°C. The times when T_H was adjusted, by altering the temperature controller setting, are indicated in Fig. 6.15a,b (vertical dashed lines).

For the unsteady heat flux entrainment experiment EU4 (Fig. 6.15), the maximum and minimum temperatures at $t = 40$ minutes were $T_a = 41.5\ °C$ and $T_m = 20.5\ °C$. The height of maximum temperature gradient d_g was approximately 12.2 cm. The origin of the time scale in Fig. 6.15 has been set so that the maximum temperature gradient at $t = 40$ minutes corresponds with the value predicted from molecular diffusion theory (Eqn. 3.4.7). At $t_s = 52.5$ minutes the circulation pump for the heating water was switched on and heating commenced. Generally, the water in the heating reservoir (Figs. 6.2 and 6.6) was preheated above the prescribed value of T_H. This reduced the time lag between the switching on of the circulation pump and the heating chamber temperature reaching T_H.

As in the numerical analysis of an unsteady heat flux entrainment experiment discussed earlier (Chapt. 4.5), the temporal variation of the temperature data from experiment EU4 is highly irregular because of the variation of Q_p. Immediately after the commencement of heating, and after T_H had been increased at 66½ and 110 minutes, the mixed layer temperature increased rapidly. At the same times, the intermittency region temperatures were rapidly decreasing. However, as Q_p decreased, the rates of change of temperature decreased. The mixed layer thickness d_m also increased more rapidly when Q_p was a maximum, although V_{em} is also dependent on the magnitude of the interfacial gradient $(\partial T/\partial z)_i$.

Vertical temperature profiles for EU4 are plotted in Fig. 6.16. Just as the curves of T_m v t and d_m v t are irregular due to variations in T_H, so too is the minimum temperature envelope d_m v T_m.

Figure 6.17 shows the vertical buoyancy heat flux profile for

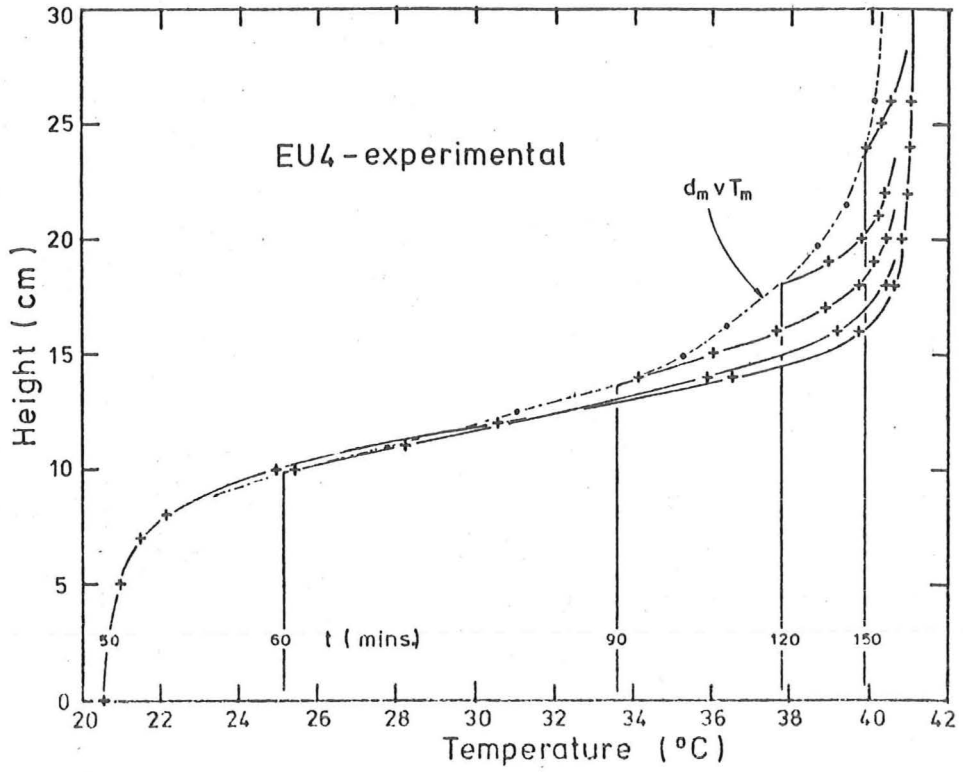

Fig. 6.16. Vertical temperature profiles from entrainment experiment EU4. Profile labels give time in minutes. Locus of mixed layer thickness and temperature is also shown.

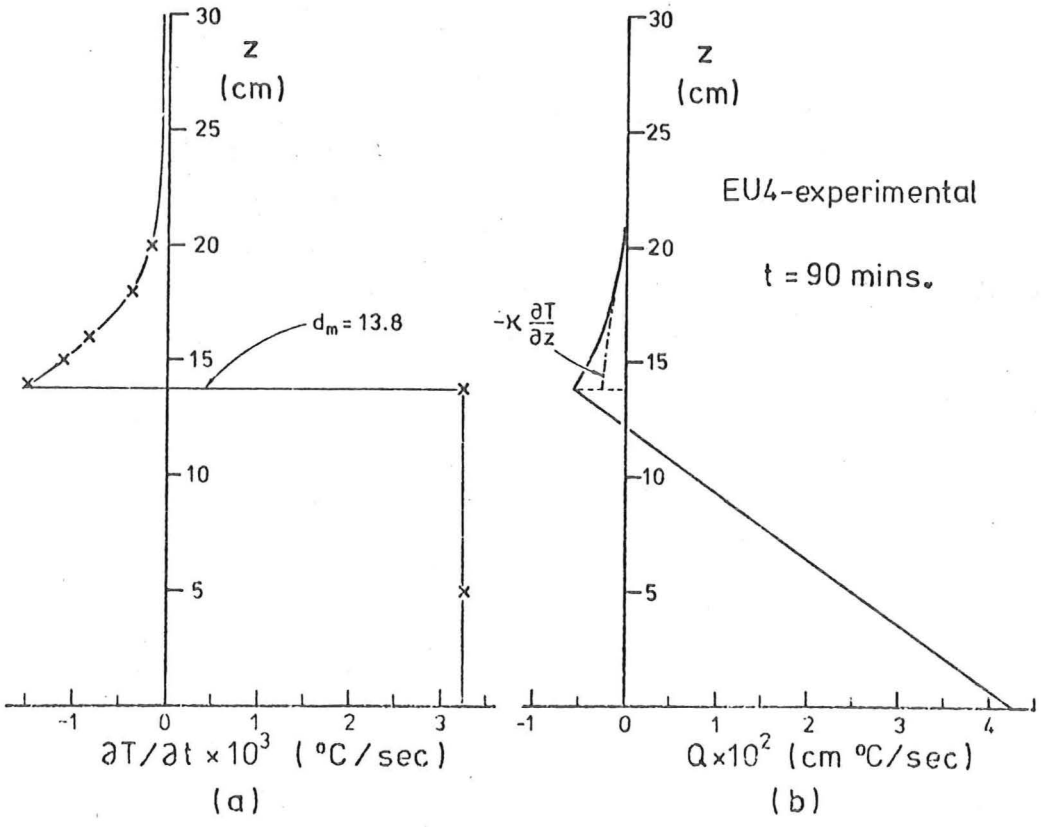

Fig. 6.17. (a) Rate of change of temperature profile from entrainment experiment EU4 at t = 90 minutes, and (b) the buoyancy heat flux profile derived from it.

EU4 at $t = 90$ mins., and the vertical profile of $\frac{\partial T}{\partial t}$, from which it was derived. The procedure for obtaining vertical heat flux profiles from experimental data is outlined in Chapt. 6.5.2. The heat flux in the diffusion region due to molecular diffusion alone ($- \kappa \frac{\partial T}{\partial z}$) is also shown (Fig. 6.17b).

For this particular example, EU4 at $t = 90$ mins., the interfacial and lower boundary heat fluxes were $Q_e = -6 \times 10^{-3}$ cm °C/sec and $Q_p = 0.043$ cm °C/sec. The entrainment ratio k_e (Eqn. 4.2.6) was therefore 0.14.

It is possible at this stage to use the experimental values of d_m, Q_p and $(\partial T/\partial z)_i$ to evaluate the empirical I.C.P.M. equations for E and k_e (Eqns. 4.4.2 and 4.3.4). At $t = 90$ minutes in experiment EU4, $d_m = 13.8$ cm and $(\partial T/\partial z)_i = 1.85$ °C/cm. Using the fluid properties given in Table 4.1, the values of $Ri = 16.1$ and $Pe = 250$ are obtained. From Eqn. 4.4.2 when $\lambda_i = 0$, $E = 8.3 \times 10^{-3}$. The resulting value of k_e from Eqn. 4.3.4 is

$$k_e = E\,Ri = 0.13$$

The experimental value of k_e and the value predicted by the empirical I.C.P.M. formulae are in good agreement for this particular example (EU4 at $t = 90$ minutes). However, it will be shown later (Chapter 7) that when the rate of rise of the interface is large ($d_m \ll d_{g0}$ or $d_m \gg d_{g0}$) the empirical I.C.P.M. formulae (e.g. Eqn. 4.4.2) do not predict the experimental results so successfully.

A final graph of the experimental results of EU4 shows the mixed layer thickness d_m as a function of ΔT_i plotted on a log-log plot (Fig. 6.18). It follows from Eqn. 5.5.2, that the slope of the data is approximately equal to $-k_m/(1 + k_e)$. For times when the interfacial temperature gradients were significant and T_H was constant, the data curve is approximately linear. For $80 < t < 110$ mins., the slope of the data is about -0.34 whilst for $120 < t < 150$ mins. the slope is approximately -0.23. This apparent constancy of slope (and hence constancy of k_m) has been reported by Denton and Wood (1974) and Jenkins (1974). As discussed in Chapter 5, it is caused by the specific lower boundary heat flux conditions (constant T_H) and is not a general result.

At $t = 90$ mins., in EU4, the rate of rise of the interface $V_{em} = 2.1 \times 10^{-3}$ cm/sec. Other major quantities were $\Delta T_i = 7.4$ °C, $Q_p = 0.043$ cm °C/sec., $d_m = 13.8$ cm and $d_h = 16.2$ cm. Hence, for $\beta = 1.08$, equations 5.1.2 and 5.3.6 yield

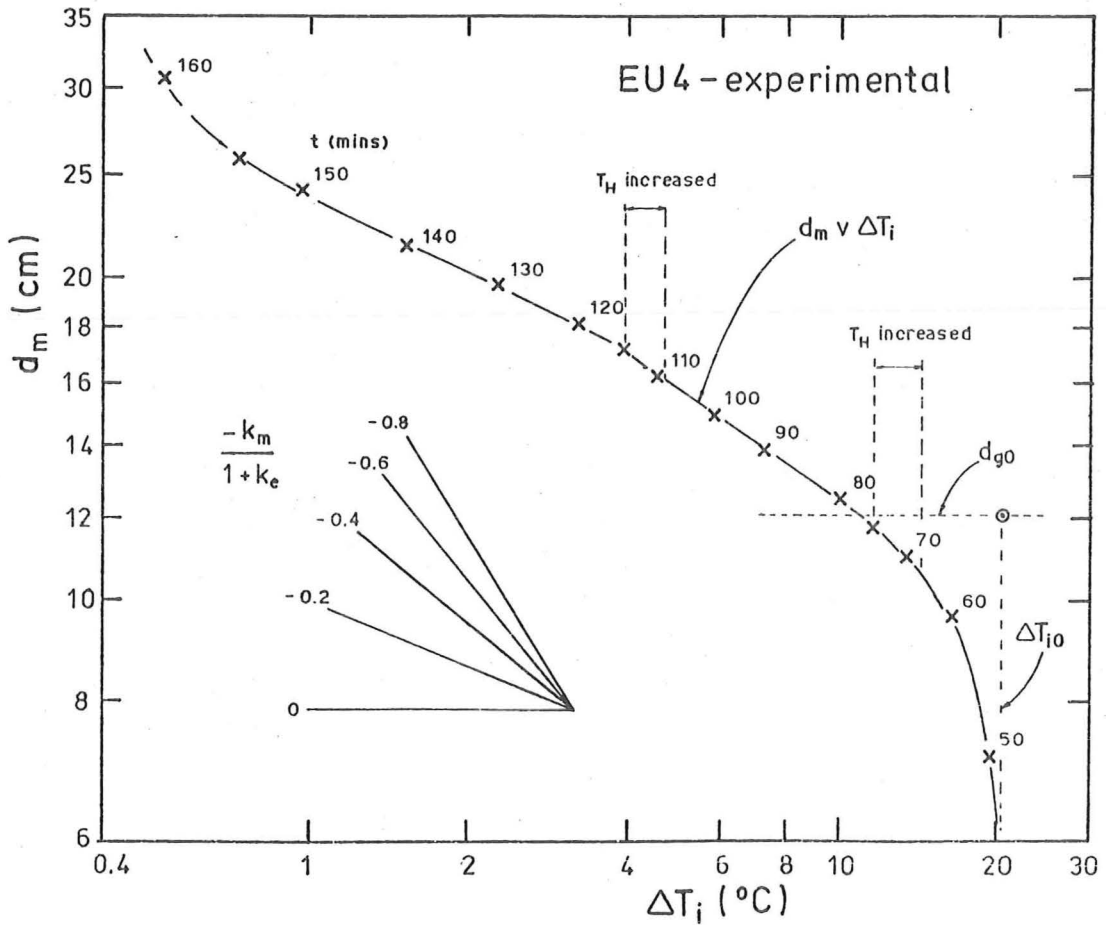

Fig. 6.18. Logarithm of the interface height d_m versus the logarithm of the interfacial temperature difference ΔT_i from entrainment experiment EU4. Data point labels give time in minutes.

$$k_m = 0.39 \ , \quad k_h = 0.34$$

From the value of k_e given above

$$\frac{- k_m}{1 + k_e} = - 0.34$$

which is consistent with the slope of the log d_m versus log ΔT_i curve (Fig. 6.18).

A numerical analysis of EU4 is discussed in Chapt. 7.4. Further unsteady heat flux experimental results have been included in the appendices (Appendix I). Because the unsteady heat flux experiments were too unsteady to illustrate the penetrative convection process clearly, the data have not been analysed further. The time axes of the data in Appendix I are related to the origin used during each experiment and are not related to a virtual I.C.P.M. time origin.

6.5 RESULTS OF THE STEADY HEAT FLUX EXPERIMENTS

The steady heat flux experiments proved more useful in gaining an understanding of the penetrative convection process. Because the external source of turbulent kinetic energy, buoyancy and heat, Q_p , was constant, the temporal behaviour of the system was greatly simplified.

6.5.1 Lower Boundary Heat Flux Calibration

In the steady heat flux experiments, the lower boundary heat flux was controlled by keeping the temperature difference across the glass layer ΔT_G constant (Chapt. 6.2.3). The heat flux per unit area through the glass layer q_G is given by

$$q_G = K_G \, \Delta T_G \qquad (6.5.1)$$

where K_G is the thermal conductivity per unit thickness of the glass layer. For constant ΔT_G , the glass heat flux was also constant. Calibrations of the control circuit were made to determine the thermopile output voltages at which the power switched off.

From the known thermocouple outputs (0.0415 mV/°C), the temperature difference across the glass layer ΔT_G for each control circuit setting could be calculated. Individual temperature measurements, using thermocouples above and below the plate, could also be used to calculate ΔT_G . However, the thermal properties of glass as listed in Table D.1 are only approximate. Equation 6.5.1 could not be used to calculate q_G accurately.

It was therefore necessary to calibrate the heating apparatus by performing a series of single layer convection experiments. This is similar to the method used to calibrate the unsteady heat flux apparatus (Chapt. 6.4.1). For a single layer of depth $d_m = h_T$, the lower boundary buoyancy heat flux Q_p is given by Eqn. 3.5.3.

$$Q_p = (\beta d_m + \beta_T) \frac{dT_m}{dt} + (W d_m + W_T)(T_m - T_{air}) \qquad (6.5.2)$$

This is the heat budget for the fluid column and insulation material above $z = 0$. To obtain the glass layer heat flux q_G in terms of q_p (where $q_p = \rho c_p Q_p$), allowance must be made for heat storage in the upper aluminium plate, its insulation and half the glass layer. Taking a second heat budget for the region between $z = 0$ and mid-height of the glass layer yields

$$q_G = q_p + S_p \frac{dT_p}{dt} + W_p (T_p - T_{air}) \qquad (6.5.3)$$

where S_p is the total heat storage of the region divided by A. It should be noted that as the plan dimensions of the glass layer and the fluid column were both 30 cm x 30 cm, area A is the same for both. The heat loss factor W_p accounts for heat losses from the region.

In the convection experiments, two glass heat flux settings (H1 and H2) were calibrated. The higher setting H2, used exclusively for the entrainment experiments, was chosen to yield $Q_p \simeq 0.023$ cm °C/sec. This corresponded to a medium buoyancy heat flux in the earlier unsteady heat flux experiments. At higher values of Q_p the mixed layer temperatures would increase much faster causing the experiments to be too unsteady. In the earlier unsteady heat flux experiments, the interfacial entrainment process appeared to break down at low heat fluxes ($Q_p < 0.012$ cm °C/sec). This is discussed in Chapt. 6.4.2. The value of Q_p corresponding to the lower setting H1 was just above this range.

As the convection layer thickness d_m is constant and the variations in fluid properties with temperature are neglected, thermal convection theory (Appendix A) gives

$$Q_p \propto \Delta T_p$$

As q_G is held constant, Eqns. 6.5.2 and 6.5.3 imply that, apart from minor heat loss effects, the rate of increase of the mixed layer temperature is constant. It also follows that the lower boundary heat flux Q_p and ΔT_p remain constant. Hence

$$\frac{dT_p}{dt} = \frac{dT_m}{dt} \qquad (6.5.4)$$

Using Eqns. 6.5.2, 6.5.3 and 6.5.4, q_G may be calibrated from measurements of $T_m(t)$. The heat storage term S_p can be calculated from the measured volumes of the materials and their thermal properties (Table D.1). The volume of the upper aluminium plate was 2630 cm^3 and the volume of half of the glass layer was 97.7 cm^3. Of the insulation, only the asbestos-cement boards adjacent to the aluminium were included in the S_p calculation. The value obtained was $S_p = 1.89$ cal/cm^2°C. The heat loss factor W_p was calculated from the thermal conductivities of the insulation (Table D.1), and applied over the region thickness (2.45 cm). For the calculated value of $W_p = 3.8 \times 10^{-6}$ cal/sec cm^2°C, the heat losses typically amounted to less than 0.2% of q_G .

Because the calculated value of S_p could not be checked by an independent calibration, several convection layer depths were tested for each of the glass heat flux settings. As d_m changed, so did dT_m/dt and hence, the proportion of the glass heat flux being lost to storage in the aluminium varied. The contribution of the S_p term to the constant q_G was therefore different in each case.

During preliminary testing of the equipment, the no fluid case ($d_m = 0$) was also tested. The top of the aluminium plate ($z = 0$) was insulated and the system heated. Hence, from Eqn. 6.5.3

$$q_G = S_p \frac{dT_p}{dt} + W_p (T_p - T_{air}) \qquad (6.5.5)$$

where the heat loss term W_p is slightly larger because of heat losses across $z = 0$. The power was then switched off and the system allowed to cool. The upper aluminium plate and the lower heating block rapidly adjusted to the equilibrium state

$$\Delta T_G = q_G = 0$$

Hence for the cooling stage

$$0 = S_p \frac{dT_p}{dt} + W_p (T_p - T_{air}) \qquad (6.5.6)$$

If equations 6.5.5 and 6.5.6 are evaluated as the block heats and cools through the same temperature T_p , then

$$q_G = S_p \left[\left.\frac{dT_p}{dt}\right|_{heat} - \left.\frac{dT_p}{dt}\right|_{cool} \right] \qquad (6.5.7)$$

Equation 6.5.7 can only be used in conjunction with the other calibrations of q_G using various fluid depths. Evaluating S_p from Eqn. 6.5.6 leads to large errors as both dT_p/dt and the heat losses are small.

TABLE 6.2 - RESULTS OF THE GLASS HEAT FLUX CALIBRATIONS

Heat Flux Setting	Experiment	d_m (cm)	$T_m - T_{air}$ (°C)	q_G ($\frac{cal}{sec\ cm^2} \times 10^2$)	ΔT_p (°C)
H2	CS1	12.9	9.5	2.65	2.7
	CS2	29.2	1.2	2.68	3.3
	CS3	34.2	7.7	2.63	3.1
	ES1	55.1	20.3	2.61	2.9
	ES4	54.8	17.7	2.63	2.9
H1	CS4	10.2	2.5	1.74	2.2
		"	7.9	1.68	2.2
	CS5	20.3	7.0	1.71	2.3
		"	14.0	1.66	2.0
	CS6	30.2	8.8	1.73	2.0
		"	10.4	1.70	2.1

The glass heat flux calibrations results for the two settings H1 and H2 are given in Table 6.2. Additional results obtained from several entrainment runs which reached the single-layer convection period ($t > t_T$, $d_m = h_T$), are also given. As discussed above, the rate of change of T_m is almost constant for each value of d_m and q_G, if the heat losses are small. The values of ΔT_{air}, q_G and ΔT_p given in Table 6.2 are those for one or two representative times during a convection run. The experimental measurements were not sensitive enough to allow an accurate and independent evaluation of the heat loss factors. The values of q_G for runs at the same heat flux setting were consistent to within ±3% in both cases.

However, it was found that there was some correlation between the values of q_G and the temperature differences between the experimental apparatus and the outside air ($T_m - T_{air}$ and $T_p - T_{air}$). This suggested that there were additional heat losses which had not been allowed for. These could have been fluid column losses (which would also be dependent on d_m) or losses from the heating apparatus. Gaps between the various sheets of insulation materials would have increased

the heat losses. To remove some of the scatter in the values of q_G (Table 6.2), an empirical heat loss term $W_{ex}\ (T_p - T_{air})$ was added to equation 6.5.3. The value of W_{ex} was set at 2.6×10^{-5} cal/sec cm^2 sec. Hence, Eqn. 6.5.3 is rewritten as

$$q_G = q_p + S_p \frac{dT_p}{dt} + (W_p + W_{ex})(T_p - T_{air}) \qquad (6.5.8)$$

When this additional heat loss term was allowed for, the average values of q_G for H1 and H2 were

$$q_G = 0.0173\ ,\ 0.0268 \text{ cal/sec cm}^2$$

respectively.

An approximate check on these values was obtained from Eqn. 6.5.1. From the control circuit calibration, it was found that the heater switched on when the thermopile outputs were 0.292 mV (H1) and 0.449 mV (H2) . As the output of individual thermocouples was 0.0415 mV/°C, the eight thermocouple thermopile had an output of 0.166 mV/°C. The glass thickness was 0.217 cm and the typical thermal conductivity of soda glass is 2.3×10^{-3} cal/sec cm °C (Table D.1). Hence,

$$K_G \approx 0.0106 \text{ cal/sec cm}^2\text{°C}.$$

From Eqn. 6.5.1, the two glass heat fluxes for H1 and H2 are

$$q_G = 0.0186\ ,\ 0.0287 \text{ cal/sec cm}^2$$

respectively. These values are approximately 8% higher than the calibrated values. Alternatively, both sets of results suggest the thermal conductivity of the glass layer was actually $K_G = 9.9 \times 10^{-3}$ cal/sec.cm^2 °C .

If heat losses from the fluid are underestimated, the method of evaluating q_G from the rate of increase of the convection layer temperature T_m , according to Eqns. 6.5.2 and 6.5.8, underestimates q_G . However, when the process is reversed to calculate the rate of increase of T_m from q_G , as in the numerical analyses, the undervalued glass heat flux largely compensates for the underestimated heat losses.

6.5.2 Entrainment Experiments

Three entrainment experiments were performed using heat flux setting H2 ($q_G = 0.0268$ cal/sec cm^2). The initial conditions for the three experiments are given in Table 6.3. In all three cases the height of the fluid column was the maximum value $h_T \approx 55$ cm. To make

TABLE 6.3 - STEADY HEAT FLUX ENTRAINMENT EXPERIMENTS

Experiment	Heat Flux Setting	d_{g0} (cm)	T_{a0} (°C)	T_{m0} (°C)	ΔT_{i0} (°C)
ES1	H2	10	40.1	17.7	22.4
ES2	"	13.9	39.2	20.5	18.7
ES3	"	23.6	38.4	10.0	28.4

the best use of the experimental apparatus, the value of ΔT_{i0} should also be as large as possible. Because of thermal expansion problems, the perspex container walls could not be heated above 42°C. This set an upper limit on T_{a0}. The fluid used for the lower layer can be cooled below room temperature provided T_{m0} is well above the maximum density temperature for water of about 4°C. Hence, the maximum value of ΔT_{i0} is also limited. The only other quantity required to define the initial conditions was the thickness of the lower layer d_{g0} (Eqn. 3.1.3).

It should be noted that the initial conditions prior to the commencement of heating are also determined by the time t_s. This describes the thickness of the density gradient region centred at height d_{g0}. In all the entrainment experiments, the heating apparatus was switched on as soon as possible after the filling of the tank was completed.

The chosen value of d_{g0} has a major influence on the temporal behaviour of an entrainment experiment. If d_{g0} is too small, the interfacial entrainment period is short and the temperature changes are too rapid. When d_{g0} is large, the interfacial period is much longer. However, if d_{g0} is too great, upper boundary effects in the diffusion region will be significant.

In this discussion of the steady heat flux entrainment experiments, the results of experiment ES2 will be presented. The lower layer thickness $d_{g0} = 13.9$ cm and initial temperature difference of $\Delta T_{i0} = 18.7$°C, for this experiment, yielded an interfacial entrainment period of about three hours. The results of the shorter experiment ES1 and much longer experiment ES3 will be presented, together with their respective numerical analyses, in Chapter 7. The experimental temperature data for ES2 are presented in Fig. 6.19 as a plot of temperature

versus time with contours of constant height. Only the temperatures measured with the vertical thermocouple probe are plotted. Additional values of T_a and T_m, measured with the side-mounted probes (at z = 8 and 41 cm), were also used to define the mixed layer and maximum temperature curves (Fig. 6.1b). The height contour curves are the best fit by eye through the available data. As discussed earlier (Chapt. 6.3.2), each temperature reading typically took about 30 seconds. This reduced the amount of temperature data that could be obtained during an experiment. The limit bars on the data in the intermittency region show the maximum or minimum range of temperature fluctuations which occurred during a fixed height reading. Also shown in Fig. 6.19, is the variation of d_m with time, which was derived from the temperature-time plot. The time scale was set to a virtual origin by comparing the temperature profile at t = 70 mins. with the solution for the molecular diffusion equation (Eqn. 3.4.7). Heating commenced at t_s = 73 mins.

The temporal behaviour of this steady heat flux experiment was similar to the numerical analysis example described earlier (Chapt. 4.5, Fig. 4.8). The temperature changes at any fixed height within the diffusion region were initially due to molecular diffusion and heat losses. Whether the fluid was cooling or increasing in temperature, the rate of change of temperature decreased. For example, at z = 17 cm in experiment ES2 (Fig. 6.19) the rate of cooling was decreasing until $t \approx 150$ mins. At this time, the interface was only 2 cm below height z = 17 cm and the fluid began to be affected by the penetrating interfacial domes. The net cooling effect of the interfacial dome motions increased as the interface rose. This is shown by the increasing rate of cooling at height z = 17 cm for $150 < t < 176$ mins. (Fig. 6.19). After t = 176 mins., however, the fluid at height z = 17 cm was part of the mixed layer and the temperature (T_m) increased. Because the thickness of the mixed layer is increasing, the rate of increase of the mixed layer temperature T_m slowly decreases.

Vertical temperature profiles from ES2 also illustrate the temporal behaviour of this steady heat flux entrainment experiment (Fig. 6.20). A comparison between numerical analyses of experiment ES2 and the experimental data is presented in Chapter 7.

Buoyancy heat flux profiles may be obtained from the experimental data in the following manner. From Eqn. 3.4.1

$$\frac{\partial Q}{\partial z} = - \beta \frac{\partial T}{\partial t} - W (T - T_{air}) \qquad (6.5.9)$$

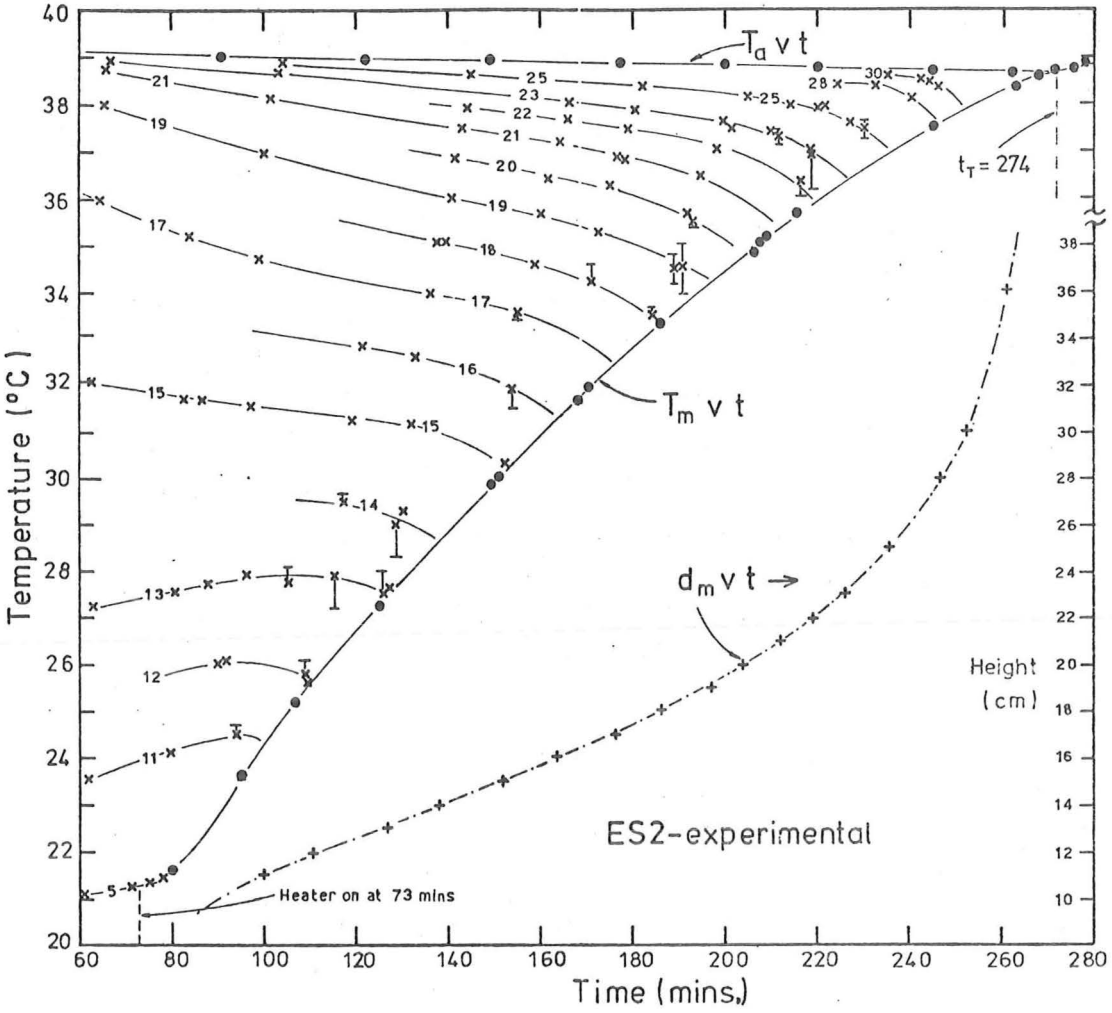

Fig. 6.19. Temperature versus time graph of data from steady heat flux entrainment experiment ES2. Contour labels give height in centimetres. Interface height d_m as a function of time is also plotted.

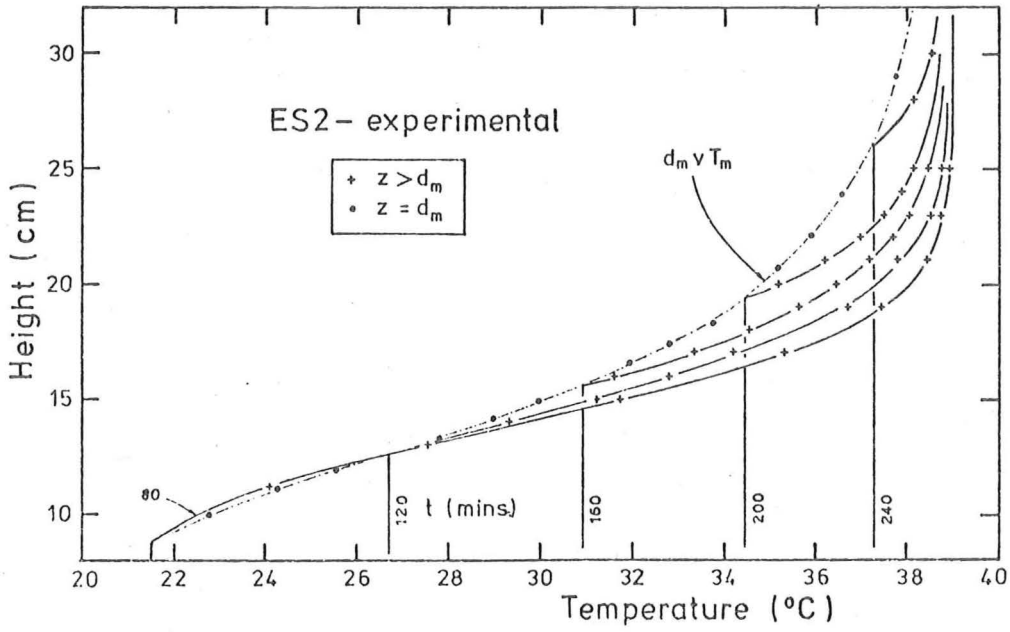

Fig. 6.20. Temperature profiles from entrainment experiment ES2. Profile labels give time in minutes. Locus of mixed layer thickness and temperature is also shown.

Integrating with respect to height from $z = 0$ to z yields

$$Q(z) = Q_p - \beta \int_o^z \frac{\partial T}{\partial t} dz - W \int_o^z (T - T_{air}) dz \qquad (6.5.10)$$

By evaluating this equation at any time t, a vertical profile of the buoyancy heat flux Q may be obtained.

The first term on the right hand side of Eqn. 6.5.10, Q_p, is evaluated from the convection calibration equation (Eqn. 6.5.8). Evaluating the second term requires the integration of the vertical profile of the partial derivative of temperature with respect to time $\partial T/\partial t$. By measuring the slope of the constant height contours on a temperature versus time graph (e.g. Fig. 6.19), at constant time, discrete values of $\partial T/\partial t$ and the value of dT_m/dt can be obtained. These can then be used to plot the required $\partial T/\partial t$ profile. Figure 6.21a shows a vertical profile of $\partial T/\partial t$ for ES2 at $t = 170$ minutes. At this time, the interface height was $d_m = 16.6$ cm. When the interface is not at an integer (centimetre) height, the value of $(\partial T/\partial z)_i$ must be obtained by extrapolating the data. This is an obvious source of error.

The first integral on the right hand side of Eqn. 6.5.10 is evaluated by graphically integrating the area under the $\partial T/\partial t$ profile using Simpson's rule. A similar procedure is required to evaluate the second integral on the right hand side of Eqn. 6.5.10, using the vertical temperature profile (e.g. Fig. 6.20). Both integrations are simple for $0 < z < d_m$ as the mixed layer temperature is uniform with height.

Equation 6.5.10 evaluated at $z = h_T$ should be approximately equal to the heat loss through the upper boundary $W_T(T_a - T_{air})$. As β_T is not accounted for in Eqn. 6.5.9, the two heat fluxes are not exactly equal.

Figure 6.21b shows the resulting buoyancy heat flux profile for ES2 at $t = 170$ mins. The buoyancy heat flux curve due to molecular diffusion in the diffusion region $\left(-\kappa \frac{\partial T}{\partial z}\right)$ is also plotted. From the values of $Q_p = 0.023$ cm °C/sec and $Q_e = -4 * 10^{-3}$ cm °C/sec at $t = 170$ minutes, the value of k_e is 0.17. Molecular diffusion contributed 77% of the interfacial heat flux Q_e.

From the experimental values of d_m, Q_p and $(\partial T/\partial z)_i$, the values of E and k_e predicted by the empirical I.C.P.M. equations (Eqns. 4.4.2 and 4.3.4) can be evaluated. At $t = 170$ minutes in

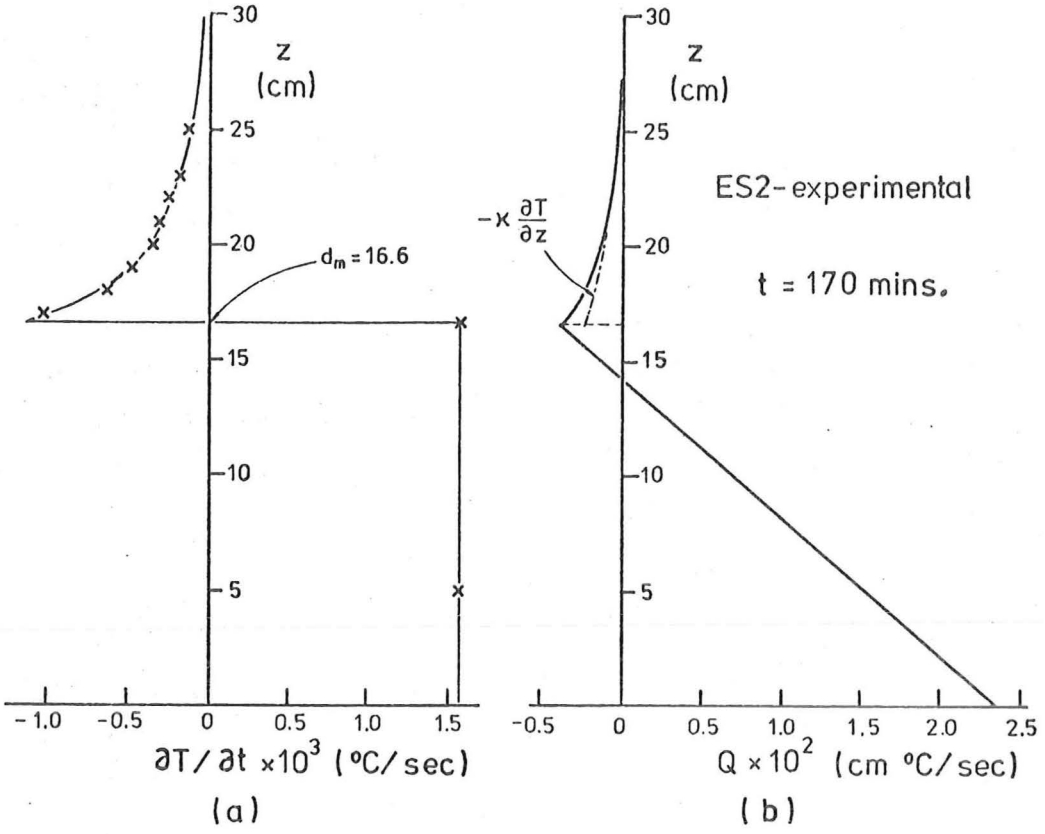

Fig. 6.21. (a) Rate of change of temperature profile for entrainment experiment ES2 at t = 170 minutes , and (b) the buoyancy heat flux profile derived from it.

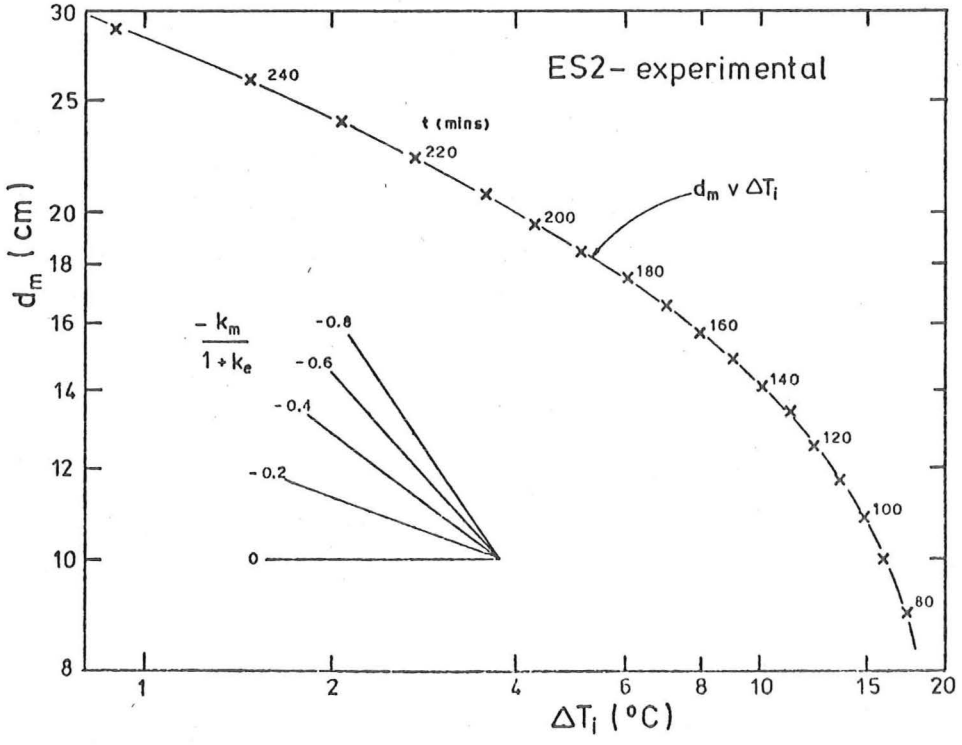

Fig. 6.22. Logarithm of the interface height d_m versus the logarithm of the interfacial temperature difference ΔT_i from entrainment experiment ES2. Data point labels give time in minutes.

the entrainment experiment ES2, d_m = 16.6 cm and $(\partial T/\partial z)_i$ = 2.03 °C/cm. Using the fluid properties listed in Table 4.1, Ri = 33.1 and Pe = 260. It follows from Eqn. 4.4.2 that if $\lambda_i = 0$, $E = 5.3 \times 10^{-3}$. From Eqn. 4.3.4, the corresponding value of k_e is 0.18. Whilst the agreement between the value of k_e from the empirical I.C.P.M. formulae and the experimental heat fluxes is good at this particular time (t = 170 mins. for ES2), the agreement is not always good. It will be shown later (Chapter 7) that when the rate of rise of the interface is large ($d_m << d_{g0}$ or $d_m >> d_{g0}$), the empirical I.C.P.M. formulae (e.g. Eqn. 4.4.2) do not predict the experimental results so successfully.

Figure 6.22 shows a plot of log d_m versus log ΔT_i from the steady heat flux entrainment experiment ES2. The data point labels give the time in minutes. As discussed in Chapt. 5.5, the slope of the data curve at any time t is $-k_m/(1 + k_e)$. For the specific case discussed above (t = 170 minutes), $V_{em} = 1.5 \times 10^{-3}$ cm/sec and the interfacial temperature difference ΔT_i = 7.0 °C. For β = 1.08 (Table 4.1) and the experimental lower boundary heat flux Q_p = 0.023 cm °C/sec, the value of k_m was 0.49. Hence, at this time, k_m was almost three times the value of k_e = 0.17. For these values of k_e and k_m, the slope of the log ΔT_i plot at t = 170 mins. should be −0.42. This appears to be consistent with the slope of the data curve in Fig. 6.22.

As the mean profile height d_h at t = 170 mins in ES2 was approximately 19.7 cm, it follows from Eqn. 5.3.6 that k_h = 0.43. The corresponding plot of log d_h versus log ΔT_i has not been presented as d_h is only useful in simplifying the theoretical equations and has no real practical value. To evaluate the mean profile height d_h from experimental data, requires the numerical integration of individual temperature profiles. Hence, the derived value of d_h is less accurate than the corresponding value of d_m.

The experimental results of the two other steady heat flux entrainment experiments ES1 and ES3 are discussed in Chapter 7 in conjunction with their respective numerical analyses.

6.6 DISCUSSION OF EXPERIMENTAL ERRORS

In the experimental investigation the temporal behaviour of the I.C.P.M. was measured in terms of the variation of temperature with time and height. The accuracy of the vertically traversing thermocouple probe and the other thermocouples was an important factor.

Some difficulty was experienced in maintaining the reference junction of the thermocouples at 0°C in the ice bath. However, the absolute temperature was only necessary for heat loss calculations. In most other applications, the partial derivatives of temperature with respect to time or height were required. The variation of T_{air} outside the experimental apparatus with respect to position and time, and uncertainties about the values of the heat loss terms (β , β_T , W , W_T), probably made greater contributions to the heat loss calculation errors.

The thermocouple amplifiers and digital voltmeters, which measured the thermocouple output, were susceptible to thermal drift. The low e.m.f. switching of the thermocouple output was another source of error. However, the thermocouple measurement system was continually checked against a zero input signal and re-zeroed where necessary.

The temperature data could also be affected by inaccurate setting of the measurement height. If, for example, the temperature gradient was 1 °C/cm , a positional error of 0.1 cm would give a 0.1 °C error in the temperature measurement.

However, the temperature fluctuations occurring within the mixed layer and in the intermittency region (Fig. 6.7) were often of greater magnitude than the accuracy of the temperature measuring equipment. The problems of discerning between the undisturbed fluid temperature and the temperature due to the presence of a thermal element, were greater sources of temperature data error.

Because of the one-dimensional nature of the temperature probe, the data may also have been influenced by non-uniform heating, large scale convective circulations due to the container geometry or horizontal gradients due to side wall heat losses. Preliminary measurements of the horizontal temperature distributions across the lower boundary and the fluid column suggested that there were no significant horizontal gradients.

A major source of error in the experimental investigation was the discontinuous nature of the temperature readings at the fixed integer (centimetre) heights above the plate. As discussed in Chapt. 6.3.2, the typical time required to take a reading at each height was about 30 seconds. At some heights, the temperatures immediately prior to the arrival of the mixed layer interface, were not measured. As a result, the temperature changes in the intermittency region were often poorly defined. The contours for constant height in other parts of the fluid column were also difficult to plot when the data was discontinous. Ideally, a large number of fixed probes at evenly spaced heights

should be used to obtain continuous temperature data. However, for a small scale laboratory experiment, a large number of probes would have too great an effect on the fluid motions.

The reduction of the experimental $T(z,t)$ data yields a number of possible sources of error. Taking the tangent of the fitted data curves to obtain either $\partial T/\partial t$ or $\partial T/\partial z$ means a further reduction in accuracy. If the interface is not at an integer height (as is typically the case), the value of $(\partial T/\partial t)_i$ must be obtained by extrapolating the diffusion region $\partial T/\partial t$ data to the interface (Fig. 6.21a). A similar problem arises in obtaining the interface height for individual temperature profiles (e.g. Fig. 6.20). However, in this case the curve for d_m versus T_m can be used to define d_m. Because the temperature measurements are not continuous with height, the vertical distributions of any quantity must always be described by discrete height data points and a fitted curve. The continuous measurement of temperature with respect to both height and time is beyond the capabilities of present day technology.

In the calibration of the lower boundary heat flux, the unsteadiness of T_m was an undesirable but unavoidable feature. To reduce this effect the unsteady heat flux convection experiments were performed using the full experimental tank height. As a result, the variation of Q_p with layer thickness was not measured. At high Rayleigh number , the variation of c_q is, however, small (Fig. A.8). In the steady heat flux convection experiments, neither the upper aluminium plate heat storage capacity S_p nor the thermal conductivity of the glass layer K_G could be calibrated independently of the glass heat flux q_G. Calculating S_p and K_G from their published thermal properties was a source of error. This also applies to the calculation of the heat loss factors for the insulation.

The aims of this research were to study the general behaviour of the I.C.P.M. and to gain some understanding of penetrative convection at low Péclet number . Although there were a number of possible sources of error in the experimental investigation, the accuracy of the experiments was considered to be sufficient to satisfy these aims. However, more detailed experiments using continuous temperature measurement probes will be required before the empirical relationships for $\gamma(z)$ and the empirical constants E_{max} and c_t (Eqn. 4.3.7) can be accurately evaluated.

In the next section, the results of numerical analyses of the theoretical I.C.P.M. and the experimental data will be compared.

CHAPTER 7

RESULTS OF NUMERICAL ANALYSES OF ENTRAINMENT EXPERIMENTS

The numerical analysis program for the I.C.P.M. (Appendix C) was used to model the entrainment experiments. In this chapter, the results of these numerical analyses will be compared with the experimental data. Three steady heat flux entrainment experiments (ES1, ES2 and ES3) will form the basis of the comparison. Their lower boundary heat flux conditions could be modelled more accurately than the unsteady heat flux experiments, and their temporal behaviour was more regular. However, a numerical analysis of unsteady heat flux experiment EU4 will also be presented.

The theoretical I.C.P.M. considers the temperature variations within the fluid column during the three time periods: molecular diffusion, interfacial entrainment and single-layer convection. Ideally, the numerical analyses of the I.C.P.M. entrainment experiments should also cover these three time periods. Several aspects of the experimental investigations make this impracticable.

Before the electrical supply to the heating apparatus was switched on and heating officially commenced (i.e. $t < t_s$), the lower boundary apparatus was generally warmer than the fluid immediately above it. This arose from the method used to create the initial temperature stratification (Chapt. 6.3.1). Therefore, contrary to the assumptions of the theoretical model, there was a small heat flux into the fluid column. Although this could be measured experimentally, there was no means of controlling it.

After $t = t_s$, thermal lag in the heating apparatus meant that the heat flux conditions did not reach a controlled state for up to 10 minutes. Before this time, the lower boundary buoyancy heat flux $Q_p(t)$ is difficult to model. It is simpler to commence the numerical analysis about 5 - 10 minutes after $t = t_s$. Any behaviour predicted by the model before this time would not contribute significantly to an understanding of penetrative convection.

Near the end of the interfacial entrainment period when $d_m \rightarrow h_T$, it becomes difficult to numerically model the penetrative convection process accurately. The interfacial temperature difference is negligible, $\gamma(z) >> \kappa$, and V_{em} becomes very large. The numerical analysis program

generally became unstable within five minutes of d_m reaching h_T (Appendix C). It should be noted that the computer program remained stable until ΔT_i was less than $0.2°C$. By extrapolating $T_m(t)$ and $T_a(t)$, the end of the interfacial entrainment period t_T could be determined.

Hence, the numerical analysis computer program was only used to model the temporal behaviour of the experiments within the interfacial entrainment period.

7.1 STEADY HEAT FLUX ENTRAINMENT EXPERIMENT ES2

The ratio of d_{g0} to h_T of 0.25 used for experiment ES2 (Table 6.3) was a good compromise between the need to have as long an entrainment period as possible and the requirement that the diffusion region be deep to reduce upper boundary effects. In this comparison of the numerical analyses with experimental data, experiment ES2 will be discussed first. This will allow experiment ES2 to act as a standard against which the effect of varying d_{g0} on the I.C.P.M. behaviour can be judged.

As discussed earlier (Chapt. 4.3.1), the turbulent diffusivity γ_i was evaluated from an experiment in which the filling velocity (Eqn. 3.9.1) was small (large Pe, stirring grid experiment). In a low Péclet number penetrative convection model, the effective value of γ_i may be less than that predicted by Eqn. 4.3.8, if the filling velocity is large. The filling velocity in the I.C.P.M. is largest when the mixed layer depth is small and the interfacial gradient is negligible ($d_m < d_{g0}$).

Modelling the I.C.P.M. experiments when $d_m < d_{g0}$ is also difficult because, initially, the temperature gradient increases with increasing height above the interface. The decay of $\gamma(z)/\gamma_i$ in the intermittency region will be affected by the increasing stability with height. This may also cause a reduction in γ_i. The penetration of the interfacial domes is more likely to be influenced by the maximum temperature gradient within the intermittency region than by the interfacial gradient.

A numerical analysis of entrainment experiment ES2 commencing at t = 150 minutes will be considered first. At this time, $d_m > d_{g0}$, and the modelling problems discussed above should not be significant. The initial temperature profile (t = 150 mins.) was matched with the experimental ES2 data.

A comparison of the temperature versus time plots for this numerical analysis (Fig. 7.1) and the experimental data (Fig. 7.2) shows generally good agreement. The numerical analysis of ES2 commencing at t = 150 mins. will be referred to as the second analysis of ES2. An earlier numerical analysis, commencing at t = 80 minutes , was presented in Fig. 4.8.

The first check on the numerical model is its ability to predict the mixed layer temperature $T_m(t)$. In a power station cooling pond, the heat loss to the atmosphere will be a function of the temperature difference between the mixed layer and the air above. The thickness of the layer d_m will be of secondary importance. The agreement between the numerical and experimental $T_m(t)$ curves for ES2 is extremely good. As shown in Fig. 7.2, the two $T_m(t)$ curves only deviate significantly after t = 210 mins. At t = 240 mins., the experimental results are underestimated by less than 0.2°C.

However, this check using $T_m(t)$ is not very sensitive. Any errors in predicting the interfacial heat fluxes mean that, at any time t , the numerical and actual interface heights will also differ. Any extra heat transferred through the interface will be distributed over a thicker mixed layer and the resulting error in T_m will be small. The same applies to a comparison between a molecular entrainment analysis and a turbulent entrainment analysis (Fig. 4.8) and a comparison between a filling model entrainment analysis and a molecular entrainment analysis (Fig. 3.9). Even as the analyses became more sophisticated, with the inclusion of additional heat transfers in the diffusion region, the increases in the corresponding values of $T_m(t)$ were relatively small.

The second check of the numerical analysis model is the variation of the interface height $d_m(t)$. In other applications of interfacial entrainment, where pollutants are released into the mixed layer, the growth of the mixed layer needs to be accurately predicted. As shown in Fig. 7.2, the temporal variation of d_m in experiment ES2 is modelled reasonably well for $150 < t < 220$ mins. After t = 220 mins, the experimental interface height is increasingly underestimated.

In the numerical I.C.P.M., the relative accuracy of the mixed layer temperature predictions means that any errors in $d_m(t)$ will be primarily due to discrepancies in the predicted diffusion region temperatures. The rates of change of temperature in the intermittency region, just above the interface, are very sensitive to the values of γ and $\partial\gamma/\partial z$ (Eqn. 3.6.1). Up to z = 22 cm, the diffusion region temperature distributions

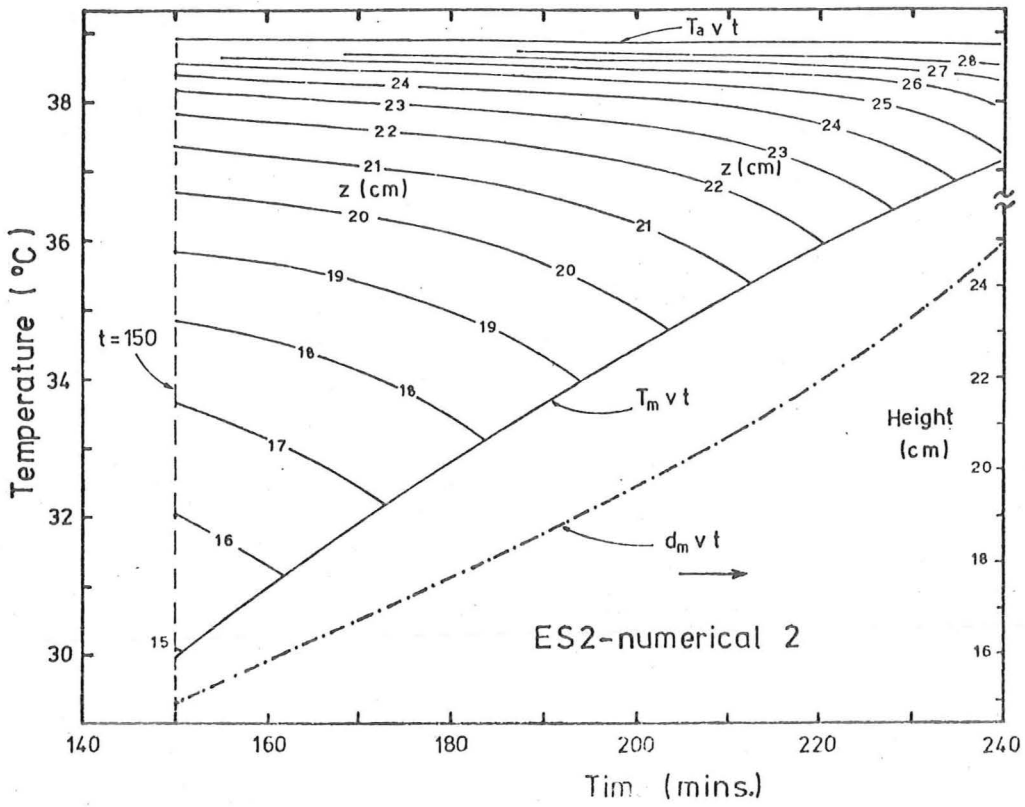

Fig. 7.1. Temperature versus time graph from second numerical analysis of entrainment experiment ES2. Contour labels give height in centimetres. Interface height d_m as a function of time is also shown.

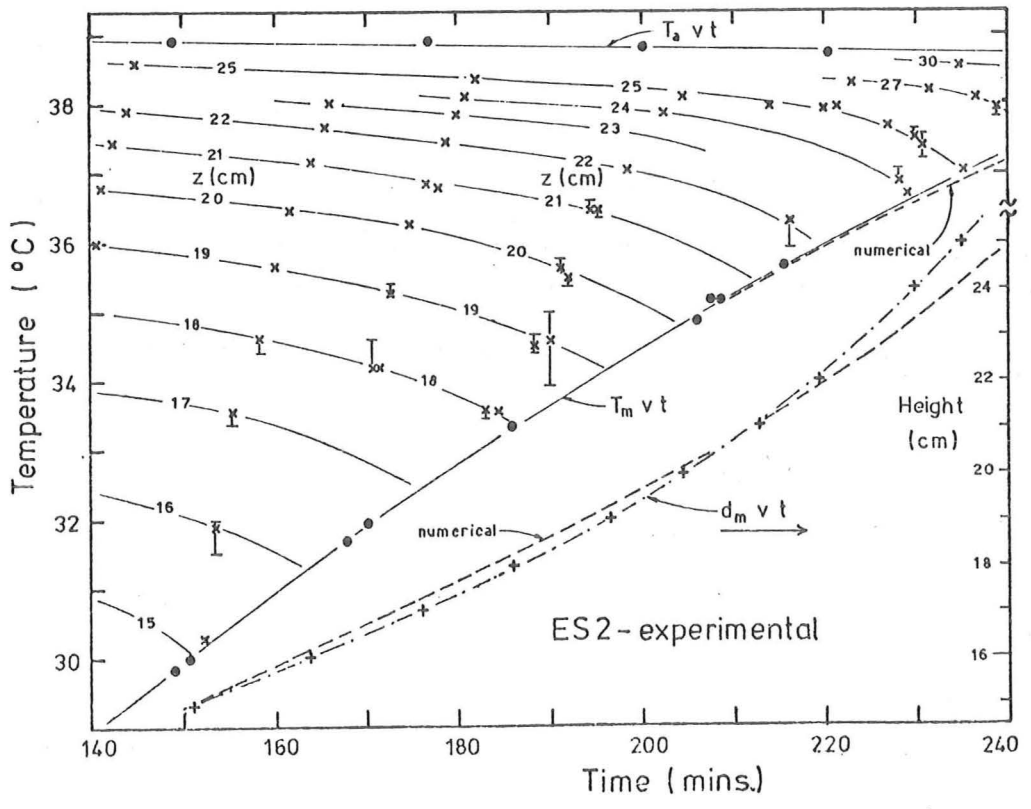

Fig. 7.2. Experimental data from entrainment experiment ES2 plotted in the same form as Figure 7.1 to allow comparison with results of second numerical analysis.

are in reasonably good agreement (Figs. 7.1 and 7.2). It appears, therefore, that the empirical formulae for $\gamma(z)$ are able to successfully model the effects of turbulent entrainment above the interface.

However, the predicted values of $T(z)$ in the diffusion region for $z > 22$ cm do not compare well with the experimental data. There are three possible reasons for this.

(i) Underestimation of the heat losses. For example, the maximum experimental temperature $T_a(t)$ is underestimated. Because the vertical temperature gradients in the region of maximum temperature ($z >> d_m$) are negligible, most of the change in T_a with time is due to heat losses. The experimental rate of cooling of T_a (Fig. 7.2) is about 2 times the corresponding rate for the numerical analysis (Fig. 7.1). This suggests the heat loss factors W and W_T were actually about twice the values calculated from the thermal properties of the insulation. Over a long period of time, the cumulative heat loss errors will become significant.

(ii) The molecular diffusivity κ was assumed to be constant for the range of experimental temperatures ($\kappa = 1.43 \times 10^{-3} cm^2/sec$). This corresponds to the value of κ at 20°C. At 40°C, however, the value of κ is approximately 6% higher. Hence, the vertical heat transfers in the upper diffusion region were underestimated by this amount.

(iii) Eventually, when ΔT_i becomes very small, the thermal elements penetrating the interface experience only weak negative buoyancy forces. They tend to penetrate further and remain in the diffusion region. In this low Ri case, the concept of a turbulent diffusion parameter is less likely to accurately describe the heat transfers. As was also discussed earlier in this section, the low Ri case is difficult to accurately analyse by numerical methods because the total thermal diffusivity becomes very large ($\gamma >> \kappa$).

Temperature profiles from the second numerical analysis of ES2 also show the comparison between the numerical model and experimental data (Fig. 7.3). The initial temperature profile ($t = 150$ mins.) was matched against the experimental results. At $t = 170$ and 190 minutes, the experimental data points lie close to the numerical curves. At $t = 210$ minutes, the interface heights and mixed layer temperatures are in good agreement but well above the interface, the additional cooling due to heat losses is apparent (e.g. the data points at $z = 24$ and 25 cm). At $t = 230$ mins.,

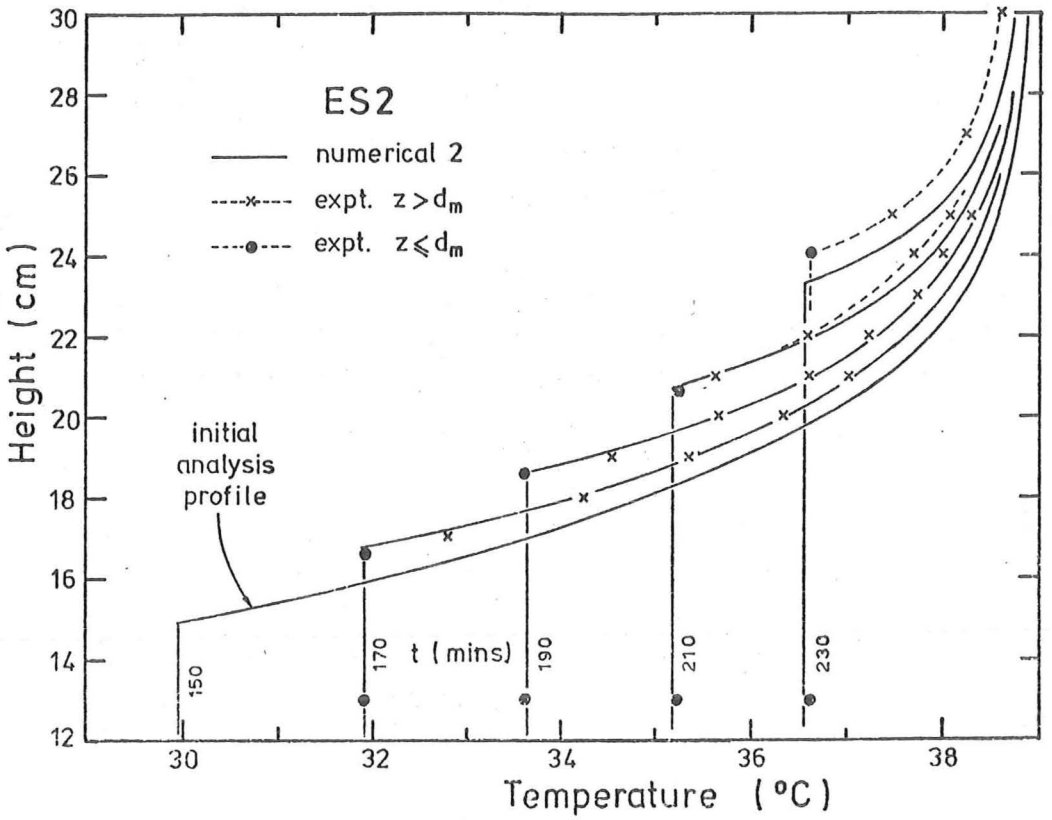

Fig. 7.3. Comparison between vertical temperature profiles from the second numerical analysis of entrainment experiment ES2 and the experimental data. Profile labels give time in minutes.

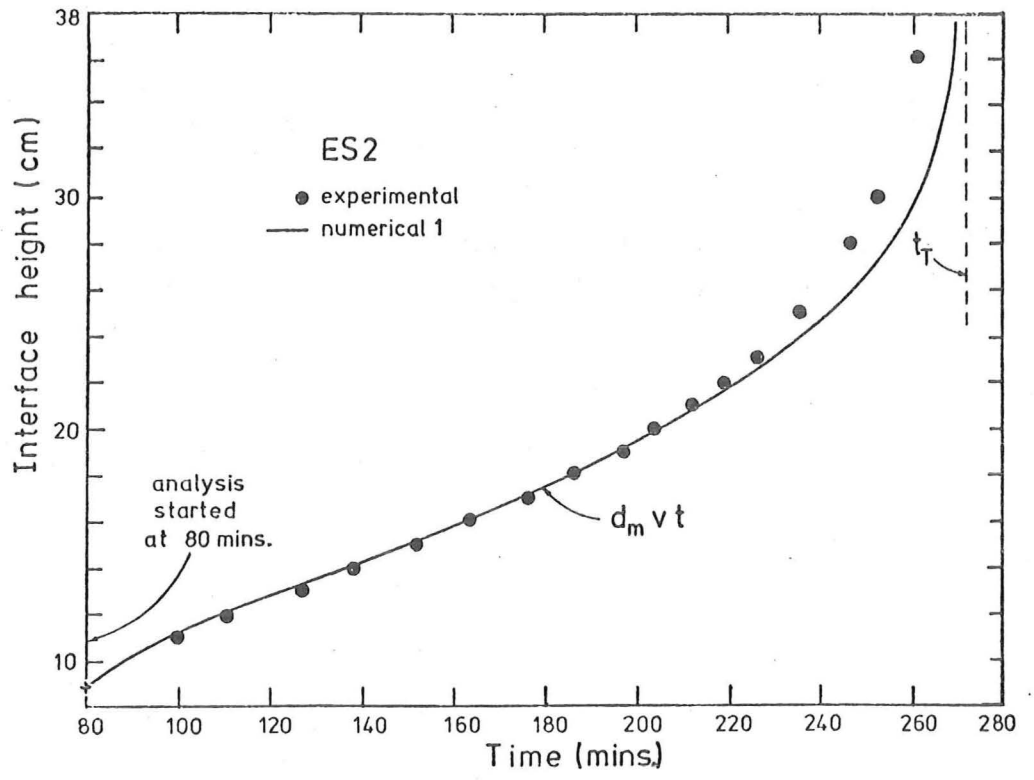

Fig. 7.4. Comparison of the interface height as a function of time from the first numerical analysis of entrainment experiment ES2 with experimental data.

the experimental temperature profile for the diffusion region is almost 1 cm higher than the numerical analysis prediction.

The accuracy of the numerical model during the initial stages of the interfacial entrainment period ($d_m < d_{g0}$) will now be considered. This will illustrate the case when the filling velocity is significant. It will also allow the effect on $\gamma(z)$ of an increasing temperature gradient in the intermittency region, to be studied.

As the penetrating interfacial domes sense all the temperature gradients over the intermittency region, the maximum temperature gradient in this region is likely to dictate the value of γ_i. This was allowed for in the numerical analysis program (Appendix C). The maximum temperature gradient over $d_m < z < d_m + z_{int}$ was found and used to calculate the Richardson number Ri. The values of γ_i and z_{int} calculated from Eqns. 4.3.8 and 4.3.14 respectively, were slightly smaller. It should be noted, however, that the results of the numerical analyses were not significantly affected by this modification.

The temperature versus time data from the first numerical analysis of ES2, which started at t = 80 mins., have already been presented (Fig. 4.8). A plot of temperature versus time for the experimental data on the same scale was shown in Fig. 6.19. The mixed layer temperature curve $T_m(t)$ for this longer numerical analysis agrees with the experimental data to within $\pm$ 0.2°C. Note that this is of the same order of magnitude as the experimental accuracy and less than the maximum possible temperature fluctuations (Chapt. 6.3.2).

A comparison of the numerical and experimental curves for $d_m(t)$ shows good agreement until about t = 220 mins. (Fig. 7.4). Thereafter, the experimental interface height is underestimated by an increasing amount. As discussed above, the poor agreement near the end of the interfacial entrainment period may be attributed to (i) an underestimation of heat losses, (ii) the use of a constant molecular diffusivity based on T = 20°C, and (iii) the inability of the turbulent diffusion parameter $\gamma(z)$ to simulate low Ri interfacial dome behaviour.

While the mixed layer temperature and height are reasonably well predicted for $d_m < d_{g0}$, the variations of the diffusion region temperatures close to the interface are not. At heights z = 11, 12 and 13 cm, the experimental temperatures in the diffusion region are initially increasing with time (Fig. 6.19). Only when the interface is within 1 cm of these heights does the fluid begin to cool. By comparison, the diffusion region temperatures at heights z = 11, 12 and 13 cm in the numerical

analysis (Fig. 4.8) start to decrease much earlier. This suggests the turbulent diffusivity term $\gamma(z)$ is overestimated. The smaller experimental values of $\gamma(z)$ may be due to either the large filling velocity term or the increase of the intermittency region temperature gradients with height, as discussed earlier in this section.

It should also be pointed out that errors in the intermittency region temperatures due to over or underestimation of $\gamma(z)$ are cumulative. However, as the interface is continually rising, the intermittency region fluid is soon incorporated into the mixed layer. This reduces the cumulative effect of these errors on later diffusion region calculations.

It is also interesting to note that the temperatures in the intermittency region predicted by the two numerical analyses of ES2 (Figures 4.8 and 7.1) were almost identical at $t = 170$ mins. Later, the two analyses were only different because the shorter analysis, for $d_m > d_{g0}$ only (Fig. 7.1), started at $t = 150$ mins. with upper diffusion region temperatures that were approximately 0.12°C cooler. Despite the longer analysis (Fig. 4.8) having covered the initial $d_m < d_{g0}$ stage as well, cumulative errors due to an overestimation of $\gamma(z)$ were not significant.

If the possible numerical and experimental errors are taken into account, the numerical model predicts the actual experimental data well over most of the interfacial entrainment period.

7.2 STEADY HEAT FLUX ENTRAINMENT EXPERIMENT ES3

In ES3, the mixed layer temperature T_m and mixed layer thickness d_m increased more slowly because the initial two-layer boundary height $d_{g0} = 22$ cm. was relatively large (c.f. ES2, $d_{g0} = 13.9$ cm). Hence, the reduction of γ_i due to the filling velocity effect should not be significant in this experiment. The numerical analysis should be in better agreement during the initial stages of the interfacial entrainment period ($d_m < d_{g0}$). Figure 7.5 shows the experimental temperature versus time curves for ES3. The experiment was ended after 5.5 hours of heating. At this stage, $d_m \approx 38$ cm. and the diffusion region was only 17 cm. thick.

At a corresponding stage during the interfacial entrainment period, the interface height for ES3 is higher than for ES2. Because $\ell_s \propto d_m$, the interfacial Richardson number Ri (Eqn. 4.1.4) is proportional to $(d_m)^{4/3}$. Typically, the experimental Richardson numbers were large so that $E \propto Ri^{-3/2}$ It follows from Eqn. 4.1.8 that,

$$\gamma_i \propto (d_m)^{-2/3}$$

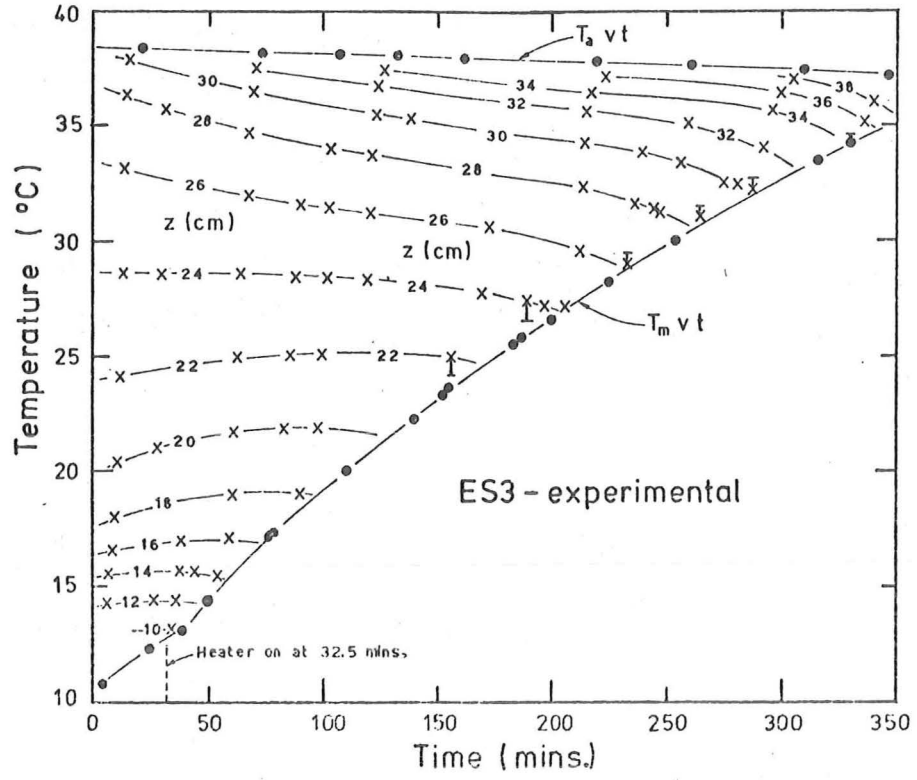

Fig. 7.5. Temperature versus time graph of experimental data from entrainment experiment ES3. Profile labels give height in centimetres.

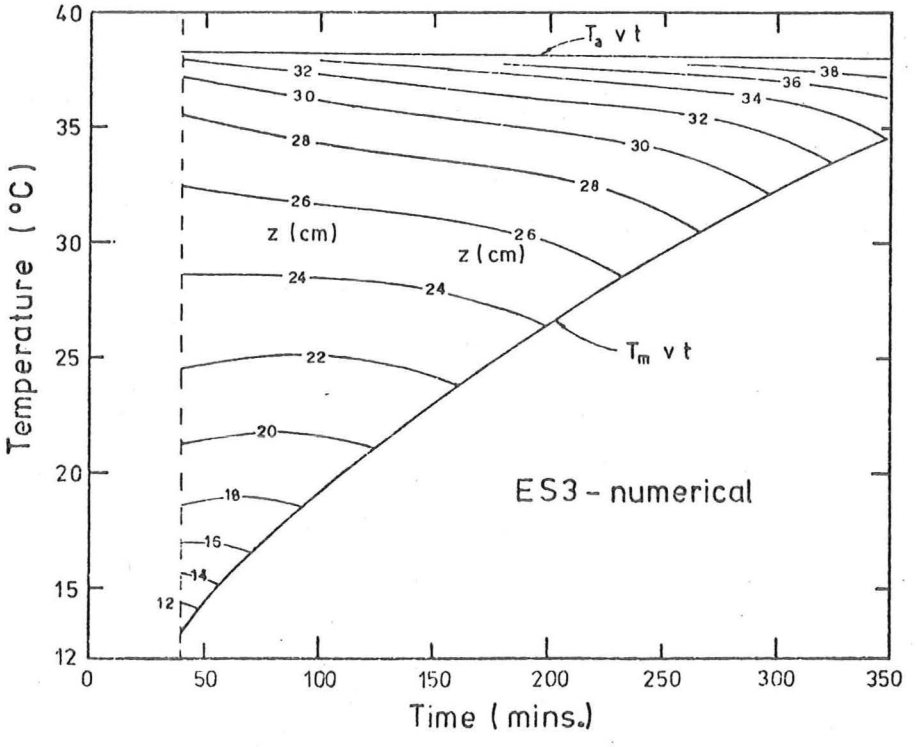

Fig. 7.6. Temperature versus time graph from numerical analysis of entrainment experiment ES3. Profile labels give height in centimetres.

Therefore, in experiment ES3, the turbulent diffusivities were correspondingly smaller and the intermittency region temperatures decreased at a slower rate (c.f. Figs. 7.5 and 6.19).

Figure 7.6 shows the temperature versus time curves for the numerical analysis of ES3. The numerical analysis started at $t = 40$ mins, with an initial temperature distribution that matched the experimental data. Because of the reduced rates of increase of T_m, a much better comparison between the numerical and experimental results is obtained during the initial period when $d_m < d_{g0}$. (Figs. 7.5 and 7.6). However, the much longer duration of the experiment meant that the cumulative effect of underestimating the heat losses is significant. The maximum temperature T_a at $t = 350$ mins. is underestimated by about 1°C. If the other diffusion region temperatures of this time were corrected by this amount, the agreement with the experimental data would improve.

The numerical analysis of ES3 predicts the mixed layer temperatures well except for $t > 250$ mins. when the experimental values are underestimated slightly. At $t = 350$ mins., the discrepancy is about 0.5°C (Figs. 7.5 and 7.6). As shown in Fig. 7.7, the interface height d_m is well modelled until $t \approx 250$ mins. after which the cumulative heat loss errors cause the experimental value of d_m to be underestimated,

7.3 STEADY HEAT FLUX ENTRAINMENT EXPERIMENT ES1

Experiment ES1 shows more clearly, than the other two experiments (ES2, ES3), the reduction of $\gamma(z)$ when the filling velocity is large. Because d_{g0} was relatively small, the mixed layer temperature increased rapidly (Fig. 7.8). The formulae for $\gamma(z)$ will predict large values of γ_i because the corresponding values of d_m are small. However, the experimental temperature versus time curves for $z < d_{g0}$ (Fig. 7.8) do not show a rapid cooling of the intermittency region fluid. Instead, the experimental temperatures above the interface initially vary in the same way as a molecular entrainment analysis (Chapt. 3.9). Only after about $t = 100$ minutes does the additional cooling due to turbulent entrainment become obvious. This means that the numerical analysis program (Fig. 7.9) poorly predicts the intermittency region temperature distribution during the initial stages of the interfacial entrainment period.

Later, when the interface has risen beyond these initial intermittency region heights, the numerical predictions improve. Because experiment ES1 is relatively short, the cumulative heat loss errors are not as significant as for ES2 and ES3. The temperature variations for $z = 15$ to 20 cm. are very well predicted.

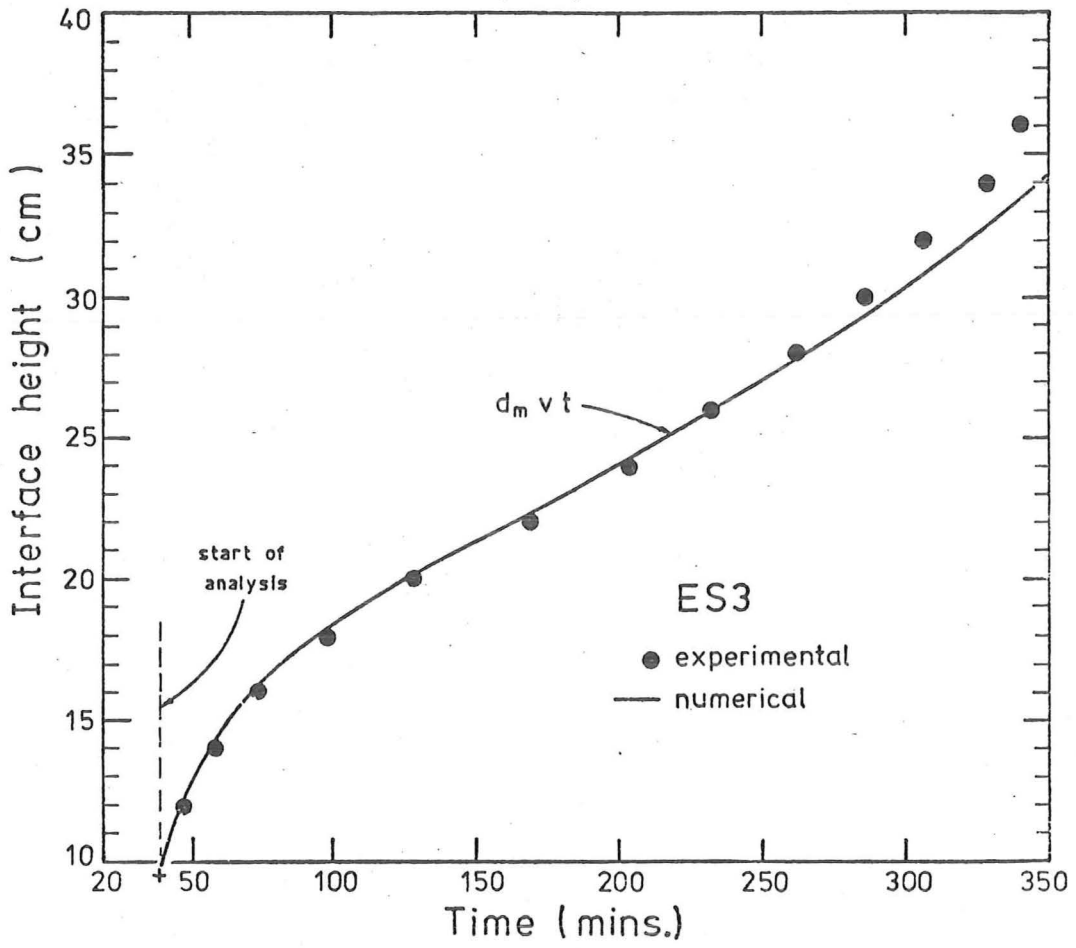

Fig. 7.7. Comparison of the interface height as a function of time from the numerical analysis of entrainment experiment ES3 with experimental data.

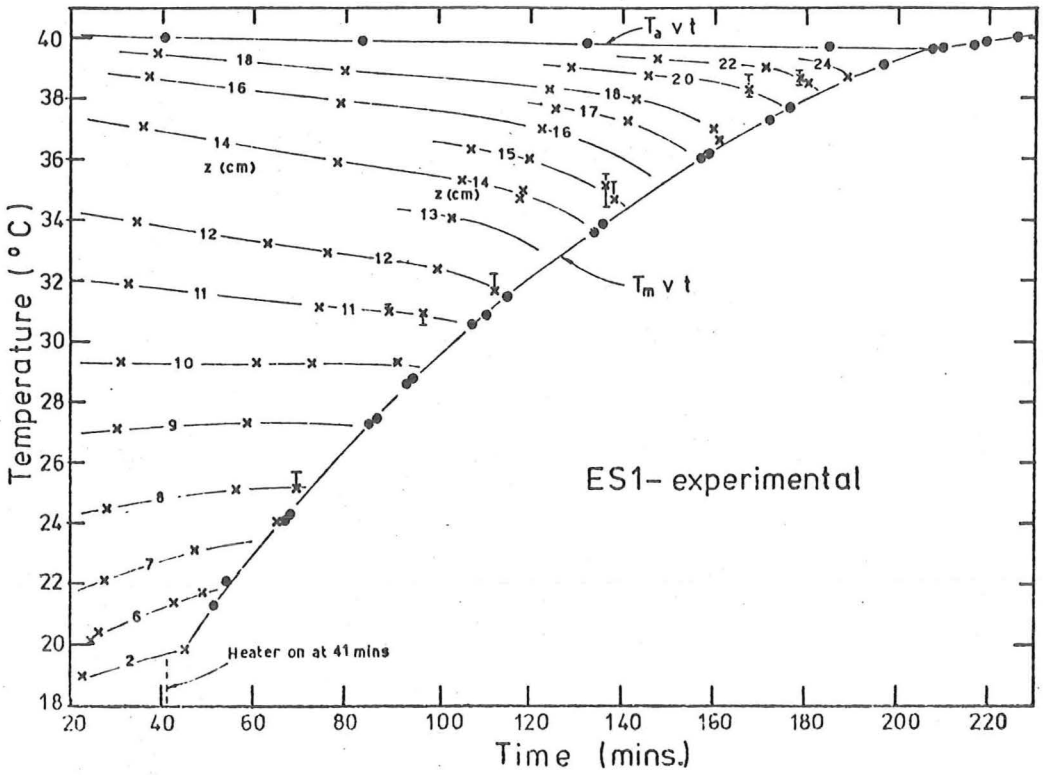

Fig. 7.8. Temperature versus time graph of experimental data from entrainment experiment ES1. Profile labels give height in centimetres.

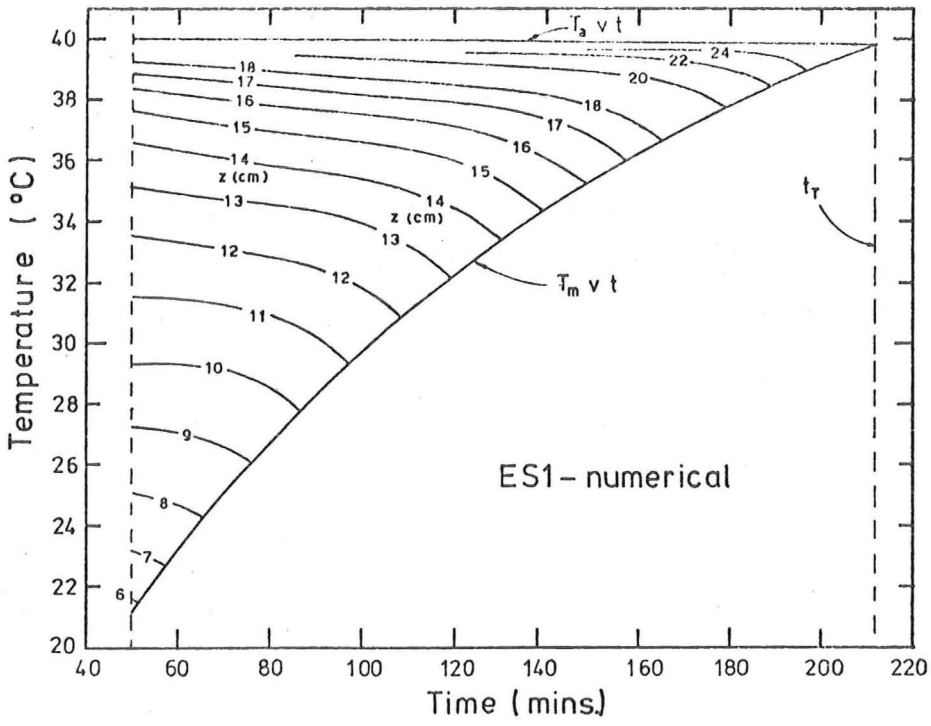

Fig. 7.9. Temperature versus time graph from numerical analysis of entrainment experiment ES1. Profile labels give height in centimetres.

A comparison of the numerical curve for $d_m(t)$ with the experimental data (Fig. 7.10) shows how the interface height is initially underestimated. This is because of the reduction of $\gamma(z)$ due to the large filling velocity term. As was discussed earlier (Chapt. 4.3.1), the turbulent entrainment effect ahead of the interface is reduced if the interface is rising rapidly.

7.4 UNSTEADY HEAT FLUX ENTRAINMENT EXPERIMENT EU4

For the numerical analysis of the unsteady heat flux entrainment experiment EU4, the initial temperature profile at $t = 55$ mins. was matched with experimental data (Figs. 7.11a and 6.15a).

To model the lower boundary heat flux Q_p, the experimental values of the circulated heating water temperature $T_H(t)$ were specified. Using these values of T_H and the mixed layer temperature T_m at any time t, ΔT_H could be obtained. The lower boundary heat flux Q_p was then calculated from ΔT_H using the convection calibration equation (Eqn. 6.4.2). This value of Q_p was used in the numerical analysis to calculate the temporal changes in the temperature distribution, and hence, the new value of T_m. It therefore follows that the lower boundary heat flux is dependent on the mixed layer temperatures calculated by the numerical analysis model. As a result, the numerical curve of $Q_p(t)$ may differ from the experimental values (Fig. 7.11b).

For the numerical analysis of EU4, experimental measurements of $T_H(t)$ were fitted with a series of straight lines. Discrepancies between the experimental $T_H(t)$ data and the fitted straight line, and departures of the empirical equation used to evaluate Q_p from ΔT_H (Eqn. 6.4.2) from the actual convection measurements, affected the accuracy of $Q_p(t)$ for the numerical analysis (Fig. 7.11b). If the mixed layer temperature T_m is poorly predicted by the numerical analysis, this affects ΔT_H and hence, Q_p. This latter source of error is partly compensated for. If T_m is too low, the values of ΔT_H and Q_p are larger which increases T_m more rapidly.

Figure 7.11b shows a comparison between the experimental and the numerical analysis curves of $Q_p(t)$ for EU4. At $t = 115$ mins., the variation in T_H was modelled as being discontinuous. In an actual unsteady heat flux experiment, the heating water temperature T_H always took at least four minutes to fully adjust to a new value. However, the agreement between the numerical analysis lower boundary heat flux and the experimental values is still reasonably good (Fig. 7.11b).

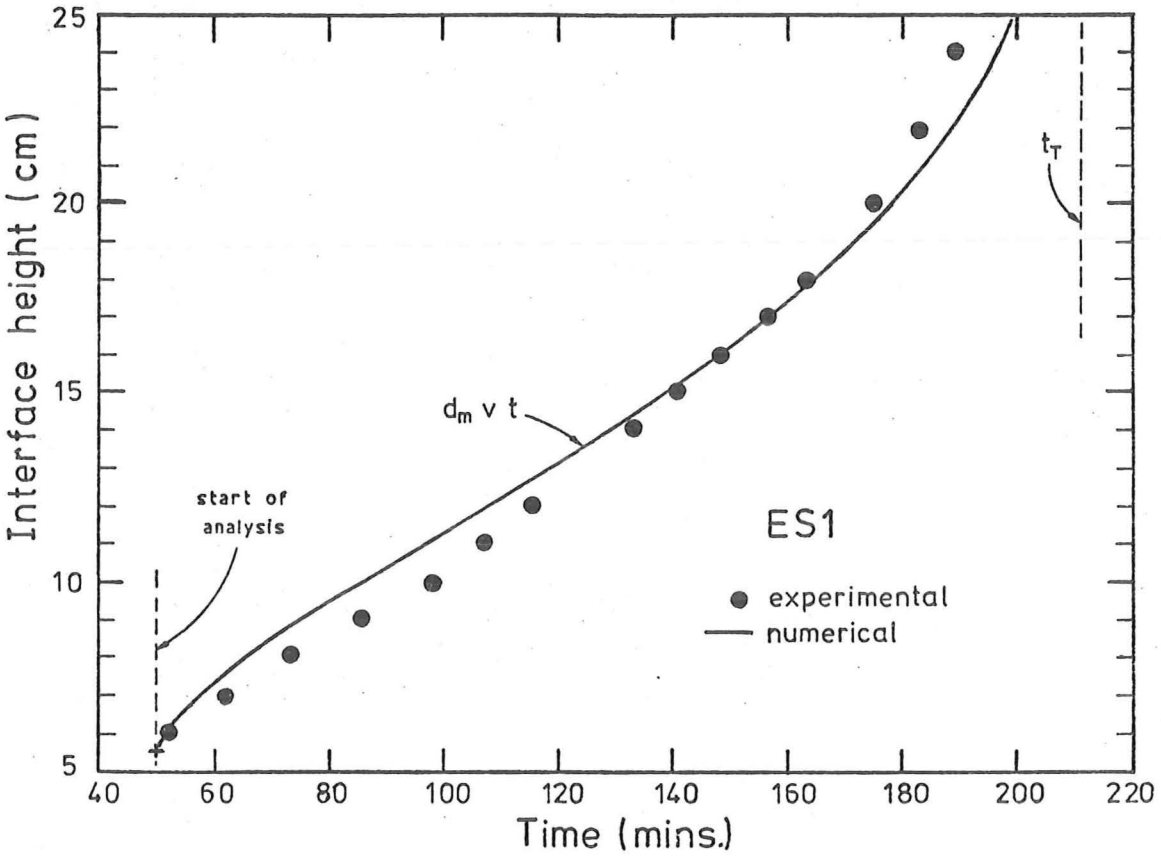

Fig. 7.10. Comparison of the interface height as a function of time from the numerical analysis of entrainment experiment ES1 with experimental data.

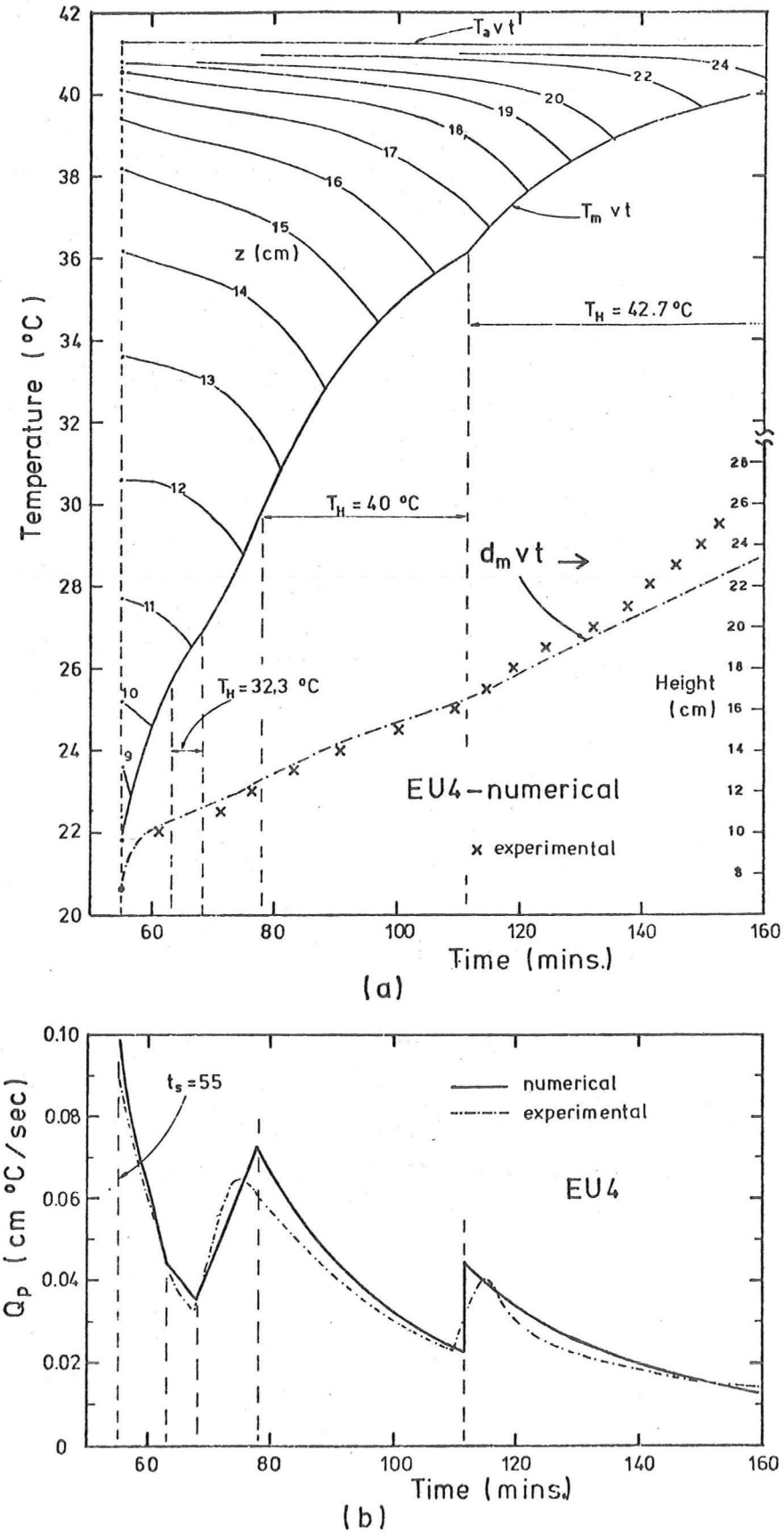

Fig. 7.11. (a) Temperature versus time graph from numerical analysis of unsteady heat flux entrainment experiment EU4. Contour labels give height in centimetres. Interface height as a function of time is also shown. (b) A comparison between the lower boundary buoyancy heat fluxes Q_p as a function of time from numerical analysis and experimental data.

It may have been more accurate to specify the lower boundary heat flux variation $Q_p(t)$ from experimental values. In this way, Q_p would not have depended on the mixed layer temperatures. However, the method of specifying $T_H(t)$ for the numerical analyses, rather than $Q_p(t)$, was chosen because it was consistent with the experimental method of controlling the lower boundary heat flux.

The temperature versus time curves from the experimental measurements (Fig. 6.15a) and the numerical analysis (Fig. 7.11a) of EU4 may be compared. Whilst the two curves for T_m are similar, the numerical analysis underestimates T_m by up to $0.5°C$. The maximum discrepancy in T_m occurs over the period when $T_H = 40°C$ in the numerical analysis (Fig. 7.11a). The comparison between the experimental and numerical heat flux curves (Fig. 7.11b) suggests that the total heat input of the numerical model was slightly greater. This should have caused a slight overestimation of T_m.

The poor prediction of $T_m(t)$ is probably a result of quantitative errors in the relationship between ΔT_H and Q_p. For the unsteady heat flux experiments (Fig. 6.13), the convection calibration data was measured with $d_m \approx 55$ cm. The deep convection layer meant the rate of increase of T_m was kept as low as possible. However, for much shallower depths, the Rayleigh number is reduced and the rate of increase of the mixed layer temperature is larger. As discussed in Chapt. 6.4.1, both these factors result in Q_p being slightly greater for a given value of ΔT_H. As the experimental heat flux Q_p was evaluated from ΔT_H using Fig. 6.13, and the numerical analysis heat flux was evaluated using Eqn. 6.4.2, both heat fluxes were possibly underestimated. This may account for the underestimation of T_m.

As the lower boundary heat fluxes for EU4 were generally much greater than the almost constant value in ES1, ES2 and ES3, the rates of increase of T_m were higher. The filling velocities were therefore larger and the reduction in the effective turbulent diffusivity $\gamma(z)$ was quite significant (Chapt. 7.1). Initially, the diffusion region temperatures, just above the interface, are very poorly predicted. The turbulent diffusivity $\gamma(z)$ is too large and the diffusion region cools too rapidly. The diffusion region temperature improves later but once $t > 130$ minutes, the temperatures start to be underestimated.

Despite the discrepancies in the mixed layer and diffusion region temperatures between the numerical and experimental data of EU4, the height of the interface d_m is well predicted up until $t > 130$ mins. (Fig.7.11a).

As with the numerical analyses of the steady heat flux experiments, experimental values of d_m after this stage are underestimated.

7.5 THE RELATIVE IMPORTANCE OF MOLECULAR AND TURBULENT DIFFUSION AND THE FILLING VELOCITY TERM IN THE I.C.P.M.

In a study of the I.C.P.M., two quantities are of major interest. These are the interfacial heat flux Q_e and the rate of rise of the interface V_{em}. As has been discussed during the development of the I.C.P.M., both turbulent interfacial entrainment (parameterized by the turbulent diffusion term $\gamma(z)$) and molecular diffusion play important roles in low Péclet number penetrative convection. It has also been shown that even if the effects of molecular and turbulent diffusion were neglected, the interface may still rise due to the "filling" of the temperature profile by the lower boundary heat flux Q_p (Chapt. 3.9).

In this section, the relative contribution of these factors to the two entrainment quantities Q_e and V_{em} will be considered. For the specific example to be considered (ES2 at $t = 170$ minutes), the turbulent entrainment parameters contribute only one-third of V_{em}. In models with a temperature discontinuity at the interface (e.g. Betts 1973) a turbulent entrainment contribution of 100% is implied. It must be stressed that this discussion will apply to a specific time in a specific experiment. In other examples, the relative contributions will differ.

Because the experimental measurements were not continuous, the evaluation of many of the parameters and their partial derivatives is both difficult and inaccurate (Chapt. 6.6). The numerical analysis data, however, is continuous and the magnitude of each of the parameters is readily available. At $t = 170$ mins. in the second numerical analysis of ES2, the numerical data agrees reasonably well with the experimental measurements (Figs. 7.1, 7.2 and 7.3). It is therefore proposed to use this data to illustrate the relative importance of κ, $\gamma(z)$ and the filling velocity term.

The values of major entrainment parameters from the numerical analysis at this time are listed in Table 7.1. Further values, of the parameters used in the computer program are given in Table 4.1.

Vertical profiles of the partial derivative of temperature with respect to time $\partial T/\partial t$ and the buoyancy heat flux $Q(z)$, from the second numerical analysis of ES2 at $t = 170$ minutes, are shown in Fig. 7.12. The corresponding experimental profiles were given in Fig. 6.21.

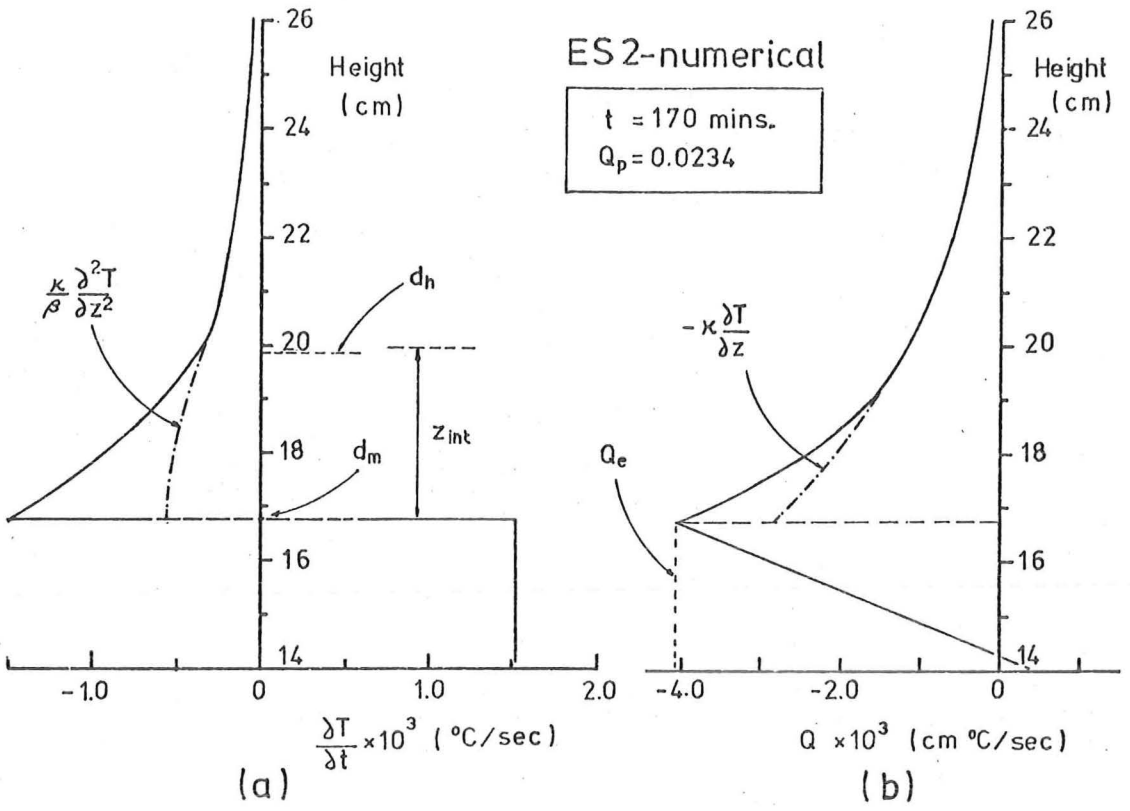

Fig. 7.12. (a) Rate of change of temperature profile, and (b) buoyancy heat flux profile from second numerical analysis of ES2 at t = 170 minutes.

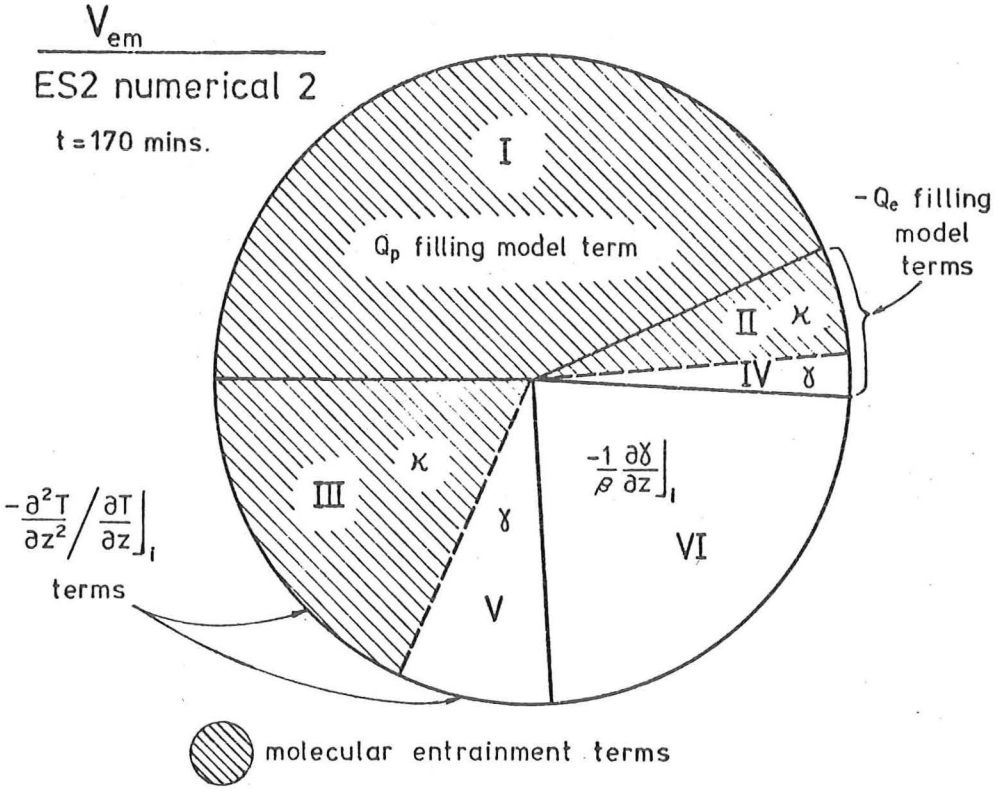

Fig. 7.13. Pie-graph showing contribution of the terms in Eqn. 7.5.4 to the rate of rise of the interface V_{em} .

TABLE 7.1

THE VALUES OF THE MAJOR ENTRAINMENT PARAMETERS FROM THE SECOND NUMERICAL ANALYSIS OF ES2 AT t = 170 MINUTES

d_m	= 16.74 cm	Q_e	= - 0.41 x 10^{-2} cm °C/sec
d_h	= 19.85 cm	k_e	= 0.174
V_{em}	= 1.509 x 10^{-3} cm/sec	k_m	= 0.392
T_m	= 31.91 °C	k_h	= 0.458
ΔT_i	= 6.99 °C	Ri	= 30.39
$\left.\frac{\partial T}{\partial z}\right\|_i$	= 2.00 °C/cm	Pe	= 248.8
$\left.\frac{\partial^2 T}{\partial z^2}\right\|_i$	= 0.416 °C/cm^2	E	= 5.72 x 10^{-3}
$\frac{dT_m}{dt}$	= 1.518 x 10^{-3} °C/sec	κ	= 1.43 x 10^{-3} cm^2/sec
$\left.\frac{\partial T}{\partial t}\right\|_i$	= - 1.499 x 10^{-3} °C/sec	γ_i	= 6.05 x 10^{-4} cm^2/sec
$\frac{dT_a}{dt}$	= - 1.24 x 10^{-5} °C/sec	z_{int}	= 3.21 cm
Q_p	= 2.34 x 10^{-2} cm °C/sec	$\left.\frac{\partial \gamma}{\partial z}\right\|_i$	= - 3.77 x 10^{-4} cm/sec.

The vertical buoyancy heat flux profile (Fig. 7.12b) gives the relative effects of molecular and turbulent diffusion directly. From Eqn. 3.3.1 when $\lambda = 0$,

$$Q(z) = - (\kappa + \gamma) \frac{\partial T}{\partial z} \qquad (7.5.1)$$

A profile for the heat flux, due to molecular diffusion alone, is also shown in Fig. 7.12b. The remaining buoyancy heat flux, for $0 < z - d_m < z_{int}$, is due to $\gamma(z)$. At the interface, the relative contributions are $\gamma_i/\kappa = 0.42$ (Table 7.1).

The experimental and numerical values of Q_e differed by less than 5% (Figs. 6.21b and 7.12b). However, the value of Q_e obtained from an experimental mixed layer heat budget is highly susceptible to errors. Apart from the minor heat losses, Q_e is the difference between two large

values; the total increase in heat storage $\beta\, d_m\, dT_m/dt$ and the lower boundary heat flux Q_p . When reliable values of $Q(z)$ and $\partial T(z)/\partial z$ are available, the experimental buoyancy heat flux profile provides a direct method of evaluating $\gamma(z)$.

Vertical profiles of the partial derivative of temperature with respect to time $\partial T/\partial t$ do not reveal the magnitude of $\gamma(z)$ directly. From Eqn. 3.6.1 when $\lambda = 0$, the diffusion region temperature changes are given by

$$\frac{\partial T}{\partial t} = \frac{\kappa}{\beta}\frac{\partial^2 T}{\partial z^2} + \frac{\gamma}{\beta}\frac{\partial^2 T}{\partial z^2} + \frac{1}{\beta}\frac{\partial \gamma}{\partial z}\frac{\partial T}{\partial z} - \frac{W}{\beta}(T - T_{air}) \qquad (7.5.2)$$

I II III IV

Both γ and its partial derivative with respect to height $\partial\gamma/\partial z$ contribute to the temperature change.

Consider the contribution of the various terms of Eqn. 7.5.2 at the interface for this example (Table 7.1). The heat losses, represented by the last term (IV) on the right hand side of Eqn. 7.5.2 make a negligible contribution ($\approx$ 0.5%) . From Fig. 7.12a, it can be seen that the contribution by molecular diffusion alone is quite significant. At the interface, the molecular diffusion term (I) contributes 36.9% of the total. As the ratio of γ_i/κ at $t = 170$ mins. in the numerical model is approximately 0.42, the corresponding contribution by γ (term II in Eqn. 7.5.2) is only 15.6% of the total. The remainder (46.9%) is accounted for by term III. Almost half of the temperature change at the interface $(\partial T/\partial t)_i$ is due to the rate of decay of $\gamma(z)$ at $z = d_m$.

To model the temperature changes in the diffusion region accurately, the relationships for γ_i and $\phi_1(z - d_m)$ both have to be correct. In choosing the power law relationship for the decay of $\gamma(z)$ with height above the interface (Eqn. 4.3.12), the gradient of $\gamma(z)$ also had to be taken into account. If the decay of $\gamma(z)$ with height had been assumed to be linear, $\partial\gamma/\partial z$ would have been constant for all $d_m < z < d_m + z_{int}$. This would have meant a major discontinuity in $\partial\gamma/\partial z$ at $z = d_m + z_{int}$ and hence, a discontinuity in the rate of change of temperature (from Eqn. 7.5.2).

The chosen square law relationship for $\gamma(z)$, Eqn. 4.3.12, yields a linear decay in $\partial\gamma/\partial z$. Although both $\gamma(z)$ and the gradient of $\gamma(z)$ become zero at $z = d_m + z_{int}$, there is still a discontinuity in $\partial^2\gamma/\partial z^2$ The effect of this discontinuity can be seen in Fig. 7.12a at $z = d_m + z_{int}$. The shape of the two profiles appear to be affected by the numerical transition from molecular diffusion to molecular and turbulent diffusion. The

actual experimental data at $t = 170$ mins. do not show similar discontinuities (Fig. 6.21a).

Increasing the power of the power relationship to 3 or higher would have meant an increase in the relative value of z_{int} to keep the interfacial gradient of $\gamma(z)$ consistent with Eqn. 4.1.10. This numerical effect was therefore accepted as a consequence of choosing a finite range for $\gamma(z) > 0$.

It is interesting that for the example given in Fig. 7.12, $d_h - d_m \approx z_{int}$. This is not typical. When $d_m < d_{g0}$, the value of $d_h - d_m$ will be much greater than z_{int}.

The contributions of the filling velocity term, and molecular and turbulent diffusion to the rate of rise of the interface V_{em}, for the second numerical analysis of ES2 at $t = 170$ mins., are shown in the form of a pie-graph in Fig. 7.13. From Eqn. 3.6.5

$$V_{em} = \left(\frac{dT_m}{dt} - \left.\frac{\partial T}{\partial t}\right|_i \right) \Big/ \left.\frac{\partial T}{\partial z}\right|_i \qquad (7.5.3)$$

In this particular example, the rate of change of temperature in the mixed layer and the diffusion region at the interface are approximately equal but have opposite signs (Table 7.1). Hence, the numerator terms on the right hand side of Eqn. 7.5.3 make almost equal positive contributions to V_{em} (Fig. 7.13).

When rearranged in terms of the filling model and molecular entrainment analysis contributions, the equation for V_{em} (Eqn. 3.6.6), for $\lambda = 0$, is

$$V_{em} = \frac{Q_p}{\beta d_m \left.\frac{\partial T}{\partial z}\right|_i} + \frac{\kappa}{\beta d_m} - \frac{\kappa}{\beta} \left.\frac{\frac{\partial^2 T}{\partial z^2}}{\frac{\partial T}{\partial z}}\right|_i + \frac{\gamma_i}{\beta d_m} - \frac{\gamma_i}{\beta} \left.\frac{\frac{\partial^2 T}{\partial z^2}}{\frac{\partial T}{\partial z}}\right|_i - \frac{1}{\beta} \left.\frac{\partial \gamma}{\partial z}\right|_i \qquad (7.5.4)$$

I II III IV V VI

The filling velocity term (I) contributed approximately 43% of V_{em} in this example (Table 7.1). The terms which constitute a molecular entrainment model (I, II and III) contribute almost 67% of the total. In this particular case, the turbulent diffusion terms (IV, V and VI) contribute only one-third of the total value of V_{em}. For penetrative convection at low Péclet numbers, such as is modelled by the I.C.P.M., the rate of rise of the interface cannot be discussed solely in terms of turbulent entrainment.

In a high Péclet number, grid-stirring experiment (e.g. Turner's

(1968) salinity experiments) both the filling velocity term, due to an external buoyancy source (I), and the molecular diffusion terms (II and III) are either zero or may be neglected. Only the turbulent entrainment effects (described by IV, V and VI) remain. However, in the I.C.P.M., the contribution of turbulent entrainment (as parameterized by $\gamma(z)$) may be dominated by the molecular entrainment and filling velocity terms.

The specific example chosen for this discussion of the relative contribution of various terms to Q_e and V_{em} (ES2 at $t = 170$ mins.), represents a situation which is most accurately modelled by the numerical I.C.P.M. program. The interfacial temperature gradient is significant and is the maximum value for the diffusion region ($z > d_m$).

However, if the maximum temperature gradient is above the interface at $z \approx d_{g0}$, as is the case when $d_m << d_{g0}$, the variation of $\partial T(z)/\partial t$ and $Q(z)$ over the diffusion region will not be as regular as for the above example (Fig. 7.12). Consider for example, the diffusion region profiles of $\partial T/\partial t$ and Q from the numerical analysis of ES3 at $t = 60$ mins. (Fig. 7.14). As can also be seen from Fig. 7.6, the interface was below the initial two-layer boundary height d_{g0} at this time. Hence, in one part of the diffusion region the temperatures are increasing with time ($17.5 < z < 23.6$ cm). There are also minimum heat flux points at both $z = d_m$ and d_g.

The relative contributions of the various terms in Eqns. 7.5.1, 7.5.2, 7.5.3 and 7.5.4 will also change for other interface heights and different initial and boundary conditions. When the filling velocity is large, the effect of turbulent entrainment above the interface is reduced. It was this reduction in $\gamma(z)$ that was not adequately modelled by the numerical analysis program. In this case, the filling velocity (term I in Eqn. 7.5.4) will contribute almost all of V_{em}. Similarly, as the Péclet number varies, the contribution made by molecular diffusion to Q_e, $(\partial T/\partial t)_i$ and V_{em} will also change.

In the next chapter, conclusions that have been drawn from the theoretical, numerical and experimental analyses of the inverted cooling pond model (I.C.P.M.) will be presented. Aspects of this research that require further study will also be discussed.

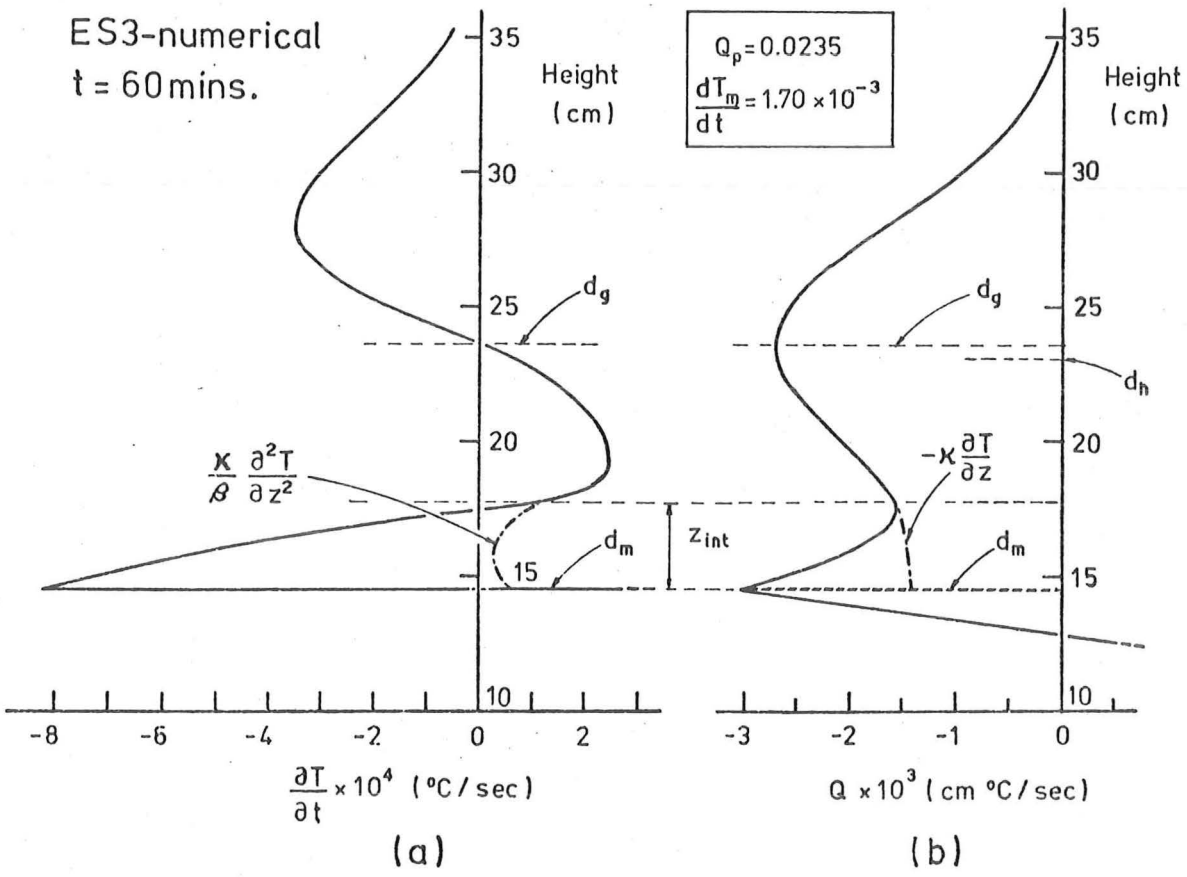

Fig. 7.14. (a) Rate of change of temperature profile and (b) buoyancy heat flux profile from numerical analysis of ES3 at t = 60 minutes ($d_m < d_{g0}$) .

CHAPTER 8

CONCLUSIONS AND RECOMMENDATIONS FOR FUTURE RESEARCH

8.1 CONCLUSIONS

8.1.1 Interfacial Entrainment

Experimental and numerical analyses have shown that penetrative convection in a temperature stratified fluid heated from below can be modelled by assuming that

(i) the turbulent convection layer is fully mixed with uniform temperature;

(ii) the heat transfer in the region of stable density gradient above the mixed layer is due to molecular diffusion and to turbulent entrainment;

(iii) the turbulent entrainment in this stable density gradient region can be parameterized by a turbulent diffusivity γ and an additional molecular diffusion factor λ. Both these parameters tend to zero at a distance of order 0.2 times the mixed layer thickness, above the interface. This is consistent with atmospheric data;

(iv) at the interface between the mixed layer and the diffusion region the partial derivatives of temperature with respect to height $(\partial T/\partial z)$ and time $(\partial T/\partial t)$ are discontinuous.

The assumption that the temperature gradient is discontinuous at the interface is a departure from previous atmospheric models (large Péclet number). In these models, the temperature $T(z,t)$ was discontinuous at the interface. At low Péclet number, when molecular diffusion is significant, the second derivatives of temperature with respect to height $\partial^2 T/\partial z^2$ will be reduced. The thickness of the region of significant density gradients at the interface will therefore be greater. However, even at large Péclet number the interfacial density gradient region will have a finite thickness (of the order of one to two turbulent length scales).

The results of the numerical analyses were in good agreement with the experimental data except when the filling velocity term was

large. The reduced effect of the interfacial domes on the diffusion region fluid (parameterized by the turbulent diffusion term γ) for large filling velocities was not accounted for in the numerical model.

For the low range of Péclet numbers studied, the numerical analyses showed that the contribution made by molecular diffusion to the temperature changes in the diffusion region, and hence, to the rate of rise of the interface, was large. The contribution of the filling velocity to the rate of rise of the interface was also significant. When the interfacial temperature gradients were large, the contributions by turbulent diffusion were relatively small. For example, the interfacial turbulent diffusion term γ in these cases was smaller than the molecular diffusivity κ .

The empirical formula for the interfacial turbulent diffusion term γ_i , developed in the model can be used to express either the non-dimensional interfacial heat flux E or the heat flux ratio k_e as functions of the gradient Richardson number at large Péclet numbers. It was shown that k_e decreases to zero at both high and low Richardson number. Hence, atmospheric models which assume k_e to be a constant are not valid. Other assumptions used in these atmospheric models, such as the temperature discontinuity at the interface (negligible interfacial thickness), have also been shown to cause inaccuracies in the values of k_e obtained from experimental data.

Deardoff, Willis and Lilly's (1969, 1974) horizontally averaged temperature profiles will not show the interfacial temperature gradient discontinuity unless the mixed layer interface is perfectly horizontal. Their temperature profiles do not present the true nature of the penetrative convection process. Similarly, their vertical buoyancy heat flux profiles obtained from time averaged temperature changes were inaccurate in the region of the interfacial discontinuity in $\partial T/\partial t$.

Experimental measurements of temperature at fixed height in the mixed layer during penetrative convection revealed the presence of rising buoyant thermal elements. Just above the interface there is a region of maximum temperature fluctuations caused by the interaction of these thermal elements with the stable interfacial gradients.

An interesting feature of the unsteady heat flux entrainment experiments was the apparent constancy of the entrainment ratio k_m . This ratio, based on the hypothetical heat flux caused by the rate of rise of the interface, hardly varied whenever the interfacial gradients

were significant and the heating fluid temperature T_H was held constant. However, as shown by the steady heat flux entrainment experiments performed later, and the numerical model, this result is not general.

The range of Péclet numbers and initial conditions for the penetrative convection model were based on the conditions in the heat loss region of a power station cooling pond. The implications of this research on the design and operation of cooling ponds should therefore be considered.

Typically, the maximum temperature difference between the warm surface layer and the air above will be of order 10 °C while the surface layer can be up to 5 metres deep. For a heavily loaded cooling pond (approximately 4 Megawatts of electricity output from the station per hectare of cooling pond surface area), the mean surface heat losses need to be greater than 0.020 cal/cm^2 sec. This is of the same order as the heat fluxes used in the steady heat flux experiments (Chapt. 6.5).

Because the surface layer is generally deep, the Rayleigh number will be large. However, it cannot be assumed from the large Rayleigh number and the experiments reported in this thesis that turbulent convection will be maintained over the full surface layer depth. In the experimental investigation, the convection layer depth was only 0.55 metres. In some areas of the pond the surface heat losses may be considerably lower than those near the power station outlet. Hence, the penetrative convection process studied in this thesis, may not be occurring over the full area of the pond.

Other factors will affect the direct applicability of this research to cooling ponds. Wind stresses at the upper surface may increase the amount of turbulent kinetic energy in the mixed layer. However, an expression to account for this additional contribution could be included in the equation for the turbulent velocity scale V_s.

Because the cooling pond is generally a closed system, density currents may be of great importance (Ryan and Harleman 1973). There will be a continuous inflow into the surface layer and most of the cooling water will be withdrawn from the deeper colder layer. Mean horizontal and vertical fluid velocities will therefore be created in the heat loss region of the pond. These flows will not cause a significant amount of shear generated turbulence and were neglected in this study. However, the net flux of fluid through the side boundaries

of the surface layer will increase its rate of deepening.

This study has illustrated the factors influencing the temporal behaviour of penetrative convection at low Péclet numbers and has introduced a method of modelling the interfacial discontinuity when the interfacial region has a finite thickness. However, some care should be taken when applying these results to actual cooling pond problems.

8.1.2 Thermal Convection

In the review of thermal convection given in the appendices, a new graphical form for plotting convection heat flux data was developed. This plot of the heat transfer coefficient c_q versus the logarithm of the Rayleigh number presents the data in greater detail than previous methods. The c_q curve represents the variation of the interplate heat flux when only the interplate spacing is varied. From the form of the c_q versus log Ra curves, it may be speculated that:

(i) At low Rayleigh numbers, between each pair of heat flux transitions, the efficiency of heat transfer increases to a maximum value as the Rayleigh number increases. With further increases in Rayleigh number, the efficiency then decreases.

(ii) At low Rayleigh number , the heat flux transitions represent a change from one type of convective motion to another. This transition occurs whenever the new type of motion becomes more efficient at transferring heat.

(iii) At low Rayleigh number and constant mean temperatures and fluid properties, there may be several different convection layer depths which will give the same heat flux.

(iv) At large Rayleigh numbers ($Ra > 10^{15}$) c_q tends to a minimum asymptote of $c_q = 0.05 \pm 0.01$.

8.2 RECOMMENDATIONS FOR FUTURE RESEARCH

There are a number of aspects of the material studied in this thesis which require further research. These will be discussed under the three headings: theoretical and numerical analyses of the inverted cooling pond model, experimental investigations, and thermal convection.

8.2.1 Theoretical and Numerical Analyses of the Inverted Cooling Pond Model

(i) The analytical inverted cooling pond model could be extended to allow for negative rates of rise of the interface. This would mean that the lower boundary heat flux could be varied over a range of positive and negative values.

(ii) A fuller empirical definition is necessary for the turbulent entrainment parameters beyond the interface. A relationship to describe the reduction in the magnitude of these parameters when the filling velocity term is large, is needed. The effect of an increase in the temperature gradient with height above the interface on the decay of these parameters with height should also be studied in more detail.

(iii) The analytical model might be improved if the mixed layer was assigned a large effective turbulent diffusivity. As with Mellor and Durbin's (1975) model, the existence of the interface would then not need to be assumed in advance. The case when the rate of rise of the interface is negative could also be modelled more easily (see (i) above). However, this type of model might not be feasible as the turbulent diffusivity should still be discontinuous at the interface. It may be difficult to allow for this discontinuity when the interface is at an intermediate height between the finite difference nodes.

8.2.2 Experimental Investigations

(i) Detailed continuous measurements of the temporal variation of temperature at fixed heights are required. These would enable better experimental evaluation of the turbulent entrainment parameters. A range of filling velocities could then be studied to obtain the empirical relationship discussed above (Chapt. 8.2.1 (ii)).

(ii) A laser doppler anenometer, recently acquired by the Department of Civil Engineering, could be used to measure the turbulent velocity field above and below the interface. This would yield information about the decay of turbulence beyond the interface and allow evaluation of some of the turbulence parameters used in the inverted cooling pond model. However, measurements in the strong temperature gradient region at the interface will be difficult because of the varying refractive index of the fluid.

(iii) The entrainment experiments could be performed for a

a wider range of steady lower boundary heat fluxes. The removal of the interfacial temperature gradient discontinuity at low heat flux, by molecular diffusion, could then be studied. However, the heat flux cannot be too large otherwise the experiments will be too unsteady.

(iv) Shadowgraph and Schlieren optical techniques could be used to visualize the penetrative convection motions. The progress of buoyant thermal elements from the heated lower boundary to the interface could then be observed.

(v) A high Péclet number penetrative convection experiment using salinity as the density producing component, could be designed and studied.

8.2.3 Thermal Convection

It is apparent from the review of thermal convection literature given in the appendices that more detailed parallel-plate experiments are required to fully describe the relationship between the Nusselt number and the Rayleigh number for a range of Prandtl numbers and aspect ratios. In particular a series of parallel-plate experiments could be performed in which the mean temperature distribution remained steady, the horizontal geometry was very large and only the plate spacing was varied. A comprehensive plot of the heat transfer coefficient c_q versus the logarithm of the Rayleigh number could then be obtained.

REFERENCES

Adrian, R.J. (1975). "Turbulent convection in water over ice". *J. Fluid Mech.* 69, pp. 753-781.

Baines, W.D. (1975). "Entrainment by a plume or jet at a density interface". *J. Fluid Mech.* 68, pp. 309-320.

Ball, F.K. (1960). "Control of inversion height by surface heating". *Quart. J. Roy. Met. Soc.* 86, pp. 483-494.

Barnum, D.C. and Rao, G.V. (1975). "Role of advection and penetrative convection in affecting the mixing-height variations over an idealized metropolitan area". *Boundary Layer Meteorology*, 8, pp. 497-514.

Bénard, H. (1901). "Les tourbillons cellulaires dans une nappe liquide transportant de la chaleur par convection en régime permanent". *Ann. Chim. Phys.* (7), 23, pp. 62-144.

Betts, A.K. (1973). "Non-precipitating cumulus convection and its parameterization". *Quart. J. Roy. Met. Soc.* 99, pp. 178-196.

Betts, A.K. (1974). "Reply to Deardoff, Willis and Lilly (1974)". *Quart. J. Roy. Met. Soc.* 100, pp. 469-471.

Brown, W. (1973). "Heat-flux transitions at low Rayleigh number". *J. Fluid Mech.* 60, pp. 539-559.

Brush, L.M. Jr. (1970). *Artificial mixing of a stratified fluid formed by salt and heat in a laboratory reservoir.* New Jersey Water Research Institute, 37 pp.

Carslaw, H.S. and Jaeger, J.C. (1965). *Conduction of heat in solids.* Oxford, Clarendon Press, 510 pp.

Carson, D.J. (1973). "The development of a dry inversion-capped convectively unstable boundary layer". *Quart. J. Roy. Met. Soc.* 99, pp. 450-467.

Cattle, H. and Weston, K.J. (1975). "Budget studies of heat flux profiles in the convective boundary layer over land". *Quart. J. Roy. Met. Soc.* 101, pp. 353-363.

Chu, T.Y. and Goldstein, R.J. (1973). "Turbulent convection in a horizontal layer of water". *J. Fluid Mech.* 60, pp. 141-159.

Clarke, R.H., Dyer, A.J., Brook, R.R., Reid, D.G., and Troup, A.J. (1971). "The Wangara Experiment: Boundary Layer Data". *C.S.I.R.O. Div. of Meteorological Physics. Technical Paper No. 19,* 340 pp.

Crapper, P.F. (1976). "Fluxes of heat and salt across a diffusive interface in the presence of grid generated turbulence". *Int. J. Heat and Mass Transfer*, 19, pp. 1371-1378.

Crapper, P.F. and Linden, P.F. (1974). "The structure of turbulent density interfaces". *J. Fluid Mech.* 65, pp. 45-63.

Cromwell, T. (1960). "Pycnoclines created by mixing in an aquarium tank". *J. Marine Research*, 18, pp. 73-82.

Deardoff, J.W. (1970). "Convective velocity and temperature scales for the unstable planetary boundary layer and for Rayleigh convection". *J. Atmos. Sci.* 27, pp. 1211-1213.

Deardoff, J.W. (1974a). "Three-dimensional numerical study of the height and mean structure of a heated planetary boundary layer". *Boundary Layer Meteorology*, 7, pp. 81-106.

Deardoff, J.W. (1974b). "Three-dimensional numerical study of turbulence in an entraining mixed layer". *Boundary Layer Meteorology*, 7, pp. 199-226.

Deardoff, J.W. and Willis, G.E. (1965). "The effect of two-dimensionality on the suppression of thermal turbulence". *J. Fluid Mech.* 23, pp. 337-353.

Deardoff, J.W. and Willis, G.E. (1967). "Investigation of turbulent thermal convection between horizontal plates". *J. Fluid Mech.* 28, pp. 675-704.

Deardoff, J.W., Willis, G.E. and Lilly, D.K. (1969). "Laboratory investigation of non-steady penetrative convection". *J. Fluid Mech.* 35, pp. 7-31.

Deardoff, J.W., Willis, G.E. and Lilly, D,K. (1974). "Comment on the paper by A.K. Betts 'Non-precipitating cumulus convection and its parameterization.' ". *Quart. J. Roy. Met. Soc.* 100 , pp. 122-123.

Denman, K.L. (1973). "A time-dependent model of the upper ocean". *J. Phys. Oceanography.* 3, pp. 173-184.

de Szoeke, R.A. and Rhines, P.B. (1976). "Asymptotic regimes in mixed-layer deepening". *J. Marine Research*, 34, pp. 111-116.

Denton, R.A. and Wood, I.R. (1974). "Convective motions and resulting entrainment in a two-layered fluid system heated from below". *Conference Proceedings-5th Australasian Conference on Hydraulics and Fluid Mechanics*, Christchurch, N.Z., Vol.II, pp. 361-368.

Elder, J.W. (1968). "The unstable thermal interface". *J. Fluid Mech.* 32, pp. 69-96.

Ellison, T.H. and Turner, J.S. (1959). "Turbulent entrainment in stratified flows". *J. Fluid Mech.* 6, pp. 423-448.

Farmer, D.M. (1975). "Penetrative convection in the absence of mean shear". *Quart. J. Roy. Met. Soc.* 101, pp. 869-891.

Fitzjarrald, D.E. (1976). "An experimental study of turbulent convection in air". *J. Fluid Mech.* 73, pp. 693-719.

Fortescue, G.E., and Pearson, J.R.A. (1967). "On gas absorption into a turbulent liquid". *Chemical Engineering Science*, 22, pp. 1163-1176.

Garon , A.M. and Goldstein, R.J. (1973). "Velocity and heat transfer measurements in thermal convection". *Physics of Fluids*, 16, pp. 1818-1825.

Gille, J. (1967). "Interferometric measurement of temperature gradient reversal in a layer of convecting air". *J. Fluid Mech.* 30, pp. 371-384.

Goldstein, R.J. and Chu, T.Y. (1969). "Thermal convection in a horizontal layer of air". *Prog. Heat and Mass Transfer*, 2, pp. 55-75.

Hollands, K.G.T., Raithby, G.D. and Konicek, L. (1975). "Correlation equations for free convection heat transfer in horizontal layers of air and water". *Int. J. Heat and Mass Transfer*, 18, pp.879-884.

Hopfinger, E.J. and Toly, J-A. (1976). "Spatially decaying turbulence and its relation to mixing across density interfaces". *J. Fluid Mech.*, 78, pp. 155-175.

Howard, L.N. (1964). "Convection at high Rayleigh number". *Proceedings - Eleventh International Congress Applied Mechanics*, Munich,(ed. H. Görtler), Berlin: Springer-Verlag, pp. 1109-1115.

Jenkins, B.S. (1973). "Studies of the flow of a fluid with density differences caused by turbidity". *Report No. 133, Water Research Laboratory (Univ. of N.S.W.)*, 201 pp.

Jenkins, B.S. (1974). "Turbulent entrainment across a density discontinuity as a result of surface cooling". *Paper presented to 5th Australasian Conference on Hydraulics & Fluid Mechanics*, Christchurch, N.Z.

Kato, H. and Phillips, O.M. (1969). "On the penetration of a turbulent layer into a stratified fluid". *J. Fluid Mech.* 37 pp. 643-655.

Keulegan, G.H. (1949). "Interfacial instability and mixing in stratified flows". *J. of Research of the National Bureau of Standards*, 43, pp. 487-500.

Krishnamurti, R. (1970a). "On the transition to turbulent convection - Part 1 - the transition from two to three dimensional flow". *J. Fluid Mech.* 42, pp. 295-307.

Krishnamurti, R. (1970b). "On the transition to turbulent convection - Part 2 - the transition to time-dependent flow". *J. Fluid Mech.* 42, pp. 309-320.

Kuo, H.L. and Sun, W.Y. (1976). "Convection in the lower atmosphere and its effects". *J. Atmos. Sci.* 33, pp. 21-40.

Lenschow, D.H. and Johnstone, W.B. Jnr. (1968). "Concurrent airplane and balloon measurements of atmospheric boundary-layer structure over a forest". *J. Applied Meteorology*, 7 , pp. 79-89.

Lettau, H.H. and Davidson, B. (1957). *Exploring the Atmosphere's First Mile. Vol.2.* New York, Pergamon Press, 578 pp.

Lilly, D.K. (1968). "Models of cloud-topped mixed layers under a strong inversion". *Quart. J. Roy. Met. Soc.* 94, pp. 292-309.

Linden, P.F. (1973). "The interaction of a vortex ring with a sharp density interface: a model for turbulent entrainment". *J. Fluid Mech.* 60, pp. 467-480.

Linden, P.F. (1975). The deepening of a mixed layer in a stratified fluid". *J. Fluid Mech.* 71, pp. 385-405.

Lofquist, K. (1960). "Flow and stress near an interface between stratified fluids". *Physics of Fluids*. 3, pp. 158-175.

Long, R.R. (1972). "Some aspects of turbulence in stratified fluids". *Applied Mechanics Review*, pp. 1297-1301.

Long, R.R. (1975). "The influence of shear on mixing across density interfaces". *J. Fluid Mech.*, 70, pp. 305-320.

Long, R.R. (1976). "Relation between Nusselt number and Rayleigh number in turbulent thermal convection". *J. Fluid Mech.*, 73, pp. 445-451.

Lumley, J.L. and Panofsky, H.A. (1964). *The structure of atmospheric turbulence*. New York, Interscience, 239 pp.

Mahrt, L. and Lenschow, D.H. (1976). "Growth dynamics of the convectively mixed layer". *J. Atmos. Sci.*, 33, pp. 41-51.

Malkus, W.V.R. (1954). "Discrete transitions in turbulent convection". *Proc. Roy. Soc. A*, 225, pp. 185-195.

Manton, M.J. (1975). "Penetrative convection due to a field of thermals". *J. Atmos. Sci.*, 32, pp. 2272-2277.

McEwan, A. (1974). "Thermal convection above a radiatively heated inversion. A laboratory simulation of stratus cloud". *Paper presented to - Fifth Australasian Conference of Hydraulics and Fluid Mechanics*, Christchurch, N.Z.

Mellor, G.L. (1973). "Analytic prediction of the properties of stratified planetary surface layers". *J. Atmos. Sci.*, 30, pp. 1061-1069.

Mellor, G.L. and Yamada, T. (1974). "A hierachy of turbulence closure models for planetary boundary layers". *J. Atmos. Sci.*, 31, pp. 1791-1806.

Mellor, G.L. and Durbin, P.A.,(1975). "The structure and dynamics of the ocean surface mixed layer". *J. Phys. Oceanography*, 5, pp. 718-728.

Moore, M.J. and Long, R.R. (1971). "An experimental investigation of turbulent stratified shearing flow". *J. Fluid Mech.*, 49, pp. 635 - 655.

Munk, W.H. and Anderson, E.R. (1948). "Notes on a theory of the thermocline". *J. Marine Research*, 7, pp. 276-295.

Niiler, P.P. (1975). "Deepening of the wind mixed layer". *J. Marine Research*, 33, pp. 405-422.

O'Toole, J.L. and Silveston, P.L. (1961). "Correlations of convective heat transfer in confined horizontal layers". *Chem. Eng. Prog. Symp.*, 57, pp. 81-86.

Pollard, R.T., Rhines, P.B. and Thompson, R.O.R.Y. (1973). "The deepening of the wind-mixed layer". *Geophysical Fluid Dynamics*, 3, pp. 381-404.

Rayment, R. and Readings, C.J. (1974). "A case study of the structure and energetics of an inversion". *Quart. J. Roy. Met. Soc.*, 100, pp. 221-233.

Readings, C.J. (1973). "Some aspects of the Cardington Research Program". *Quart. J. Roy. Met. Soc.*, 99, pp. 764-767.

Rouse, H. and Dodu, J. (1955). "Diffusion turbulente à travers une discontinuité de densité". *La Houille Blanche*, 10, pp. 522-532.

Ryan, P.J. and Harleman, D.R.F. (1973). "An analytical and experimental study of transient cooling pond behaviour". *Ralph M. Parsons Laboratory for Water Resources and Hydrodynamics, Report No. 161*, 439 pp.

Sarachik, E.S. (1974). "The tropical mixed layer and cumulus parameterization". *J. Atmos. Sci.*, 31, pp. 2225-2230.

Schiller, E.J. and Sayre, W.W. (1973). "Vertical mixing of heated effluents in open-channel flow". *Iowa Institute of Hydraulic Research, Report No. 148.*, 146 pp.

Schmidt, E. and Silveston, P.L. (1959). "Natural convection in horizontal liquid layers". *Chem. Eng. Prog. Symp.*, 55, pp. 163-169.

Shirtcliffe, T.G.L. (1973). "Transport and profile measurements of the diffusive interface in double-diffusive convection with similar diffusivities". *J. Fluid Mech.*, 57, pp. 27-43.

Sparrow, E.M., Husar, R.B., and Goldstein, R.J. (1970). "Observations and other characteristics of thermals". *J. Fluid Mech.*, 41, pp. 793-800.

Stull, R.B., (1973). "Inversion rise model based on a penetrative convection". *J. Atmos. Sci.*, 30, pp. 1092-1099.

Stull, R.B. (1976a). "The energetics of entrainment across a density interface". *J. Atmos. Sci.*, 33, pp. 1260-1267.

Stull, R.B. (1976b). "Mixed-layer depth model based on turbulent energetics". *J. Atmos. Sci.*, 33, pp. 1268-1278.

Telford, J.W. and Warner, J. (1974). "Fluxes of heat and water vapour in the lower atmosphere derived from aircraft observations". *J. Atmos. Sci.*, 21, pp. 539-548.

Tennekes, H. (1973). "A model for the dynamics of the inversion above a convective boundary layer". *J. Atmos. Sci.*, 30, pp. 558-567.

Tennekes, H. (1975). "Reply to Zilitinkevich (1975)". *J. Atmos. Sci.*, 32, pp. 992-995.

Thomas, D.B. and Townsend, A.A. (1957). "Turbulent convection over a heated horizontal surface". *J. Fluid Mech.*, 2, pp. 473-492.

Thompson, S. and Turner, J.S. (1975). "Mixing across an interface due to turbulence generated by an oscillating grid". *J. Fluid Mech.*, 67, pp. 349-368.

Thorpe, S.A. (1973). "Turbulence in stably stratified fluids. A review of laboratory experiments". *Boundary Layer Meteorology*, 5, pp. 95-119.

Threlfall, D.C. (1975). "Free convection in low-temperature gaseous helium". *J. Fluid Mech.*, 67, pp. 17-28.

Townsend, A.A. (1959). "Temperature fluctuations over a heated horizontal surface". *J. Fluid Mech.*, 5, pp. 209-241.

Townsend, A.A. (1964). "Natural convection in water over an ice surface". *Quart. J. Roy. Met. Soc.*, 90, pp. 248-259.

Townsend, A.A. (1976). *The structure of turbulent shear flow*. 2nd. ed., Cambridge University Press.

Turner, J.S. (1965). "The coupled turbulent transports of salt and heat across a sharp density interface". *Int. J. Heat and Mass Transfer*, 8, pp. 759-767.

Turner, J.S. (1968). "The influence of molecular diffusivity on turbulent entrainment across a density interface". *J. Fluid Mech.*, 33, pp. 639-656.

Turner, J.S. (1973). *Buoyancy effects in fluids*. Cambridge University Press. 367 pp.

Turner, J.S. and Kraus, E.B. (1967). "A one-dimensional model of the seasonal thermocline - Pt. I - A laboratory experiment and its interpretation". *Tellus*, 19, pp. 88-97.

Willis, G.E. and Deardoff, J.W. (1967a). "Development of short-period temperature fluctuations in thermal convection". *Physics of Fluids*, 10, pp. 931-937.

Willis, G.E. and Deardoff, J.W. (1967b). "Confirmation and renumbering of the discrete heat flux transitions of Malkus". *Physics of Fluids*, 10, pp. 1861-1866.

Willis, G.E. and Deardoff, J.W. (1974). "A laboratory model of the unstable planetary boundary layer". *J. Atmos. Sci.*, 31, pp. 1297-1307.

Wolanski, E.J. and Brush, L.M.Jr. (1975). "Turbulent entrainment across stable density step structures". *Tellus*, 27, pp. 259-268.

Wu, J. (1973). "Wind-induced turbulent entrainment across a stable density interface". *J. Fluid Mech.*, 61,pp. 275-287.

Zeman, O. and Tennekes, H. (1977). "Parameterization of the turbulent energy budget at the top of the daytime atmospheric boundary layer". *J. Atmos. Sci.*, 34, pp.111-123.

Zilitinkevich, S.S. (1975). "Comments on 'A model for the dynamics of the inversion above a convection boundary layer'". *J. Atmos. Sci.*, 32, pp. 991-992.

APPENDIX A

THERMAL CONVECTION ABOVE OR BELOW HORIZONTAL BOUNDARIES

A.1 INTRODUCTION

In the inverted cooling pond model (I.C.P.M.) the rate of rise of the interface is directly linked to the thermal convection processes occurring above the heated lower boundary. The convective heat flux q_p through the lower boundary represents a transfer of both heat and turbulent kinetic energy.

The net heat input causes the mixed layer fluid to become more buoyant than the diffusion region fluid immediately above it, thereby allowing the interface to rise (Chapt. 3.6). Turbulent kinetic energy caused by the buoyancy flux at the lower boundary is transported throughout the mixed layer. Some of the turbulent kinetic energy is available at the interface for turbulent entrainment. This also contributes to the rate of rise of the interface.

As part of this I.C.P.M. study, it is important to understand both the heat transfer properties and the convective motions of a fluid layer heated from below.

The convective flow induced by the temperature differences between two horizontal plates has been studied extensively since the turn of the century (Bénard 1901). The original incentive for this study was the similarity of this flow with flows induced by heat transfer from the earth's surface. However, the flow has inherent interest in that, with large distances between the plates (d) or large interplate temperature differences (ΔT) , the source of energy for the turbulent motion comes from the potential energy supplied by the heating (the buoyancy flux) and the flow is not complicated by any mean shearing mechanism. In spite of this apparent simplicity, very little progress has been made in understanding the flow processes. Indeed, Townsend (1976) states that the only firm predictions that can be made are dimensional ones.

Experiments designed to study thermal convection above or below horizontal boundaries, typically consist of a fluid confined between two horizontal plates of plate spacing d and minimum horizontal dimension L . The lower plate is maintained at temperature T_p and the upper plate at a lower temperature, $T_p - \Delta T$. In these parallel-

plate experiments, the mean vertical temperature distribution adjusts to a steady state profile with the resultant heat flux q_p being uniform across the fluid. A special case is the single-plate experiment, where only the lower plate is conducting and the upper surface, either free or fixed, is insulated. The disadvantage of this type of experiment is that there is a net heat flux into the fluid and the mean fluid temperature T_m is continually increasing. For single-plate convection, the vertical heat flux decreases linearly from Q_p at the lower boundary to zero at the upper insulated boundary.

Because parallel-plate experiments can be maintained in a steady state, the majority of thermal convection experiments reported in the literature and discussed in this appendix, take that form.

As the interfacial heat flux Q_e in the I.C.P.M. is negative, no buoyancy instabilities are created at $z = d_m$. The thermal convection process more closely resembles single-plate convection. However, Q_e does contribute to the increase in heat content of the mixed layer. Because the upper boundary of the convecting layer in the I.C.P.M. consists of a stable density gradient, it is more responsive to vertical motions than an air-water interface. Despite these differences, single- and parallel-plate convection experiments illustrate similar thermal convection processes to those occurring in the I.C.P.M.

In this appendix, previously published measurements of heat transfer, mean temperature profiles and r.m.s. values of the velocity and temperature fluctuations for thermal convection are reviewed. As part of the review of heat flux data, a new data plotting method is developed. Howard's (1964) phenomenological theory of turbulent convection above a heated plate is also discussed. This theory provides an explanation for the presence of rising thermal elements in the mixed layer of the I.C.P.M.

A.2 EXPERIMENTAL HEAT FLUX DATA

In a parallel-plate convection experiment, the heat flux per unit area q_p will depend upon the minimum plan dimension of the horizontal plates L and the distance d and temperature difference ΔT between them. When the lower plate is hotter (ΔT positive), the resulting heat flux per unit area q_p is positive. The fluid properties affecting q_p are the density ρ, kinematic viscosity ν, molecular thermal diffusivity κ, specific heat per unit mass c_p and the thermal coefficient of volumetric expansion α where

$$\alpha = -\frac{1}{\rho}\frac{\partial \rho}{\partial T} \qquad \text{(A.2.1)}$$

If the normal Boussinesq approximation is made, dimensional analysis yields

$$\frac{Q\,d}{\kappa\,\Delta T} = \phi\left[\alpha g \frac{\Delta T}{\nu\kappa} d^3, \frac{\nu}{\kappa}, \frac{L}{d}\right] \qquad \text{(A.2.2)}$$

where Q is the buoyancy heat flux per unit area, given by

$$Q = q_p / \rho c_p$$

The term on the left hand side of Eqn. A.2.2 is the Nusselt number Nu. It is the ratio of the actual buoyancy flux to the flux that would occur by molecular diffusion alone. The first term on the right hand side of Eqn. A.2.2 is the Rayleigh number Ra. This is the ratio between the buoyancy force and the two diffusive processes. The remaining terms are the Prandtl number Pr and the aspect ratio.

The ranges of Prandtl number, Rayleigh number and aspect ratio for the parallel- and single-plate convection experiments reported in the literature are listed in Table A.1. Empirical formulae for Nu obtained from some of these experiments are also given.

A.2.1 Previous Methods of Plotting Heat Flux Data

In the majority of the early experiments, it was assumed that the aspect ratio L/d was sufficiently large for the effect of the width L to be negligible. Experimental results were then plotted as a graph of Nusselt number versus Rayleigh number on a log-log scale, with the Prandtl number as a parameter. A number of these experimental results are plotted in Fig. A.1.

Below a critical Rayleigh number Ra_c, heat is tranferred by conduction alone, so $Nu = 1$. The value of $Ra_c = 1708$, determined theoretically by linear stability theory (Turner 1973), is well verified.

At large plate spacings (d) and hence, large Ra, it might be expected that the heat transfer will be independent of d. This would suggest a slope of one-third for the high Rayleigh number data in Fig. A.1. However, the results shown suggest slopes slightly less than one-third. Whilst each experimenter's results are consistent, there is considerable variation between individual sets of results. This cannot be explained purely in terms of Prandtl number dependence.

TABLE A.1 - DETAILS OF PREVIOUSLY REPORTED THERMAL CONVECTION EXPERIMENTS

PARALLEL PLATE EXPERIMENTS

Experimenter	Prandtl No.	Range of Rayleigh Nos.	Heat Flux in Turbulent Regions	Aspect Ratio
Malkus 1954	3.7 - 7	$\rightarrow 10^{10}$	$Nu = 0.08456\ Ra^{0.325}$	0.5 - 77
Thomas & Townsend 1957	0.71	8.52×10^4 3.76×10^5 6.75×10^5	-	5.1 - 10.3
Schmidt & Silveston 1959	3 - 4000	$\rightarrow 10^5$	$Nu = 0.10\ Ra^{0.31}\ Pr^{0.05}$	15.3 - 137
O'Toole & Silveston 1961	0.03 - 10^4	$10^3 - 10^9$	$Nu = 0.104\ Ra^{0.305}\ Pr^{0.084}$	1.9 - 137
Deardoff & Willis 1967	0.71	6.3×10^5 2.5×10^6 1×10^7	Nu = 6 (4.5 - 6.5) Nu = 8.2 (5.5 - 11) Nu = 11 (9 - 17)	5.2 - 9.4
Willis & Deardoff 1967 a	0.71 - 57	$5 \times 10^3 - 2 \times 10^6$	-	33 - 76
Willis & Deardoff 1967 b	0.71 - 57	$\rightarrow 2.8 \times 10^6$	-	6.7 - 76
Gille 1967	0.71	2.6×10^3, 6.8×10^3, 2.85×10^4		8.2 - 12.8
Goldstein & Chu 1969	0.71	$6.88 \times 10^6 - 1.23 \times 10^8$	$Nu = 0.123\ Ra^{0.294}$	1.0 - 4.7
Krishnamurti 1970 a & b	0.71 - 8500	$10^3 - 10^6$	-	9.8 - 98
Chu & Goldstein 1973	6	$2.76 \times 10^5 - 1.05 \times 10^8$	$Nu = 0.183\ Ra^{0.278}$	1.5 - 6.0
Garon & Goldstein 1973	5.5	$1.36 \times 10^7 - 3.29 \times 10^9$	$Nu = 0.130\ Ra^{0.293}$	2.5 - 4.5
Wendell Brown 1973	0.71	$10^3 - 5.4 \times 10^4$	-	12 - 53
Threlfall 1975	0.66 - 0.91	$60 - 2 \times 10^9$	$Nu = 0.173\ Ra^{0.28}$	2.5
Fitzjarrald 1976	0.71	$4 \times 10^4 - 7 \times 10^9$	$Nu = 0.13\ Ra^{0.30}$	1.9 - 58

SINGLE PLATE EXPERIMENTS

For these cases the Rayleigh Number has been computed assuming that ΔT is twice temperature difference between the plate and its surroundings and d is twice depth from the plate to the unheated surface

Thomas & Townsend 1957	6.7	3.43×10^9 9.10×10^9 1.36×10^{10}	Nu = 120.1 Nu = 145.6 Nu = 169.8	2.0
Townsend 1959	0.71	$1.39 \times 10^9 - 1.74 \times 10^{10}$	Nu = 79.6 - 179.7	0.5 - 1.1

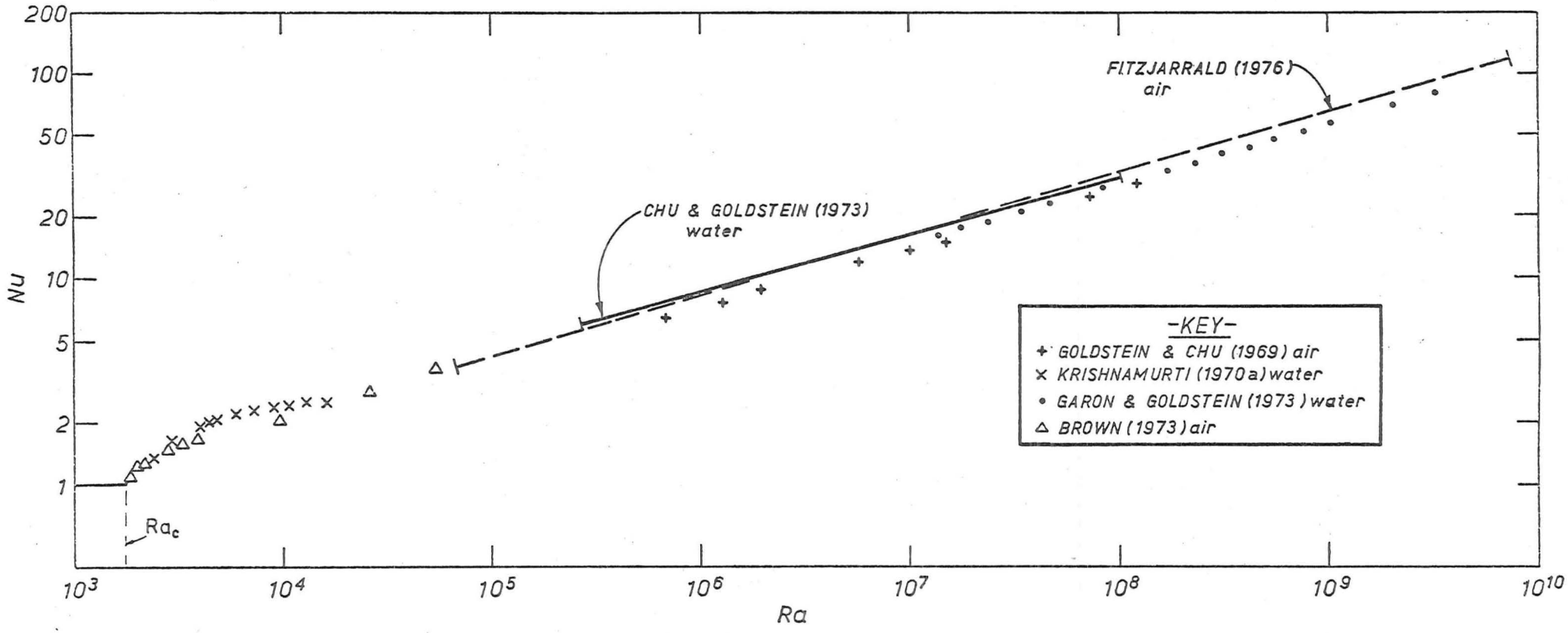

Fig. A.1. Nusselt number data from parallel-plate experiments plotted as a function of Rayleigh number. Both axes have logarithmic scales.

For practical reasons, parallel plate convection experiments are generally carried out for a small number of plate spacings and a large range of interplate temperature differences. For each run it is therefore more logical to use dimensionless numbers which separate Q and ΔT. Malkus (1954) introduced this idea by rewriting Eqn. A.2.2 in the form

$$Nu\ Ra = \phi(Ra, Pr, L/d) \qquad (A.2.3)$$

The product $Nu\ Ra$ removes ΔT from the left hand side of the equation. If d and the fluid properties are not varied, $Nu\ Ra$ is a non-dimensional heat flux. When plotted in the form $Nu\ Ra$ versus Ra, heat flux data from runs with one type of fluid appear as a series of straight lines with sharp transitions in slope (Fig. A.2).

Krishnamurti (1970 a,b) has studied in great detail the occurrence of heat flux transitions over a wide range of Prandtl numbers (Fig. A.3). The first transition at Ra_c is the onset of convection. Immediately above the critical Rayleigh number, two-dimensional rolls occur. The second transition occurs in conjunction with a change to a steady three-dimensional hexagonal cells. Between the third and fifth transitions, the flow has a time dependent nature. The intermittent nature of the convective flow over the same range of Rayleigh numbers has also been reported by Willis and Deardoff (1967a). At higher Rayleigh number, the flow becomes turbulent.

The heat flux transitions above Ra_c are Prandtl number dependent for $Pr < 100$ (Fig. A.3). At high Prandtl numbers, the buoyant fluid retains its heat but its motions are damped. The flow motions therefore remain steady up to high Rayleigh number. However, at low Pr, the transitions to turbulent flow occur at much lower Rayleigh number. In the case of mercury ($Pr = 0.025$), the onset of turbulent flow occurs immediately above Ra_c (Turner 1973).

Even in the turbulent convection region there must be some organization of the flow. This is apparent from the transitions in slope of $Nu\ Ra$ versus Ra plots at moderately high Rayleigh number. Figure A.2 shows a heat flux transition in the data of Garon and Goldstein (1973) at $Ra = 1.3 \times 10^8$.

The occurrence of heat flux transitions appears to be well established. Figure A.4 and A.5 show the transition Rayleigh numbers reported by other investigators (Table A.1). They are plotted on the empirical heat flux curves of O'Toole and Silveston (1961) given by

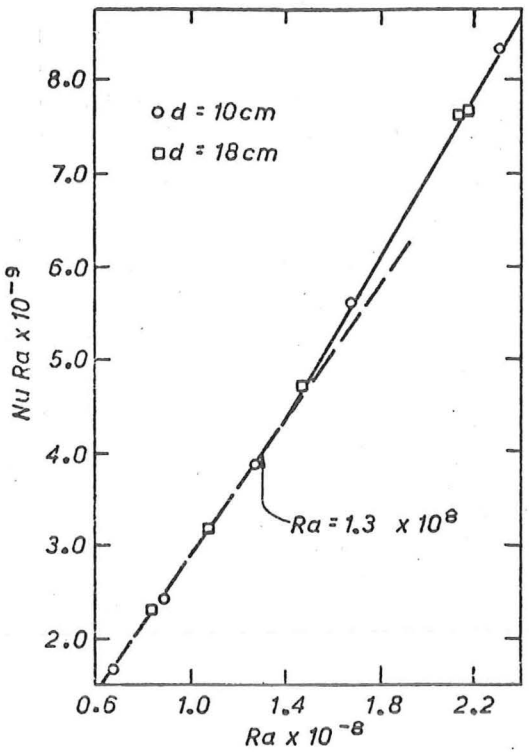

Fig. A.2. Non-dimensional heat flux Nu Ra as a function of Rayleigh number at high Ra showing a heat flux transition. (From Garon and Goldstein 1973).

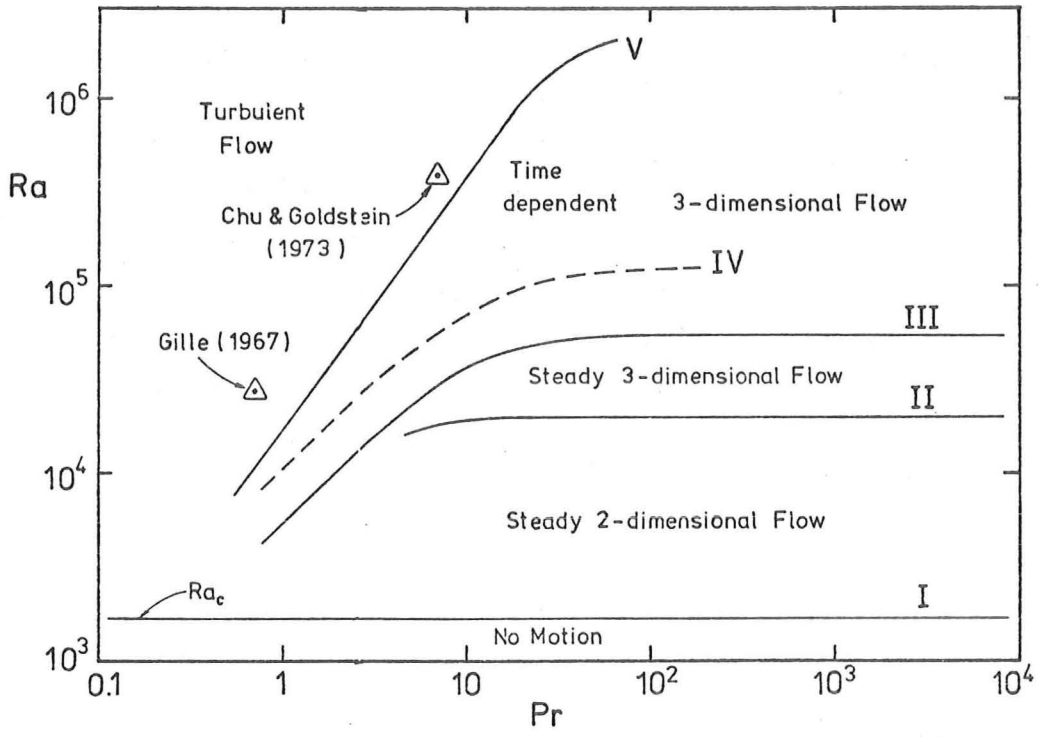

Fig. A.3. Diagram showing the heat flux transitions and the types of convective flow observed between them as functions of Rayleigh number and Prandtl number. (From Krishnamurti 1970a,b.). Triangular data points show Rayleigh numbers at which temperature gradient reversals have been observed in air and water.

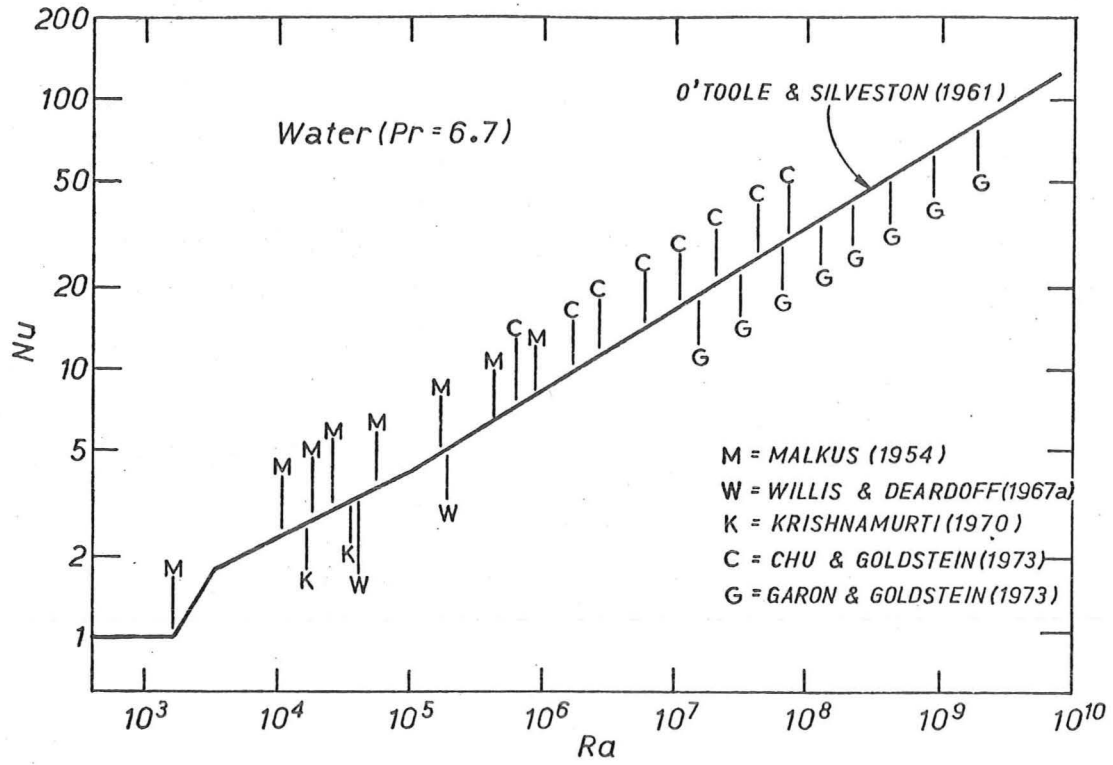

Fig. A.4. Heat flux transition Rayleigh numbers for water (Pr = 6.7) plotted on the empirical curves of O'Toole and Silveston (1961).

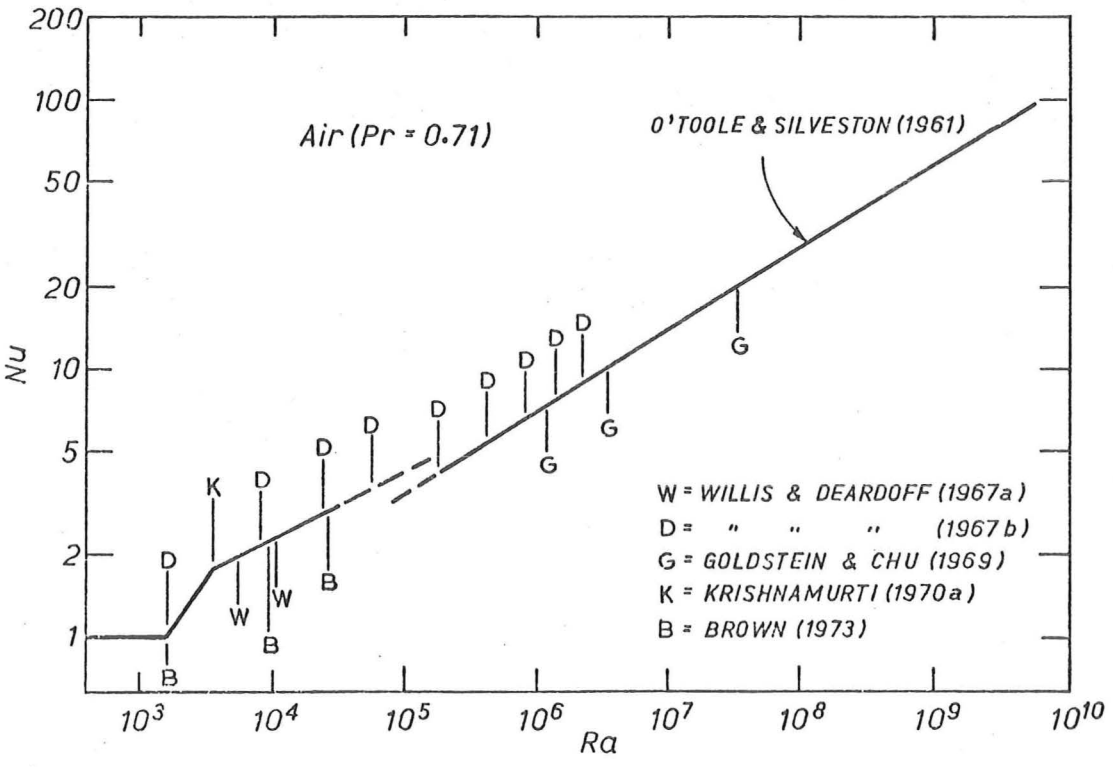

Fig. A.5. Heat flux transition Rayleigh numbers for air (Pr = 0.71) plotted on the empirical curves of O'Toole and Silveston (1961).

$$
\begin{aligned}
Nu &= 2.38 \times 10^{-3}\, Ra^{0.816} && 1700 < Ra < 3500 \\
Nu &= 0.229\, Ra^{0.252} && 3500 < Ra < 10^{5} \\
Nu &= 0.104\, Ra^{0.305}\, Pr^{0.084} && 10^{5} < Ra < 10^{9}
\end{aligned}
\qquad \text{(A.2.4)}
$$

The regularity of the transition Rayleigh numbers for each set of results is remarkable. At high Ra , the spacings represent approximate multiples of two.

Some confusion arises when the work of Willis and Deardoff (1967b) is considered. For air and silicon oil (Pr = 0.71 and 57) , they obtained approximately the same transition Rayleigh numbers (for $Ra > 2.5 \times 10^{4}$) as Malkus (1954). Both sets of transition Rayleigh numbers are listed in Table A.2. They are also shown as points D and M in Figs. A.5 and A.4 respectively. Because Malkus' experiments were for acetone and water (Pr = 3.7, 7) , this correspondence seems to suggest that heat flux transitions are independent of Prandtl number. However, this conflicts with the measurements of Krishnamurti (1970 a,b) in which the dependence of the heat flux transitions on the Prandtl number is clearly shown (Fig. A.3).

TABLE A.2 - A COMPARISON OF THE HEAT FLUX TRANSITION RAYLEIGH NUMBERS MEASURED BY WILLIS AND DEARDOFF (1967b) AND MALKUS (1954) AT DIFFERENT PRANDTL NUMBERS

Transition Number	Willis & Deardoff (1967b) Pr = 0.71 (57)	Malkus (1954) Pr = 3.7, 7
1	1750	1700
2	8200 (8000)	
3	2.4×10^{4} (2.5)	1.8×10^{4}
4	5.6×10^{4} (5.4)	5.5×10^{4}
5	1.8×10^{5}	1.7×10^{5}
6	4.1×10^{5}	4.25×10^{5}
7	8.3×10^{5}	8.6×10^{5}
8	1.4×10^{6}	1.7×10^{6}
9	2.25×10^{6}	-

If the curves of heat flux data on a $Nu\ Ra$ versus Ra plot are approximately linear between transitions they should appear as a series of shallow concave downwards arcs on a $\log Nu$ versus $\log Ra$ plot (e.g. Fig. A.1). However, the plot of $\log Nu$ versus $\log Ra$ presents heat flux data in much less detail than a $Nu\ Ra$ versus Ra plot so that only the arc between the first and second transitions is generally apparent. With increasing Rayleigh number, the arcs become less distinct.

Except for Threlfall (1975), all the other experimenters discussed in this appendix (Table A.1) have presented their heat flux data in the forms $\log Nu$ versus $\log Ra$ and $Nu\ Ra$ versus Ra. To remove the mean trend of his data Threlfall (1975) plotted $Nu/Ra^{\frac{1}{4}}$ versus $\log Ra$. His choice of the $\frac{1}{4}$ power appears to have been arbitrary with no theoretical basis. However, there is another method of plotting heat flux data for which the ordinate also takes the form of a non-dimensional heat flux (c.f. $Nu\ Ra$). To the writer's knowledge, this plotting form has not previously been reported. It is discussed in the next section.

A.2.2 The Graphical Form c_q Versus the Logarithm of the Rayleigh Number

The product $Nu\ Ra$ has previously been described as the non-dimensional heat flux because, for fixed interplate spacing d, a plot of $Nu\ Ra$ versus Ra represents the variation of the buoyancy heat flux Q with changes in ΔT. The variation of the fluid properties is assumed to make a minor contribution.

However, Q is also a function of d. For this I.C.P.M. study, it would be interesting to know the variation of the buoyancy heat flux Q with convection layer thickness, as this would reveal at what stage the heat transfer becomes independent of d_m.

It can easily be shown that the plotting form corresponding to Q versus d if all other quantities (ΔT, Pr, L/d) are fixed, or in the case of the aspect ratio have negligible effect, is

$$Nu/Ra^{\frac{1}{3}} \quad \text{versus} \quad Ra^{\frac{1}{3}}$$

The ratio $c_q = Nu/Ra^{\frac{1}{3}}$ will hereafter be referred to as the heat transfer coefficient c_q. With the exception of Brown (1973), experiments with constant ΔT and variable d are seldom performed due to the practical problems of continuously varying d. To evaluate the heat transfer coefficient c_q from previously published data it will be assumed that,

for constant aspect ratio and Prandtl number, there is only one value of Nu for each value of Ra. Hence, data from variable ΔT experiments can be used to plot the hypothetical c_q data from a variable d experiment.

The most detailed method of presenting heat flux data, used in the literature, is the graphical form $Nu\ Ra$ versus Ra. If the data between the heat flux transitions in this form is held to be linear, then between transitions X_i and X_{i+1}

$$Nu\ Ra = m_{i,i+1}\ Ra - c_{i,i+1} \qquad (A.2.5)$$

where m and c are the slope and negative intercept of the straight line.

When this linear relationship between $Nu\ Ra$ and Ra is mapped onto a $c_q = Nu/Ra^{1/3}$ versus $\log Ra$ plane, it yields a series of distinct concave downwards curves (Fig. A.6). The logarithmic scale is used for the Rayleigh number abscissa because it allows a greater range of points to be plotted. However, as heat flux transition Rayleigh numbers appear to be more regular on a logarithmic scale (Figures A.4 and A.5), the c_q curves will also be more regular when a $\log Ra$ abscissa is used.

Figure A.6 shows the c_q versus $\log Ra$ data from the experiments of Krishnamurti (1970a) and Silveston (as reported by Brown 1973), for water between transitions X_1 and X_2. The fitted curves are transformed straight line data from a $Nu\ Ra$ versus Ra plot. The slopes of the straight line data, reported by Krishnamurti (1970a), were $m_{12} = 2.72$ and $m_{23} = 4.4$. For transitions X_1, X_2 and X_3, the transition Rayleigh numbers were Ra_c, $10\ Ra_c$ and $21\ Ra_c$ respectively. Also plotted are O'Toole and Silveston's (1961) empirical curves for $1700 < Ra < 3500$ and $3500 < Ra < 10^5$ (Eqn. A.2.4). It is quite apparent that the transformed straight line only fits the c_q versus $\log Ra$ data for the higher Rayleigh numbers between transitions X_1 and X_2 (Fig. A.6).

On a plot of $Nu\ Ra$ versus Ra, the departure of the lower Rayleigh number data from a straight line fit is not so obvious. For instance, the data above the maximum c_q Rayleigh number ($Ra \approx 4320$) in Fig. A.6 will occupy three-quarters of the corresponding $Nu\ Ra$ versus Ra plot because the abscissa is linear. The data below this maximum c_q Rayleigh number, which does not agree with the transformed straight lines, is presented in much less detail.

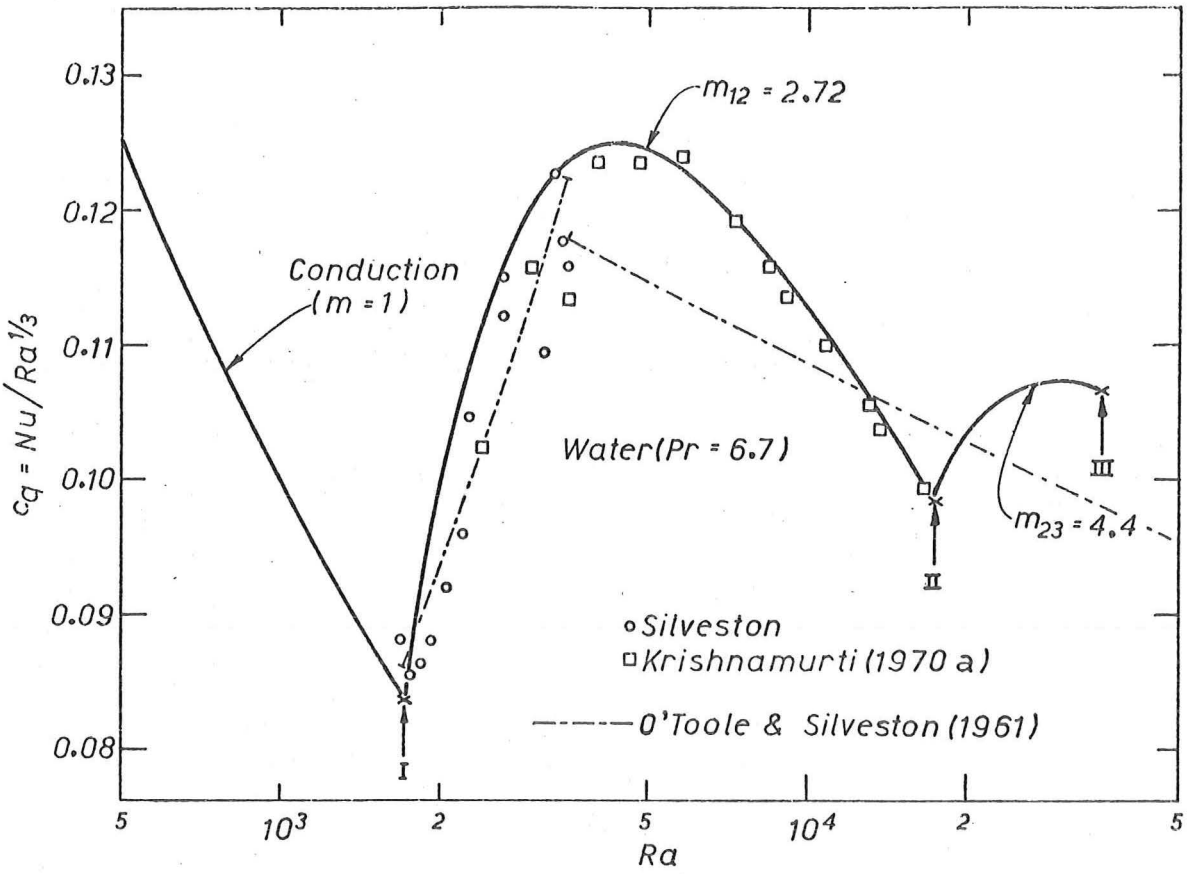

Fig. A.6. Heat transfer coefficient c_q for water (Pr = 6.7) at low Rayleigh number plotted against the logarithm of the Rayleigh number.

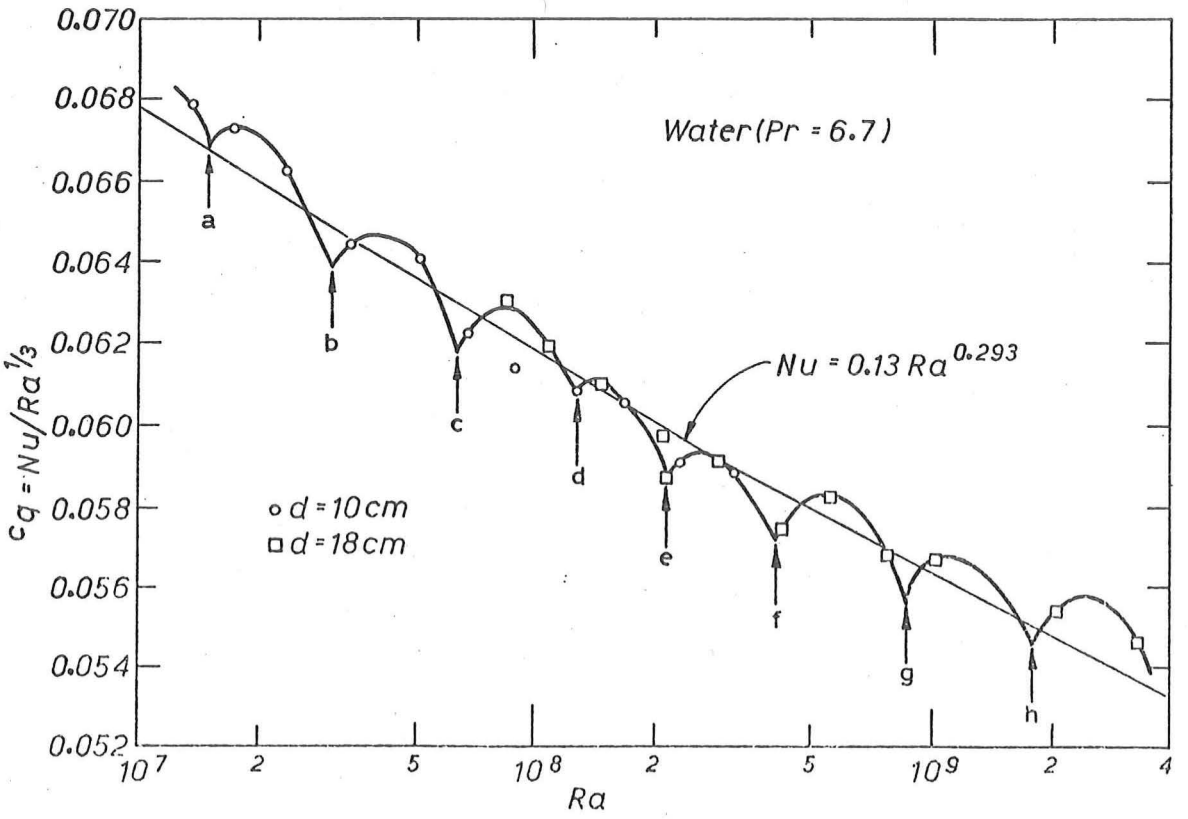

Fig. A.7. Heat transfer coefficient c_q for water (Pr = 6.7) at high Rayleigh number plotted against the logarithm of the Rayleigh number.

A similar c_q versus log Ra plot for high Rayleigh number can be obtained from Garon and Goldstein's (1973) data (Fig. A.7). Garon and Goldstein reported four heat flux transitions (corresponding to transitions c , d , e and f in Fig. A.7). However, their data suggest four more transitions, although these are not accurately defined. For instance, only one data point occurred above transition a , and between transitions g and h (Fig. A.7). In these cases, the slope of the straight line on a Nu Ra versus Ra plot was chosen by assuming that the spacing of the transition Rayleigh numbers on a logarithmic scale is regular (e.g. Figs. A.4 and A.5).

High Rayleigh number data produces less distinct c_q versus log Ra curves (Fig. A.7). Consider, for instance, the data point (for d = 10 cm) which does not lie on the arc between transitions c and d . If it is in fact inaccurate then the experimental scatter is as great as the amplitude of the c_q versus log Ra arcs. It should be noted that if this data point is accurate then Garon and Goldstein's (1973) results for d = 10 and 18 cm could be fitted with two separate curves. This would suggest c_q has an additional dependence of the plate spacing d and would not support the form of the c_q curves in Fig. A.7. However, if the apparent linearity of Nu Ra versus Ra data is accepted then the occurrence of the concave downward arcs between the heat flux transitions on a c_q versus log Ra plot must also be accepted.

Because the graphical form c_q versus log Ra presents the data in greater detail than previous plotting forms, the adequacy of earlier empirical fits of convection data can be judged. In Fig. A.6, O'Toole and Silveston's power curves (Eqn. A.2.4) are shown to fit the data only for the low Rayleigh number range. These power curves, obtained by fitting straight lines to log Nu versus log Ra data, do not allow for heat flux transitions. Even the straight line fits of the Nu Ra versus Ra data in Fig. A.6 appear to be inadequate over the lower range of inter-transitional Rayleigh numbers. This suggests other empirical curves might be obtained which provide a better fit to a c_q versus Ra plot whilst remaining indistinguishable from straight lines on a Nu Ra versus Ra plot.

Consider an experiment in which the fluid properties and ΔT remain constant and d is increased. A plot of c_q versus log Ra plots then represents the variation of heat flux with d . The form of these curves suggests that the heat flux increases (with increasing d) until a maximum is reached for the particular flow type (Figs. A.6

and A.7). Once d is increased beyond this point, the heat flux decreases until another flow type becomes marginally more efficient. A transition in the flow pattern then occurs (Fig. A.3), although the hysterisis effects noted by Krishnamurti (1970 a), for increasing and decreasing Ra, may tend to complicate the changeover. The curves for c_q therefore allow one to speculate that heat flux transitions are caused by some form of maximization of heat transfer.

The regularity of the c_q curves for a logarithmic Rayleigh number abscissa suggests that the changes in the efficiency of heat transfer may depend on the fractional change in depth $(\delta d/d)$ relative to the maximum c_q depth, rather than the absolute change.

It is also apparent from the shape of the c_q curves that, for the same temperature difference ΔT, there may be two or sometimes as many as four or five different plate spacings which will produce the same heat flux Q. For example, from Fig. A.6, the same value of $c_q = 0.105$ is obtained for plate spacings represented by Rayleigh numbers of approximately 9×10^2 (conduction), 2.5×10^3, 1.3×10^4 and 2.2×10^4. This is not obvious from the previously used methods of presenting thermal convection data (Appendix A.2.1).

The point of maximum c_q is the maximum heat flux obtainable for a particular flow regime and interplate temperature difference. From the straight-line assumption given by Eqn. A.2.5, it can easily be shown that the maxima will occur at

$$Ra = \frac{4\, c_{i,i+1}}{m_{i,i+1}}, \quad Nu = \frac{3}{4}\, m_{i,i+1} \qquad (A.2.6)$$

However, as the straight-line only provides an approximate fit to the data, these maxima values are also approximate.

With increasing Rayleigh number the maximum c_q values for each pair of transitions decrease. This mean variation of c_q is discussed in the next section.

A.2.3 The Mean Variation of c_q with Rayleigh Number

The value of c_q has been discussed previously in the literature in the context of the high Rayleigh number equation

$$Nu = c_q\, Ra^{1/3}$$

Turner (1973) suggested that for water and air the values of c_q for this equation are 0.09 and 0.08 respectively. A plot of c_q from the available data over the full experimental range of Ra is shown in Fig.

A.8. Where only a power relationship of the form $Nu = c_1 Ra^n$ was available this was plotted but a comparison of Fig. A.1 with Figures A.6 and A.7 show a substantial loss of detail occurs. Figure A.8 highlights both the approximate consistency of each experiment and the marked difference between different experiments. It shows more clearly than Fig. A.1 that the differences are unlikely to be explained by simple Prandtl number dependence at high Rayleigh number. A possible reason for these differences is aspect ratio dependence.

To calculate the Rayleigh number for the single-plate experimental data on Fig. A.8 (Townsend 1959 and the writer's unsteady heat flux experiments), the temperature difference between the plate and the mean fluid temperature (ΔT_p) was assumed to be equal to $\frac{1}{2}\Delta T$. Twice the height of the enclosed fluid column was used for d. This likens the single-plate experiments to the lower half of a parallel-plate experiment. It is, however, debatable whether twice the fluid depth or the actual depth should be used. The latter case would give a Rayleigh number one-eighth the value of that calculated.

A plot of Long's (1976) theory, with constants obtained by fitting the two extreme points of Garon and Goldstein's data, is also shown. Long's factor $s = \frac{1}{3}$ has been assumed.

The overall variation of c_q with Rayleigh number (Fig. A.8) suggests that over the experimental range of higher Rayleigh numbers, c_q decreases with increasing Ra. At much higher Rayleigh numbers ($Ra > 10^{15}$), c_q tends to a probable asymptote between 0.04 and 0.06.

To avoid confusion, O'Toole and Silveston's (1961) empirical curves (Eqn. A.2.4) have not been plotted on Fig. A.8. However, they do provide good agreement with the plotted data. An empirical formula suggested by Hollands, Raithby and Konicek (1975) which include the large Rayleigh number asymptote of $c_q = 0.0555$, also agrees well with the data in Fig. A.8. Empirical formulae based on $Ra^{\frac{1}{3}}$ do not allow for the decreasing value of c_q at high Ra.

The data plotting method introduced in this section (c_q versus log Ra) allows the data to be plotted in greater detail than previously. The plotting form also shows the effect that varying only the interplate spacing has on the heat flux Q. Further research is needed to gain an understanding of the physical effects of varying d.

The published heat flux data (Fig. A.8) suggest that, within the limits of experimental accuracy, the assumption that c_q does not vary for $Ra > 10^{10}$ is sufficiently accurate. This assumption is used in

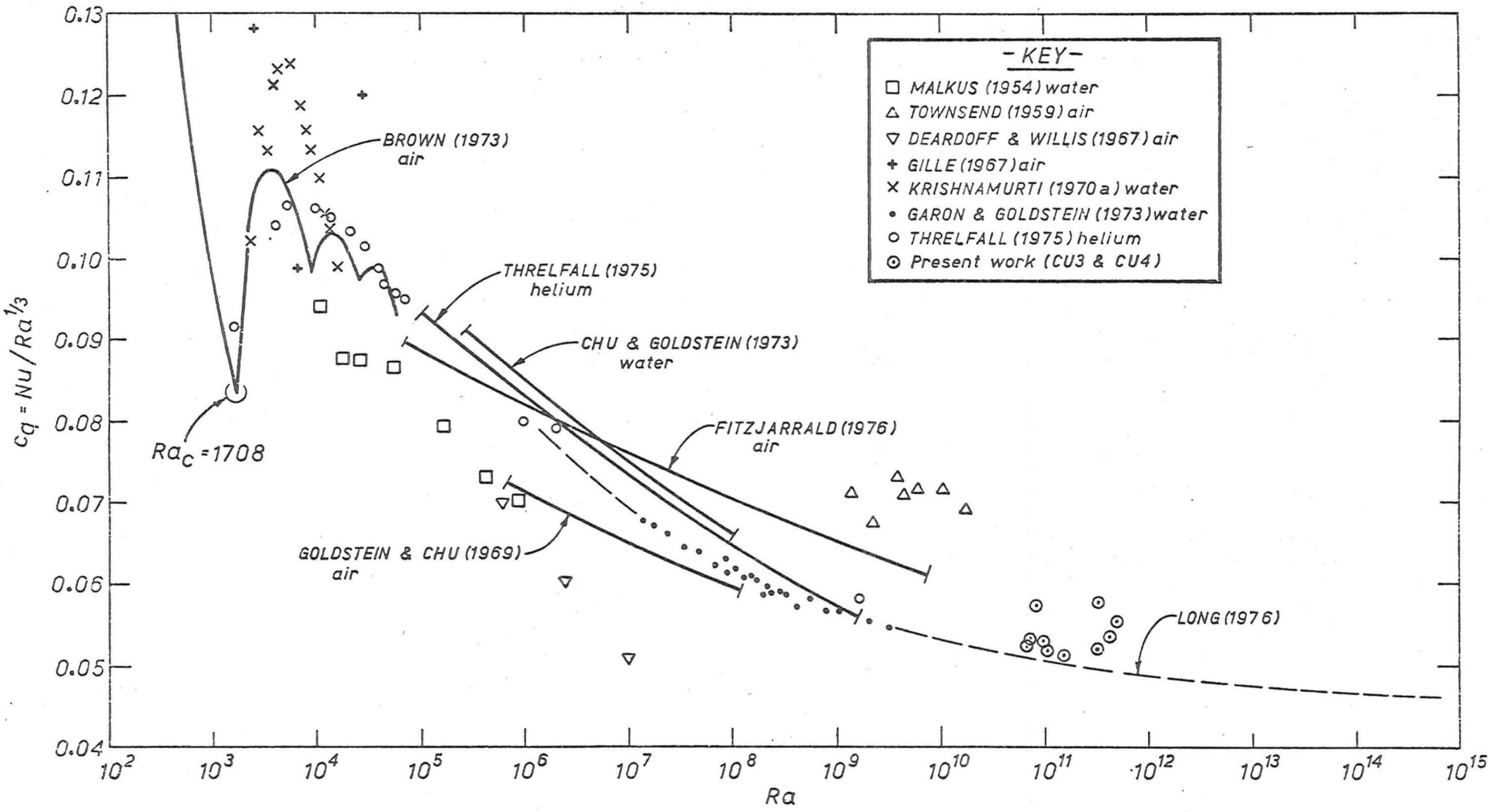

Fig. A.8. Heat transfer coefficient c_q from parallel - and single-plate convection experiments plotted as a function of Rayleigh number over the full experimental range of Ra .

the I.C.P.M.

A.3 VERTICAL TEMPERATURE PROFILE

Measurements of the mean vertical temperature profiles in a convecting layer of air between two parallel plates are shown in Fig. A.9. The data are from the low Rayleigh number experiments of Gille (1967) and the high Rayleigh number experiments of Deardoff and Willis (1967).

Below the critical Rayleigh number Ra_c the fluid heat transfer is by conduction and the temperature profile is linear across the layer. As the Rayleigh number increases above Ra_c, the temperature distribution in the central portion of the convecting layer becomes less stable. At $Ra = 2.7 \times 10^4$ for air, Gille (1967) found that the central region temperature gradient was reversed (i.e. stable). At much higher Rayleigh numbers, the temperature profiles consist of a thin buoyancy production region of unstable temperature distribution at each boundary and a central region which has an essentially uniform temperature distribution.

Similar profiles have been measured at other Prandtl numbers. However, as with Krishnamurti's (1970a,b) heat flux transition measurements (Fig. A.3), the profiles are Prandtl number dependent. For instance, Chu and Goldstein (1973) found that the temperature gradient reversal for water was a maximum at $Ra \approx 4 \times 10^5$. On Krishnamurti's heat flux transition diagram (Fig. A.3), the gradient reversals determined by Gille (1967) and Chu and Goldstein (1973) lie in the turbulent flow regime.

Chu and Goldstein (1973) suggested that temperature gradient reversals are the result of thermals reaching the opposite boundary and coalescing to form stable blobs. At much higher Ra, the thermals undergo persistent horizontal motions, which restrict the formation of stable blobs.

For the purposes of the I.C.P.M. it can be assumed that at high Rayleigh numbers $(Ra > 10^{10})$, the vertical temperature profile consists of an isothermal central region and a buoyancy production region at the heated boundary.

A.4 VERTICAL PROFILES OF THE ROOT MEAN SQUARE VALUES OF THE VELOCITY AND TEMPERATURE FLUCTUATIONS

Measurements of the r.m.s. vertical velocities (σ_w) in a

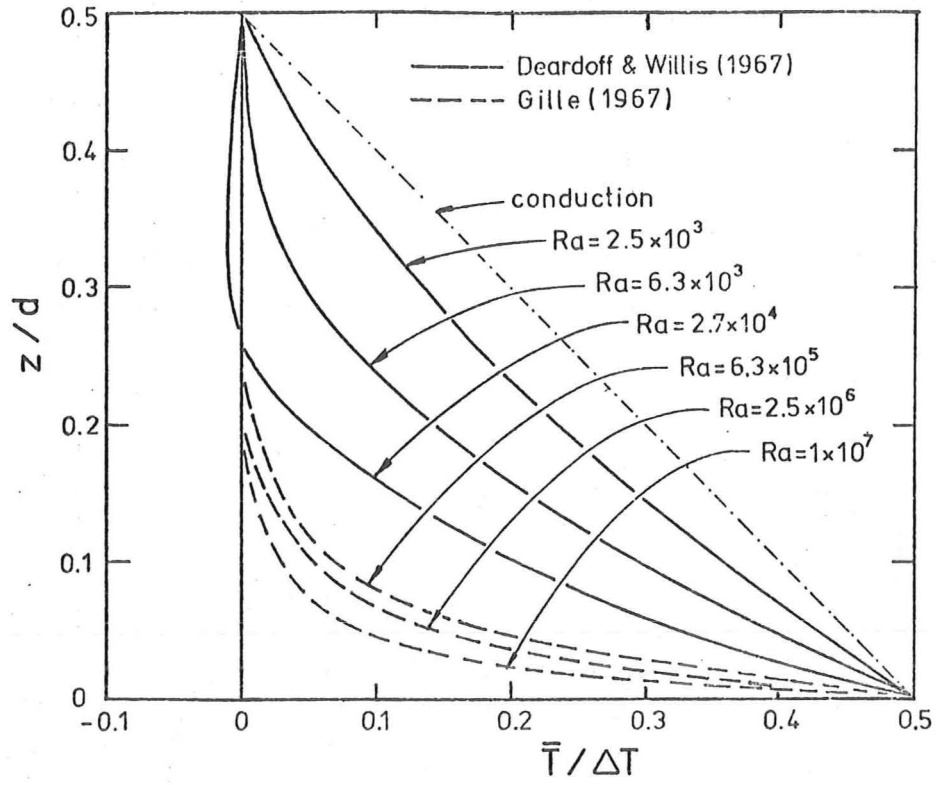

Fig. A.9. Non-dimensional temperature profiles in air from parallel-plate convection experiments over the experimental range $1700 < Ra < 10^7$.

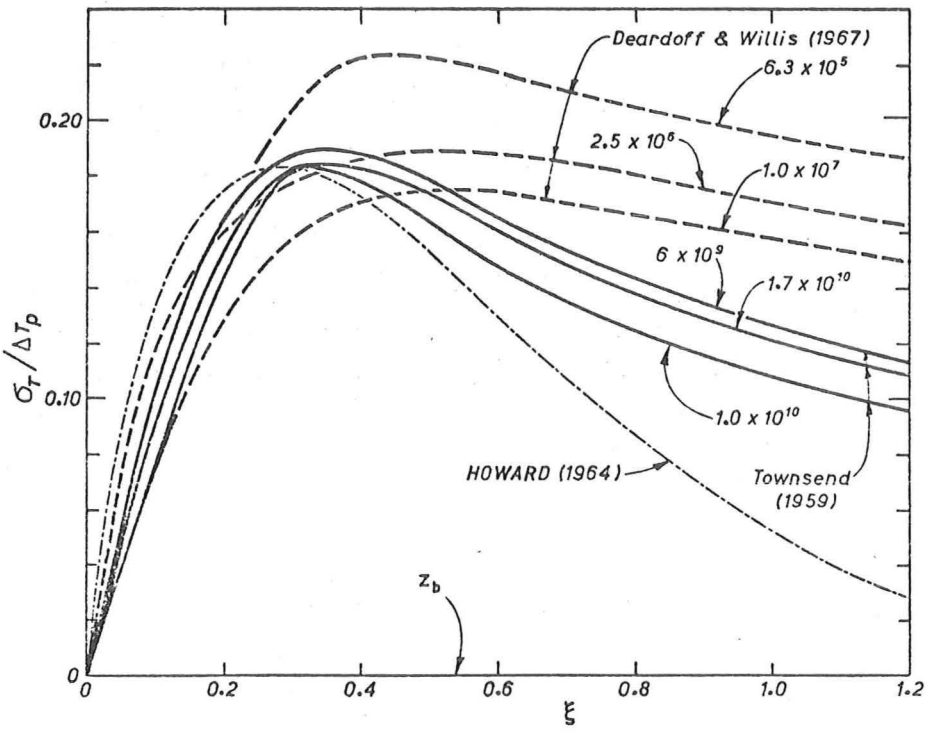

Fig.A.10. Root mean square temperature fluctuation σ_T non-dimensionalized by the plate-fluid temperature difference ΔT_p plotted against Howard's (1964) non-dimensional distance ξ. Howard's theoretical curve is compared with experimental data.

convecting air layer between two horizontal plates ($6.3 \times 10^5 < Ra < 10^7$) have shown that σ_w increases from zero at the heated boundaries to a maximum midway between the plates (Deardoff and Willis 1967). The maximum r.m.s. value of the horizontal velocity fluctuations occurred near the outer edge of the buoyancy production region. In the central region σ_u was about 70% of the maximum.

Similarly, Deardoff and Willis (1967) found that the r.m.s. value of the temperature fluctuations σ_T increased to a maximum near the outer edge of the buoyancy production layer (Fig. A.10). Again, σ_T decreased in the central region to approximately 70% of the maximum. Townsend's (1959) measurements in air, at higher Rayleigh number, above a single heated plate, showed a similar variation of σ_T with height.

For penetrative convection, the profiles of σ_w, σ_u and σ_T are different because there is only one buoyancy production region (Chapt. 2.2). For example, the maximum value of σ_w occurs at $z/d_m \approx 0.4$ rather than at $z/d_m = 0.5$, as is the case for parallel-plate convection. The value of σ_T is also affected by the oscillation of the stable temperature gradient at $z = d_m$.

In the isothermal central region of a high Rayleigh number turbulent convection layer, molecular diffusion and viscosity may be neglected. As discussed in Chapt. 4.2, the velocity and temperature scales for turbulent convection (V_s and T_s) are dependent only upon the heat flux Q and the interplate spacing d. Hence

$$V_s \propto (\alpha g Q d)^{1/3}$$

$$T_s \propto Q/(\alpha g Q d)^{1/3}$$

Deardoff (1970) took the proportionality constants to be unity and defined the convection scales w_* (Eqn. 2.2.19) and T_* (Eqn. 2.2.21). He found that Deardoff and Willis' (1967) measurements of σ_w, for parallel plate convection, scaled well with w_*. The maximum value at midheight was

$$(\sigma_w)_{max} / w_* = 0.90 \pm 0.05$$

A similar value (0.95 ± 0.05) has been reported by Fitzjarrald (1976). Deardoff and Willis' (1976) temperature fluctuation measurements at mid-height scaled according to

$$\sigma_T / T_* = 1.9 \pm 0.1$$

However, more recent measurements by Fitzjarrald (1976) of σ_T at mid-

height yielded

$$\sigma_T / T_* = 0.98 \pm 0.05$$

but no explanation for this discrepancy is available.

To scale the r.m.s. values of the temperature fluctuations close to a heated plate (single-plate convection), Townsend (1959) used a temperature scale which neglected the effect of the fluid layer depth (which was large) and included the fluid molecular diffusivity κ. Dimensional analysis revealed

$$T_s \propto (Q^3 / \alpha g \kappa)^{1/4}$$

The corresponding length and velocity scales for this boundary region were

$$\ell_s \propto (\kappa^3 / \alpha g Q)^{1/4}$$

$$V_s \propto (\alpha g Q \kappa)^{1/4}$$

Whilst Townsend (1959) found this temperature scale satisfactory for his measurements of σ_T close to the bouncary, his scales have no use in the I.C.P.M. as the buoyancy production region has negligible thickness.

A.5 HOWARD'S (1964) CONVECTION THEORY

To complete this review of thermal convection, the convection theory of Howard (1964) will be discussed. Howard considered the convection process occurring at the heated lower boundary of a deep fluid layer (large Ra) as the periodic buildup of a molecular boundary layer, followed by its subsequent rapid breakup due to buoyancy instabilities. If, at $t = 0$, the fluid layer has uniform temperature T_m and the lower boundary is at a higher temperature T_p then the temperature of fluid close to the boundary increases by molecular diffusion according to

$$T(z) = \Delta T_p \left[1 - \mathrm{erf}\left(\frac{z}{2\sqrt{\kappa t}} \right) \right] \qquad \text{(A.5.1)}$$

where $\Delta T_p = T_p - T_m$. At time t^*, the buoyancy forces overcome the retarding viscosity and diffusive effects and the buoyant layer breaks up. For Prandtl numbers greater than unity, Howard (1964) assumed the breakup time to be small relative to the diffusive period t^*. The convective process can therefore be discussed in terms of Eqn. A.5.1 for $0 < t < t^*$.

Support for this type of phenomenological model comes from the

work of Elder (1968) and Sparrow, Husar and Goldstein (1970). Using flow visualization techniques (Chapt. 6.3.3), Sparrow et al. were able to observe the regular spatial and temporal generation of thermals above a flat heated plate. When the heat flux Q increased, the rate of generation of thermals at each site decreased.

By integrating the temperature distribution (Eqn. A.5.1) with respect to time over the time period $0 < t < t^*$ a mean vertical temperature profile may be obtained

$$\overline{T} = \Delta T_p \left[(1 + 2\xi^2)(1 - \text{erf } \xi) - \frac{2}{\sqrt{\pi}} \xi \exp(-\xi^2) \right] \qquad (A.5.2)$$

where $\xi = z / 2\sqrt{\kappa t^*}$.

In terms of the I.C.P.M., the thickness of the buoyancy production layer is

$$z_b = -\Delta T_p \Big/ \left.\frac{\overline{\partial T}}{\partial z}\right|_{z=0}$$

Hence from Eqn. A.5.2,

$$z_b = \sqrt{\pi \kappa t^*} / 2 \qquad (A.5.3)$$

It also follows that the Nusselt number is given by

$$Nu = \frac{Q\, d}{\kappa \Delta T} = \frac{d}{\sqrt{\pi \kappa t^*}} \qquad (A.5.4)$$

Howard (1964) described the buoyant layer breakup criterion in terms of a critical Rayleigh number based on a representative buoyancy production layer thickness, rather than the full layer depth. Comparison of his mean temperature profile (Eqn. A.5.1) with experimental measurements by Townsend (1959) and Elder (1968) at high Ra showed good agreement.

However, whilst Howard's theory describes the method of generation of buoyant thermal elements, it does not include the effect of their convective transport. In the parallel plate case, the interaction of buoyant elements from adjacent boundary layers will cause major departures from the theory. This is apparent from the temperature profiles in Fig. A.9. At lower Rayleigh number, the interaction of buoyant elements causes temperature gradient reversals (Chu and Goldstein 1973).

If Eqn. A.5.1 is used to obtain the r.m.s. value of the temperature fluctuations for the time period $0 < t < t^*$, the following equation results.

$$\sigma_T = \Delta T_p \left[(1 + 2\xi^2).(1 - \text{erf}\,\xi)^2 - \frac{4\xi}{\sqrt{\pi}} . (1 - \text{erf}\,\xi).\exp(-\xi^2) + \frac{4\xi^2}{\pi} \cdot E_I(2\xi^2) - \overline{T}^2 \right]^{\frac{1}{2}} \qquad (A.5.5)$$

where

$$E_I(x) = \int_x^\infty \frac{e^{-t}}{t}\, dt$$

is the exponential integral and $\overline{T}$ is the mean temperature (Eqn. A.5.2).

The theoretical curve from Howard's (1964) theory and the experimental results of Deardoff and Willis (1967) and Townsend (1959) are compared in Fig. A.10. The maximum r.m.s. value of the temperature fluctuations is quite well predicted. However, further from the boundary, where the passage of thermal elements is important, the theory breaks down.

Despite the restraints on Howard's (1964) theory discussed above, it does provide a reasonable description of the transfer of heat away from a heated boundary by convective motion. It suggests that the mixed layer in the I.C.P.M. will contain rising thermal elements, which will serve to transport heat and turbulent kinetic energy throughout the layer.

APPENDIX B

LINEARLY STRATIFIED ATMOSPHERIC MODEL

In this appendix, penetrative convection equations for a linearly stratificated model will be derived. The model differs from the I.C.P.M. in that the temperature well above the interface increases linearly with height (Fig. B.1). As discussed in Chapt. 2.2.2, models of this type have been used to analyse atmospheric boundary layer growth (e.g. Betts 1973).

The model developed in this appendix will incorporate the I.C.P.M. assumption that the partial derivatives of temperature, with respect to height and time, are discontinuous at the interface and not $T(z,t)$. As this makes allowance for the finite thickness of the interfacial region even at high Péclet numbers, it is an improvement on previous models. Because the linearly stratified case is primarily of interest in atmospheric modelling, only high Péclet number entrainment will be considered. To simplify the analysis, heat losses are neglected, i.e.

$$\beta = \beta_T = 1 \qquad W = W_T = 0$$

temperature gradient for $z >> d_m$, Γ, will be assumed to be constant with respect to height and time.

Only the derivations of the model equations will be given. This will allow the validity of earlier atmospheric modelling assumptions to be discussed. No numerical analyses of the linearly stratified case will be presented.

B.1 GENERAL EQUATIONS

The vertical temperature profile for the linearly stratified case ($\Gamma > 0$) is shown in Fig. B.1. Below the interface, the profile is identical to the I.C.P.M. Above the interface, the temperature gradient tends to Γ for $z >> d_m$. The temperature T_a is defined as the temperature of the extrapolated linear diffusion region profile (gradient Γ) at $z = d_m$. The interfacial temperature difference ΔT_i is therefore defined in the same way as the I.C.P.M., by

$$\Delta T_i = T_a - T_m$$

For the linearly stratified model, the mean temperature profile d_h is given by

$$d_h = d_m + \frac{1}{\Delta T_i} \int_{d_m}^{h_T} (T_a + \Gamma\,(z - d_m) - T)\, dz \qquad (B.1.1)$$

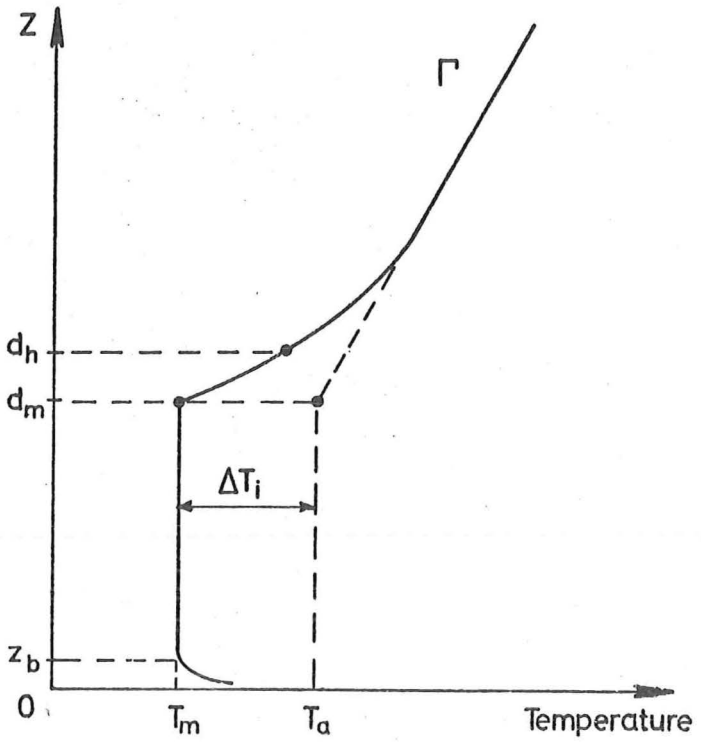

Fig. B.1. Vertical temperature profile for linearly stratified model.

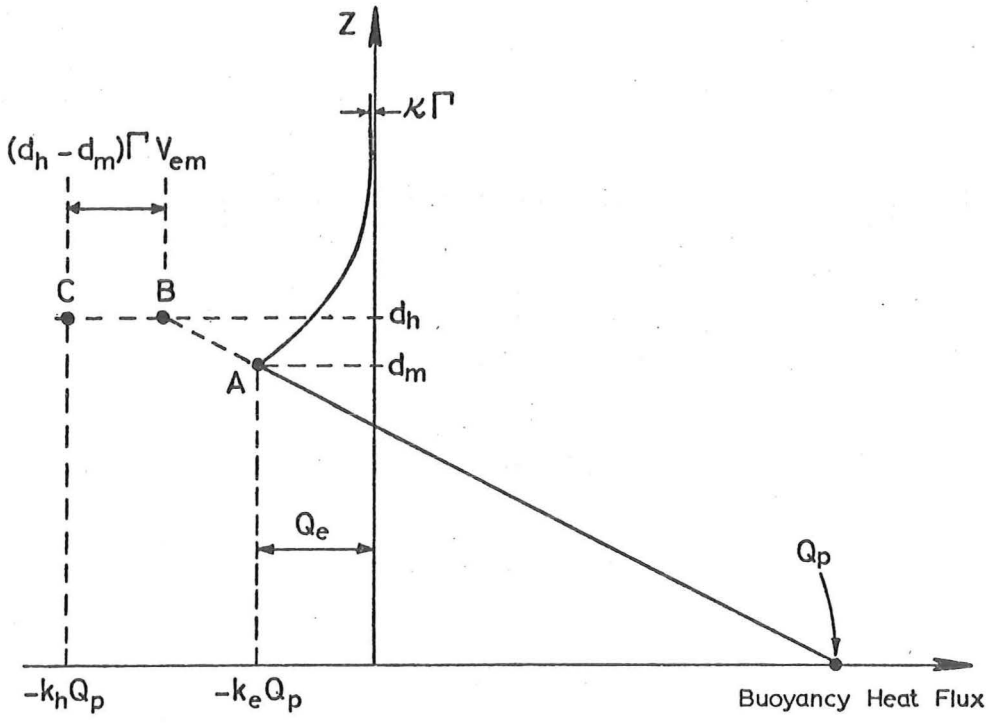

Fig. B.2. Buoyancy heat flux profile for linearly stratified model.

Height h_T is assumed to be large, so that at $z >> d_m$

$$T = T_a + \Gamma (z - d_m)$$

In the diffusion region, the same equations for the buoyancy heat flux $Q(z)$ and the rate of change of temperature apply (Eqns. 3.3.1 and 3.4.3). The mixed layer heat budget equation is also the same as for the I.C.P.M. (Eqn. 3.5.2).

$$Q_p - Q_e = d_m \frac{dT_m}{dt} \tag{B.1.2}$$

However, the full fluid column heat budget equations differ.

In the linearly stratified case, the heat flux at the upper boundary ($z = h_T$), $- \kappa\Gamma$, must be accounted for. Also T_a increases as d_m increases and this will contribute to the changes in ΔT_i. Integrating Eqn. 3.4.1 over the full fluid column, yields

$$- \kappa\Gamma - Q_p = - \int_0^{h_T} \frac{\partial T}{\partial t} dz \tag{B.1.3}$$

From the definition of d_h, it follows that

$$\int_0^{h_T} T \, dz = T_a \, h_T + \frac{\Gamma}{2} (h_T - d_m)^2 - d_h \, \Delta T_i \tag{B.1.4}$$

Partial differentiation with respect to time gives

$$\int_0^{h_T} \frac{\partial T}{\partial t} dz = h_T \frac{dT_a}{dt} - \Gamma (h_T - d_m) V_{em} - \frac{d}{dt} (d_h \, \Delta T_i) \tag{B.1.5}$$

The rate of change of T_a is simply given by

$$\frac{dT_a}{dt} = \Gamma V_{em} \tag{B.1.6}$$

Substituting equations B.1.5 and B.1.6 into Eqn. B.1.3, and rearranging, yields

$$Q_p + \kappa\Gamma + V_{eh} \Delta T_i = - d_h \frac{d(\Delta T_i)}{dt} + d_m \Gamma V_{em} \tag{B.1.7}$$

It follows from the definition of ΔT_i and Eqn. B.1.6 that

$$\frac{d}{dt} (\Delta T_i) = \Gamma V_{em} - \frac{dT_m}{dt} \tag{B.1.8}$$

An alternative form for the full fluid column heat budget is therefore

$$Q_p + \kappa\Gamma + V_{eh} \Delta T_i = d_h \frac{dT_m}{dt} + (d_h - d_m) \Gamma V_{em} \tag{B.1.9}$$

In atmospheric models (large Pe), molecular diffusion is negligible and the upper boundary heat flux ($- \kappa\Gamma$) may be neglected. Even in Willis and Deardoff's (1974) laboratory experiments for water (typical

values, $\Gamma = 0.45$ °C/cm and $Q_p = 0.13$ cm °C/sec), the upper boundary heat flux was less than 0.5% of Q_p .

Consider the two heat budget equations (Eqns. B.1.2 and B.1.9) expressed in terms of k_e and k_h respectively.

$$Q_p (1 + k_e) = d_m \frac{dT_m}{dt} \tag{B.1.10}$$

$$Q_p (1 + k_h) = d_h \frac{dT_m}{dt} + (d_h - d_m)\Gamma V_{em} \tag{B.1.11}$$

Eliminating dT_m/dt from both equations yields

$$(1 + k_h) = \frac{d_h}{d_m} (1 + k_e) + \frac{(d_h - d_m)\Gamma V_{em}}{Q_p} \tag{B.1.12}$$

This is similar to the I.C.P.M. result (Eqn. 5.3.6) but there is an additional term. The value of k_h in a linearly stratified model will be larger than the corresponding I.C.P.M. value.

Consider the buoyancy heat flux profile sketched in Fig. B.2. As with the I.C.P.M., the heat flux at the interface (point A) is $Q_e = - k_e Q_p$. This follows from Eqn. B.1.10. The value of k_e can therefore be evaluated from the heat flux profile. However, from the full fluid column heat budget (Eqn. B.1.11), the heat flux given by an extrapolation of the linear mixed layer heat flux profile to $z = d_h$ (point B) is

$$- k_h Q_p + (d_h - d_m)\Gamma V_{em}$$

Hence, the value of k_h cannot be evaluated directly from the heat flux profile using the I.C.P.M. method (Chapt. 5.3). The heat flux $- k_h Q_p$ will be more negative than the extrapolated value (i.e. point C in Fig. B.2). In the I.C.P.M. point B and C coincide because $\Gamma = 0$.

B.2 HEAT BUDGET EQUATION SOLUTION

Because the k values (k_e , k_m and k_h) are not generally constant with time, Betts' (1973) solution of his heat budget equation is invalid (Chapts. 2.2 and 5.4). However, in this section the same constant k assumption will be made to solve the full fluid column heat budget equation for d_h as a function of k_h and Q_p . This solution will also have doubtful validity. However, by comparing it with Betts' result, other major errors which occur when Betts' model equations are used to analyse atmospheric data, will be illustrated.

In the linearly stratified atmospheric model (large Pe), $\partial^2 T/\partial z^2$ is typically negative in the diffusion region. This follows from the initial conditions (Chapt. 3.1)

$$T(z,0) = T_{m0} + \Gamma z$$

The large Pe relationship for ℓ_i , assumed in Chapt. 4.3 (Eqn. 4.3.2), will therefore hold. From Eqn. 4.2.5

$$\ell_i = 0.1\, d_m$$

Because molecular diffusion effects are negligible, turbulent diffusion will control the shape of the interfacial region. The mean profile height d_h will therefore be related to ℓ_i . It follows that

$$d_h = c_i\, d_m \qquad \text{(B.2.1)}$$

where c_i will be a constant value of about 1.05 - 1.10. Hence, the rates of change of d_m and d_h are related according to

$$V_{eh} = c_i\, V_{em} \qquad \text{(B.2.2)}$$

In the linearly stratified model, V_{eh} is greater than V_{em} . This is the reverse of the typical I.C.P.M. case. For simple initial conditions in the linearly stratified model, $d_h = d_m = 0$ at $t = 0$ whereas in the I.C.P.M., $d_h = d_{g0}$.

From Eqn. B.2.1, the relationship between k_h and k_e (Eqn. B.1.12) reduces to

$$1 + k_h = c_i\,(1 + k_e) + (c_i - 1)\,\frac{d_m\,\Gamma\,V_{em}}{Q_p} \qquad \text{(B.2.3)}$$

Substituting for k_h and c_i in Eqn. B.1.7 yields (for large Pe)

$$\frac{1 + k_h}{k_h}\,V_{eh}\,\Delta T_i + d_h\,\frac{d(\Delta T_i)}{dt} = \frac{\Gamma}{c_i^2}\,d_h\,V_{eh}$$

If this equation is multiplied on both sides by d_h to the power of $1/k_h$, then, following the constant k_h assumption, it can be rearranged to give

$$\frac{d}{dt}\left[d_h\,\frac{1 + k_h}{k_h}\,\Delta T_i\right] = \frac{k_h}{1 + 2k_h}\,\frac{\Gamma}{c_i^2}\,\frac{d}{dt}\left[d_h\,\frac{1 + 2k_h}{k_h}\right] \qquad \text{(B.2.4)}$$

Again assuming k_h is constant, Eqn. B.2.4 is integrated with respect to time from $t = t_v$ to t . The time t_v is when ΔT_i was last equal to zero. This yields

$$\Delta T_i = \frac{k_h}{1 + 2k_h} \frac{\Gamma}{c_i^2} \left[d_h - d_{hv} \left(\frac{d_{hv}}{d_h} \right)^{\frac{1 + k_h}{k_h}} \right] \qquad (B.2.5)$$

where d_{hv} is the mean temperature profile height (Eqn. B.1.1) at $t = t_v$. From the definition of k_h (Eqn. 5.1.3) it follows that

$$\left[d_h - d_{hv} \left(\frac{d_{hv}}{d_h} \right)^{\frac{1 + k_h}{k_h}} \right] V_{eh} = (1 + 2k_h) \frac{c_i^2}{\Gamma} Q_p \qquad (B.2.6)$$

In the simplest case, the two heights d_m and d_h are zero at time t_v . i.e. $t_v = d_m = d_h = \Delta T_i = 0$. These initial conditions were assumed by Betts (Chapt. 2.2.2). In his model, the interfacial thickness was neglected so that $d_h = d_m$ and $k = k_h$. Hence, Eqns. B.2.5 and B.2.6 reduce to Eqns. 2.2.11 and 2.2.13.

$$\Delta T_i = \frac{k}{1 + 2k} \Gamma d_m \qquad (B.2.7)$$

$$d_m V_{em} = \frac{(1 + 2k)}{\Gamma} Q_p \qquad (B.2.8)$$

As these equations all depend on the assumption that k_h and k_e are constant with time, their validity is in doubt. However, a comparison of Eqns. B.2.5 and B.2.6 with Eqns. B.2.7 and B.2.8 shows that other factors can affect the accuracy of the k values obtained from Betts' model. Firstly, the value of k_h is larger than k_e (from Eqn. B.2.3) so that the value of k derived from Eqn. B.2.7 will be larger than the ratio of the interfacial and lower boundary heat fluxes (k_e).

Secondly, if the atmospheric conditions do not satisfy the assumption that $d_{hv} = 0$ (i.e. the virtual height where $\Delta T_i = 0$ is not zero) then Betts' (1973) equations should not be used. Combining Eqns. B.2.6 and B.2.8 yields

$$(1 + 2k) = (1 + 2k_h) \Big/ \left[1 - \left(\frac{d_{hv}}{d_h} \right)^{\frac{1 + 2k_h}{k_h}} \right] \qquad (B.2.9)$$

For $d_{hv} > 0$, the value of k is greater than k_h . However, for $d_h >> d_{hv}$, the effect of the initial conditions becomes negligible (Stull 1973, Farmer 1975).

Equations of the type developed by Betts (1973) have been used

extensively to evaluate k (Carson 1973, Deardoff 1974a, Sarachik 1974, Barnum and Rao 1975, Farmer 1975). From the discussions given in this section and Chapter 5, it is apparent the values of k obtained from these analyses will not be representative of the interfacial heat flux ratio $k_e = - Q_e/Q_p$.

APPENDIX C

NUMERICAL ANALYSIS COMPUTER PROGRAMS

A number of numerical analyses were performed using the University of Canterbury's Burroughs B6718 computer. The main numerical analysis was a temporal solution of the turbulent entrainment model. For molecular entrainment ($\gamma = \lambda = 0$), the diffusion region temperature distribution is unaffected by the mixed layer. The computer program required was therefore much simpler. A filling model entrainment analysis could be performed using the molecular entrainment program by setting $\kappa = 0$.

Computer programs were also written to study the diffusion of heat through the fluid column container walls and insulation, and to evaluate the analytical solutions of the molecular diffusion equation for finite and infinite boundary conditions (Eqns. 3.4.6 and 3.4.7). These latter programs were straightforward and will not be discussed further.

In all cases, the programs were written in Fortran. Where an analytical solution was not available, finite difference methods were used to obtain a numerical solution. The explicit forward difference scheme was used in all the finite difference calculations. Variations in fluid properties with temperature were neglected.

C.1 MOLECULAR ENTRAINMENT ANALYSIS

For a molecular entrainment analysis, the effect of interfacial turbulence on the diffusion region temperature distribution is neglected ($\gamma = \lambda = 0$). The diffusion region temperature distribution at any time t can therefore be calculated from an analytical solution of the molecular diffusion equation (Chapt. 3.9). For the range of experimental conditions analysed, the differences between the finite and infinite boundary solutions were not significant. Hence, the simpler infinite boundary solution was used (Eqn. 3.4.7).

A listing of the molecular entrainment computer program for steady heat fluxes is given in Appendix J.1. The computer program for the unsteady heat flux case was only slightly different to allow for the variation of Q_p.

At any time t, the temperature distribution in the diffusion region $T(z,t)$ could be evaluated from Eqn. 3.4.7. The rate of rise

of the interface for molecular entrainment is given by Eqn. 3.9.2

$$V_{em} = \frac{Q_p}{\beta\, d_m \left.\frac{\partial T}{\partial z}\right|_i} + \frac{\kappa}{\beta\, d_m} - \frac{\kappa}{\beta} \left.\frac{\frac{\partial^2 T}{\partial z^2}}{\frac{\partial T}{\partial z}}\right|_i \qquad \text{(C.1.1)}$$

Equations for the temperature gradient $\partial T/\partial z$ and rate of change of temperature gradient $\partial^2 T/\partial z^2$ are easily derived from Eqn. 3.4.7. These could be evaluated for the known value of d_m at time t to obtain $(\partial T/\partial z)_i$ and $(\partial^2 T/\partial z^2)_i$ for Eqn. C.1.1. Hence, at any time t, the rate of rise of the interface V_{em} could be calculated. Using the finite difference statement

$$(d_m)^{t+\delta t} = (d_m)^t + V_{em}\, \delta t \qquad \text{(C.1.2)}$$

the new height of the interface at time $t + \delta t$ was then obtained.

As the mixed layer temperature T_m and the diffusion region temperature $T(z,t)$ must match at the interface, T_m could be evaluated from Eqn. 3.4.7 using the known value of d_m at time t. Because the derivation of the equation for V_{em} (Chapt. 3.6) includes the mixed layer heat budget, the resulting changes in d_m and T_m will satisfy the heat budget requirements.

At time intervals of either 2 or 10 minutes, the relevant parameters were calculated and printed out. Equations for d_h and V_{eh} in terms of d_m and t enabled these parameters to be calculated at the given time intervals (Appendix E.4).

The molecular entrainment analysis program listed in Appendix J.1 includes the calculation of a non-dimensional time parameter

$$(t - t_s) \;/\; (t_T - t_s)$$

and a non-dimensional interfacial height parameter

$$(d_m - d_{g0}) \;/\; 2\sqrt{\frac{\pi \kappa}{\beta}\left[\frac{t_s + t_T}{2}\right]}$$

Whilst these have no practical value, they served to reduce $d_m(t)$ output for different values of t_s, Q_p and d_{g0} to a similar form. This allowed the net effect of varying each parameter to be studied.

To perform a filling model entrainment analysis, the same computer program was used with the molecular diffusivity κ set to zero. In some cases, alternative logical statements were required where $\kappa = 0$ simplified the equations. Similarly, if the heat loss factor W was

set to zero for either analysis, alternative logical statements were needed. Otherwise, equations such as Eqn. 3.8.2 would be divided by zero. An analytical solution for filling model entrainment (Appendix E.3) was used to check the time t when the interface reached height d_m.

C.2 TURBULENT ENTRAINMENT ANALYSIS

In the turbulent entrainment analysis of the I.C.P.M., the effect of penetrating interfacial domes of mixed layer fluid on the diffusion region heat transfer is allowed for by the turbulent diffusivity term $\gamma(z)$. The mixed layer therefore affects the diffusion region temperature changes. Unlike the molecular entrainment analysis ($\gamma(z) = 0$), there is no analytical solution for the diffusion region temperature distribution. Instead, a numerical solution was found using a finite difference method.

The diffusion region was represented by a one-dimensional array of equally spaced finite difference nodes, Δz apart (Fig. C.1). At each time step, the turbulent entrainment parameters γ_i and z_{int} were calculated from the interfacial entrainment terms (Ri , Pe etc.). The turbulent diffusivities between each pair of nodes in the intermittency region ($d_m < z < d_m + z_{int}$) were then evaluated. Hence, the temperature changes in the diffusion region could be calculated from the heat budget for a nodal element of thickness Δz centred at the height of each node. This was performed using a forward difference equation based on Eqn. 3.4.3.

After each time step, the mixed layer height d_m and temperature T_m were obtained numerically by matching the mixed layer profile against the up-dated diffusion region profile according to the mixed layer heat budget (Eqn. 3.5.2).

A flow diagram outlining the major program steps and their order of computation is given in Fig. C.2. The full turbulent entrainment computer program is listed in Appendix J.2.

The program was designed to study a number of different interfacial entrainment cases. Initial temperature profile data could be generated according to the initial condition equations for the I.C.P.M. (an error function diffusion profile) or the linearly stratified model. Alternatively, the temperature data could be read into the computer at 10 Δz intervals. Intermediate node temperatures were obtained by linear interpolation. Four different heating conditions were able to

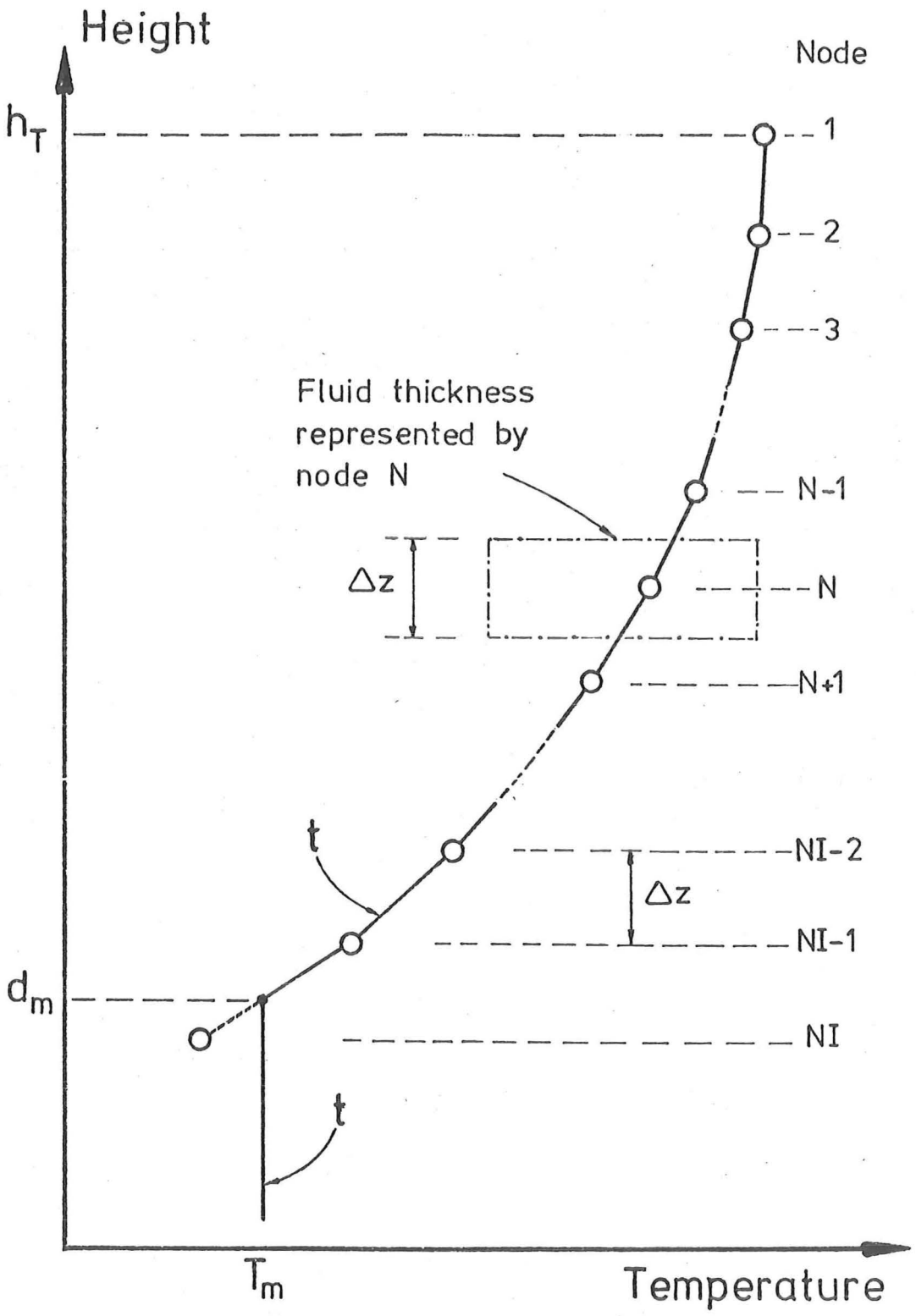

Fig. C.1. Finite difference nodes for calculating the changes in the diffusion region temperature distribution.

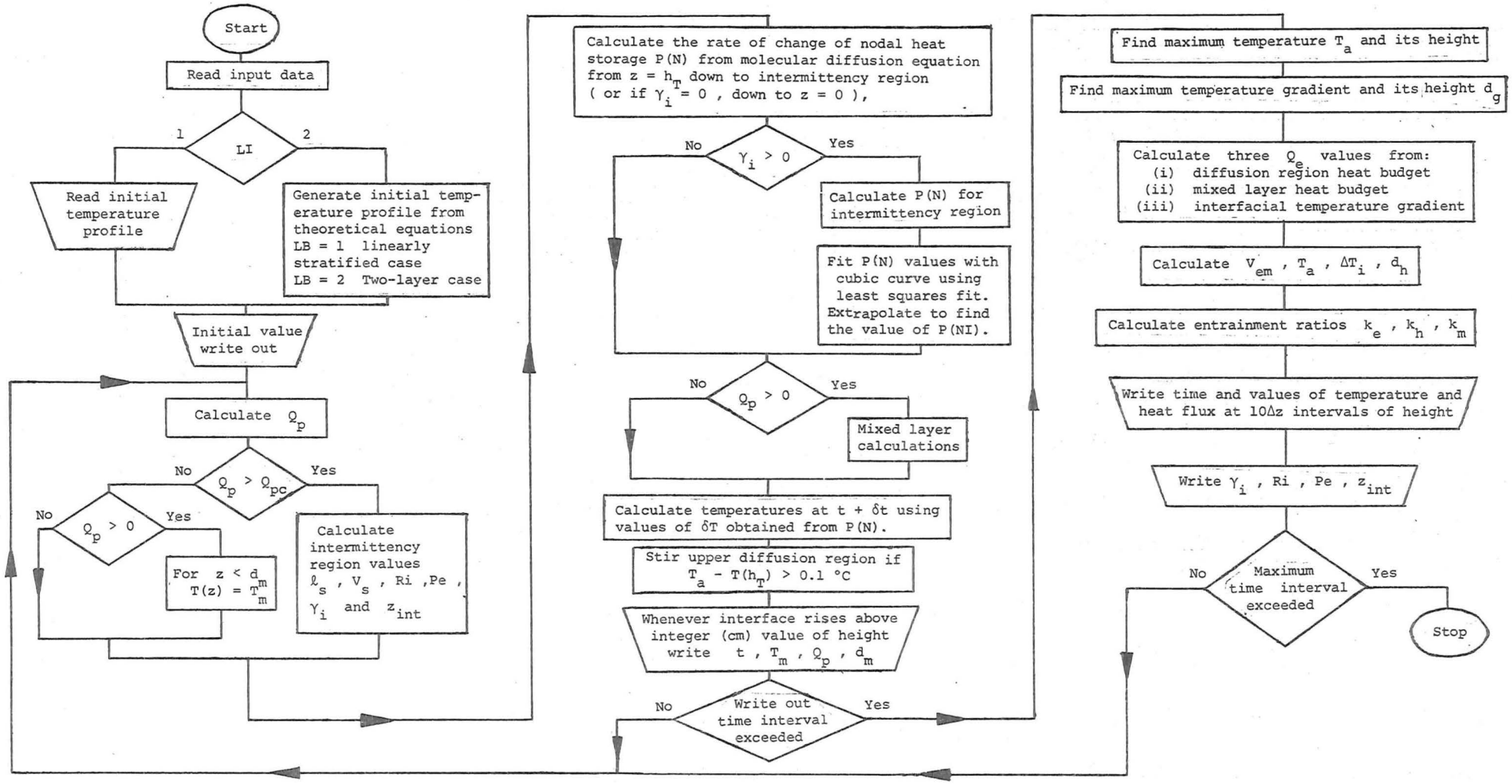

Fig. C.2 Flow diagram for turbulent entrainment analysis computer program

be specified: constant lower boundary heat flux q_p , constant glass layer heat flux q_G , constant heating water temperature T_H , or a half-sinusoidal input which approximated the diurnal heating cycle for the atmospheric boundary layer.

By setting $\gamma(z)$ to zero, the program could be used to perform a molecular entrainment analysis. This took a great deal more computational effort than was required for the simpler program described in the previous section. As will be discussed later, these molecular entrainment analyses provided a check of the numerical methods used in the program.

To translate the theory of the I.C.P.M. into a numerical analysis model, a number of additional assumptions were necessary. The assumptions that were most likely to have influenced the numerical analyses, are discussed below.

(i) The turbulent diffusion decay function

In Chapt. 4.3, the decay of the turbulent diffusivity $\gamma(z)$ with increasing height above the interface was discussed. The decay function $\phi_1(z - d_m)$ appeared to be approximately exponential. However, to simplify the numerical analysis, the turbulent diffusivity was assumed to be equal to zero at a finite distance z_{int} above the interface.

The decay function was defined by the power curve (Eqn. 4.3.12)

$$\phi_1(z - d_m) = \left[1 - \left(\frac{z - d_m}{z_{int}} \right) \right]^2 \qquad \text{(C.2.1)}$$

for $0 < z - d_m < z_{int}$

and the intermittency region thickness over which $\gamma(z)$ varied was defined empirically by (Eqn. 4.3.14)

$$z_{int} = \frac{2.5\, \ell_s}{1 + 0.01\, Ri} \qquad \text{(C.2.2)}$$

This empirical relationship for z_{int} accounts for the increased penetration of the interfacial domes as Ri decreases but also puts a finite maximum limit on z_{int} (Chapt. 4.3.3). For the typical range of experimental Richardson numbers, the empirical relationship is consistent with Eqn. 4.3.11, viz.

$$\left. \frac{\partial \phi_1}{\partial z} \right|_i \approx - \frac{1}{\ell_s}$$

Only the value of γ_i is needed to calculate the interfacial buoyancy heat flux Q_e from the diffusion region temperature distribution at time t. However, the decay function $\phi_1(z - d_m)$ for $\gamma(z)$ is important in the calculations of the rates of change of intermittency region temperature. As discussed in Chapter 7, the overall temporal behaviour of the I.C.P.M. is therefore influenced by the choice of the empirical relationship for $\phi_1(z - d_m)$.

(ii) Calculation of the temperature change at the lower boundary of the diffusion region

Consider the finite difference nodes for the diffusion region at time t (Fig. C.1). The nodes are numbered downwards from node $N = 1$ at the upper boundary ($z = h_T$) and are spaced Δz apart. Because the mixed layer interface was typically at an intermediate height between nodes, all the nodal temperatures down to the node NI immediately below the interface, were stored in the computer. The mixed layer temperature profile was defined by the stored values of its height d_m and temperature T_m.

To compute the new temperatures at time $t + \delta t$, the forward difference form of Eqn. 3.4.3 was used. In the computer program, the temperature change at node N was stored in terms of the rate of change of nodal heat storage $P(N)$. Generally ($2 \leq N \leq NI$)

$$P(N) = \beta \, \delta T \, \Delta z / \delta t$$

However, at the upper boundary (node $N = 1$) the thickness of the nodal volume was only $\Delta z/2$ and the heat storage in the upper boundary insulation had to be included. Hence

$$P(1) = \left(\beta_T + \frac{\beta \, \Delta z}{2} \right) \frac{\delta T}{\delta t}$$

At a later stage, the temperature change δT could be evaluated from $P(N)$. The new node temperature was then calculated.

To calculate $P(N)$ from Eqn. 3.4.3 using a forward difference scheme, information about the temperatures above and below each node must be known. At the upper boundary ($N = 1$), the conditions above the node are controlled by the upper boundary heat losses. For nodes $2 \leq N \leq NI - 1$, the node temperatures above and below each node are known at time t. However, no information about the heat flux below diffusion region node NI was known. This follows from the I.C.P.M. assumption that the temperature gradients are discontinuous at the interface. The temperature change of node NI could not be calculated using Eqn. 3.4.3.

Because the rise in the interface δd_m with each time step δt was typically much less than Δz, it was necessary to know the temperature of node NI at time $t + \delta t$. This temperature was therefore obtained by extrapolation.

The diffusion region variable that was extrapolated was the rate of change of nodal heat storage P(N). Because this term is directly related to $\partial T/\partial t$, this was the same as extrapolating the rate of change of temperature profile. The values of P(N) for five nodes immediately above node NI were fitted to the simplified cubic equation

$$P(N) = ax^2 + bx + c \qquad (C.2.3)$$

using a least squares fit. The variable x is the nodal distance above node NI and a, b and c are constant coefficients. The magnitude of the coefficient c was the required value of P(NI), (i.e. $x = 0$).

The accuracy of the extrapolation method could be checked by setting $\gamma(z) = 0$ and performing a molecular entrainment analysis. For $\gamma(z) = 0$, the diffusion region is independent of the mixed layer. Hence, a second molecular entrainment analysis could be performed in which the diffusion region temperatures for $0 \leq z < d_m$ were retained as a "ghost" profile. The temperature change calculations for this profile are unaffected by the mixed layer. In the second molecular analysis, the lower boundary condition was $\partial T/\partial z = 0$ at $z = 0$. The agreement between the two analyses was good. However, no independent check on the fully turbulent I.C.P.M. case ($\gamma(z) > 0$) was available.

A second extrapolation method was also tested. The interfacial temperature gradient (between nodes NI and NI - 1) was calculated from other inter-nodal temperature gradients according to the formula

$$G_0 = \left[\frac{G_1}{G_2}\right]^3 \cdot G_3 \qquad (C.2.4)$$

where G_j is the temperature gradient between nodes NI - j and NI - j - 1. The formula was derived from the error function profile for molecular diffusion between two infinitely deep layers (Eqn. 3.4.7). A check of this formula using the two types of molecular entrainment analysis (i.e. an extrapolation formula at $z = d_m$ and "ghost" profile to $z = 0$) showed that this formula was very accurate for $\gamma(z) = 0$. However, it is doubtful whether the error function based extrapolation formula will be valid when the turbulent diffusivity $\gamma(z)$ is non-zero.

An approximate comparison of the two extrapolation methods for

turbulent entrainment (Eqns. C.2.3 and C.2.4) was made. Using Eqn. C.2.3, a turbulent entrainment analysis was performed. The numerical value of G_0 resulting from this analysis was then compared with the value calculated from the other temperature gradients (G_1, G_2 and G_3) using Eqn. C.2.4. The difference relative to $G_0 - G_1$ was seldom more than 0.1%.

Despite this apparent consistency of the temperature gradient extrapolation method (Eqn. C.2.4), preliminary tests showed it to be potentially unstable. The rate of change of nodal heat storage formula (Eqn. C.2.3) had very good stability over the range of conditions tested and was therefore used in all analyses of experimental runs (Chapter 7).

The lower boundary of the diffusion region where the extrapolation technique had to be used is an area of great importance. The interfacial gradient $(\partial T/\partial z)_i$ controls the values of $\gamma(z)$ and the interfacial heat flux Q_e. It is also an important contributing factor to V_{em} (Eqn. 3.6.6). However, the good agreement between the experimental results and the numerical analyses, and the stability of the numerical analysis model, suggest that the extrapolation method (Eqn. C.2.3) was acceptable.

Because an extrapolation formula was necessary at node NI, an implicit scheme could not be used for the finite difference calculations. Implicit schemes have the advantage that they remain stable for larger δt. The time step can be increased, thereby reducing the computational time.

(iii) Setting the interface height d_m

In the finite difference scheme, the distance between nodes was $\Delta z = 0.1$ cm and the time increment was generally $\delta t = 1$ second. As the minimum values of V_{em} were about 10^{-3} cm/sec it could take as many as 10^2 time steps for the interface to rise from one node to another. The interface height d_m after each time step δt was therefore matched to a linear interpolation of the nodal temperatures. The computational scheme is shown diagrammatically in Fig. C.3.

From Eqn. 3.5.2, the finite difference equation for the mixed layer heat budget is

$$Q_p + \overline{(\kappa + \gamma_i)\frac{\partial T}{\partial z}\Big|_i} - W\left[(T_m - T_{air})\left(d_m + \frac{\delta d_m}{2}\right) + \left(\frac{d_m}{2} + \frac{\delta d_m}{3}\right)\delta T_m\right] = \beta\left(d_m + \frac{\delta d_m}{2}\right)\frac{\delta T_m}{\delta t} \qquad (C.2.5)$$

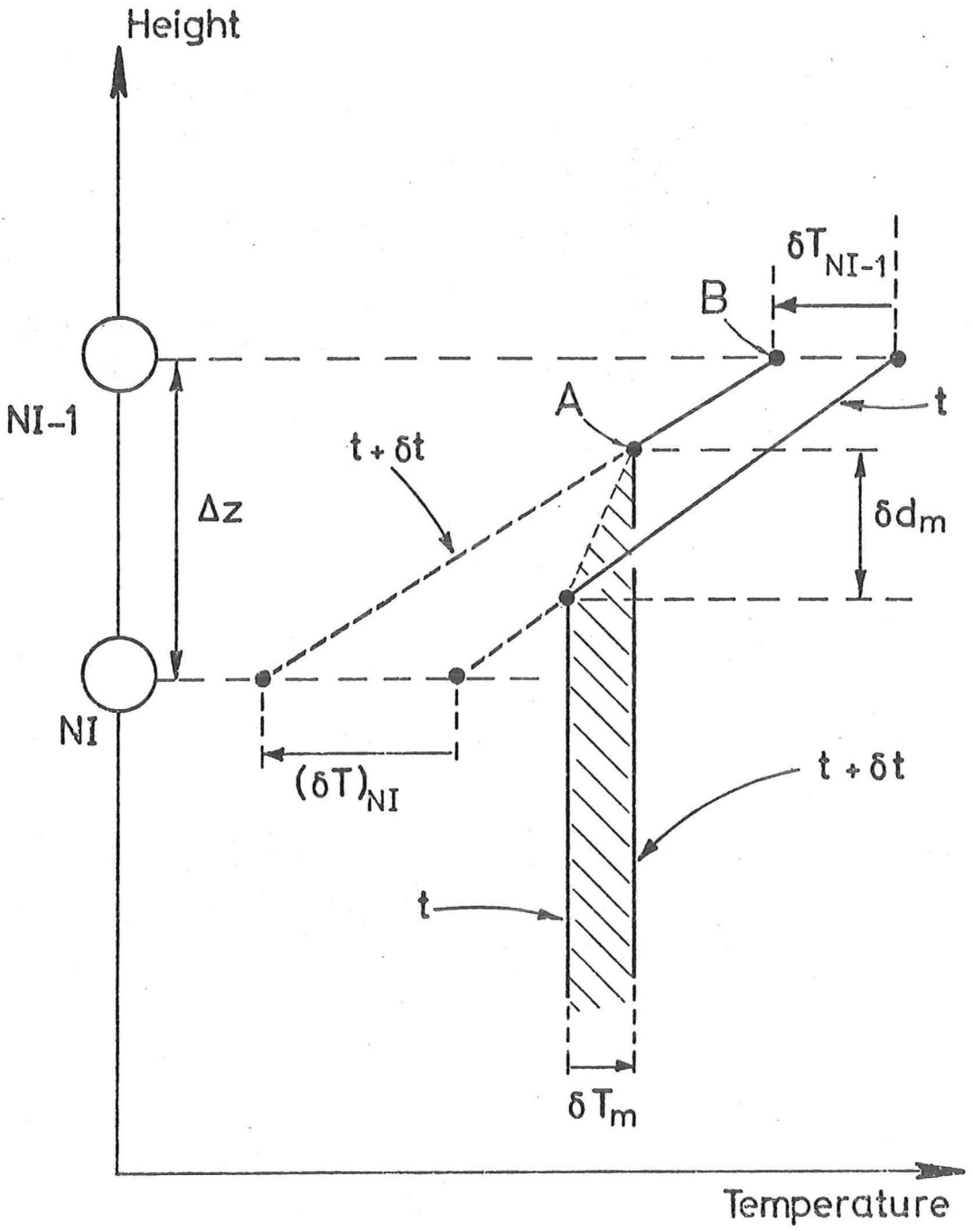

Fig. C.3. Diagram of finite difference scheme used to calculate the incremental rise of the interface.

where the overbar denotes the average of the values at t and $t + \delta t$. In this equation, the increases in mixed layer temperature δT_m and interface height δd_m are unknowns. However, from geometry it also follows that

$$d_m + \delta d_m = z_{NI} + (T_m + \delta T_m - T_{NI}^{t+\delta t}) / (\frac{\partial T}{\partial z})_i^{t+\delta t} \qquad \text{(C.2.6)}$$

where Z_{NI} is the height of node NI, $T_{NI}^{t+\delta t}$ is the temperature of this node at $t + \delta t$ and $(\partial T/\partial z)_i^{t+\delta t}$ is the interfacial temperature gradient at $t + \delta t$ given by

$$(\frac{\partial T}{\partial z})_i^{t+\delta t} = \frac{T_{NI-1}^{t+\delta t} - T_{NI}^{t+\delta t}}{\Delta z}$$

Equations C.2.5 and C.2.6 can be combined, by eliminating δd_m, to give a quadratic equation for δT_m. Once δT_m had been evaluated, the incremental rise of the interface δd_m was obtained from Eqn. C.2.6.

However, before calculating δT_m and δd_m a check was always made to ensure that the matched height (point A, Fig. C.3) was not going to be above the upper node (point B, Fig. C.3). This will occur whenever the interface is about to rise above the node at $NI-1$. The check was made by setting δT_m so that point A = point B. A quadratic equation was then solved to find the time $\delta t'$ required for the mixed layer temperature to increase by this amount. If $\delta t'$ was less than the actual time increment δt then d_m was allowed to rise in two steps. First to the height of node $NI-1$ (in time $\delta t'$) and then above it (in time $\delta t - \delta t'$). Both computations complied with the heat budget equation.

(iv) Other programming assumptions

The numerical analysis of the fully turbulent I.C.P.M. ($\gamma > 0$) was also influenced by the assumption that the fluid properties (ρ, c_p, ν, α and κ) did not vary with temperature. As discussed in Chapter 7, the constant molecular diffusivity κ assumption was probably significant. The value of $\kappa = 1.43 \times 10^{-3}$ cm^2/sec. used in the program corresponded to $T = 20°C$. Hence, at $T = 40°C$, the molecular heat transfers were underestimated by about 6%.

The rate of change of temperature in the intermittency region, and several nodes above it, were calculated in time steps of $\delta t/4$. This allowed for the decrease of the stability factor

$$\frac{(\kappa + \gamma)\ \delta t}{(\Delta z)^2}$$

as γ increased. The critical stability case occurs at the interface where the turbulent diffusivity is a maximum (γ_i). For the node spacing of $\Delta z = 0.1$ cm and the maximum time increment used, $\delta t = 2$ seconds, the stability factor of 0.5 was only exceeded once $\gamma_i > 6\kappa$. At this stage, the forward difference scheme was potentially unstable. In the numerical analyses presented in Chapter 7, this minimum stability criterion was only exceeded within five minutes of t_T.

As discussed in more detail in Chapter 7, the computer program calculated the interfacial gradient Richardson number from the maximum temperature gradient within the intermittency region $d_m < z < d_m + z_{int}$. It was assumed that the interfacial dome motions were controlled by the maximum intermittency region temperature gradient rather than the interfacial gradient. These two gradients were only different initially, when $d_m < d_{g0}$ and $(\partial^2 T/\partial z^2)_i > 0$. The slight reduction in γ_i resulting from the larger value of Ri did not appear to significantly affect the results of the numerical analyses.

To prevent the build-up of an unstable temperature distribution at the upper boundary due to heat losses, the upper diffusion region was "stirred". Whenever $T_a - T(h_T) > 0.1$ °C, the upper boundary temperature distribution was re-organized into a uniformly mixed layer of the same heat content so that the fluid column was again statically stable. As the temperature difference with the air in this upper region was about 18 °C, the effect of this numerical stirring on the heat losses was negligible.

The computer program also included an empirical simulation of the apparent breakdown of interfacial dome action at low Q_p in an unsteady heat flux experiment (Chapt. 6.4). If the heat flux was too small, there was insufficient turbulent kinetic energy in the thermal convective elements to maintain a fully mixed layer up to the existing interface. At this stage molecular diffusion took over, smoothing the interface and effectively reducing d_m.

This was modelled in the computer program, whenever Q_p was less than a minimum value Q_{pc}. The turbulent diffusivity $\gamma(z)$ was set to zero and the diffusion region was extended down to $z = 0$ with the temperatures below $z = d_m$ set equal to T_m. As there was then a large positive rate of change of temperature gradient at the interface, the temperature of node NI increased rapidly. After the mixed layer

calculation that followed, the new value of d_m was typically lower than before ($V_{em} < 0$) and the value of $\partial^2 T/\partial z^2$ at the previous interface height was reduced. This mode of behaviour differs from turbulent entrainment where the mixed layer turbulence maintains the interfacial temperature gradient discontinuity.

APPENDIX D

EXPERIMENTAL HEAT LOSSES

As the fluid column temperatures were generally higher than the external air temperature (T_{air}), heat was continually being lost to the air through the tank insulation. Heat was also stored in the tank walls and insulation. The amount of stored heat increased as the temperatures increased.

The experimental heat losses consisted of

(i) side wall losses from the mixed layer;
(ii) side wall losses from the diffusion region;
(iii) upper boundary losses;
(iv) losses through the filling reservoir;
(v) heating apparatus losses ($z < 0$).

In the first three cases, heat was lost from the fluid column through the tank wall (1.22 cm thick perspex) and the sheets of polystyrene insulation. For $0 < z < d_m$, the inner boundary of the side walls is in contact with convecting fluid of uniform temperature T_m. Typically T_m was increasing at a rate of order 10^{-3}°C/sec. In the case of the diffusion region losses, the fluid in contact with the inner wall is essentially motionless and slowly cooling. A typical rate was -5×10^{-5} °C/sec. Fluid heat transfer is by molecular diffusion.

These diffusion region heat losses will create slight buoyancy instabilities at the side walls and the upper boundary and horizontal temperature gradients within the fluid column. However, the buoyancy instabilities may cause weak convective circulations which would tend to remove any horizontal variation of temperature. As the heat losses were minor, these effects were negligible. The fluid column was therefore assumed to be one-dimensional.

Heat transfer through the filling reservoir also caused a net loss of heat from the fluid column. Whether the filling reservoir remained full of water or was drained, heat was transmitted through the experimental tank wall into the filling reservoir and then to the air. During the steady heat flux runs, the exterior of the filling reservoir was insulated with a minimum of 4.5 cm of polystyrene (Fig. 6.4).

An experiment to adequately measure the heat losses from the fluid column was difficult to design. If the tank was filled with hot water

and left to cool, most of the heat losses would have occurred through the conducting lower boundary. Insulating this boundary would have introduced additional unknown insulation. Instead, the heat losses were calculated from the thermal properties of the insulation and container materials (Table D.1). These values were obtained from the Handbook of Physics and Chemistry (54th Edition) and from manufacturers' specifications.

TABLE D.1 - TYPICAL THERMAL PROPERTIES OF FLUIDS, CONSTRUCTION MATERIAL AND INSULATION USED IN THE EXPERIMENTAL INVESTIGATION

Material	Thermal Conductivity cal/cm sec°C	Density (ρ) $_3$ gm/cm^3	Specific heat (c_p) cal/gm°C	Typical thicknesses cm	Usage
Aluminium	0.49	2.7	0.214	2.34, 7.3	Steady heat flux apparatus
Brass	0.28	8.55	0.088	0.635	Unsteady heat flux apparatus
Glass	2.3×10^{-3}	2.48	0.16	0.217	Steady heat flux apparatus
Water	1.43×10^{-3}	1.0	1.0	5 → 55	Experimental fluid
Asbestos Cement Board	9.3×10^{-4}	1.97	0.20	1.0	Insulation of steady heat flux apparatus
Perspex	5×10^{-4}	1.19	0.35	0.6, 1.22	Experimental tank construction
Polystyrene	8.6×10^{-5}	0.026	0.32	5.1, 7.6	Insulation
Air	6×10^{-5}	1.2×10^{-3}	0.24	-	-

Because the temperatures in the fluid column were changing with time the temperature distribution through the side walls and insulation did not remain steady. This was most significant for $0 < z < d_m$. To find out the variation of temperature in the mixed layer walls and insulation, a simple numerical analysis using a one-dimensional heat diffusion equation was performed. It showed that the temperature distribution adjusts rapidly to changes in T_m as both perspex and polystyrene have relatively high thermal diffusivities. Within each layer, the temperature gradients were approximately linear.

The perspex walls were thin and had a higher thermal conductivity

than the polystyrene. It could therefore be assumed that the perspex wall temperatures were horizontally uniform and equal to T_m. If the temperature differential between the outer polystyrene wall and the air due to convective transfer was neglected, the temperatures in the polystyrene could be assumed to decrease linearly from T_m to T_{air}. With these simplifications, the heat transfer and heat storage, due to the rate of change of T_m, was easily calculated.

It follows that the heat storage term for the insulated fluid column per unit height β is the heat storage capacity of the fluid and perspex walls, and half the thickness of the polystyrene insulation. An additional heat storage term β_T was required to account for the tank top storage.

For a temperature differential of $T_m - T_{air} = 20\,°C$ and side wall insulation of 1.22 cm of perspex and 7.6 cm of polystyrene, the calculated heat losses through the side walls over a height of $h_T = 55$ cm are 1.45 cal/sec. In the steady heat flux experiments, the total heat flux entering through the lower boundary was typically 20 cal/sec.

Heat losses via the filling reservoir were difficult to calculate. If the reservoir remained filled with water, the majority of heat lost was stored in this fluid as it slowly increased in temperature. If the reservoir was drained during an experimental run, the air temperature would have risen at a similar rate to T_m with little heat storage in the reservoir. However, the temperature differential between the filling reservoir and the external air would have been higher. This would have resulted in larger heat losses to the air outside the apparatus.

In the unsteady heat flux experiments it was not necessary to know the losses for $z < 0$. The circulating water temperature was maintained at T_H despite heat losses. In the steady heat flux experiments, the losses from the region between the glass plate (mid-height) and $z = 0$ needed to be known to complete the heat budget. In these experiments, the heat flux across the glass plate q_G was held constant. The insulation for this region typically consisted of a total of 2 cm of asbestos cement board and about 9 cm of polystyrene. As the height of this heat loss region was small (2.45 cm), the total heat losses were small compared to the fluid column losses.

Because the tabulated thermal properties of the insulation material and other heat loss factors are uncertain (Table D.1), the heat loss calculations were only approximate. As discussed in Chapters 6 and 7 the experimental heat losses appear to have been underestimated by a factor of two or three.

APPENDIX E

MATHEMATICAL SOLUTIONS

In this appendix, mathematical solutions of a number of I.C.P.M. equations are obtained. These are: finite and infinite boundary solutions to the molecular diffusion equation; a solution of the full column heat budget equation which yields an expression for t_T ; and an analytical solution of the filling model entrainment equations.

Equations for d_h and V_{eh} for molecular entrainment are also derived.

E.1 SOLUTIONS OF THE MOLECULAR DIFFUSION EQUATION

For the molecular diffusion period of the I.C.P.M. $(0 < t < t_s)$, there is no mixed layer and the turbulent entrainment parameters are zero. Equation 3.4.3 reduces to

$$\beta \frac{\partial T}{\partial t} = \kappa \frac{\partial^2 T}{\partial z^2} - W(T - T_{air}) \qquad \text{(E.1.1)}$$

The variation of molecular diffusivity with temperature and hence, height has been neglected. Equation E.1.1 is the molecular diffusion equation.

In the I.C.P.M. the initial conditions are (Eqn. 3.1.3)

$$T(z,0) = T_{m0} \qquad 0 \leq z < d_{g0}$$

$$T(z,0) = T_{a0} \qquad d_{g0} < z \leq h_t$$

Solutions for two different sets of boundary condition will be obtained. For the first solution, the boundaries at $z = ,0$ and h_T will be assumed to be perfectly insulated although side wall heat losses will still be included. Therefore,

$$\frac{\partial T(0,t)}{\partial z} = \frac{\partial T(h_T,t)}{\partial z} = 0$$

The second solution will be for the case where the two fluid layers are infinitely deep.

To remove the effect of the side wall heat losses, the transformation

$$\theta = (T - T_{air}) \exp\left(\frac{Wt}{\beta}\right) \qquad \text{(E.1.2)}$$

is used. Equation E.1.1 becomes

$$\frac{\partial \theta}{\partial t} = \frac{\kappa}{\beta} \frac{\partial^2 \theta}{\partial z^2} \qquad \text{(E.1.3)}$$

As both solutions have been widely reported only brief outlines of the solution methods will be given.

(i) Finite boundaries

The solution for $\theta(z,t)$ is found by the separation of variables technique, i.e.

$$\theta(z,t) = S(z) + F(z).\ G(t)$$

where $S(z)$ is the steady state solution. The complete solution is

$$T(z,t) = T_{air} + \left[T_{a0} - \frac{\Delta T_{i0}\, d_{g0}}{h_T} - T_{air} - \frac{2}{\pi}\,\Delta T_{i0} \sum_{n=1}^{\infty} \frac{1}{n} \cdot \sin\left(\frac{n\pi\, d_{g0}}{h_T}\right) \cdot \cos\left(\frac{n\pi z}{h_T}\right) \cdot \exp\left(-\zeta_n^2 t\right) \right] . \exp\left(-\frac{Wt}{\beta}\right)$$

where $$\Delta T_{i0} = T_{a0} - T_{m0}$$

and $$\zeta_n = \frac{n\pi}{h_T}\sqrt{\frac{\kappa}{\beta}}$$

(ii) Infinite boundaries

Following Carlsaw and Jaeger (1965), Eqn. E.1.3 is rewritten in terms of the variable

$$\eta = \frac{z - d_{g0}}{2\sqrt{\frac{\kappa t}{\beta}}}$$

Therefore

$$\frac{\partial^2\theta}{\partial\eta^2} = -\,2\,\eta\frac{\partial\theta}{\partial\eta}$$

The complete solution (after reversing the transformation using Eqn. E.1.2) is

$$T(z,t) = T_{air} + \left[\frac{(T_{a0} + T_{m0})}{2} - T_{air} + \frac{\Delta T_{i0}}{2}\ \mathrm{erf}\ \eta \right] .\ \exp\left(-\ \frac{Wt}{\beta}\right)$$

E.2 SOLUTION OF THE FULL COLUMN BUDGET EQUATION AND AN EXPRESSION FOR TIME t_T.

At any time $t_s < t < t_T$, the heat budget for the full fluid column is given by Eqn. 3.7.1. Ignoring upper boundary losses ($Q(h_T) = 0$), it follows that

$$Q_p - W\int_0^{h_T} (T - T_{air})\ dz = \beta \int_0^{h_T} \frac{\partial}{\partial t}\,(T - T_{air})\ dz$$

The total heat storage S is defined as

$$S = \beta [(T_a - T_{air}) h_T - \Delta T_i d_h]$$

so that

$$\int_0^{h_T} (T - T_{air}) dz = \frac{S}{\beta}$$

Hence

$$Q_p - \frac{WS}{\beta} = \frac{dS}{dt}$$

Rearranging and multiplying by $\exp(Wt/\beta)$ yields

$$\frac{d}{dt} \left[S \exp(\frac{Wt}{\beta}) \right] = Q_p \exp(\frac{Wt}{\beta})$$

Integrating with respect to time from $t = t_s$ to t gives

$$S \exp(\frac{Wt}{\beta}) - S_s \exp(\frac{Wt_s}{\beta}) = \int_{t_s}^{t} Q_p \exp(\frac{Wt}{\beta}) dt \qquad (E.2.1)$$

From Eqn. 3.4.7 ,

$$T_a - T_{air} = (T_{a0} - T_{air}) \exp(- \frac{Wt}{\beta}) \qquad (E.2.2)$$

Substituting for S and S_s in Eqn. E.2.1 using Eqn. E.2.2, yields

$$- \beta \Delta T_i d_h \exp(\frac{Wt}{\beta}) + \beta (\Delta T_i d_h)_s \exp(\frac{Wt_s}{\beta}) = \int_{t_s}^{t} Q_p \exp(\frac{Wt}{\beta}) dt \qquad (E.2.3)$$

At $t = t_s$, $\Delta T_i = \Delta T_{i0} \exp(- \frac{Wt_s}{\beta})$ and $d_h = d_{g0}$.

If Eqn. E.2.3 is evaluated at $t = t_T$, then $\Delta T_i = 0$, so that

$$\int_{t_s}^{t_T} Q_p \exp(\frac{Wt}{\beta}) dt = \beta \Delta T_{i0} d_{g0}$$

In the special case, where Q_p is held constant, it follows that

$$t_T = \frac{\beta}{W} \ell n \left[\exp(\frac{Wt_s}{\beta}) + \frac{W \Delta T_{i0} d_{g0}}{Q_p} \right] \qquad (E.2.4)$$

E.3 SOLUTION OF THE FILLING MODEL ENTRAINMENT EQUATIONS

If the initial temperature profile at $t = t_s$ in a filling model entrainment analysis is given by the infinite boundary solution to the molecular diffusion equation (Eqn. 3.4.7), an analytical solution can be found for the filling model equation (Eqn. 3.9.1)

$$V_{em} = \frac{Q_p}{\beta\, d_m \left.\frac{\partial T}{\partial z}\right|_i} \qquad \text{(E.3.1)}$$

From Eqn. 3.4.7

$$\left.\frac{\partial T}{\partial z}\right|_i = \frac{\Delta T_{i0}}{a\sqrt{\pi}} \exp(-\eta^2) \exp(-\frac{Wt}{\beta}) \qquad \text{(E.3.2)}$$

where

$$a = 2\sqrt{\frac{\kappa t_s}{\beta}}$$

and

$$\eta = (d_m - d_{g0})/a$$

From Eqns. E.3.1 and E.3.2,

$$\frac{d}{dt}(d_m) = \frac{a\, B \exp(\frac{Wt}{\beta})}{d_m \exp(-\eta^2)} \qquad \text{(E.3.3)}$$

where $B = \dfrac{Q_p \sqrt{\pi}}{\beta\, \Delta T_{i0}}$

As $\dfrac{d\eta}{dt} = \dfrac{1}{a} \dfrac{d(d_m)}{dt}$, Eqn. E.3.3 may be rewritten in terms of η so that

$$(d_{g0} + a\,\eta) \exp(-\eta^2) \frac{d\eta}{DT} = B \exp(\frac{Wt}{\beta})$$

Integrating with respect to time from t_s to t yields

$$\frac{\sqrt{\pi}}{2} d_{g0} (\text{erf}\ \eta + 1) - \frac{a}{2} \exp(-\eta^2)$$

$$= B \frac{\beta}{W} \left[\exp(\frac{Wt}{\beta}) - \exp(\frac{Wt_s}{\beta})\right] \qquad \text{(E.3.4)}$$

To be consistent with the use of Eqn. 3.4.7, the infinite boundary assumption was made in evaluating the integral. Hence, it followed that

$$\text{erf}\ \eta_s = 1 \qquad \exp(-\eta_s^2) = 0$$

where $\eta_s = -d_{g0}/a$ at $t = t_s$.

Rearranging Eqn. E.3.4 in terms of $\exp[W(t - t_s)/\beta]$ and taking the logarithm of both sides, yields

$$t = t_s + \frac{\beta}{W} \ell n \left[1 + \frac{W}{\beta} \psi \exp(-\frac{Wt_s}{\beta})\right] \qquad \text{(E.3.5)}$$

where $$\psi = \frac{\beta \Delta T_{i0}}{2 Q_p} \left[d_{g0} (\text{erf } \eta + 1) - \frac{a}{\sqrt{\pi}} \exp(-\eta^2) \right]$$

$$a = 2\sqrt{\frac{\kappa t_s}{\beta}}$$

$$\eta = (d_m - d_{g0})/a$$

The time t, when the filling model entrainment interface is at height d_m, is given explicitly by Eqn. E.3.5.

If there are no heat losses $(W = 0)$, the solution simplifies to

$$t = t_s + \psi$$

E.4 EQUATIONS FOR d_h AND V_{eh} FOR MOLECULAR ENTRAINMENT

An equation for d_h as a function of d_m and t for a molecular entrainment analysis can be derived. The diffusion region temperature profile is given by Eqn. 3.4.7 for all $0 < t < t_T$ (Chapt. 3.9). From the relationship for $d_h = \phi(d_m, t)$, an equation for V_{eh} may be obtained. Both results are used in the molecular entrainment computer program (Appendix C.1).

The mean temperature profile height d_h is given by Eqn. 3.7.2.

$$d_h = \frac{1}{\Delta T_i} \int_0^{h_T} (T_a - T)\, dz \qquad \text{(E.4.1)}$$

For the mixed layer $(0 \leq z < d_m)$, $T_a - T = \Delta T_i$. From Eqn. 3.4.7 it follows that, in the diffusion region $(z > d_m)$,

$$T_a - T = \frac{\Delta T_{i0}}{2} (1 - \text{erf } \eta) \exp(-\frac{Wt}{\beta})$$

where $$\eta = \frac{z - d_{g0}}{2\sqrt{\frac{\kappa t}{\beta}}}$$

Therefore, Eqn. E.4.1 can be rewritten as

$$d_h = d_m + \frac{1}{(1 - \text{erf } \eta_m)} \int_{d_m}^{h_T} (1 - \text{erf } \eta)\, dz \qquad \text{(E.4.2)}$$

where $\eta = \eta_m$ at $z = d_m$. The integral of the complementary error function is

$$\int (1 - \text{erf } \eta)\, dz = 2\sqrt{\frac{\kappa t}{\beta}} \left[\eta(1 - \text{erf } \eta) - \frac{\exp(-\eta^2)}{\sqrt{\pi}} \right]$$

Therefore, from Eqn. E.4.2

$$d_h = d_{g0} + 2\sqrt{\frac{\kappa t}{\pi \beta}} \quad \frac{\exp(-\eta_m^2)}{(1 - \text{erf}\ \eta_m)} \tag{E.4.3}$$

From the value of d_m at any given time t, the corresponding mean temperature profile depth d_h can be calculated.

The rate of increase of d_h with time is

$$V_{eh} = \frac{d}{dt}\ (d_h) \tag{E.4.4}$$

Consider the operator

$$\frac{d}{dt} = \frac{\partial}{\partial t} + \frac{dz}{dt} \cdot \frac{\partial}{\partial z}$$

As $$\eta = \frac{z - d_{g0}}{2\sqrt{\frac{\kappa t}{\beta}}}$$

then $$\frac{\partial}{\partial z} = \frac{1}{2\sqrt{\frac{\kappa t}{\beta}}} \quad \frac{\partial}{\partial \eta}$$

and $$\frac{\partial}{\partial t} = -\frac{\eta}{2t} \quad \frac{\partial}{\partial \eta}$$

Therefore

$$\frac{d}{dt} = \left[-\frac{\eta}{2t} + \frac{\frac{dz}{dt}}{2\sqrt{\frac{\kappa t}{\beta}}} \right] \frac{\partial}{\partial \eta} \tag{E.4.5}$$

If we define

$$G(\eta) = \frac{\exp(-\eta^2)}{(1 - \text{erf}\ \eta)} \tag{E.4.6}$$

then substituting G into Eqn. E.4.3 yields

$$d_h = d_{g0} + 2\sqrt{\frac{\kappa t}{\pi \beta}}\ G_m \tag{E.4.7}$$

where G_m is evaluated at $z = d_m$. From the definition of η and Eqn. E.4.7 it follows that

$$\eta_h = \frac{G_m}{\sqrt{\pi}} \tag{E.4.8}$$

From Eqns. E.4.4 and E.4.7

$$V_{eh} = \frac{d}{dt} \left[d_{g0} + 2\sqrt{\frac{\kappa t}{\pi \beta}}\ G_m \right]$$

Differentiating using the operator (Eqn. E.4.5) yields

$$V_{eh} = 2\sqrt{\frac{\kappa t}{\pi\beta}}\left[\frac{G_m}{2t} + \left(-\frac{\eta_m}{2t} + \frac{V_{em}}{2\sqrt{\frac{\kappa t}{\beta}}}\right)\left.\frac{\partial G}{\partial \eta}\right|_m\right] \qquad \text{(E.4.9)}$$

where $dz/dt = V_{em}$ in Eqn. E.4.5 as G is evaluated at $z = d_m$. The differential of G with respect to η from Eqn. E.4.6 is

$$\frac{\partial G}{\partial \eta} = -2\eta G + \frac{2}{\sqrt{\pi}} G^2$$

so that, from Eqn. E.4.8

$$\left.\frac{\partial G}{\partial \eta}\right|_m = 2 G_m (\eta_h - \eta_m)$$

Hence, Eqn. E.4.9 can be rewritten as

$$V_{eh} = \left(\frac{d_h - d_{g0}}{2t}\right)\left[1 + 2\left(V_{em}\sqrt{\frac{\beta t}{\kappa}} - \eta_m\right)(\eta_h - \eta_m)\right] \qquad \text{(E.4.10)}$$

The value of V_{eh} can therefore be obtained explicitly from Eqn. E.4.10 using the previously calculated values of d_m and d_h at time t.

APPENDIX F

REFORMULATION OF THE ATMOSPHERIC MODEL OF MELLOR AND DURBIN (1975)

The approach used by Mellor and Durbin (1975) in their oceanographic model is similar to that used in the I.C.P.M. (Chapt. 2.3.2). The turbulent Reynolds stresses and vertical turbulent heat flux $\overline{wT}$ were related to the vertical gradients of horizontal velocity and temperature respectively, by Richardson number dependent stability factors $\tilde{S}_M$ and $\tilde{S}_H$ (Eqns. 2.3.1 and 2.3.2). The stability factor $\tilde{S}_H$, which corresponds to E for large Pe, is related to the flux Richardson number Ri_f (Eqn. 2.3.3) according to

$$\tilde{S}_H = 0.537 - 1.98 \left(\frac{Ri_f}{1 - Ri_f} \right) \qquad (F.1)$$

At a critical value $Ri_f = 0.213$, $\tilde{S}_H$ equals zero and turbulence is suppressed. When $Ri_f = 0$, the shear flow is fully homogeneous (no temperature gradients). The negative range of Ri_f does not apply to the I.C.P.M. as this represents unstable (negative) interfacial gradients.

Because the I.C.P.M. has no mean horizontal flows, the model of Mellor and Durbin (1975) is not directly applicable. It is possible, however, to reformulate Mellor and Durbin's (1975) relationship for $\tilde{S}_H$ (Eqn. F.1) in terms of an effective gradient Richardson number

$$Ri^* = \alpha g \frac{\partial T}{\partial z} \frac{B_1 \ell_s^{*2}}{V_s^{*2}} \qquad (F.2)$$

where V_s^* and ℓ_s^* are Mellor and Durbin's (1975) turbulence scales and B_1 is a constant (= 15.0). The turbulent length scale ℓ_s^* is defined by

$$\ell_s^* = \frac{0.1 \int_0^\infty z \, V_s^* \, dz}{\int_0^\infty V_s^* \, dz} \qquad (F.3)$$

and the corresponding velocity scale V_s^*, equivalent to the square root of twice the turbulent kinetic energy, is given by Eqn. 2.3.4. From Eqns. 2.3.1, 2.3.2 and 2.3.4,

$$\frac{V^{*3}}{B_1 \ell_s^*} = \ell_s^* V_s^* \tilde{S}_M \left(\left(\frac{\partial U}{\partial z}\right)^2 + \left(\frac{\partial V}{\partial z}\right)^2 \right) - \alpha g \ell_s^* V_s^* \tilde{S}_H \frac{\partial T}{\partial z} \qquad (F.4)$$

Similarly Eqns. 2.3.1, 2.3.2 and 2.3.3 yield

$$Ri_f = \frac{\alpha g \tilde{S}_H \frac{\partial T}{\partial z}}{\tilde{S}_M \left(\left(\frac{\partial U}{\partial z}\right)^2 + \left(\frac{\partial V}{\partial z}\right)^2 \right)} \qquad (F.5)$$

It follows from Eqns. F.4 and F.5, that

$$Ri^* = \frac{1}{\tilde{S}_H} \frac{Ri_f}{(1 - Ri_f)} \qquad (F.6)$$

Rewriting Mellor and Durbin's (1975) relationship for $\tilde{S}_H$ (Eqn. F.1) in terms of Ri^* yields

$$\tilde{S}_H = \frac{0.537}{1 + 1.98\ Ri^*} \qquad (F.7)$$

Note that in this form, the critical value of Ri^*, when $\tilde{S}_H$ tends to zero, is infinity (c.f. the critical value $Ri_f = 0.213$ in Eqn. F.1).

APPENDIX G

EVALUATION OF THE RANGE OF ℓ_i/ℓ_s FROM CRAPPER AND LINDEN'S (1974) DATA

Crapper and Linden (1974) measured the thickness of the interfacial region between two mixed layers stirred by vertically oscillating stirring grids (Chapt. 2.2.1). The experimental apparatus was the same as used by Turner (1968) and a similar range of experimental conditions were studied (Fig. 2.1.). Crapper and Linden measured the thickness of the interfacial region in terms of

$$h_i = \Delta T_i / (\partial T/\partial z)_c \qquad (G.1)$$

where $(\partial T/\partial z)_c$ is the gradient over the central 50% of the interfacial region. On the basis of their results, they assumed that the variation of h_i/ℓ_s was independent of the overall Richardson number Ri_o. Their results plotted in the form h_i/ℓ_s versus Péclet number on a log-log graph are shown in Fig. G.1.

Thompson and Turner's (1975) turbulence scales (ℓ_{sT} , σ_{uT}) were used in the data analysis so that

$$Pe_{CL} = \frac{\sigma_{uT}\,\ell_{sT}}{\kappa} \qquad (G.2)$$

For decreasing Péclet number, the thickness of the interfacial region increased. At low Péclet number, a diffusive core formed in the central interfacial region (Fig. 2.1). Shadowgraph observations confirmed that this diffusive core was non-turbulent.

The buoyancy heat flux should be approximately constant with height in the interfacial region between the two mixed layers. If the heat transfer through the diffusive core is by molecular diffusion alone, then

$$Q_e = -\kappa \left.\frac{\partial T}{\partial z}\right|_c \qquad (G.3)$$

Crapper and Linden (1974) found this equation held for $Pe_{CL} < 120$. For higher Péclet number, the diffusive core was eroded by the turbulent diffusion regions at each interface (Fig. 2.1) and the ratio

$$R_q = -\kappa \left.\frac{\partial T}{\partial z}\right| \Big/ Q_e \qquad (G.4)$$

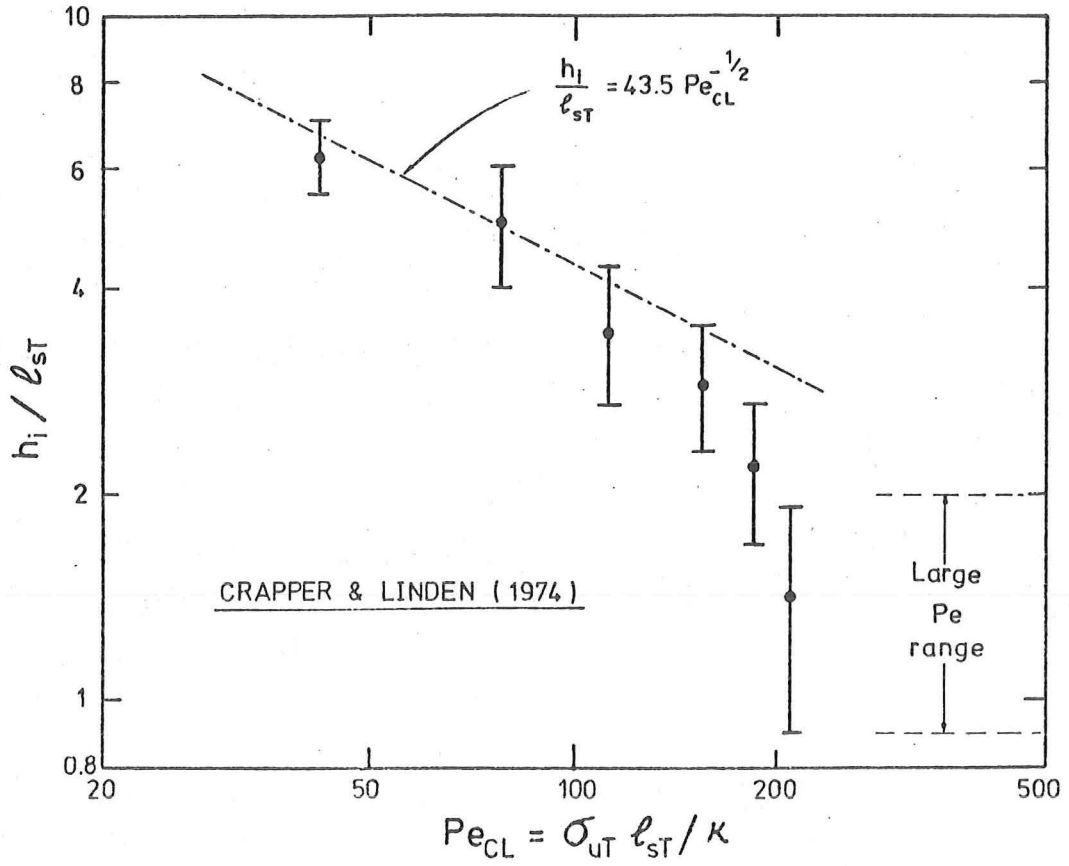

Fig. G.1. Thickness of the interfacial region between two grid-stirred layers as a function of Péclet number. (After Crapper and Linden 1974.)

Combining the definitions of E_o, h_i and R_q (Eqns. 2.1.3, G.1 and G.4) yields

$$\frac{h_i}{\ell_s} = \frac{1}{R_q\ E_o\ Pe} \qquad (G.5)$$

At low Péclet number, Crapper and Linden's (1974) data suggest the relationship

$$h_i / \ell_s \propto Pe^{-\frac{1}{2}}$$

From Eqn. G.5, this is consistent with the results of Fortescue and Pearson (1967). They measured the entrainment of carbon dioxide gas into a turbulent water layer (large Ri) and found

$$E_o \propto Pe^{-\frac{1}{2}}$$

From this result and Eqn. 4.4.3, it follows that, if molecular diffusion effects are important relative to turbulent diffusion effects, (γ_i / κ is small),

$$\ell_i / \ell_s \propto Pe^{-\frac{1}{2}}$$

This relationship can be approximately evaluated using Crapper and Linden's (1974) results (Fig. G.1). A good fit of the low Pe data is

$$h_i/\ell_{sT} = 43.5\ Pe_{CL}^{-1/2} \qquad (G.6)$$

Taking into account the velocity scale transformation needed to relate the Péclet number and E_o to the I.C.P.M. (Chapter 4), Eqns. G.5 and G.6 yield

$$E_o = 0.0172\ \ Pe^{-1/2} \qquad (G.7)$$

or from Eqn. 4.4.3

$$\ell_i/\ell_s = 58.1\ \ Pe^{-1/2} \qquad (G.8)$$

These relationships only apply to the range of low Péclet numbers studied by Crapper and Linden (1974) and to their type of experiment (i.e. double-layer grid stirring). However, the experimental conditions of Turner (1968) and Crapper and Linden (1974) were similar. Equation G.8 will also be assumed to be applicable to Turner's low Pe data.

APPENDIX H

AN EXPLANATION FOR THE LARGE k VALUES REPORTED BY CARSON (1973)

Carson (1973) and Stull (1973) both analysed the O'Neill data for the 25th August 1953 (Lettau and Davidson 1973) but obtained very different values of k. Stull's analysis is implied $k \approx 0.15$ whereas Carson (1973) obtained a range of k values from zero to a maximum of 0.5. This maximum value of $k = 0.5$ has been used recently to evaluate empirical constants in other atmospheric models (Tennekes 1975, Zeman and Tennekes 1977). However, Carson's higher values of k may be explained by comparing his data analysis assumption with the assumptions used to derive his model equations.

To analyse the atmospheric data, Carson divided the boundary layer growth into three phases. The first phase was the rapid erosion of the nocturnal inversion and the second was the boundary layer growth up to 850 metres. In both these phases, k was assumed to be zero. Thereafter, k was taken as non-zero (phase three).

For this theoretical model, Carson assumed that the interface had negligible thickness. Hence, $d_h = d_m$ and $k = k_e = k_h = k_m$. He also assumed that $d_m = 0$ when $\Delta T_i = 0$. These are the same assumptions used by Betts (1973), (Chapt. 2.2.2).

As shown in Appendix B, the value of k evaluated by Carson (1973) from Eqn. B.2.8 is related to k_h according to Eqn. B.2.9. Because Carson assumed $k = 0$ up to 850 metres then $d_{hv} \approx 850$ metres (i.e. ΔT_i was still zero up to this height).

In order to evaluate k in terms of k_h and d_h (Eqn. B.2.9), the value of k_h is required. Consider Eqn. B.2.3 rewritten in terms of k_h and c_i where $c_i = d_h/d_m = k_h/k_m$ is assumed to be constant (Appendix B.2).

$$(1 + k_h) = c_i\ (1 + k_e) + \frac{(c_i - 1)}{c_i^2}\ \frac{d_h \Gamma\ k_h}{\Delta T_i}$$

Substituting for ΔT_i from Eqn. B.2.5 yields

$$(1 + k_h) = c_i\ (1 + k_e) + \frac{(c_i - 1)(1 + 2\ k_h)}{\left[1 - \left(\frac{d_{hv}}{d_h}\right) \frac{1 + 2k_h}{k_h}\right]} \qquad \text{(H.1)}$$

This relationship implies a value of k_h greater than k_e .

Consider the specific example of d_h = 1200 metres. For the atmospheric case (large Pe) $\ell_i = \ell_s = 0.1\, d_m$ so that $c_i \approx 1.06$ (Fig. B.1). Stull's (1973) analysis of the same data used by Carson suggests k_e is about 0.15. Substituting these values (d_{hv} = 850 metres) into Eqn. H.1, yields implicitly the value of $k_h = 0.34$ (c.f. $k_e = 0.15$). From Eqn. B.2.9, this value of k_h corresponds to a value of k from the simple model of $k = 0.53$. In other words, the simple Betts' (1973) model, with initial values, overestimates the value of k_e by over 250%. The value of $k = 0.53$ is consistent with Carson's (1973) result.

With increasing d_h , the equations are less dependent on the initial values of d_{hv} (Stull 1973). The values of k and k_h decrease with increasing height. For the particular assumed values of k_e and c_i used in this specific example, the asymptotic value of k at large d_h (Eqns. B.2.9 and H.1) is $k = 0.32$. However, k_e will have decreased as the heat flux Q_p decreased in the late afternoon. In Carson's (1973) analysis, the minimum value of k calculated was $k = 0.25$.

Whilst the values used in this example only approximate the actual atmospheric conditions, the effects of assuming the initial conditions $d_m = \Delta T_i = 0$ and neglecting the interfacial thickness are clearly illustrated. This suggests that Carson's (1973) value of $k = 0.5$ is not representative of atmospheric values of k_e . As discussed in Chapters 4 and 5, a range of $0 < k_e < 0.2$ more accurately describes atmospheric behaviour.

APPENDIX I

ENTRAINMENT DATA FROM THE UNSTEADY HEAT FLUX EXPERIMENTS

Because the temporal behaviour of the unsteady heat flux entrainment experiments was irregular, these experiments do not present a clear picture of the penetrative convection process. The irregular temporal behaviour was caused by the numerous increases in T_H. These were necessary whenever the buoyancy heat flux Q_p became too small to maintain a fully turbulent mixed layer.

The unsteady heat flux entrainment experiments also had rapidly varying values of T_m and d_m due to the relatively large heat fluxes. In some cases, the lower boundary buoyancy heat fluxes were as high as 0.130 cm °C/sec whereas Q_p in the steady heat flux entrainment heat flux experiments was maintained at approximately 0.023 cm °C/sec. The unsteady heat flux experiments were therefore shorter which meant fewer temperature measurements could be taken.

Four unsteady heat flux entrainment experiments will be presented in this thesis (EU1, EU2, EU3 and EU4). In these experimental runs, the changes in T_H were kept to a minimum and the mixed layer temperatures T_m did not increase too rapidly. Run EU4 is presented in greater detail in Chapter 6.

The experimental data from the other three unsteady heat flux runs are given in Figs. I.1, I.2 and I.3. The graphs show the temperature versus time data at integer (centimetre) heights in the diffusion region and for the mixed layer. The time scale is set to an arbitrary experimental origin and is not related to a virtual I.C.P.M. origin. The variation of T_H, the fluid temperature below the lower boundary, is also shown. From the temperature difference $\Delta T_H = T_H - T_m$, the heat flux Q_p may be calculated using either Eqn. 6.4.2 or Fig. 6.13.

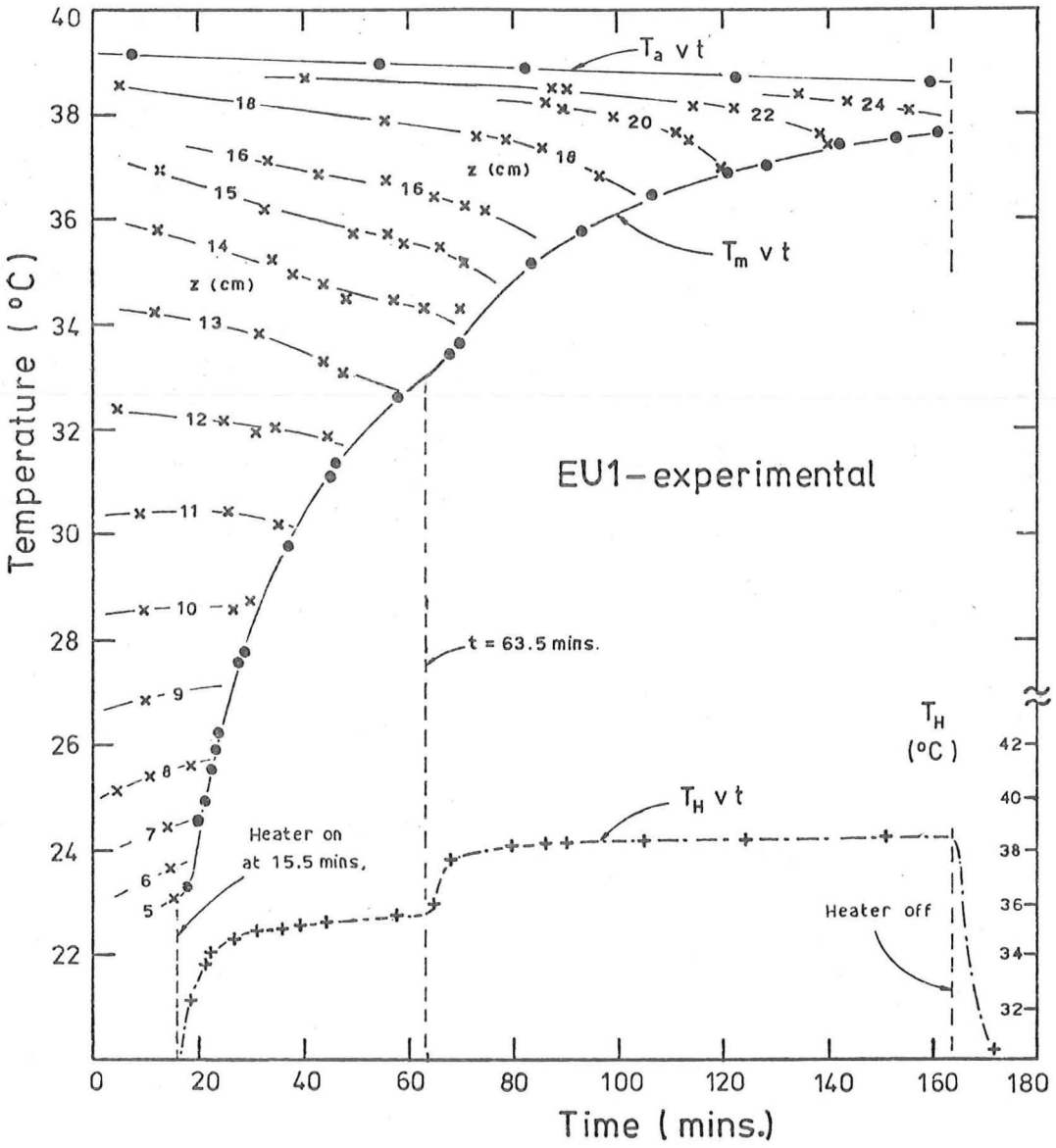
Temperature (°C)
Time (mins.)
T_a v t
T_m v t
T_H v t
T_H (°C)
z (cm)
18
16
15
14
13
12
11
10
9
8
7
6
5
20
22
24
EU1-experimental
t = 63.5 mins.
Heater on at 15.5 mins.
Heater off
40
38
36
34
32
28
26
24
22
0
20
40
60
80
100
120
140
160
180
42
40
38
36
34
32

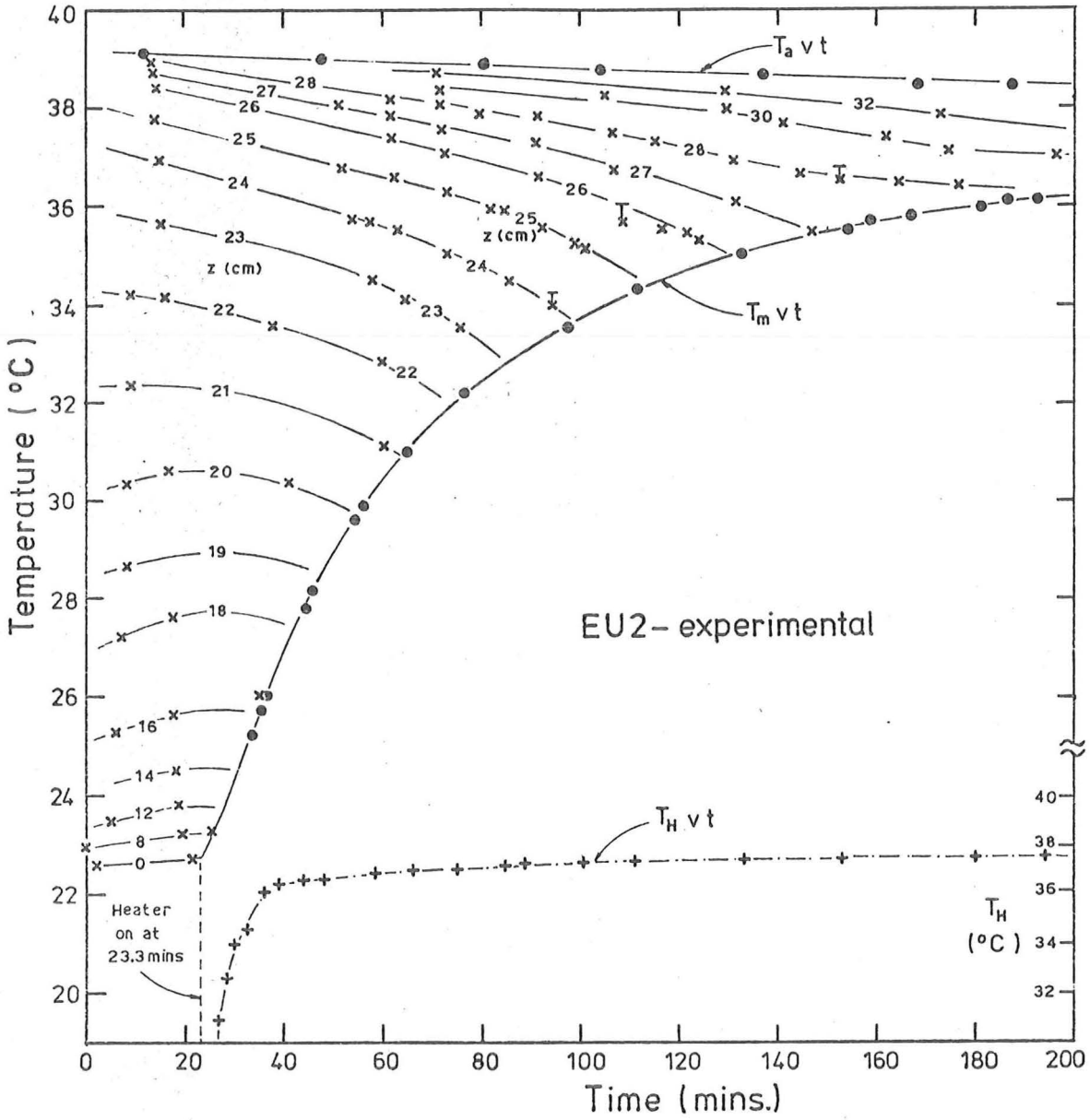
Temperature (°C)
Time (mins.)
T_a v t
T_m v t
T_H v t
T_H (°C)
z (cm)
EU2- experimental
Heater on at 23.3 mins

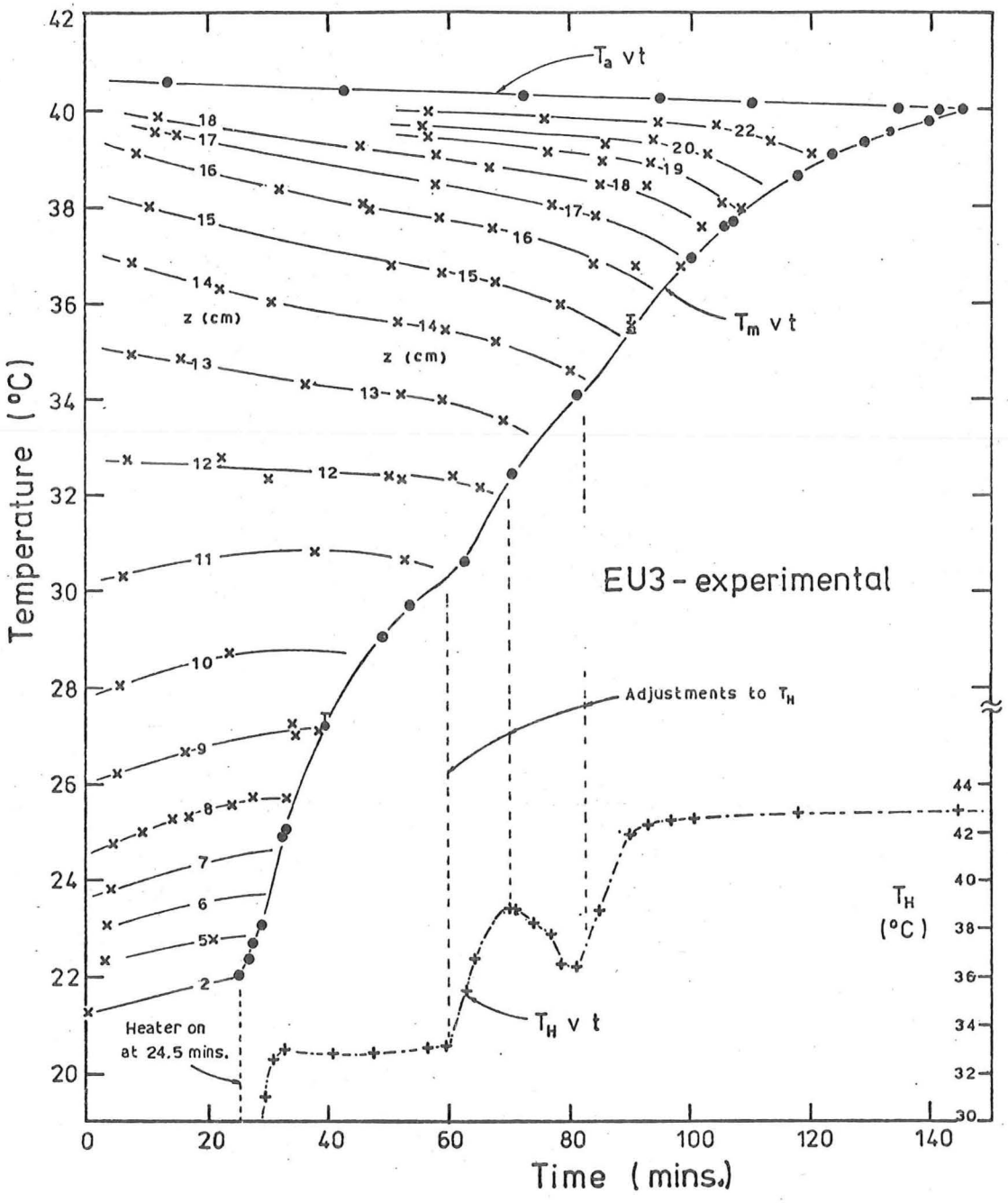

Fig. I.3. Temperature versus time graph from unsteady heat flux entrainment experiment EU3. Contour labels give height in centimetres. The temperature of the circulated heating water T_H as a function of time is also shown.

APPENDIX J

LISTINGS OF COMPUTER PROGRAMS

J.1 MOLECULAR ENTRAINMENT ANALYSIS

Selected variable names used in this computer program and the terms they represent are listed (alphabetically) below.

ALPHA	$t_T - t_s$	ES	t_s
BETA	β	ET	time t
CK	κ	ET*	non-dimensional time
CKE	k_e	GRAD	$(\partial T/\partial z)_i$
CKH	k_h	HT	h_T
CKM	k_m	QP	Q_p
CS	W	SF	ρc_p
CST	K_V	SL	plan dimension L
DGO	d_{g0}	TA	T_{air}
DH	d_h	TM	T_m
DIT	ΔT_i	VEM	V_{em}
DM	d_m (previous)	VEF(N)	filling velocity
DM*L	non-dimensional d_m	VMAX	$(V_{em})_{max}$
DT	time increment δt	ZM	d_m (updated)

Three data cards are required. All the data are input and output in c.g.s. units except for the elapsed time parameters t , t_s and t_T . These are given in minutes.

A listing of the molecular entrainment analysis computer program follows.

```
C
C     ****************************************************************
C     **                                                            **
C     **   MOLECULAR AND FILLING MODEL ENTRAINMENT ANALYSES OF      **
C     **   THE I.C.P.M. FOR CONSTANT LOWER BOUNDARY HEAT FLUX       **
C     **                                                            **
C     ****************************************************************
C
      READ(5,500)DT,CK,BETA
  500 FORMAT(F10.2,E10.2,F10.3)
      READ(5,502)QP,DITO,TMO,DGO,ES
  502 FORMAT(F10.4,F10.3,F10.3,F10.3,F10.3)
      READ(5,504) CST,TA,SL,SF
  504 FORMAT(E10.3,F10.3,F10.3,E10.3)
      DIMENSION BST(90),DML(90),DMF(90),CKM(90),CKH(90)
      DIMENSION BEF(90),BDM(90),VEF(90),BSF(90)
      L=0
      L2=0
      CY1=1.0
    3 CONTINUE
    5 CONTINUE
      L2=L2+1
      N=0
      TOL=1.0E-08
      ET=DT*0.5+ES*60.0
      PI=3.14159
      HT=54.0
      WMAX=1.5
      EP=ES*60.0
      DM=0.0
      ZM1=DM+1.0
      ZM3=-WMAX*DT
      CS=CST*4.0/(SL*SF)
      ALPHA=BETA*DITO*DGO/(QP*60.0)
      A1=QP*2.0/(BETA*DITO)
      A2=CK/BETA
      A3=SQRT(PI)
      A5=EXP(-CS*ES*60.0/BETA)
      IF(CST.GT.0.0) ALPHA=ALOG(1.0+CS*ALPHA*60.0*A5/BETA)*BETA
     1/(CS*60.0)
      F1=2.0*SQRT(CK*ES*60.0/BETA)
      F4=F1*A3
      GRAD=DITO/(F4*A5)
      WRITE(6,590)
  590 FORMAT('1',T5,'CONSTANT BOUNDARY HEAT FLUX CASE'/)
      IF(L2.EQ.1) WRITE(6,620)
  620 FORMAT('0',T5,'MOLECULAR ENTRAINMENT ANALYSIS'/)
      IF(L2.EQ.2) WRITE(6,621)
  621 FORMAT('0',T5,'FILLING MODEL ENTRAINMENT ANALYSIS'/)
      WRITE(6,600)DT,CK,BETA
  600 FORMAT('0',T6,'DT=',F5.2,T17,'CK=',+1PE10.2,T33,'BETA=',0PF5.2)
      WRITE(6,602)QP,DGO,ES
  602 FORMAT('0',T6,'QP=',F8.4,T20,'DGO=',F7.3,T35,'ES=',F7.2)
      WRITE(6,606)TMO,DITO,ALPHA,GRAD
  606 FORMAT('0',T6,'TMO=',F7.3,T20,'DITO=',F7.3,T35,'ALPHA=',F8.3,T53,'
     1GRAD(MAX)=',F6.3)
      IF(CST.GT.0.0)WRITE(6,612)CST,TA,SL,SF
  612 FORMAT('0',T5,'HEAT LOSS CASE    CST=',+1PE11.3,'    TA=',0PF7.3,
     1'    SL=',F6.2,'    SF=',+1PE11.3/)
      IF(CST.EQ.0.0)WRITE(6,614)
  614 FORMAT('0',T5,'NO HEAT LOSSES     CST=0.0'/)
      WRITE(6,604)
  604 FORMAT('0',T5,'N',T9,'ET(MINS)',T23,'DM',T35,'VEM',T48,'DH',T57
     1,'GRAD',T69,'TM',T79,'DIT',T91,'QP',T101,'CKE',T109,'ERROR(VEM)'/)
   15 CONTINUE
C
C
C     CALCULATION OF NEW DEPTH OF INTERFACE
C     -------------------------------------
C
      A4=SQRT(ET*PI*CK/BETA)
   20 ZM=ZM1
      W1=EXP(-CS*ET/BETA)
      B1=(DM+ZM-2.0*DGO)*0.5
      D1=B1/F1
      B2=B1*B1*BETA/(4.0*CK*ET)
      B3=(DM+ZM)/2.0
      B4=EXP(-B2)
      IF(B4.LT.TOL)GO TO 25
      IF(L2.EQ.1) ZM1=DM+(A1*A4/(B3*B4*W1)+A2/B3+0.5*B1/ET)*DT
      IF(L2.EQ.2) ZM1=DM+A1*F4*0.5*DT/(EXP(-D1*D1)*W1*B3)
      IF(ZM1-DM.GT.WMAX*DT)GO TO 25
      IF(ABS(ZM1-ZM).GT.TOL)GO TO 20
   26 CONTINUE
      IF(ET/60.0.GE.ALPHA+ES-1.0)GO TO 60
      IF(ET.GT.EP)GO TO 30
      ET=ET+DT
      ZM3=DM
      DM=ZM1
      GO TO 15
   25 ZM1=DM+WMAX*DT
      GO TO 26
C
C
C     CALCULATION OF PARAMETERS FOR PRINTOUT
C     --------------------------------------
C
   30 EP=EP+600.0
      IF(EP/60.0-ES.LT.20.0)EP=EP-480.0
      IF(ALPHA+ES-EP/60.0.LT.10.0)EP=EP-480.0
```

```
      N=N+1
      ET=ET-DT*0.5
      W1=EXP(-CS*ET/BETA)
      F3=(DM-DGO)/F1
      G1=EXP(-F3*F3)
      G2=ERF(F3)
      IF(L2.EQ.2)GO TO 33
C
CC
C     MOLECULAR ENTRAINMENT
C     ---------------------
C
      C1=SQRT(CK*ET/BETA)
      C3=(DM-DGO)*0.5/C1
      C4=EXP(-C3*C3)
      C5=1.0-ERF(C3)
      IF(C5.LT.TOL) GO TO 60
      DIT=DITO*0.5*C5*W1
      TM=TA+(TMO+DITO-TA-DITO*0.5*C5)*W1
      GRAD=(C4*DITO*0.5*W1)/(C1*A3)
      IF(DM.EQ.0.0)DM=TOL
      VEM=A1*C1*A3/(DM*C4*W1)+A2/DM+(DM-DGO)*0.5/ET
      DH=DGO+2.0*C1*C4/(A3*C5)
      GO TO 34
C
CC
C     FILLING MODEL ENTRAINMENT
C     -------------------------
C
   33 CONTINUE
      IF(1.0-G2.LT.TOL) GO TO 60
      DIT=DITO*0.5*(1.0-G2)*W1
      TM=TA+(TMO-TA+DITO*0.5*(1.0+G2))*W1
      GRAD=DITO*W1*G1/F4
      IF(DM.LT.TOL) DM=TOL
      VEM=QP/(BETA*DM*GRAD)
      DH=DGO+F1*G1/(A3*(1.0-G2))
   34 CONTINUE
      IF(VEM.GT.WMAX)VEM=WMAX
      ERR=(ZM1-ZM3)*0.5/DT-VEM
      CKE=CK*GRAD/QP
      IF(L2.EQ.2)CKE=0.0
      CKM(N)=DIT*BETA*VEM/QP
      CKH(N)=DH*(1.0+CK*GRAD/QP)/DM-1.0
      IF(L2.EQ.2)CKH(N)=DH/DM-1.0
      BST(N)=(ET/60.0-ES)/ALPHA
      DML(N)=(DM-DGO)/SQRT(PI*CK*(ES+ALPHA*0.50)*60.0/BETA)
      EO=(DGO*(G2+1.0)-F1*G1/A3)/A1
      IF(CST.EQ.0.0) GO TO 58
      EO=ALOG(1.0+CS*EO*A5/BETA)*BETA/CS
      W1=EXP(-CS*(EO+ES*60.0)/BETA)
   58 BEF(N)=EO/60.0+ES
      GRAF=G1*DITO*W1/F4
      VEF(N)=QP/(BETA*DM*GRAF)
      BDM(N)=DM
      BSF(N)=(BEF(N)-ES)/ALPHA
      DMF(N)=(DM-DGO)*2.0/F4
      EH=ET/60.0
      WRITE(6,700)N,EH,DM,VEM,DH,GRAD,TM,DIT,QP,CKE,ERR
  700 FORMAT('0',I4,T9,F7.2,T20,F7.3,T30,+1PE11.3,T45,0PF7.3,T56,F6.3,
     1T66,F7.3,T77,F7.3,T87,F8.4,T99,F6.3,T109,+1PE9.1)
      DM=ZM1
      ET=ET+DT*1.5
      GO TO 15
   60 CONTINUE
      WRITE(6,702)
  702 FORMAT(///'0',T5,'N',T11,'ET*',T22,'DM*L',T33,'DM*F',T44,'CKM',
     1T54,'CKH',T62,'EF(MINS)', T76,'DM',T88,'VEF',T100,'EF*'/)
      DO 61 I=1,N
      WRITE(6,704)I,BST(I),DML(I),DMF(I),CKM(I),CKH(I),BEF(I),
     1BDM(I),VEF(I),BSF(I)
  704 FORMAT('0',I4,T9,F7.4,T20,F7.4,T31,F7.4,T42,F6.3,T52,F6.3,T62,
     1F7.2,T73,F7.3,T83,+1PE11.3,T98,0PF7.4)
   61 CONTINUE
      IF(L2.EQ.1) GO TO 5
      GO TO 63
      L=L+1
      IF(L.EQ.1)CY1=0.5
      IF(L.EQ.2)CY1=4.0
      IF(L.EQ.3)CY1=0.75
      IF(L.EQ.4)GO TO 63
      GO TO 3
   63 CONTINUE
      STOP
      END
```

J.2 TURBULENT ENTRAINMENT ANALYSIS

Selected variable names used in this computer program and the terms they represent are listed (alphabetically) below.

BETA	β	GS(N)	$\partial T(z)/\partial z$
BETAR	β_T	HT	h_T
CK	κ	PECLET	Pe
CKE	k_e	PER	diurnal heating period
CKH	k_h	PI	π
CKM	k_m	Q(N)	Q(z)
CRT	K_T	QGK	q_G
CST	K_V	QP	Q_p
CT	c_t	QR	$Q(h_T)$
CVEXP	α	RICH	Ri
DG	d_g	RTM	dT_m/dt
DH	d_h	SA	S_p
DIT	ΔT_i	SF	ρc_p
DLTM	δT_m	SL	plan dimension L
DM	d_m (previous)	T(N)	T(z)
DMA	d_m (updated)	TA	T_{air}
DSCAL	ℓ_s	TAX	T_a
DT	time increment δt	TH	T_H
DZ	nodal spacing Δz	TM	T_m
EMAX	E_{max}	VEM	V_{em}
ET	time t	VSCAL	V_s
ETDF	t_s	WR	W_T
GAMMA	γ_i	WS	W
GMB(N)	$\gamma(z)$	ZINT	z_{int}
GRAD	Γ		

Eight input data cards are required unless the initial temperature profile data are to be read in. For this case additional data cards are needed at the end of the input data deck. All data are input and output in c.g.s. units (cm, gm, sec, cal, °C) except for the elapsed time parameters (t, t_s, t_T) which are given in minutes.

For the second input data card, seven input labels need to be specified. These allow a choice of initial and boundary conditions and the experimental fluid. The final label determines the type of analysis to be performed. The input labels and the conditions they represent for given values, are presented below.

LI	=	1	read initial temperature data
	=	2	generate initial temperature data
LB	=	1	linearly stratified case
	=	2	two-layer case
	=	3	general profile case
LR	=	1	upper boundary heat losses
	=	2	constant upper boundary temperature
LQ	=	1	constant Q_p
	=	2	constant q_G
	=	3	constant T_H
	=	4	diurnal heating cycle
LF	=	1	fluid is water
	=	2	fluid is air
LL	=	1	heat losses
	=	2	zero losses ($W = W_T = 0$)
LAMX	=	1	molecular entrainment ($\gamma = 0$)
	=	2	turbulent entrainment

A listing of the turbulent entrainment analysis computer program follows.

```
C
C ***********************************************
C *                                             *
C *   INVERTED COOLING POND ENTRAINMENT MODEL   *
C *                                             *
C ***********************************************
C
C
C     INPUT PARAMETERS AND LABELS
C    -----------------------------


      READ(5,500)DT,DZ

  500 FORMAT(F10.2,F10.2)
      WRITE(6,600)

  600 FORMAT('0',T5,'TIME INCREMENT DT',T30,
     1'HEIGHT INCREMENT DZ')
      WRITE(6,601)DT,DZ
  601 FORMAT('0',T8,F5.2,' SECONDS',T35,F5.2,' CM'////)
      READ(5,502)LI,LB,LR,LQ,LF,LL,LAMX
  502 FORMAT(I2,2X,I2,2X,I2,2X,I2,2X,I2,2X,I2,2X,I2)
      WRITE(6,602)LI,LB,LR,LQ,LF,LL,LAMX
  602 FORMAT('0',T5,'LI=',I2,T15,'LB=',I2,T25,'LR=',
     1I2,T35,'LQ=',I2,T45,'LF=',I2,T55,'LL=',I2,T65,'LAMX=',I2///)
      GO TO(7,8,9)LB
    7 WRITE(6,650)
  650 FORMAT('0',T5,'*** LINEARLY STRATIFIED CASE ***')
      GO TO 6
    8 WRITE(6,652)
  652 FORMAT('0',T5,'*** TWO LAYER CASE ***')
      GO TO 6
    9 WRITE(6,654)
  654 FORMAT('0',T5,'*** HYBRID PROFILE CASE ***')
    6 CONTINUE
      READ(5,504)SS,SR,CST,CRT,HT,SL
  504 FORMAT(F10.2,F10.2,E10.3,E10.3,F10.2,F10.2)
      READ(5,506)TH,QPC,SA,TOL
  506 FORMAT(F10.3,F10.6,F10.3,E10.2)
      READ(5,508)QGK,GRAD,RTM
  508 FORMAT(F10.5,F10.3,E10.2)
      READ(5,510)TA,DM,TM,ET,DG,EP,ETDF
  510 FORMAT(F10.3,F10.3,F10.3,F10.3,F10.3,F10.3,F10.3)
      READ(5,512)XETA,PER,QSN,PI
  512 FORMAT(F10.3,F10.2,F10.5,F10.5)
      DIMENSION P(600),T(600),Q(600),GS(60)
      DIMENSION GMB(150),PA(150)
      EMAX=0.66
      CT=2.31
      CE2=2.5
      CE3=0.01
      WCORR=0.0233
      WALP=3.427E-03
      MCON=4
      N=DM
      DM5=1+N
      ET=ET*60.0
      EP=EP*60.0
      ETDF=ETDF*60.0
      PER=PER*60.0
      DMA=DM+DZ*0.5
      NM=HT/DZ+TOL+1
      NI=DM/DZ+TOL
      NI=NM-NI
      N=HT
      NO=NM-N*10
      IF(NO.EQ.1) NO=11
      NR=1
      NWT=0
      QP=QPC
      READ(5,522)T(NM),T(1)
  522 FORMAT(F10.3,F10.3)
      GO TO(11,12)LF
   11 SF=1.0
      CF=1.43E-03
      FQ=0.0359
      CVEXP=2.5E-04
      WRITE(6,604)
  604 FORMAT('0',T5,'WORKING FLUID IS WATER')
      GO TO 13
   12 SF=2.89E-04
      CF=6.0E-05
      FQ=1.003
      CVEXP=3.5E-03
      WRITE(6,606)
  606 FORMAT('0',T5,'WORKING FLUID IS AIR')
   13 GO TO(15,16)LL
   16 SS=0.0
      SR=0.0
      CST=0.0
      CRT=0.0
      WRITE(6,608)
  608 FORMAT('0',T5,'NO HEAT LOSSES')
      GO TO 18
   15 WRITE(6,610)
  610 FORMAT('0',T5,'HEAT LOSSES INCLUDED')
   18 CK=CF/SF
      WS=CST*4.0/(SF*SL)
      WR=CRT/SF
      BETA=(SF*SL*SL+SS)/(SF*SL*SL)
      BETAR=BETA+SR*2.0/(SF*SL*SL*DZ)
      DSZ=BETA*DZ
```

```
      GO TO(21,22)LR
   21 WRITE(6,612)
  612 FORMAT('0',T5,'UPPER BOUNDARY LOSSES')
      GO TO 24
   22 WRITE(6,614)
  614 FORMAT('0',T5,'CONSTANT TOP TEMPERATURE')
   24 GO TO(26,27,28,29)LQ
   26 WRITE(6,620)QGK
  620 FORMAT('0',T5,'CONSTANT HEAT FLUX CASE',T35,'HEAT FLUX=',F8.6,
     1'CM*DEG C /SEC'///)
      GO TO 30
   27 WRITE(6,622)QGK
  622 FORMAT('0',T5,'CONSTANT HEAT INTO ALUMINIUM BASE',
     1T45,'GLASS HEAT FLUX =  ',F8.6,' CAL/CM*CM*SEC'///)
      GO TO 30
   28 WRITE(6,624)TH
  624 FORMAT('0',T5,'CONSTANT WATER BATH TEMPERATURE',
     1T43,'TEMP=',F8.3,' DEGREES CELCIUS'///)
      GO TO 30
   29 DIT=(XETA-1.0)*QSN
      QSA=-QSN
      WRITE(6,626)DIT,QSA
  626 FORMAT('0',T5,'SINUSOIDAL HEAT INPUT',T35,
     1'MAX VALUE=',F10.5,T65,'MIN VALUE=',F10.5///)
   30 GO TO(33,34)LI
C
C     READ INPUT TEMPERATURES
C     -----------------------
C
   33 MN=HT+1
      IF(NO.EQ.11) MN=MN-1
      READ(5,520)(T(M),M=2,MN)
  520 FORMAT(8F10.3)
      GS(1)=T(1)-TO
      DO 36 N=1,MN
   36 GS(N)=T(N+1)-T(N)
      GS(MN+1)=(T(NM)-T(MN))/(NO*DZ)
      DO 38 N=2,11
   38 T(N)=T(N-1)+GS(1)*DZ
      DO 37 M=1,MN-1
      N=M*10
      DO 37 I=2,11
   37 T(N+I)=T(N+I-1)+GS(M+1)*DZ
      DO 35 I=2,NO-1
      N=MN*10
   35 T(N+I)=T(N+I-1)+GS(MN+1)*DZ
      GO TO 45
C
C     GENERATE INPUT TEMPERATURES
C     ---------------------------
C
   34 CONTINUE
      GO TO(41,42)LB
   41 GRAD=(T(1)-T(NM))/HT
      DO 44N=2,NM-1
   44 T(N)=T(1)-GRAD*N*DZ
      GO TO 45
   42 TE=(T(1)+T(NM))/2.0
      DIT=(T(1)-T(NM))/2.0
      AKT=2.0*SQRT(CK*ET)
      DO 43 N=2,NM-1
   43 T(N)=TE+DIT*ERF((HT-(N-1)*DZ-DG)/AKT)
      GRAD=0.0
   45 CONTINUE
      EH=ET/60.0
      WRITE(6,630)EH
  630 FORMAT('0',T5,'INITIAL TIME =',F10.3,' MINS'///)
      WRITE(6,632)
  632 FORMAT('0',T5,'HEIGHT (CMS)',T20,'TEMPERATURE (DEG C)')
      WRITE(6,634)HT,T(1)
      DO 50 N=NO,NM,10
      HD=HT-(N-1)*DZ
      IF(T(1)-T(N).LT.0.001)GO TO 50
      WRITE(6,634)HD,T(N)
  634 FORMAT('0',T6,F8.3,T23,F8.3)
   50 CONTINUE
      WRITE(6,636)TM,TA
  636 FORMAT('0',T5,'MIXED LAYER TEMP =',F8.3,T35,
     1'ROOM TEMP =',F8.3//)
      WRITE(6,638)
  638 FORMAT('0',T5,'MIXED LAYER HEIGHT',T26,'INFLEXION HEIGHT',
     1T45,'TOTAL CELL HEIGHT',T66,'CELL WIDTH')
      WRITE(6,640)DM,DG,HT,SL
  640 FORMAT('0',T9,F8.3,T30,F8.3,T49,F8.3,T66,F8.3 )
      WRITE(6,771)
  771 FORMAT('0',T4,'FLUID HEAT',T18,'FLUID HEAT',T32,'SIDE WALL',T44
     1,'WALL INSULATION',T63,'TOP BOUNDARY',T79,'TOP INSULATION')
      WRITE(6,772)
  772 FORMAT(' ',T3,'CONDUCTIVITY',T19,'CAPACITY',T31,'CONDUCTION',
     1 T44,'STORAGE CAPACITY',T64,'CONDUCTION',T78,'STORAGE CAPACITY')
      WRITE(6,773)CF,SF,CST,SS,CRT,SR
  773 FORMAT('0',T3,+1PE10.3,T17,+1PE10.3,T30,+1PE10.3,T47,
     1OPF8.3,T63,+1PE10.3,T81,OPF8.3/)
      WRITE(6,774)QPC,TOL
  774 FORMAT('0',T5,'DIFFUSION HEAT TRANSITION =  ',F8.6,T43,
     1'CM*DEG C/SEC     TOL =',+1PE10.2)
      WCORR=WCORR/(SL*SL)
      WALP=WALP/(SL*SL)
```

```
      NTRAP=5
      DO 51 I=1,NTRAP
      SAP1=SAP1+I
      SAP2=SAP2+I*I
      SAP3=SAP3+I*I*I
      SAP4=SAP4+I**4
      SAP6=SAP6+I**6
   51 CONTINUE
      ATRAP=(SAP4-SAP6*SAP1/SAP3)/(SAP2-SAP4*SAP1/SAP3)
      ATPOP=(SAP3-SAP6*NTRAP/SAP3)-ATRAP*(SAP1-SAP4*NTRAP/SAP3)
C
C
C     LOWER BOUNDARY HEAT FLUX CALCULATION
C     ------------------------------------
C
 1975 CONTINUE
      QP2=QP
      GO TO(66,67,68,69)LQ
   66 QP=QGK
      GO TO 64
   67 QP=(QGK-SA*RTM/(SL*SL)-(WCORR+WALP)*(TM-TA+3.0))/SF
      IF(QP.LE.0.0) QP=1.0E-6
   64 IF(ET.LT.ETDF) QP=0.0
      GO TO 63
   68 CONTINUE
   65 QP=(7.98*(TH-TM)-8.30)*1.0E-03
      GO TO 64
   69 QP=QSN*(XETA*SIN(PI*ET/PER)-1.0)
      IF(QP.LE.-QSN) QP=-QSN
   63 CONTINUE
      IF(NWT.LE.NWT2)NWT=0.0
      NWT2=NWT
C
C
C     DIFFUSION REGION.TEMPERATURE PROFILE
C     ------------------------------------
C
      GAMMA=0.0
      M=NM-1
      LAM=1
      IF(QP.GT.QPC)LAM=LAMX
      IF(NI.EQ.NM)LAM=1
      IF(QP.GT.0.0)GO TO 79
      IF(QP2.LE.0.0)GO TO 73
   79 IF(QP.GT.QPC)GO TO 76
      DO 71N=NI,NM
   71 T(N)=TM
      NI=NI+1
      IF(NI.GT.NM)NI=NM
      DM=HT-(NI-1)*DZ
      GO TO 73
   76 IF(LAM.EQ.1) GO TO 73
      DSCAL=0.10*DM
      IF(DSCAL.LT.2.0*DZ) DSCAL=2.0*DZ
      VSCAL=(CVEXP*981.0*QP*DSCAL)**(1.0/3.0)
      GIN=(T(NI-1)-T(NI))/DZ
      RICH=CVEXP*981.0*GIN*DSCAL*DSCAL/(VSCAL*VSCAL)
      ZINT=CE2*DSCAL/(1.0+CE3*RICH)
      M4=ZINT/DZ+TOL
      M4=NI-M4-4
      M=M4
      GINZ=GIN
      I=0
  260 I=I+1
      IF(I.GE.NI-M4-4)GO TO 262
      GINT=(T(NI-I-1)-T(NI-I))/DZ
      IF(GINT.LE.GINZ)GO TO 262
      GINZ=GINT
      GO TO 260
  262 RICK=RICH*GINZ/GIN
      GAMMA=EMAX*DSCAL*VSCAL/(1.0+CT*RICK*SQRT(RICK))
   73 P(1)=0.0
      GO TO(60,61)LR
   60 P(1)=(CK*T(2)/DZ+WR*TA+WS*DZ*TA*0.5)-(CK*T(1)/DZ+WR*T(1)+WS
     1*DZ*0.5*T(1))
   61 CONTINUE
      DO 250N=2,M
  250 P(N)=(CK*(T(N+1)+T(N-1))/DZ+WS*TA*DZ)-(CK*2.0*T(N)/DZ
     1+WS*DZ*T(N))
      IF(LAM.EQ.2)GO TO 252
      P(NM)=(CK*T(NM-1)/DZ+WS*DZ*0.5*TA)-(CK*T(NM)/DZ+WS*DZ*0.5*T(NM))
      GO TO 245
  252 P4M=P(M4)/MCON
      DO 251 N=M4,NI
  251 P(N)=0.0
      DO 253N=M4+1,NI-1
      KK=NI-N
      XINT=(NI-1-N)*DZ
      YINT=1.0-XINT/ZINT
      IF(N.EQ.M4+1) GMB(KK+1)=0.0
      GMB(KK)=0.0
      IF(XINT.GE.ZINT)GO TO 253
      GMB(KK)=GAMMA*YINT*YINT
  253 CONTINUE
  254 DO 256K=1,MCON
      DO 257 N=M4+1,NI-1
      KK=NI-N
  257 PA(KK)=((CK+GMB(KK))*(T(N+1)+P(N+1)*DT/DSZ)/DZ+(CK+GMB(KK+1))
     1*(T(N-1)+P(N-1)*DT/DSZ)/DZ+WS*DZ*TA)-(T(N)+P(N)*DT/DSZ)
     2*((2.0*CK+GMB(KK)+GMB(KK+1))/DZ+WS*DZ)
      DO 258N=M4+1,NI-1
      KK=NI-N
  258 P(N)=PA(KK)/MCON +P(N)
```

```
C
C
C     CUBIC EXTRAPOLATION OF P(NI)
C     ----------------------------
C
      PAP1=0.0
      PAP2=0.0
      PAP3=0.0
      DO 55 I=1,NTRAP
      PAP1=PAP1+P(NI-I)
      PAP2=PAP2+P(NI-I)*I
      PAP3=PAP3+P(NI-I)*I*I*I
   55 CONTINUE
      PAP2=PAP2-SAP4*PAP1/SAP3
      PAP3=PAP3-SAP6*PAP1/SAP3
      PAP3=PAP3-ATRAP*PAP2
      P(NI)=PAP3/ATPOP
  256 P(M4)=K*P4M
  245 CONTINUE
      GOP=(T(NI-1)+P(NI-1)*DT/DSZ)/DZ-(T(NI)+P(NI)*DT/DSZ)/DZ
      G1=(T(NI-2)+P(NI-2)*DT/DSZ)/DZ-(T(NI-1)+P(NI-1)*DT/DSZ)/DZ
      G2=(T(NI-3)+P(NI-3)*DT/DSZ)/DZ-(T(NI-2)+P(NI-2)*DT/DSZ)/DZ
      G3=(T(NI-4)+P(NI-4)*DT/DSZ)/DZ-(T(NI-3)+P(NI-3)*DT/DSZ)/DZ
      G4=(T(NI-5)+P(NI-5)*DT/DSZ)/DZ-(T(NI-4)+P(NI-4)*DT/DSZ)/DZ
      G5=(T(NI-6)+P(NI-6)*DT/DSZ)/DZ-(T(NI-5)+P(NI-5)*DT/DSZ)/DZ
      G6=(T(NI-7)+P(NI-7)*DT/DSZ)/DZ-(T(NI-6)+P(NI-6)*DT/DSZ)/DZ
C
C
C     MIXED LAYER TEMPERATURE AND HEIGHT CALCULATIONS
C     -----------------------------------------------
C
      IF(QP.LE.0.0)GO TO 94
      SUM1=0.0
      D1=DM
      LAB=0
      CON=1.0
      IF(NI.EQ.NM)CON=2.0
      IF(NI.EQ.NM) TM=T(NI)+P(NI-1)*2.0*DT/DSZ
      T1=TM
   75 LAB=LAB+1
      D2=HT-(NI-2)*DZ
      T5=T(NI)+P(NI)*SUM1*CON/DSZ
      T2=T(NI-1)+P(NI-1)*SUM1/DSZ
      CY1=T2-T1
      CY2=P(NI-1)/DSZ
      CY3=BETA*(D1+D2)/2.0
      CY4=QP+(CK+GAMMA)*(T2-T5)/DZ-WS*(T1-TA)*(D1+D2)*0.5
      CY5=(CK+GAMMA)*(P(NI-1)-P(NI)*CON)/(2.0*DZ*DSZ)
      CY6=WS*(2.0*D2+D1)/6.0
      BY1=CY5-CY6*CY2
      BY2=CY4-CY6*CY1-CY2*CY3
      BY3=-CY1*CY3
      BY5=BY2*BY2-4.0*BY1*BY3
      IF(ABS(BY1).LE.TOL*TOL) GO TO 1601
      IF(BY5.LE.0.0) GO TO 1601
      SUM2=(-BY2+SQRT(BY2*BY2-4.0*BY1*BY3))/(2.0*BY1)+SUM1
      IF(SUM2.GE.DT)GO TO 74
      SUM1=SUM2
      NI=NI-1
      CON=1.0
      D1=D2
      T1=T(NI)+P(NI)*SUM1/DSZ
      GO TO 75
 1601 WRITE(6,1600)TM,GAMMA,CY1,CY2,CY3,CY4,CY5,CY6
 1600 FORMAT('0',T5,8(E11.3,2X))
      WRITE(6,1600)ZINT,DM,BY5,BY1,BY2,BY3,SUM2,T(NI)
      GO TO 198
   74 T6=T(NI-1)-T(NI)+DT*(P(NI-1)-P(NI)*CON)/DSZ
      T3=T(NI)+P(NI)*DT*CON/DSZ
      CX1=(QP+(CK+GAMMA)*(T6+T2-T5)/(2.0*DZ)-WS*(T1-TA)*0.5*D1)*
     1(DT-SUM1)
      CX2=WS*(T1-TA)*(DT-SUM1)*0.5
      CX3=D1*(WS*(DT-SUM1)/6.0+0.5*BETA)
      CX4=WS*(DT-SUM1)/3.0+BETA*0.5
      CX5=HT-(NI-1)*DZ+DZ*(T1-T3)/T6
      CX6=DZ/T6
      BX1=CX4*CX6
      BX2=CX3+CX4*CX5+CX2*CX6
      BX3=-CX1+CX2*CX5
      DLTM=(-BX2-SQRT(BX2*BX2-4.0*BX1*BX3))/(2.0*BX1)
      DLTM=BX3/(BX1*DLTM)
      DMA=CX5+CX6*DLTM
C
C
C     UPDATING OF TEMPERATURE VALUES
C     ------------------------------
C
   80 RTM=(T1+DLTM-TM)/DT
      TM=T1+DLTM
      IF((DMA-DM).LE.0.0)GO TO 82
      IF(SUM2.LT.DT )GO TO 82
      IF(QP.GT.QPC+5.0E-05)GO TO 83
      IF(QP.GT.QPC-1.0E-04)GO TO 82
      GO TO 83
   82 EH=(ET+DT)/60.0
      NWT=NWT+1
      WRITE(6,788)EH,TM,QP,DMA
  788 FORMAT('0','** TIME = ',F9.3,' MIXED TEMP = ',F9.5,' HEAT FLUX ='
     1,F11.8,' MIXED LAYER HEIGHT = ',F10.5)
      WRITE(6,790)NI,SUM1,P(NI),P(NI-1),P(NI-2)
  790 FORMAT(' ',' NI = ',I4,' SUM1 = ',+1PE12.5,' P(NI) = ',+1PE12.5,
     1' P(NI-1) = ',+1PE12.5,' P(NI-2) = ',+1PE12.5)
      WRITE(6,789)T(NI),T(NI-1),T1,DM,T(NI-2)
```

```
  789 FORMAT(' ',' T(NI) = ',F9.5,' T(NI-1) = ',F9.5,' T1 = ',F9.5,
     1' DM = ',F10.5,' T(NI-2) = ',F9.5)
      WRITE(6,791)LAB,DLTM,SUM2
  791 FORMAT(' ',' LAB = ',I6,' DLTM = ',+1PE12.5,' SUM2 = ',+1PE12.5/)
      IF(NWT.GT.10)GO TO 198
      GO TO 83
   94 P(NM)=P(NM)+QP
      NI=NM
      DMA=0.05
      RTM=P(NM)*2.0/DSZ
      TM=T(NM)+RTM*DT
   83 T(1)=T(1)+P(1)*DT/(BETAR*DZ*0.5)
      IF(LAM.EQ.2)M=NI
      DO 85 N=2,M
   85 T(N)=T(N)+P(N)*DT/DSZ
      IF(LAM.EQ.2)GO TO 247
      T(NM)=T(NM)+P(NM)*DT*2.0/DSZ
  247 CONTINUE
C
C
C     UPPER DIFFUSION REGION CONVECTION
C     ---------------------------------
C
      IF(LR.EQ.2)GO TO 210
      QR=WR*(T(1)-TA)
      IF(QR.LE.0.0)GO TO 210
      TMX=T(1)
      N=2
  212 IF(TMX.GE.T(N))GO TO 211
      TMX=T(N)
      N=N+1
      GO TO 212
  211 NG=N-1
      IF(TMX-T(1).LT.0.1) GO TO 210
      NR=NG
  213 DRA=(NR-1)*DZ
      SUM=0.0
      DO 214 N=2,NR
  214 SUM=SUM+(TMX-((T(N)+T(N-1))/2.0))*DZ
      PR=SUM/DRA
      PR1=TMX-T(NR+1)
      IF(PR1.GE.PR) GO TO 215
      NR=NR+1
      GO TO 213
  215 TAMB=TMX-PR
      DO 216 N=1,NR
  216 T(N)=TAMB
  210 CONTINUE
C
C
C     TEST IF TIME INTERVAL EXCEEDED
C     ------------------------------
C
      ET=ET+DT
      IF(DMA.GE.DM5)GO TO 95
   98 CONTINUE
      IF(ET.GE.EP)GO TO 100
      IF(T(1).GT.TM+0.01)GO TO 96
      WRITE(6,644)
  644 FORMAT('1',T5,'END POINT REACHED')
      EH=ET/60.0
      WRITE(6,788)EH,TM,QP,DMA
      GO TO 198
   95 EH=ET/60.0
      WRITE(6,788)EH,TM,QP,DMA
      DM5=DM5+1.0
      GO TO 98
   96 DM=DMA
      GO TO 1975
C
C
C     LOCATE MAXIMUM TEMPERATURE
C     --------------------------
C
  100 EP=EP+600.0
      NG=1
      TMX=T(1)
      GO TO (105,103)LR
  105 N=2
  104 IF(TMX.GE.T(N))GO TO 106
      TMX=T(N)
      N=N+1
      GO TO 104
  106 NG=N-1
      IF(NG.EQ.1)GO TO 103
      RTA=P(NG)/DSZ
      GO TO 108
  103 RTA=0.0
  108 CONTINUE
C
C
C     COMPUTE INFLEXION DEPTH
C     -----------------------
C
      GMM=(T(1)-T(2))/DZ
      DG=HT
      DO 109 N=3,NI
      GM1=(T(N-1)-T(N))/DZ
      IF(GM1.LE.GMM)GO TO 109
      GMM=GM1
```

```
      DG=HT-(N-1)*DZ
  109 CONTINUE
      IF(DI.LT.DMA)DI=DMA
C
C     COMPUTE APPARENT HEAT FLUXES
C     ----------------------------
C
  110 Q(1)=WR*(T(1)-TA)
      IF(LR.EQ.2)Q(1)=CK*(T(2)-T(1))/DZ-WS*DZ*(T(1)-TA)/2.0
      Q(2)=P(1)+P(2)/2.0+Q(1)
      IF(QP.GT.0.0)GO TO 116
      DO 117N=3,NM
  117 Q(N)=Q(N-1)+(P(N-1)+P(N))/2.0
      ERR=Q(NM)-QP +P(NM)/2.0
      GO TO 120
  116 DO 118N=3,NI-1
  118 Q(N)=Q(N-1)+(P(N-1)+P(N))/2.0
      DMC=(HT-(NI-2)*DZ-DMA)/DZ
      QM=Q(NI-1)+DMC*DMC*(P(NI)-P(NI-1))/2.0+DMC*P(NI-1)
      QME=QP-RTM*BETA*(DMA+DM)/2.0-WS*((TM-RTM*DT-TA)*(DMA+DM)*0.5
     1+RTM*DT*(2.0*DMA+DM)/6.0)
      QMA=(CK+GAMMA)*(T(NI)-T(NI-1))/DZ
      ERR=QMA-QME
C
C
C     ENTRAINMENT VELOCITY AND INTERFACE TEMP DIFFERENCE
C     --------------------------------------------------
C
      VEM=(DMA-DM)/DT
      IF(LB.GT.1)GO TO 113
      NR=NI*0.5
      GRAD=(T(NR+2)-T(NR-2))/(4.0*DZ)
      TAX=T(NR)-GRAD*(HT-(NR-1)*DZ-DM)
      DIA=DM
      DIT=TAX-TM
      DH=0.0
      IF(DIT.LE.0.0)GO TO 114
      SUM=(TAX*2.0-TM-T(NI-1)+GRAD*DMC*DZ)*DZ*0.5
      DO 119 N=NR+1,NI-1
  119 SUM=SUM+DZ*(T(NR)-GRAD*(N-NR-0.5)*DZ-(T(N)+T(N-1))*0.5)
      DH=SUM/DIT+DMA
      GO TO 114
  113 TAX=TMX
      GRAD=0.0
      DIA=HT-(NR-1)*DZ
      DIT=TAX-TM
      SUM=(TMX-T(NG+1))*DZ/2.0
      DO 122 N=NG+2,NI-1
  122 SUM=SUM+(TMX-(T(N)+T(N-1))/2.0)*DZ
      SUM=SUM+DMC*(TMX-(T(NI-1)+TM)/2.0)*DZ
      DH=SUM/(TMX-TM)+DMA
  114 CONTINUE
C
C
C     VALUES OF COEFFICIENT " K "
C     ---------------------------
C
      CKE=-QMA/QP
      CKM=BETA*VEM*DIT/QP
      CKH=(BETA*RTM*DH+WS*DH*(TM-TA))/QP-1.0
      IF(LB.EQ.1)CKH=(BETA*RTM*DH+GRAD*((DH-DMA)*BETA*VEM-CK)
     1+WS*((TAX-TA)*HT+GRAD*0.5*(HT-DMA)*(HT-DMA)-DIT*DH))/QP-1.0
  120 EH=ET/60.0
      WRITE(6,700)EH
  700 FORMAT('1',T5,'TIME=',F8.2,' MINS')
      GO TO(125,126,127)LB
  125 WRITE(6,702)
  702 FORMAT('+',T28,'LINEAR GRADIENT ,')
      GO TO 128
  126 WRITE(6,704)
  704 FORMAT('+',T29,'TWO LAYER CASE ,')
      GO TO 128
  127 WRITE(6,706)
  706 FORMAT('+',T29,'HYBRID PROFILE ,')
  128 IF(QP.LE.0.0)GO TO 130
      IF(QP.LE.QPC)GO TO 132
      WRITE(6,708)
  708 FORMAT('+',T46,'ENTRAINMENT PROFILE')
      GO TO 134
  130 WRITE(6,710)
  710 FORMAT('+',T46,'MOLECULAR DIFFUSION')
      GO TO 150
  132 WRITE(6,712)
  712 FORMAT('+',T46,'DIFFUSIVE ENTRAINMENT')
C
C
C     WRITE OUT THE MAJOR PARAMETERS
C     ------------------------------
C
  134 WRITE(6,719) VEM
  719 FORMAT('0',T5,'RATE OF RISE OF INTERFACE(VEM)=',+1PE12.5)
      WRITE(6,714)
  714 FORMAT('0',T5,'INTERFACE HEIGHT',T23,'HEATING HEIGHT',T39,
     1'INFLEXION HEIGHT',T57,'AMBIENT HEIGHT')
      WRITE(6,716)DMA,DH,DG,DIA
  716 FORMAT('0',T8,F8.3,T25,F8.3,T42,F8.3,T59,F8.3)
      N=(HT-DG)/DZ+TOL+1
      TDG=T(N)
      N=(HT-DH)/DZ+TOL+1
      TDH=T(N)
      WRITE(6,718)TM,TDH,TDG,TAX
  718 FORMAT('0','TEMPS=',T9,F7.3,T26,F7.3,T43,F7.3,T60,F7.3//)
      WRITE(6,720)
```

```
  720 FORMAT('0',T3,'INTERFACE TEMP DIFF',T25,
     1'MAX TEMP',T42,'MIXED TEMP',T59,'AIR TEMP')
      WRITE(6,722)DIT,TMX,TM,TA
  722 FORMAT('0',T9,F7.3,T26,F7.3,T43,F7.3,T60,F7.3//)
      WRITE(6,724)
  724 FORMAT('0',T5,'BASE HEAT FLUX',T23,'INTERFACE FLUX',
     1T40,'MIN TEMP CHANGE',T57,'MAX TEMP CHANGE')
      WRITE(6,726)QP,QMA,RTA,RTM
  726 FORMAT('0',T7,F9.6,T25,F9.6,T41,+1PE12.5,T58,+1PE12.5//)
      WRITE(6,728)
  728 FORMAT('0',T5,'ENTRAINMENT RATIOS')
      WRITE(6,730)CKE,CKH,CKM
  730 FORMAT('0',T5,'KE= ',F6.3,4X,'KH= ',F6.3,4X,'KM= ',F6.3//)
      GO TO 160
  150 N=(HT-DG)/DZ+TOL+1
      TDG=T(N)
      WRITE(6,732)
  732 FORMAT('0',T5,'BASE HEAT FLUX',T23,'INFLEXION HEIGHT',
     1T40,'MAX TEMP GRADIENT',T60,'INFLEXION TEMP',T80,'MIN TEMP')
      WRITE(6,734)QP,DG,GMM,TDG,T(NM)
  734 FORMAT('0',T8,F8.6,T26,F8.3,T44,F8.4,T64,F7.3,T80,F7.3//)
  160 WRITE(6,735)
  735 FORMAT('0',T28,'ACTUAL',T55,'RATE OF CHANGE',T73,'APPARENT'
     1,T89,'RATE OF CHANGE')
      WRITE(6,736)
  736 FORMAT(' ',T5,'HEIGHT',T13,'TEMPERATURE',T27,'HEAT FLUX',
     1T39,'TEMP GRADIENT',T55,'OF TEMPERATURE',T73,'HEAT FLUX'
     2,T88,'OF TEMP GRADIENT'/)
      WRITE(6,737)
  737 FORMAT(' ',T6,'(CM)' ,T15,'(DEG C)',T24,'(CM*DEG C/SEC)',
     1T41,'(DEG C/CM)',T57,'(DEG C/CM)',T71,'(CM*DEG C/SEC)'
     2,T89,'(DEG C /CM*CM)'/)
C
CC
C     WRITE OUT VALUES AT ONE CENTIMETER INTERVALS
C     --------------------------------------------
C
      GTO=(T(1)-T(2))/DZ
      QTO=-CK*GTO
      PTMP=P(1)/(BETAR*DZ*0.5)
      WRITE(6,738)HT,T(1),QTO,GTO,PTMP,Q(1)
      N=NO
      IF(LR.EQ.2)GO TO 156
      IF(NG.EQ.1)GO TO 154
  161 GT=(T(N)-T(N+1))/DZ
      IF(N.GE.NG)GO TO 158
      QTN=-CK*GT
      HD=HT-(N-1)*DZ
      PTMP=P(N)/DSZ
      WRITE(6,738)HD,T(N),QTN,GT,PTMP,Q(N)
  738 FORMAT('0',T3,F8.3,T15,F7.3,T26,F9.6,T40,F8.4,T57,+1PE10.3
     1,T72,0PF9.6,T91,F9.6)
      N=N+1/DZ
      IF(TMX-T(N).GE.0.01) GO TO 161
  158 CONTINUE
      HD=HT-(NG-1)*DZ
      WRITE(6,740)HD,T(NG),RTA,Q(NG)
  740 FORMAT('0',T3,F8.3,T15,F7.3,T28,'( MAXIMUM TEMPERATURE )',
     1T57,+1PE10.3,T72,0PF9.6)
  155 N=N+1/DZ
  154 IF(TMX-T(N).LT.0.02) GO TO 155
  156 IF(QP.GT.0.0) GO TO 170
  157 GT=(T(N-1)-T(N+1))/(2.0*DZ)
      SMZ=(T(N-1)+T(N+1)-2.0*T(N))/(DZ*DZ)
      QTN=-CK*GT
      HD=HT-(N-1)*DZ
      PTMP=P(N)/DSZ
      WRITE(6,738)HD,T(N),QTN,GT,PTMP,Q(N),SMZ
      N=N+1/DZ
      IF(N.LT.NM)GO TO 157
      GT=(T(NM-1)-T(NM))/DZ
      WRITE(6,742)T(NM),QP,GT
  742 FORMAT('0',T4,'( BASE )',T15,F7.3,T27,F8.6,T40,F8.4//)
      GO TO 180
  170 GT=(T(N-1)-T(N+1))/(2.0*DZ)
      SMZ=(T(N-1)+T(N+1)-2.0*T(N))/(DZ*DZ)
      XINT=(NI-1-N)*DZ
      GAMB=0.0
      GAMC=0.0
      IF(GAMMA.LE.0.0)GO TO 173
      IF(XINT.GE.ZINT)GO TO 173
      KK=NI-N
      GAMB=GMB(KK)
      IF(XINT.GE.ZINT-DZ)GO TO 173
      GAMC=GMB(KK+1)
  173 QTN=((CK+GAMB)*(T(N+1)-T(N))+(CK+GAMC)*(T(N)-T(N-1)))/(2.0*DZ)
      HD=HT-(N-1)*DZ
      PTMP=P(N)/DSZ
      WRITE(6,738)HD,T(N),QTN,GT,PTMP,Q(N),SMZ
      N=N+1/DZ
      IF(T(N).LE.TM+DIT*0.75) N=N-0.5/DZ
      IF(N.LE.NI-1)GO TO 170
C
CC
C     MIXED LAYER VALUES PRINTOUT
C     ---------------------------
C
      GT=(T(NI-1)-T(NI))/DZ
      SMZ=(T(NI-2)+T(NI)-2.0*T(NI-1))/(DZ*DZ)
      PTMP=(P(NI-1)+DMC*P(NI)-DMC*P(NI-1))/DSZ
      WRITE(6,738)DMA,TM,QMA,GT,PTMP,QM,SMZ
      WRITE(6,744)
  744 FORMAT(' ',T4,'INTERFACE VALUES')
```

```
      N=NM
172   N=N-5/DZ
      IF(N.GT.NI)GO TO 172
174   N=N+5/DZ
      HD=HT-(N-1)*DZ
      Q(N)=QP-RTM*HD*BETA-WS*(TM-TA)*HD
      WRITE(6,738)HD,TM,Q(N)
      IF(N.LT.NM)GO TO 174
      WRITE(6,746)
746   FORMAT('+',T41,'( BASE )'///)
      WRITE(6,792)NI,T(NI),T(NI-1),T(NI-2),T(NI-3),T(NI-4)
792   FORMAT('0',T5,' T(NI =',I4,' ) AND ABOVE  ',F9.5,2X,F9.5,2X,
     1F9.5,2X,F9.5,2X,F9.5)
      WRITE(6,794)GOP,G1,G2,G3,G4,G5,G6
794   FORMAT('0',T5,' GO =',F10.7,' G1 =',F10.7,' G2 =',F10.7,' G3 =',
     1F10.7,' G4 =',F10.7,' G5 =',F10.7,' G6 =',F10.7)
      WRITE(6,793) P(NI),P(NI-1),P(NI-2),P(NI-3),P(NI-4),P(NI-5),
     1P(NI-6)
793   FORMAT('0',T5,'P0 =',+1PE12.4,'P1 =',E12.4,'P2 =',E12.4,'P3 =',
     1E12.4,'P4 =',E12.4,'P5 =',E12.4,'P6 =',E12.4/)
      IF(LB.EQ.1)GO TO 176
      WDM=ALOG10(DMA)
      WDH=ALOG10(DH)
      WDT=ALOG10(DIT)
      WRITE(6,748)
748   FORMAT('0',T9,'LOG(DMA)',T22,'LOG(DH)',T34,'LOG(DIT)')
      WRITE(6,750)WDM,WDH,WDT
750   FORMAT('0',T7,F9.5,T20,F9.5,T32,F9.5/)
176   CONTINUE
      WRITE(6,659)QME
659   FORMAT('0',T8,'APPARENT HEAT FLUX INTO MIXED LAYER',F10.6)
      IF(LAM.EQ.2)GO TO 184
      N=NO
186   N=N+10
      IF(N.LT.NI) GO TO 186
      IF(N .GT.NM-12) GO TO 184
      TT1=T(N)
      HT1=HT-(N-1)*DZ
      TT2=T(N+10)
      HT2=HT-(N+9)*DZ
      WRITE(6,760)
760   FORMAT('0',T5,'NEXT TWO CONDUCTION TEMPERATURES BELOW INTERFACE')
      WRITE(6,761)HT1,TT1
      WRITE(6,761)HT2,TT2
761   FORMAT('0',T3,F8.3,T15,F7.3)
184   CONTINUE
180   WRITE(6,752)ERR
752   FORMAT('0',T8,'ERROR IN HEAT FLUX =',+1PE15.7)
      WRITE(6,657) GMM
657   FORMAT('0',T8,'MAX TEMP GRADIENT ',F7.4)
C
C
C     TANK PROPERTIES PRINTOUT
C     ------------------------
C
      GO TO (230,231,232,233)LQ
230   WRITE(6,776)QGK
776   FORMAT('0',T5,'*** CONSTANT BOUNDARY HEAT FLUX CASE',T45,
     1'( QP =',F10.6,' CM*DEG C/SEC )')
      GO TO 234
231   WRITE(6,777)QGK,SA
777   FORMAT('0',T5,'*** CONSTANT GLASS PLATE HEAT FLUX ( QG=',F10.6,
     1' CAL/CM*CM*SEC )',T75,'ALUMINIUM STORAGE =',F10.3,' CAL/DEG C')
      GO TO 234
232   WRITE(6,778) TH
778   FORMAT('0',T5,'*** CONSTANT WATER BATH TEMPERATURE ( TEMP =',F8.2,
     1' DEG C )',T68,'QP=(7.98*(TH-TM)-8.3)*1.0E-03')
      GO TO 234
233   QSS=(XETA-1.0)*QSN
      PERH=PER/3600.0
      WRITE(6,779)QSS,QSA,PERH,XETA
779   FORMAT('0',T5,'*** SINUSOIDAL HEAT INPUT',T32,'( MAX =',
     1F9.5,T56,'MIN =',F9.5,' )',T74,'PERIOD =',F8.3,
     2' HOURS',T100,'XETA =',F6.2)
234   CONTINUE
      IF(LAM.EQ.1)GO TO 246
      PECLET=DSCAL*VSCAL/CK
      WRITE(6,784)RICH,PECLET,GAMMA,ZINT
784   FORMAT('0',T5,'RICHARDSON NO.=',F7.3,4X,'PECLET NO.=',F8.3,
     14X,'GAMMA=',+1PE11.3,4X,'ZINT=',0PF6.3/)
246   CONTINUE
      WRITE(6,780)EH
780   FORMAT('0',T5,'TIME =',F8.2,' MINS')
      IF(EP.GT.3.E+4)GO TO 198
      GO TO 96
198   CONTINUE
      STOP
      END
```

Classn:

ENTRAINMENT BY PENETRATIVE CONVECTION AT LOW PÉCLET NUMBERS

Richard A. Denton

ABSTRACT: Theoretical, experimental and numerical analyses of the temporal behaviour of a stable two-layered temperature distribution heated from below are reported. Molecular diffusion is shown to be important. Also presented are an empirical relationship for turbulent interfacial buoyancy transfer and a new graphical form for thermal convection data.

U. of Cant. C. Eng. Dept. Res. Report No. 78/1